MASSACHUSETTS INSTITUTE OF TECHNOLOGY

APOLLO

GUIDANCE, NAVIGATION AND CONTROL

PREPARED UNDER
CONTRACT NAS 9-4065, TASK ORDER 42
FOR NASA MANNED SPACECRAFT CENTER
HOUSTON, TEXAS
UNDER TECHNICAL DIRECTION OF
NASA GODDARD SPACE FLIGHT CENTER
GREENBELT, MARYLAND

MIT
CAMBRIDGE MASSACHUSETTS 02139

CHARLES STARK DRAPER LABORATORY

MASSACHUSETTS INSTITUTE OF TECHNOLOGY

APOLLO

GUIDANCE, NAVIGATION AND CONTROL

Approved: ______________ Date: 8 Feb 1972
G. OGLETREE, DEPUTY ASSOCIATE DIRECTOR
SIMS Trade Study Project Leader

Approved: ______________ Date: 8 Feb 72
N. E. SEARS, ASSOCIATE DIRECTOR
Director, Apollo G & N Systems

Approved: ______________ Date: 8 Feb 72
D. G. HOAG, ASSOCIATE DIRECTOR
Director, Apollo Project

Approved: ______________ Date: 10 Feb 72
R. R. RAGAN, DEPUTY DIRECTOR
Director, NASA Programs

E-2630

INTERIM TECHNICAL REPORT No. 2 CANDIDATE CONFIGURATION TRADE STUDY, STELLAR-INERTIAL MEASUREMENT SYSTEM (SIMS) FOR AN EARTH OBSERVATION SATELLITE (EOS)

by

G. Ogletree, J. Coccoli, R. McKern
M. Smith and R. White

31 January 1972

MIT CHARLES STARK DRAPER LABORATORY

CAMBRIDGE, MASSACHUSETTS, 02139

Prepared Under Contract NAS 9-4065, Task Order 42, for NASA Manned Spacecraft Center, Houston, Texas, under Technical Direction of NASA Goddard Space Flight Center, Greenbelt, Maryland.

ACKNOWLEDGEMENT

This report was prepared under DSR Project 55-39200, sponsored by the Manned Spacecraft Center of the National Aeronautics and Space Administration through Task Order No. 42 of Contract NAS 9-4065 with the Massachusetts Institute of Technology. Technical Direction of the effort was provided by Mr. John W. Kelly and Dr. Arun K. Guha of NASA Goddard Space Flight Center.

Authorship of the technical sections was as follows: Section Three - Richard A. McKern, IARU Studies Task Leader; Section Four - Joseph D. Coccoli, Star Sensor Studies Task Leader; Section Five - Robert L. White, Star Availability Studies and Error Analysis and Simulation Studies Task Leader; and Section Six - Mark A. Smith, Technical Advisor.

Technical assistance or supporting authorship in these sections included: Section Three: Harry McOuat and Martin Landey - General Writing and Editorial Assistance; George L.Suntheimer and Arthur J. Boyce - SIMS-D IARU Mechanical Design Study; Alfred D. Hoch - SIMS-D IARU Thermal Design Study; Roscoe Cooper - Resolver/Inductosyn Evaluation; Raymond J. Cushing - SIMS-D Electronics, including Readout Electronics; Julius Feldman - Instrument Error Modeling; and Howard Musoff - IARU Reliability Considerations. Section Four: Lawrence Yorgy - Star Tracker Investigations; George Karthas - Optics Consultation; and Peter C. Vernam - Programming and Computation in Support of Subsection 4.2.0. Section Five: Frederick D. Grant - SIMS Candidate Math Models; Peter C. Vernam - Star Availability Studies; Dr. Donald C. Fraser - Data Processing Methods; and Ronald A. Harris - Gyro Error Models.

Glenn Ogletree wrote Sections One and Two and prepared and edited the overall report for publication. The report was typed by Gladys Grover. Illustrations were prepared by William Eng and David Farrar. Publication was accomplished by the MIT/CSDL Technical Publications Department.

E-2630

INTERIM TECHNICAL REPORT NO. 2-- CANDIDATE CONFIGURATION TRADE STUDY STELLAR-INERTIAL MEASUREMENT SYSTEM (SIMS) FOR AN EARTH OBSERVATION SATELLITE (EOS)

ABSTRACT

A nine month trade study for the NASA Manned Spacecraft Center by the Charles Stark Draper Laboratory Division of the Massachusetts Institute of Technology, under the technical direction of NASA Goddard Space Flight Center, is reported on near the end of the seventh month.

The ten candidate SIMS configurations, defined in the first interim report in November 1971, have been reduced to three - as documented in the first and, now, the second interim reports - in preparation for the final trade comparison. The final report, planned for 31 March 1972, together with these interim reports, is intended to facilitate NASA decisions pertaining to gimbaled versus structure-mounted star sensors, and combinations thereof suitable for the EOS and similar applications.

Whereas the first interim report emphasized SIMS configuration definitions and preliminary trade considerations, this second report emphasizes subsystem design trades, star availability studies, data processing (smoothing) methods, and the analytical and simulation studies at subsystem and system levels from which candidate accuracy estimates will be presented in the final report. It is planned that the final report will contain a tabular comparison of the three candidates (SIMS-A: structure-mounted gyros with structure-mounted star mapper; SIMS-B: structure-mounted gyros with gimbaled star tracker; and SIMS-D: gimbaled gyros with structure-mounted star mapper), with supporting technical discussions, on the basis of which NASA can proceed to the SIMS configuration selection using program- and spacecraft-related weighting factors.

by G. Ogletree, J. Coccoli, R.McKern,
M. Smith and R. White

Charles Stark Draper Laboratory Division
Massachusetts Institute of Technology
Cambridge, Massachusetts 02139

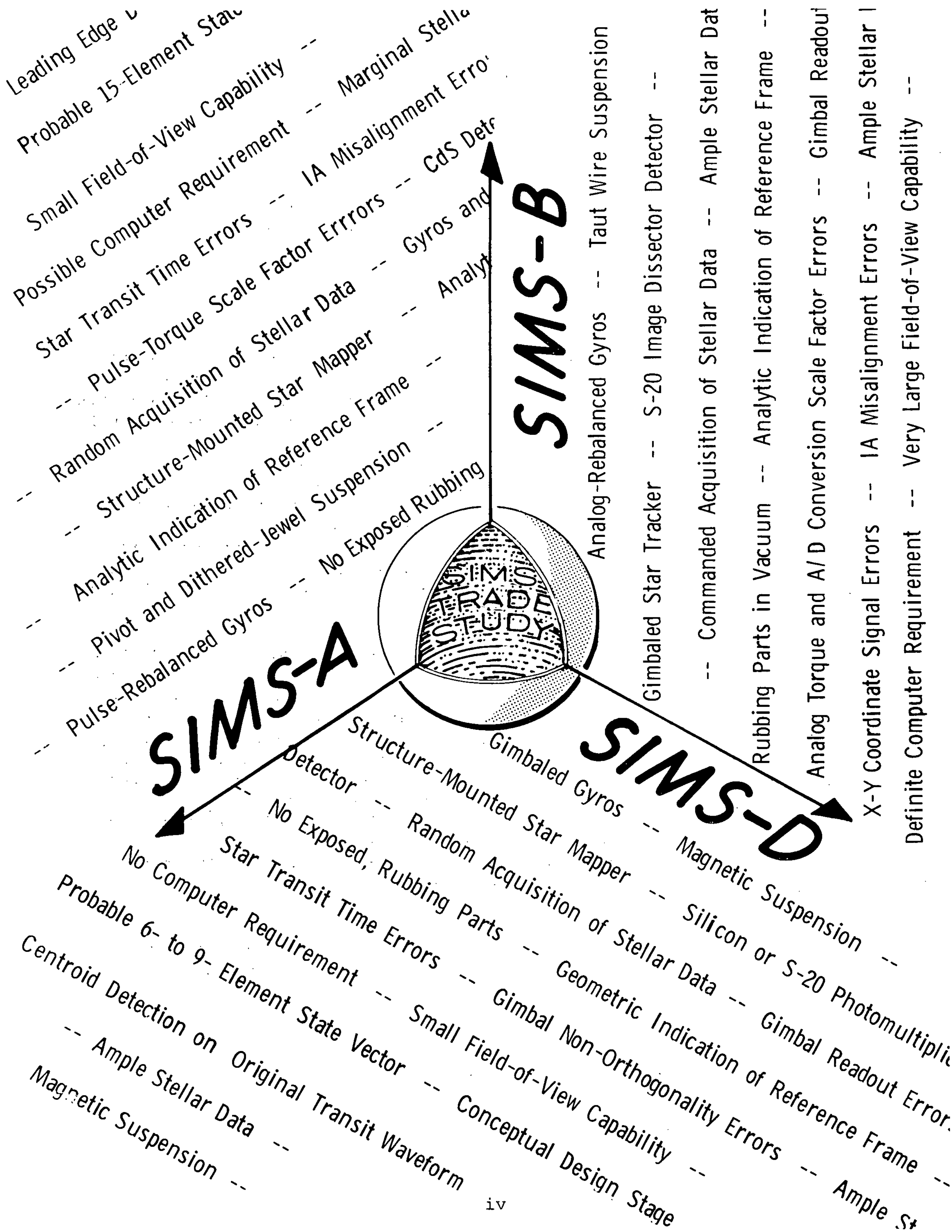
SIMS TRADE STUDY
SIMS-A
SIMS-B
SIMS-D
Probable 15-Element State
Small Field-of-View Capability -- Marginal Stellar
Possible Computer Requirement -- IA Misalignment Errors
Star Transit Time Errors -- CdS Dete
-- Pulse-Torque Scale Factor Errrors -- Gyros and
Random Acquisition of Stellar Data -- Analyt
-- Structure-Mounted Star Mapper --
Analytic Indication of Reference Frame --
-- Pivot and Dithered-Jewel Suspension --
Pulse-Rebalanced Gyros -- No Exposed Rubbing
Analog-Rebalanced Gyros -- Taut Wire Suspension
Gimbaled Star Tracker -- S-20 Image Dissector Detector --
-- Commanded Acquisition of Stellar Data -- Ample Stellar Dat
Rubbing Parts in Vacuum -- Analytic Indication of Reference Frame --
Analog Torque and A/D Conversion Scale Factor Errors -- Gimbal Readout
X-Y Coordinate Signal Errors -- IA Misalignment Errors -- Ample Stellar
Definite Computer Requirement -- Very Large Field-of-View Capability --
Gimbaled Gyros -- Magnetic Suspension --
Structure-Mounted Star Mapper -- Silicon or S-20 Photomultiplie
Detector -- Random Acquisition of Stellar Data -- Gimbal Readout Error
No Exposed, Rubbing Parts -- Geometric Indication of Reference Frame --
Star Transit Time Errors -- Gimbal Non-Orthogonality Errors -- Ample St
No Computer Requirement -- Small Field-of-View Capability --
Probable 6- to 9- Element State Vector -- Conceptual Design Stage
Centroid Detection on Original Transit Waveform
-- Ample Stellar Data --
Magnetic Suspension --

PREFACE

This report is rendered at a point of significant and demonstrable progress in primary task areas of the SIMS Trade Study. Star availability studies, now complete, are providing predicted insights in terms of requirements imposed on SIMS gyros. A clearer understanding of how errors arise and are propagated in each SIMS candidate is resulting from math modeling and simulations. Detailed analysis and design studies while answering some questions have posed new ones, such as: "How is adequacy of stellar data affected by a need to estimate additional error and error rate biases?"; "Does response time, as well as responsivity, vary along a CdS slit detector's length?"; etc.

One important result to date is an increasing confidence among team members, that the SIMS attitude determination accuracy goal of $.001^{o}$ (1σ)/axis may indeed be realizable in the EOS environment. The validity of that confidence remains to be tested, of course. (Few initially felt that better than $.003^{o}$, or even $.005^{o}$ (1σ)/axis would be reasonable to expect in a rotating, librating, long-life satellite.)

The essential question appears to be what should be gimbaled and how should it or they be gimbaled, rather than whether or not to gimbal the SIMS sensors. Advantages apparently to be gained in structure-mounting SIMS gyros are diminished when a star availability study shows that star sensor gimbaling may be the most practical, companion choice. (Conversely, the advantages of structure-mounting the star sensor <u>may</u> be shown to be available to the designer only if the gyros are gimbaled.) Similarly, whether it is preferable to gimbal gyros or star sensors is put into better perspective by noting that the vacuum lubrication of rubbing parts and the inclusion of an on-board computer are quite possibly attendant upon star sensor - but not gyro - gimbaling in a SIMS application.

This Trade Study has been an interesting, educational and challenging one. The search for guidelines of a general nature continues.

CONTENTS

CONTENTS (Cont.)

CONTENTS (Cont.)

CONTENTS (Cont.)

CONTENTS (Cont.)

CONTENTS (Cont.)

CONTENTS (Cont.)

CONTENTS (Cont.)

ILLUSTRATIONS

ILLUSTRATIONS (Cont.)

ILLUSTRATIONS (Cont.)

ILLUSTRATIONS (Cont.)

ILLUSTRATIONS (Cont.)

TABLES

TABLES (Cont.)

SECTION 1

INTRODUCTION AND SUMMARY

1.1 INTRODUCTION

This report has been prepared as the Second Interim Technical Report covering work from 1 November 1971 through 21 January 1972, performed by the Charles Stark Draper Laboratory Division of the Massachusetts Institute of Technology (MIT/CSDL), on the "Candidate Configuration Trade Study--Stellar-Inertial Measurement System (SIMS) for a Proposed Earth Observation Satellite (EOS)" for the NASA Goddard Space Flight Center (GSFC). A prior Interim Technical Report[85*] and six Monthly Letter Reports [58-60, 86-88] have been published. Three additional Monthly Letter Reports and a Final Report are planned. Excerpts from the MIT/CSDL Technical Proposal No. 71-173, dated June 1971, including the basic statement of work and CSDL comments thereon, were provided as Appendix **A** of ref. 85. The first interim technical report documented the reference data assimilation and candidate configuration definition phases of the study. This report contains configuration and subsystem design studies and star availability and error analysis studies. Both of the interim reports provide some information relative to the Configuration Trades aspects of the study. The treatment of that subject is planned to be completed in the Final Report, together with an overview of the work. Any MIT recommendations proceeding from the study will also appear in the Final Report.

---

*Superscripts refer to similarly-numbered references in Section 7, REFERENCES. Note that reference numbers 1 through 84 called out in the the prior report, reference 85, are continued herein.

1.1.1 BACKGROUND

Section 1.1.1 of ref. 85 provided a brief description of the NASA EOS program and described the relevance of the SIMS Trade Study at MIT to that program. As footnoted on p. 1-11 thereof, certain EOS program and Thematic Mapper data presented is in need of review and revision. For example (ref. 89), an image surface-scanning thematic mapper design was tentatively selected by NASA to eliminate the need for a massive plane mirror nodding with extreme precision over an appreciable angle at 10 Hz. Also, further NASA work is currently in progress to more completely define and specify the thematic mapper to be developed for EOS. Such errors as these in the background descriptions of ref. 85 do not seriously impact the design or other decision processes in the SIMS Trade Study at MIT. Hence, no effort will be expended here to update the prior material. Interested readers are referred to NASA EOS Program documents for more current descriptions of the evolving definition of EOS and its payloads and subsystems.

In view of certain EOS program delays such as those associated with the thematic mapper studies, NASA/GSFC was able to grant an MIT request for a one month extension of the original contract period to improve the content and scope of this and subsequent reports and technical presentations.

1.1.2 PROJECT ACTIVITIES

The SIMS Study Team continues to function in the organizational manner indicated in Fig. 1-4 of ref. 85.

Efforts in this reporting period were concentrated in preliminary studies of each of the configurations using the data previously acquired and assimilated (refs 8 through 57) and the internal SIMS-related documents prepared from those and other sources (refs 62-76, 78, 83). This work has led to the convergence on a single generic type of SIMS-D candidate: fully-gimbaled gyros and a body-fixed star mapper (as in SIMS-D1-A, ref 85). With the elimination of SIMS-C in ref. 85 as well as the MIT introduction and elimination of SIMS-E therein, the candidates are reduced to three in this report, as Final Report preparation begins:

SIMS-A	Strapped Down Gyros and Strapped Down Star Mapper	Derived from Honeywell SPARS
SIMS-B	Strapped Down Gyros and Gimbaled Star Tracker	Derived from TRW PPCS/PADS
SIMS-D	3-Axis Gimbaled Gyro Platform and Strapped Down Star Mapper	Subsystems being Defined by MIT

The detailed work of the Task Leaders is reported on in this document, and will be further amplified as necessary in the Final Report. Again in this report as in ref. 85, the Technical Advisor has provided an overview section dealing with configuration trade considerations. For the Final Report, he will compile the trade tabulation data from the cognizant engineers. With the Project Leader, he and the Consultants and Task Leaders will ensure that the accomplishment and the presentation of final trade comparisons is as adequately, accurately and objectively done as can be accomplished within available time and resources.

Three monthly letter reports, ref's 86 through 88, provided NASA with an account of technical and financial activities and status during this reporting period. The First Technical Review Meeting was held at NASA/GSFC on 11 November 1971, one month later than originally planned, as noted in ref. 85, p. 1-12. That meeting was documented in ref. 87.

Some of the GSFC inputs to MIT, then and since, have affected the course of the study and are discussed explicitly or implicitly in this report. Specifically, the following inputs by GSFC personnel, on 11 November and subsequently, are discussed in the indicated sections of this report:

GSFC Input	See Subsection
1. Inductosyn gimbal angle readout is flagged as problem area.	3.3.2.2.2
2. Large scale factor error in pitch should not have to be incurred.	3.1.2.4; and Appendix A
3. Advantages and disadvantages of strapping down or gimbaling gyros should be explicitly stated.	3.3.1; 6.3; and 6.4
4. MIT may assume that continuous SIMS data is available on the ground if it is necessary	Implicitly in 5.4
5. Thermal studies may be based on a ±2°C variation about nominal at mounting structure.	3.3.2.2.3
6. MIT should determine if "pulse-bursting" will be a problem in SIMS-A.	3.1.2.1
7. Effects of launch environment should be discussed.	3.3.2

The star availability studies reported on in subsection 5.3 herein are also to be accomplished independently by GSFC personnel, using star catalogs in common use at GSFC. This is to increase mutual confidence in the results obtained. All MIT information pertaining to the study has been made available to GSFC (as reported on in refs. 87 and 88). It is understood that the GSFC results will be formatted similarly to MIT's for ease of comparison.

With reference to SIMS-A studies, three 1968 Honeywell Customer Engineering Letters (references 90-92) were obtained from Honeywell Aerospace Division. Copies were disseminated to team members and were forwarded to Dr. A. Guha at GSFC.

This report was delayed one month, as will be the Second Technical Review Meeting at GSFC (planned for 18 February 1972) and the Final Report (planned for 31 March 1972.)

1.2 SUMMARY

(The material in this subsection supersedes the similar material in subsection 1.2 of ref. 85; it reflects the updating permitted by the viewpoint near the end of the seventh month of the study.)

1.2.1 SUMMARY DESCRIPTION OF THE CANDIDATES

Four categories of candidate SIMS configurations were originally required to be evaluated and compared in this study:

Category	Chief Characteristics
A	Strapped Down Gyros and Star Sensors
B	Strapped Down Gyros; Gimbaled Star Sensor
C	No Gyros; Gimbaled Cluster of Star Trackers
D	Gimbaled Gyros; Gimbaled or Strapped Down Star Sensor(s)

An additional category, Category E, was defined in ref. 85 as one of potential interest, as follows:

E	No Gyros; Individual, Separately-Gimbaled Star Sensors

and Category D was subdivided in ref. 85 as follows:

D1-A	Gyros Fully Gimbaled; Strapped Down Star Sensor(s)
D1-B	Gyros Fully Gimbaled; Gimbaled Star Sensor
D2-A	Gyros Gimbaled in One Axis; Strapped Down Star Sensor(s)
D2-B	Gyros Gimbaled in One Axis; Gimbaled Star Sensor

D1-B and D2-B were further subdivided in ref. 85 according to star sensor moding, as follows:

D1-B1	Gyros Fully Gimbaled; Gimbaled Star Sensor; Star Sensor Programmed in Roll to Acquire Known Stars
D1-B2	Gyros Fully Gimbaled; Gimbaled Star Sensor; Star Sensor Executes Roll Scan, Acquires and Tracks Stars at Random
D2-B1	Gyros Gimbaled in One Axis; Gimbaled Star Sensor; Star Sensor Programmed in Roll to Acquire Known Stars

D2-B2 Gyros Gimbaled in One Axis; Gimbaled Star Sensor; Star Sensor Executes Roll Scan, Acquires and Tracks Stars at Random

Thus, ten candidate categories (A,B,C,D1-A,D1-B1,D1-B2, D2-A, D2-B1,D2-B2,E) were defined as potential SIMS design approaches at the time of the First Interim Technical Report, ref. 85. Of these, Categories C and E were recommended therein to be dropped from further study, as discussed in para's 2.4, and 2.6 of ref. 85. NASA accepted the recommendation. Categories D1-B2 and D2-B2 were given reduced emphasis in the earlier report, due to the unavailability of a suitable star sensor candidate for them, as indicated in para's 2.5.3 and 2.5.6 of ref. 85. The remaining six (A,B,D1-A,D1-B1,D2-A, D2-B1) were retained as primary candidates as the study continued. (Note, however, that the effort to define a -B2 type star sensor was continued for a time.)

In the study segment reported on herein, the candidates have, as mentioned in subsection 1.1.2, been further reduced in number to three (A,B, and D1-A) as a result of selection of the -D1- rather than the -D2-type of SIMS-D gyro configuration, and because of the determination that not only a gimbaled star tracker but also a star mapper would meet the SIMS-D star sensor requirements, regardless of choice of gyro configuration. (See sections 3. and 4. of this report where the fully-gimbaled IARU and star mapper selections for SIMS-D are documented.) In the remainder of the study effort, the three final candidates will be designated simply as SIMS-A, SIMS-B, and SIMS-D, as was indicated in subsection 1.1.2.

1.2.2 TECHNICAL APPROACH TO THE TRADE STUDY

As noted in para 1.1.1 of ref. 85, the aim of the present study is to provide "adequate data which may be used (by NASA) to select an 'optimum' configuration (of a SIMS) for a particular (the EOS-C or similar) application".* The need is for MIT to define the several configurations, to establish appropriate figures of merit for each, at least in terms of trade factors established by NASA, and to present these findings in a tabular or other appropriate manner,** supported by narrative discussion as required to clarify the points of comparison.

The actual NASA trade study to select an optimum approach will require knowledge of the proper weight for each of the several trade parameters. The weights are not yet established by NASA, and in any case are not likely to be available to MIT during the contract period. Therefore, it would be relatively meaningless for MIT to conduct such a trade study using only the results of this work and to produce a specifically-recommended approach. However, in the course of studying the various candidates and preparing their figures of merit, etc., there will undoubtedly be trade comparisons that are general in nature and can lead to some fairly strong, if not specific, recommendations for NASA to consider. [An example was the recommendation to discontinue investigations pertaining to SIMS-C (see para's 1.2.1 and 2.3 of ref. 85.)]

The outline below indicates the elements of the step-by-step approach shown in ref. 85, subsection 1.2.2, for achieving the objectives of this study, and thus establishes the goals of the various task areas. In view of time and personnel-availability limitations, it was then and still is

---

*See Appendix A, para. II.1, of ref. 85

**See Appendix A of ref. 85, and Section 6 of this report.

anticipated that not all of the indicated steps will be accomplished. Every effort will be made by the study team to fulfill all essential contract objectives. The outline follows:

I. Define stellar data requirements and availability
   A. Define fields of view and moding of star sensors
   B. Define stellar update requirements
   C. Conduct star availability studies
      1. Establish star catalog for each detector
      2. Impose field-of-view, moding constraints
      3. Include representatives of all orbits
      4. Select "typical" and "average" cases
         a. Repeat for several limiting magnitudes
      5. Prepare data inputs for simulations

II. Define SIMS candidate configurations
   A. Prepare functional block diagrams
      1. Identify major subsystems, components
      2. Include signal flow
      3. Include operating modes
      4. Include switching logic
      5. Include any necessary modifications to existing design work
   B. Prepare interface specifications
      1. Electrical
      2. Mechanical
      3. Thermal
      4. Data-handling
   C. Define ground control/command operations
   D. Define data-processing requirements
   E. Perform preliminary design
      1. Define specifications for major components

2. Specify
    a. Performance
    b. Weight
    c. Power
    d. Telemetry requirement
    e. Field-of-view requirement
3. Specify modifications to existing candi date configurations

F. Develop error models
1. Emphasize error components that increase with time

III. Perform error analyses

A. Simulate realistic environment
1. Spacecraft rotational dynamics
2. Typical and average case stellar updates

IV. Perform sensitivity analyses

A. Determine effect on SIMS performance, power, reliability, etc.
1. Field-of-view available
2. Gyro performance variation
3. Star sensor performance variation
4. Other expected parametric variations

V. Prepare Candidate Configuration Comparisons

A. Tabulate and/or otherwise present:
1. Cost (development and production)
2. Accuracy
3. Weight
4. Power requirement
5. Telemetry requirement
6. Total unobstructed field-of-view required
7. Simplicity of design and reliability

8. Modularity of design and growth potential
9. Cost of ground support equipment
10. Complexity of ground control/command/data processing
11. System availability

B. Provide supporting engineering discussions

VI. Conduct limited trade study

A. Emphasize potential for achieving performance goals

B. Discuss availability and development risks

VII. Develop and present any MIT recommendations

- - - - - - - - - - - -

In Section 2, the configuration candidates are discussed briefly, at their present levels of definition. Sections 3, 4 and 5 provide descriptions by the Primary Task Leaders of the work in their task areas. In Section 3, evaluations of SIMS-A and -B IARUs and the design studies of SIMS-D IARUs are presented. Section 4 contains a comprehensive treatment of star sensor characteristics and errors. Included are detailed comparative data on many of the candidates. The error studies are reported on in Section 5, including a complete presentation of the Star Availability Studies and results to date of efforts to model all the SIMS candidates and to simulate their performance in realistic orbital situations. The preliminary trade considerations presented in Section 3 of ref. 85 are updated briefly in Section 6 of this report, in light of the current study status and pending the vital output of the error simulations after final formulation of the error models is completed.*

*On the latter point, for example, see the footnote on page 5-57 in Section 5.

In Appendix A, a new concept is presented for enabling a strapped down gyro loop to adapt automatically to a constant (e.g. orbital rate) component of its angular velocity input, and thereby to avoid or reduce the scale factor error resulting from pulse-rebalancing of the gyro (or from digitally-encoding an analog rebalance loop's D.C. torquing current) in the presence of such constant input rate component. The star catalog developed for the several detectors (see subsection 5.3.4) is included as Appendix B. The specialized plots discussed in subsection 5.3.5 for presenting the results of the star availability studies for visual evaluation are displayed in Appendix C. Sections 7 and 8 list the References and Distribution, respectively, of this report.

SECTION 2

SIMS CONFIGURATIONS

2.1 INTRODUCTION

In section 2 of ref. 85, each SIMS candidate was presented from an essentially common viewpoint; i.e., the presentation of each was developed according to a common plan, to the extent that the configurations and their levels of definition were appropriate to that approach. The candidate presentations were preceded by a brief exposition of the basic principles underlying SIMS operation. This was to emphasize viewing the spacecraft-borne hardware of an operational SIMS as, essentially, a data-gathering system, with the data utilization being done on the ground, "after the fact", using smoothing techniques to improve the accuracy of attitude estimation.

The presentation of the candidates in Section 2 of ref. 85 was - more by coincidence than by design - more complete in treating the candidates rejected therein (SIMS-C and -E) and the candidates emerging in this report as the primary candidates for final comparison (SIMS-A, -B and -D1-A) than in treating the other (MIT-defined) candidates that have since been dropped. While it would have been of interest to develop the definitions of each candidate to a common status and document the definitions, limitations on available time have forced concentration, in this report, on supporting the documentation of progress in and status of the Primary Task areas. That documentation, as found in Sections 3, 4 and 5 of this report, taken in context with the information presented in ref. 85, does provide a reasonably complete exposition of SIMS-A, -B and "-D". Accordingly, it is assumed that the candidates are adequately defined;

discussions of them in this section will be largely concentrated on noting their essential characteristics, in the limited comparison suggested symbolically on p. iv.

2.1.1 SPECIFIC-VS-GENERIC LIMITATIONS

As this trade comparison study has progressed, the specific details of the candidates have at times threatened to obscure the basic, generic comparisons of instrumentation approaches that are at issue here. Thus, the acquisition of hard, substantiated data concerning the realistic mathematical modeling of the error characteristics of specific gyros, gyro rebalance loop implementations and star sensors has consumed a large proportion of time. Such modeling has not yet reached a stable condition (not only in terms of determination of the coefficients or sensitivities in the models but of the mathematics of the models themselves), and may very well still be indefinite as the study period ends. It is clear that error simulations will produce results that are no more valid than are the instrument and mechanization error models used to produce them. Any instabilities in the SIMS candidate model definitions are bound to raise questions of the validity of the final trade comparisons in terms of accuracy, settling time, stellar data requirements, ground data processing requirements, etc.

It should not be inferred from the foregoing that individuals contacted in regard to sensor models have done other than to provide their best information. The sources derived their descriptions from carefully-obtained test data and have every reason to believe in what they have contributed as inputs to the study. The problem is in achieving model descriptions, useful in simulation studies, on which all competent sources can agree.

An alternative approach, namely, conducting a generic, parametric set of simulations in which key model parameters are varied over a wider-than-probable range, would offer the desired placing of limits on and determining parametric sensitivities of candidate configuration capabilities. The costs paid would be the very large increase in computation time, and data reduction, display and interpretation time involved, as well as a nagging concern that the models assumed do not adequately describe the real sensors and their implementations. The latter concern can be alleviated by also varying the model mathematics, but only at a still larger, attendant increase in the former cost in computer time and labor required. And there still might be a doubt as to the certain inclusion of the "true" models in the range of models considered.

NASA/GSFC, in opting for comparison of SIMS configuration approaches using certain specific candidates, has risked obtaining non-generic results. Yet the motivations for the option - limitations on time, and on resources available to support this study, and a practical need to evaluate potential candidates at hand - were ample justification for it. The MIT and NASA challenges are: MIT - Conduct the study and present the results in such a way that generic implications of trades are revealed; NASA - Interpret and utilize the presented results in such a way that generic, technical implications (especially those having high impact on long-term program costs or probability of mission success) are the basis for pre-development decisions related to SIMS configuration selection.

2.2 SIMS-A

The technology from which SIMS-A is derived, developed under the USAF/Lockheed/Honeywell SPARS program, is the most advanced of its type that is available to NASA for consideration in the EOS program. Prototype versions of both the star sensor assembly (SSA) and the inertial sensor assembly (ISA) have been fabricated and tested. Further development has been halted. However, the design status would permit efficient resumption of development under renewed or new support.

The pivot and dithered-jewel type of suspension used in the SPARS GG334A gyros, and their ternary torque-to-balance moding, are among ISA subjects treated in some depth in subsection 3.1. A proposed method of incorporating an adaptive circuit feature to minimize scale factor error arising from orbital rate applied constantly to the pitch axis gyro is discussed briefly in subsection 3.1.2.4 and in more detail in Appendix A.

Test data is being accumulated on GG334A gyros, at least at Honeywell, at the CSDL, at NASA/GSFC, at Lockheed and at certain USAF installations. Efforts to model the instrument's errors are of course, not complete* (see subsection 5.5 and the footnote on page 5-57). As the star availability studies of subsection 5.3, discussion pertaining to them in subsections 5.1 and 6.3, and the SPARS-like CdS star mapper studies of subsection 4.2.2 have revealed, the stellar data available to a SIMS-A is marginal at best for the EOS application. Thus, it becomes quite important to use the most realistic estimates of gyro performance available, to assess the feasibility for EOS of the SIMS-A concept.

The SPARS star mapper characteristics and errors are examined in detail in subsection 4.2.2. The extremely high responsivity of the cadmium sulfide detector is shown to be an asset that must be traded against the target star population limitations imposed by its narrow spectral bandpass, the large variation in responsivity along each slit, and its very long

---

*Gyros, like women, will always be studied, but never be fully understood, by men.

(≈300 ms) time constant which limits detector signal output amplitude and complicates star "transit time" determination (see subsection 4.2). The techniques for leading edge detection on a delayed star transit waveform, using the peak detected on an undelayed waveform, are ingenious and apparently quite effective on uncorrupted star transits. The performance is less clear when noise stars are present, especially for the dimmer target stars.

The star availability problem is not easily ameliorated in a SPARS-like approach due to field-of-view limitations of the body-fixed sensor. These limitations constrain star data acquisition to take on the randomness dictated by actual star distributions, with no control of data rate possible. Options to increase stellar data rate or SSA performance or both include use of a silicon detector (e.g., see subsections 4.2.3, 4.2.4) or, possibly, a photomultiplier detector (e.g., see subsections 4.2.6, 4.2.7) to increase the detectable star population and/or to improve signal-to-noise ratio in transit time determination. Use of multiple SSA's, or one or more SSAs with increased individual fields-of-view is another possibility.

The complete absence of rubbing parts exposed to vacuum in a SIMS-A implementation is an important consideration in terms of the SIMS operational life goal of three or more years. In view of OAO gimbaled star tracker performance in extended space flights the "no exposed rubbing parts in vacuum" consideration is not overriding; however, it is strong and should be weighted accordingly.*

---

*The OAO experience provides, primarily, data on the survival of exposed rubbing parts in space; it does not provide all the information necessary in regard to maintenance of calibration as affected by bearing wear, e.g., regarding the feasibility of calibration after significant wear has occurred.

Sensitivity of the system to input-axis misalignment, the possibility of the need for an algorithm computer on board (see subsection 3.3, ref. 85), and the probability of at least a 15-element state vector in ground data processing (see subsections 5.1 and 6.3) are further difficulties to be dealt with in SIMS-A. Even if none of these proves to be a limiting factor they all must take their properly-weighted place in trade considerations.

2.3 SIMS-B

This configuration rests primarily on TRW's PPCS/PADS technology. The development work to date has emphasized an advanced solution to the long lifetime, high accuracy, gimbaled star tracker design problem, and fabrication and preliminary testing of an engineering model of the tracker represents the bulk of the hardware status at this time (see subsection 4.3.1).

The gyro package design of SIMS-B uses three Nortronics Gl-K7G gyros in a structure-mounted, analog-rebalanced configuration (see subsection 3.2). The gyro floats are positioned relative to their cases by a taut-wire suspension system. Gyro error rates (additional to gyro drift rate) arise in connection with input-axis misalignment errors, and analog torquing current and analog-to-digital conversion scale factor errors. These are typical strapdown system errors and must be minimized by careful design and compensated for by techniques such as enlargement of the state vector to at least fifteen elements to include estimation of biases in ground data processing (see subsections 3.2.1.1, 5.1 and 5.5.2).

The gimbaled star tracker is the critical subsystem in SIMS-B (see Section 6.4). With its very large field-of-view capability and its S-20 image dissector detector, star selection update frequency may be chosen - and the tracker may be commanded to acquire stars - to accommodate virtually any reasonable gyro performance (see subsections 5.3.5.2 and 6.4, and Appendix C.) There are, of course some costs to be assessed. The rubbing-mechanical contacts in gimbal bearing assemblies, when exposed to the extremely low-pressure space environment and made more difficult as a lubrication problem by the high preloading dictated by accuracy requirements, are chief among them (in light of SIMS reliability goals). The requirement for relatively large angular freedom of two adjacent gimbals poses the usual gimbal non-orthogonality problems such as those discussed in subsection 3.3.2.1 for SIMS-D. These have been mitigated to some extent in the TRW PPCS/PADS star tracker design, which contains a number of unique techniques (e.g., single ball/cup bearings and three-point flexure suspensions). However, they must still be treated as formidable problems until testing and experience have proved the validity of their solutions. Similarly, the large friction torque levels resulting from the preloading present unusual gimbal servo design problems in order to maintain small following errors. Again, this is relieved by the encoding and recovery of image dissector detector X-Y coordinate error signals in addition to the outputs of gimbal readouts. This increases the complexity and errors of the angular readout problem by introducing system errors due to errors in the electronic detector output signals; these would ordinarily be driven to null and settled out before readout.

Computers in space are viewed by some as a solved problem. Others, considering the concurrent requirements of high accuracy and speed, low power and very high (and unattended) reliability, are considerably less sure. One thing does seem self-evident, however: An on-board computer is a major subsystem. With that fact in mind, it is noted that a SIMS-B derived from the PPCS/PADS approach would require an on-board computer to command the star tracker. Alleviation of this requirement by "programming" the tracker in roll only, to acquire anticipated stars (see subsection 2.3, ref. 85)*, might still result in a programmer that can best be described as a computer (see subsections 2.3, 2.5.4, 2.5.7 and 3.4 of ref. 85). Provision of a star tracker for random acquisition of stars (as in SIMS-D-B2; see subsections 2.5.2 and 2.5.5, ref. 85) would eliminate the computer requirement in SIMS as it did in the USAF/MIT PROFILE configuration (ref. 38), but would also entail major modification or complete redesign of the PPCS/PADS star tracker. The objectives of such a redesign are not known, at this time, to be achievable.

2.4 SIMS-D

The star mapper of SIMS-D is derived from the same body-fixed star mapper technology as is SIMS-A, (see subsection 4.2.2) but with the strong probability of a silicon or a photomultiplier tube detector.

The SIMS-D IARU design is presently at the conceptual design stage, in that no known 3-axis gimbaled gyro platform has been designed and fabricated to meet EOS/SIMS requirements. As shown in subsection 3.3.2, the design appears to be feasible, including control of gimbal non-orthogonality errors, in view of the special SIMS, gimbaled-IARU moding (see subsection 2.5 of ref. 85) which permits very limited gimbal angular freedom on the platform's middle and outer gimbal axes (which axes always lie in or near the orbit plane).

---

*Note that programming in roll only would have to be tested as an alternative by a complete redo of the SIMS-B error simulations, due to the different stellar data rate associated with acquisition of one star at a time at times dictated by spacecraft orbital anomaly.

The proposed, MIT-designed Third Generation Gyros (TGG-G1A) utilize magnetic float suspension. They are the result of an advanced design based on improvements of well-established technology, and feature high reliability as well as high performance in the very low frequency region of the gyro drift rate noise spectrum (see subsection 5.5; also, subsection 2.5.1.3 of ref. 85). The anticipated attitude error rates of the indicated reference frame (which frame is associated directly with the inertially non-rotating inner member of the platform, as opposed to being represented analytically in computer registers as in SIMS-A and -B) are sufficiently low that relatively-infrequent stellar updates are required. Hence, the selection of a body-fixed star mapper, having an attendant limited field-of-view and uncontrolled acquisition of stellar data, is made possible and provides ample stellar data. This enabled the definition of a SIMS-D with no exposed rubbing parts and no requirement for an on-board computer, certainly two strong merits of this configuration. Though the 3-axis gimbaled platform is a more complex mechanical assembly than a body-fixed gyro triad, it is drawn from a well-developed and easily-analyzed technology, and is made tractable by the enclosing outer case which permits the use of a pressurizing gas, conventional lubricating techniques, and a "more nearly conventional" advanced thermal design approach (see subsection 3.3.2.2.3).

Star transit time errors will probably be kept small in the final star mapper detector selection by choosing a fast-response detector to enable image-centroid estimation on original transit waveforms (see subsections 4.2.3,4.2.4,4.2.6,4.2.7).

Readout errors will pose some difficult engineering design, fabrication and calibration problems. However, with the limited gimbal freedom on two axes those problems are considerably reduced in severity (see subsection 3.3.2.2).

Of the three SIMS candidates, SIMS-D appears to offer the best possibility of holding the state vector in ground-based estimation down to six elements (vehicle inertial attitude error and gyro bias drift rate uncertainty, each in three axes). Estimation of various static, residual bias errors such as subsystem alignment error biases, gimbal readout zeroing biases, etc., would not be required on a continuous basis (as with any biases in SIMS-A and SIMS-B that do not result in error rate uncertainties), since none of the system errors produced by these are apt to be time-dependent on other than an extremely-low frequency basis.

Finally, as discussed in subsection 6.4 the SIMS-D should be the most adaptable of the three candidates to implementation of advanced configurations (described in subsection 3.2 of Appendix B of ref. 85) in which data from the SIMS or its subsystems would be integrated with data from EOS primary payload sensors to enhance the performance of or simplify one or the other, or both. As but one of the several examples, consider implementing a landmark-inertial attitude determination system. Assume an accurate, radar-determined ephemeris of a spacecraft; then a line in space connecting the spacecraft and a known point (landmark) on the earth at a given instant defines a known direction in an inertially non-rotating frame of reference, just as would, regardless of time, a line from the spacecraft to a star. Thus, the star sensor of a SIMS should be replaceable, for "primary attitude fix" purposes in an EOS, by a means for referring to the gyro reference frame the vector directions to known, suitably-separated landmarks at known times. Such a means is readily provided in a satellite designed for automated, high-resolution earth observation, since payload sensors (e.g., the EOS Thematic Mapper, or the Return Beam Vidicon or Multi-Spectral Scanner of an Earth Resources Technology

Satellite, etc.) provide, in their imagery, the coordinates of sightline vectors to recognizable earth features at known times. A SIMS-D gimbaled gyro platform, by providing both a stabilized inner member of very low angular error rates plus a set of whole-word gimbal Euler-angle readouts, is an ideal "inertial" portion of a landmark-inertial system. Landmarks the coordinates of which are indicated in the body-fixed reference frame by a payload sensor are readily transformed to stable member coordinates in ground data processing. By this technique, using just a few well-separated points in the payload sensor's imagery in each orbit, a known, on-board inertial reference frame is mechanized with which, together with ephemeris data, all other points in the imagery of the same or several sensors may be geographically referenced in ground processing of recovered data. The gyro reference packages of SIMS-A and SIMS-B would very probably be unsuited to the implementation of a landmark-inertial system. This is because, even without a comprehensive "landmark availability" study (see subsection 3.2 of Appendix B of ref. 85), the absence of accurate attitude fixes during the night half plus the twilight and dawn portions of each orbit (not to mention open-ocean, glacier, jungle, desert, and other orbit portions over trackless regions) would result in insufficient data to adequately bound the attitude errors of the strapped down gyro reference frames. Thus, SIMS-D alone would appear to have this particular flexibility and growth potential that may be fairly important in future NASA planning.

SECTION 3

INERTIAL ATTITUDE REFERENCE UNITS

3.0 INTRODUCTION

3.0.1 EOS-SIMS IARU REQUIREMENTS

In order to evaluate the IARU for the EOS/SIMS application the following preliminary requirements have been tabulated.

3.0.1.1 Statement of Work Requirements

(a) Continuously determine SIMS attitude with respect to an inertial frame (within 0.001°/axis - 1σ)

(1) The IARU should be mechanized within an allotment of 0.00056°/axis - 1σ(2 $\widehat{\text{sec}}$).

(b) Configuration selection to be based upon the following factors.

(1) Accuracy, cost, weight, power, telemetry requirements, reliability of components, simplicity of design, flexibility and modularity, cost of ground support equipment, complexity of ground control/command operation.

(c) Spacecraft attitude maintained in all axes to within $\pm 0.5^\circ$ + 0.2 degrees (1σ) and rates shall be below 0.005 degrees/second (3σ). Acceleration at time of attitude control jet firing is $2.9^\circ/\text{sec}^2$.*

*Jet firing occurs only when momentum wheel system is being unloaded, and this will be done in orbital segments during which high resolution payload is not required. SIMS accuracy requirement is relieved during jet firing and for a time interval to be determined afterward.

3.0.1.2 Mission-Related Requirements

(a) Maximum expected input rate due to earth orbit (4^{o}/min)

(b) A minimum expected operating life of in excess of 3 years is required.

(c) The IARU pitch axis will require full circle readout capability; however, the system roll and yaw axes will require a maximum readout to ±5 degrees at specified accuracy.

(d) Separate capability to cage the gimbal system roll and yaw axes is required at some interval to be determined.*

(e) Attitude reference celestial updates will be available for absolute attitude determination at least every 90 minutes. It is assumed that a three dimensional attitude update is required.

3.1 SIMS-A (SPARS-LIKE IARU)

3.1.1 IMPLEMENTATION OF IARU

The basic IARU package designated the GG2200 has been under development on Air Force Program 467 since late 1967 [17]. This IARU consists of three orthogonally-mounted GG334A gas bearing gyros operating in a ternary torque-to-balance loop. To minimize temperature loop power requirements, separate temperature sensors mounted within the gyro tend to compensate both the gyro loop forward gain and the torquing scale factor loop for variations of gyro temperature over a limited temperature range. The ternary loop is interrogated at 9.6KHz and carries

---

*Jet firing occurs only when momentum wheel system is being unloaded, and this will be done in orbital segments during which high resolution payload is not required. SIMS accuracy requirement is relieved during jet firing and for a time interval to be determined afterward.

a dual pulse weight with nominal fine loop quantization of 0.065 $\widehat{\text{sec}}$/pulse[90]. Because of this fine loop quantization a limit cycle frequency will be induced resembling a binary loop output. This resultant lower frequency limit cycle obtained is expected to produce lower variance in the net pulse count distribution than is possible with a straight binary loop. This variance is a measure of loop noise and this loop mechanization is expected to lower the overall attitude uncertainty.

The classical ternary loop implementation is normally employed such that the non-symmetry between positive and negative torquing pulses does not reflect into the loop as an additional constant drift effect that would be present in an equivalent binary loop. Notice, this implementation takes advantage of this basic ternary loop characteristic to a limited extent.

3.1.1.1 GG2200 Error Model Estimates

The following error model information has been obtained from either Honeywell literature, from MIT/DL test data and/or strapdown loop testing experience. The parameters shown in Table 3-1 are to be interpreted as standard deviations of the expected short term stability defined as intervals in the area of sixty minutes or less.

Table 3-1 GG2200 Single-Axis Error Model

BD	=	0.005 Degrees/Hr
SF STABILITY	=	10 PPM
IA ALIGNMENT	=	10 $\widehat{\text{sec}}$
QUANTIZATION	=	0.065 $\widehat{\text{sec}}$/pulse

A very interesting test series is currently being conducted by MIT/DL for GSFC involving all gyroscopes being considered in this study effort[93]. This testing effort determines the power spectral density of the gyroscope drift down to frequency ranges of .01 Hz and below. The present model which describes the measured GG334A noise characteristics is

$$\sigma^2 = \left[(6 \times 10^{-12})\Delta t^3 + 4 \times 10^{-4}\right] \widehat{\sec}^2 \qquad (3\text{-}1)$$

where Δt is the time since the last stellar update in seconds.

This model is valid only for frequencies above 10^{-3} Hz* and represents an approximate error of $\sigma = 0.5\ \widehat{\sec}$ after a one hour period. The non-time dependent offset shown represents the torquing loop quantization uncertainty assuming uniform distribution.

3.1.1.2 GG2200 Characteristics

The GG2200 package has the following characteristics:

WEIGHT	=	18 LBS
SIZE	=	9" × 9" × 6.5"
POWER	=	50 WATTS

3.1.1.3 Attitude Algorithm

The attitude algorithm is implemented using the second-order Runge-Kutta mechanization iterated at a ten update per second rate [16]. These attitude algorithm requirements are obviously not dictated by the orbital rate portions of the mission as they represent a greater computational burden than is required by the orbital environment. Information concerning EOS/SIMS attitude algorithm requirements are included in the next section of this report.

*GG334 applications require use of gyro information down to frequencies of 10^{-4} Hz. Extrapolation of this model from 10^{-3} Hz to 10^{-4} Hz should be valid, according to Ronald A. Harris (see subsection 5.5).

3.1.2 APPLICABILITY OF THE GG2200 IRA TO EOS/SIMS

3.1.2.1 Evaluation of Instrument Performance

It is apparent that the basic gyroscope design must include considerations of the fine attitude determination requirements. An example of this can be seen in Table 3-2 which examines the forward gain for several candidate instruments. This, of course, assumes similar basic signal-to-noise ratios exist at the signal generator output.

Table 3-2 Comparison of Gyroscope Forward Gains

	H/C	SSG $\left(\frac{MV}{MR}\right)$	H/C SSG $\left(\frac{MV}{MR}\right)$
GG334A	0.445	28	12.46
2FBG-6F-OAO	1.9	55	104.5
18 IRIG-MOD B	0.33	18	5.94
K7G	5.25	40	210.0
TGG	1.0	15	15.0

Another important consideration concerning the gyroscope and the overall loop performance is caused by the gyro time constant being longer than the expected decision interval which is required from the torque-to-balance loop design. The present GG2200 ternary torquing loop has a .065 sec/pulse quantization and a 9600 pps interrogation rate. If this loop is applied to the EOS problem the nominal orbital rate would require a 40% duty cycle from the torquing loop. This means that torquing decisions will occur at 250 μ sec intervals which compares to a GG334A time constant of 450 μ seconds. We therefore are attempting to make torquing decisions at a faster rate than the mechanical response capabilities of the gyro. The overall effect of this is to cause a "pulse bursting" which increases the attitude uncertainty. By compensating the loop for the float time constant (a technique presently not performed for the SPARS

System) the pulse bursting described above can be eliminated and short term attitude performance improved.

Table 3-3 is a distribution of the pulse torque patterns taken at MIT/DL for an uncompensated ternary torquing loop when operated at 1/4 of maximum rate and an interrogation frequency of 14,400 pps. The first column represents the number of times that a particular mode occurred. The second column represents the number of ON pulses of the pattern while the third column represents the number of OFF pulses which followed. The table illustrates the number of times each pulse pattern occurred over the test period. The most common patterns occurred near 7 ON followed by 21 OFF pulses, 6 ON followed by 18 OFF pulses and 8 ON followed by 24 OFF pulses. Other pulse patterns occurred less frequently. This table illustrates the ambiguous information available in a string of pulses describing the rate inputs for an uncompensated pulse torque loop.

Table 3-4 shows the pulse torque distribution for a compensated loop for the same input rate and interrogation frequency of Table 3-3. A pattern of 1 ON followed by 3 OFF pulses occurs most of the time with slight variations due to table rate variations. More importantly, the system never produces more than one ON pulse in a row. Compensating the gyro lags has reduced the multiplicity of patterns by eliminating pulse bursts. For this reason, the compensated system will have a smaller error in indicated attitude than the uncompensated system.

Figure 3-1 is a plot of the pulse burst length vs. input rate for three interrogation frequencies. Burst lengths that occurred less than 5% of the time were not plotted in the range shown for each case. This figure is essentially a graph of resolution versus IRA rate. For rates up to one half maximum rate, a burst is defined as the number of adjacent ON pulses.

Table 3-3

Gyro Moding Patterns -
Gyro Lag Compensation OUT

GG334A1 S/N C-5
TABLE RATE ~0.25 RAD/SEC
2/25/70

INTERROGATION FREQUENCY
14.4 kHz

NUMBER OF OCCURRENCES	ON	OFF	NUMBER OF OCCURRENCES	ON	OFF
3	1	1	1	5	1
1	1	2	2	5	11
1	1	18	5	5	12
1	2	3	75	5	13
1	2	5	195	5	14
1	2	9	282	5	15
1	3	3	249	5	16
1	3	4	102	5	17
2	3	5	22	5	18
3	3	6	4	5	19
3	3	7	2	5	20
1	3	8	12	6	15
1	3	9	227	6	16
1	3	10	964	6	17
3	3	11	1797	6	18
3	3	13	1588	6	19
1	3	14	442	6	20
1	3	15	58	6	21
1	3	17	3	6	22
1	4	5	6	7	18
3	4	7	252	7	19
1	4	8	2156	7	20
4	4	9	4095	7	21
8	4	10	2149	7	22
22	4	11	339	7	23
31	4	12	12	7	24
33	4	13	7	8	21
12	4	14	196	8	22
4	4	15	1026	8	23
2	4	16	1380	8	24
2	4	17	507	8	25
1	4	19	41	8	26
1	4	20	3	9	25
			40	9	26
			36	9	27
			3	9	28

Table 3-4

Gyro Moding Patterns -
Gyro Lag Compensation IN

GG334A1 S/N C5
TABLE RATE~0.25 RAD/SEC
5/25/70

INTERROGATION FREQUENCY
14.4 kHz

NUMBER of OCCURRENCES	ON	OFF
390	1	2
4095	1	3
379	1	4
1	1	5
1	1	6

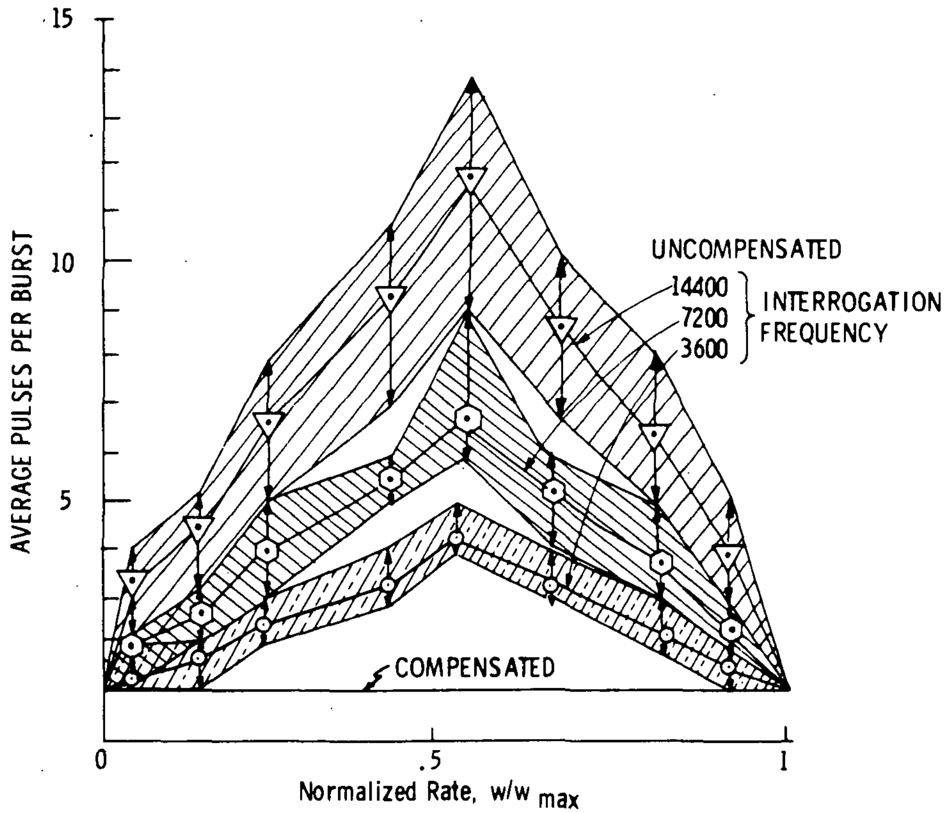

Figure 3-1 Burst Length vs Rate

Above this rate, a burst is defined as the number of adjacent OFF pulses. The large number of pulses per burst occurring near half maximum rate represents a loss of resolution and accuracy of the indicated angle. The higher interrogation frequencies yielded the larger burst lengths showing that shortening the sample period alone cannot improve the quantization beyond a certain point. For all interrogation frequencies and all input rates tested, multiple pulsing occurred with the uncompensated loop, whereas it was eliminated by the compensation. This data demonstrates the effectiveness of compensation in eliminating multiple pulsing and thereby reducing the error in indicated attitude.

3.1.2.2 Evaluation of the Instrument Error Model

3.1.2.2.1 It is interesting to look at our Apollo space performance experience with the 25 IRIG which illustrates the capability of present-day operational gyros. Fifty-one gyros have already been flown with good performance and no in-flight failures. Figure 3-2 shows the in-flight performance obtained from six separate command module flights with 200 hour mission durations. The resulting drift uncertainty ranged from .09 to .30 meru for the entire sample. It should be noted that these drift calibrations assumed no system quantization or alignment errors and should be considered upper error limits.

The high reliability and performance in the Apollo program has been achieved by applying strict screening techniques to ground based IMU testing. By using this screening procedure, an in-flight Mean Time Between Failures (MTBF) of 100,000 hours with a 98% confidence level was achieved.

Comparing the in-flight Apollo results with the SIMS-A gyro error model shows the $.005^{\circ}$/hr bias uncertainty to be reasonable.

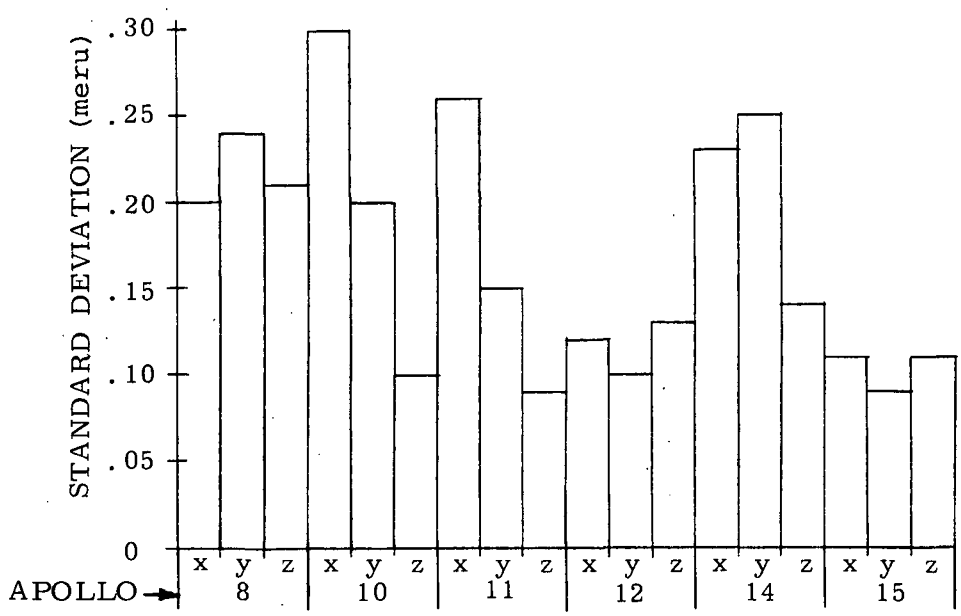

Figure 3-2 Standard Deviation of In-Flight Gyro Drift for the Apollo Primary Guidance Systems

3.1.2.2.2 The GG334A float is supported by a pivot and dithered jewel suspension. A rate about the output axis acting on gyro momentum results in a torque about the input axis. This torque will load the pivot-jewel support and cause an uncertainty in input axis alignment accuracy. Calibration data from the Agena system using GG334 gyros shows from system testing, an input axis alignment standard deviation of greater than 10 $\overset{\frown}{\text{sec}}$[94]. A similar-type system measurement taken on the SIRU system from the magnetically-suspended 18 IRIG MOD B instrument shows the long term input axis alignment standard deviation to be about two arc seconds.

3.1.2.3 <u>Algorithm Requirements</u>

The EOS application shows very modest environmental requirements. The principal constant rate orbital input is essentially along a single axis. To avoid dealing at this time with the many considerations in attitude algorithm design and computer selection, only a few general observations will be made concerning this unique application. Attitude algorithm design for aircraft or booster application depend heavily on maximum dynamic range considerations, available loop quantization, and expected vibrational environment. None of these considerations represent concern for the EOS application.

If a conventional first-order algorithm using either a quaternion or direction cosine implementation were used the orbital rate input (.0012 rad/sec) would imply update rate requirements in the 10 update/second category. By using a third-order algorithm expression, update rate requirements would be reduced into the 1 to 0.1 update/second region. The lower limit on update requirements here could probably be determined more by bandwidth considerations than by slew error requirements. It is also clear that since input rate is principally single axis, a hybrid algorithm could be developed which would have different update rate requirements for the pitch axis than that of the other two axes.

3.1.2.4 Torque Loop Design for Maximum Attitude Accuracy

It is now generally accepted that the principal additional sources of error of the strapdown system implementation are the torquing loop scale factor uncertainties and gyroscope input-axis alignment errors. Other error propagation characteristics of gyroscopes such as non-gravity sensitive bias are similar for both gimbaled and strapdown implementations. The additional strapdown errors due to dynamic effects have been shown [95] to be of little significance for all but very severe environmental applications. The additional errors associated with output-axis coupling and other bandwidth considerations are troublesome but are completely understood and as such can be properly designed to be very small.

For scale factor errors with the pulse-torquing loop operating in either ternary or binary, the error propagation characteristics for constant slewing or sinusoidal-type inputs are similar. It is due to the difference between the actual pulse weight and a nominal pulse weight in slewing and the difference between the positive and negative pulse weights with sinusoidal inputs. (Notice, if an analog loop were implemented the slew error would directly depend upon the ability to read out the incremental slew angle. With a sinusoidal input the analog loop implementation would cause no significant net error, assuming readout errors will cancel out on each revolution.)

The gyroscope input-axis alignment uncertainty error in a constant-slew environment propagates in a plane perpendicular to the constant-slew vector and is proportional to the misalignment angle. For sinusoidal inputs, there are no net gyroscope input-axis alignment errors.

In summary both torquing-loop scale factor errors and gyroscope input-axes alignment uncertainties have a direct influence upon strapdown system performance. For a constant slewing input, scale factor error propagation will appear along the slew vector and instrument misalignment effects appear perpendicular to the vector.

For a three-axis orthogonal triad of strapdown gyroscopes with their torque-balancing electronics, it can be shown that a 25 ppm scale factor error and a 5 $\widehat{\text{sec}}$ input-axis alignment uncertainty will cause equal three-dimensional error propagation magnitudes in any slew environment. In a sinusoidal environment only scale factor effects along the sinusoidal input-axis will propagate errors in proportion to the positive and negative pulse weight difference and all alignment errors will be cancelled over a complete sinusoidal input cycle time.

An adaptive, fixed-direct current, torquing-loop implementation which is designed specifically to operate in the EOS/SIMS orbital environment with minimum scale factor error propagation is described in Appendix A of this report. It is this torque-loop mechanization which is proposed for implementation of a SIMS-A configuration.

3.2 SIMS-B (PPCS/PADS IARU)

3.2.1 IMPLEMENTATION OF IARU

This strapdown package for EOS SIMS would require six GI-K7G gyros whose input axes form a unique symmetrical pattern that corresponds to the array of normals to the faces of a dodecahedron. Achieving true redundancy from this configuration implies individual electronics and power supplies to allow independent loop operation.

The information available shows both analog and pulse-torquing rebalance methods have been considered. The analog rebalance loop appears as the preferred mechanization although neither mechanization was presented in enough detail for evaluation.

3.2.1.1 GI-K7G Error Model Estimate

The following error model information has been obtained from either PPCS/PADS literature or from MIT/DL strapdown loop testing experience. The parameters shown in Table 3-5 are to be interpreted as standard deviations of the expected short term stability, with short term defining intervals in the area of sixty minutes or less.

Table 3-5 Single-Axis Error Model (GI-K7G)

BD	=	0.002 Degrees/hr
SF STABILITY	=	10 PPM
IA ALIGNMENT	=	10 $\widehat{sec}$
QUANTIZATION	=	0.2 $\widehat{sec}$/pulse

The GI-K7G gyro has also been modeled by MIT/DL for a NASA/GSFC study[93]. This testing determines the power spectral density of the gyroscope drift down to frequency ranges of .01 Hz and below. The present model which describes the measured noise characteristics is:

$$\sigma^2 = \left[(5\times10^{-7})\Delta t + 3\times10^{-3}\right]\widehat{sec}^2 \qquad (3\text{-}2)$$

where Δt is the time since the last stellar update in seconds.

This model is valid only for frequencies above 10^{-3} Hz and represents an approximate error of $\sigma = 0.06$ $\widehat{sec}$ after a ten minute period. The non-time dependent offset shown represents the torquing-loop quantization uncertainty assuming uniform distribution.

3.3 SIMS-D

3.3.1 IMPLEMENTATION OF IARU

Two different gimbaled configurations have been presented (ref. 85) as SIMS-D candidates. The first system is a conventional three-axis gimbaled system using very limited freedom on the outer two gimbals. The second is a single-axis platform mechanization in which two torque-to-balance loop gyros are mounted on the platform with input axes normal to the single, stabilized platform axis.

The EOS/SIMS requirements present an unusual application for an IARU in that the short term incremental attitude accuracy is critical while the environment requirements are minimal. For the conventional application of guidance and control in such an environment the strapdown system is an obvious candidate. This application, however, presents very stringent incremental attitude accuracy requirements which represent a state-of-the-art challenge for either a strapdown or a gimbaled implementation. Basically, the problem of attitude accuracy in either configuration is one of gyro loop noise levels, readout resolution and system error propagation due to implementation errors in strapdown due to scale factor and alignment uncertainties when exposed to constant orbital rate inputs.

Notice, both proposed SIMS-D configuration candidates provide isolation from orbital rate inputs.

3.3.2 SIMS-D1 THREE-AXIS GIMBALED IARU

3.3.2.1 IARU Error Allocation

The three-axis gimbal system geometry is illustrated in Figure 3-3. This figure also shows the gimbal axis definitions which are assumed with respect to the orbit. (Axes do not correspond to those defined in subsection 5.2.)

3.3.2.1.1 Gimbal Non-Orthogonality Errors - Due to machining and assembly tolerances there will always exist an angular error (ε) from a true orthogonal position between any given gimbal and its adjacent gimbal. The non-perpendicularity between the inner gimbal axis (IGA) and the middle gimbal axis (MGA) is defined in the figure as ε_{IGA}. Likewise, the non-perpendicularity error associated with the middle to outer gimbal axes and the outer gimbal to navigation base axes are defined as ε_{MGA} and ε_{OGA} respectively.

In our application, notice the ε_{IGA} error source will reflect directly into the overall attitude accuracy. That is, a five arc second ε_{IGA} error will propagate as a five arc second amplitude sinusoidal error on both the middle and outer gimbal axes. The resulting attitude errors from either an ε_{MGA} or ε_{OGA} non-orthogonality is a second order error source described by the product of the error magnitude and the sine of the gimbal angles which are limited to five degrees.

The resulting attitude readout errors must either be controlled to a specified minimum by close tolerances and extremely accurate machining and assembly, or else must be calibrated into the attitude readout chain. In either case it is necessary to know the nature and magnitude of these error sources.

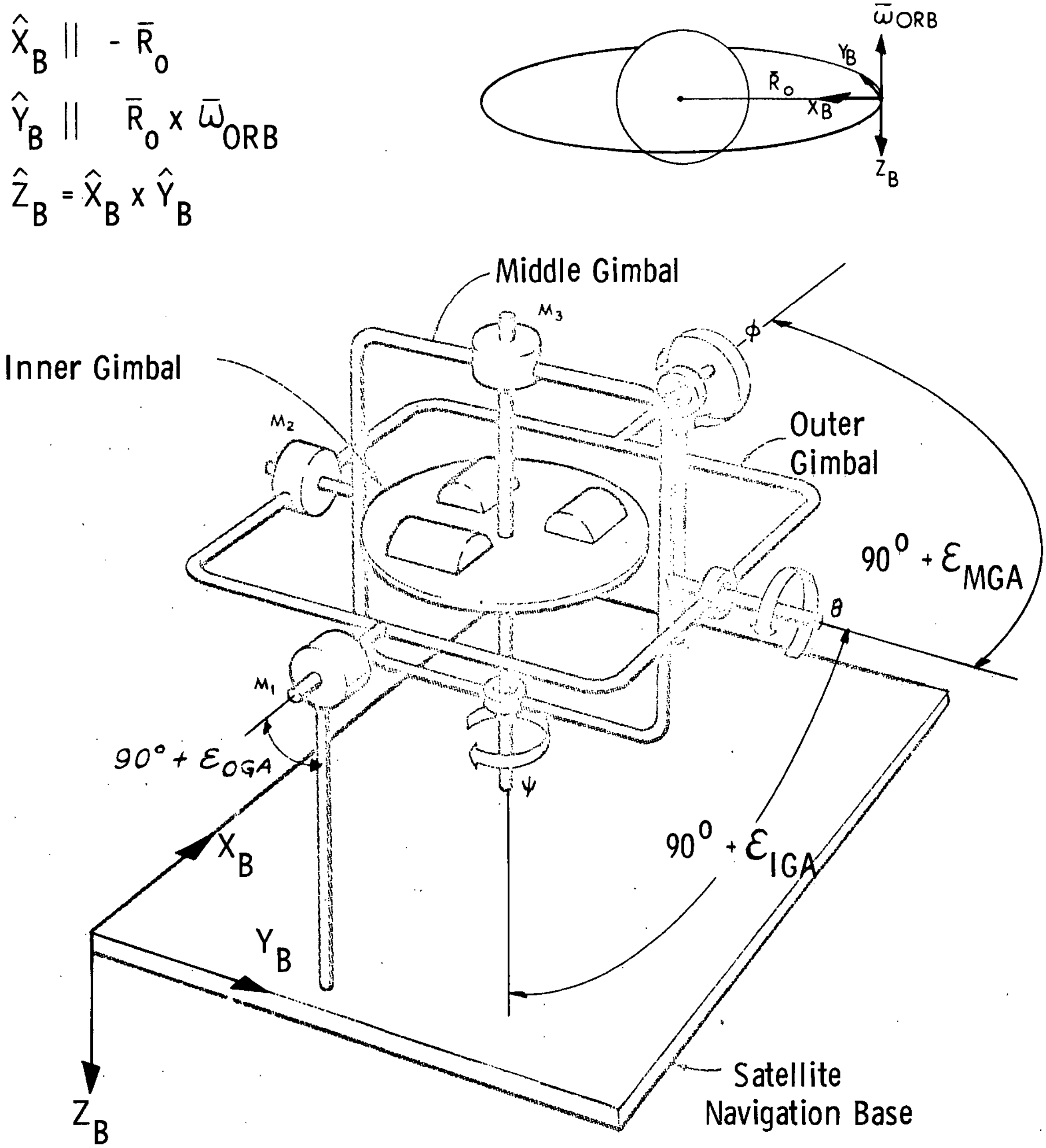

Gimbal orientation is shown at t = 0 (gimbal angles = zero).

Figure 3-3 Three-Axis Gimbal System Geometry Used in Gimbal System Error Study

3.3.2.1.2 Bearing cyclic errors - Errors in attitude readout can result from eccentricities found in the gimbal axis bearings. If the center of the bearing bore is accepted as the rotational center of the axis, a shaft coning angle results because the actual rotational center is defined by the center of the inner race. Although this coning angle can be minimized by alignment of the high spots of the bearing pairs, there is always a residual error because of the variation in eccentricity between bearings and an uncertainty of proper alignment.

From Figure 3-4, defining the eccentricity on shaft end #1 as ε_1, eccentricity on shaft end #2 as ε_2, and the angular displacement of high spot alignment as δ, the effective eccentricity becomes:

$$\varepsilon = \left[(\varepsilon_1 \sin\delta)^2 + (\varepsilon_1 \cos\delta - \varepsilon_2)^2\right]^{1/2} \qquad (3\text{-}3)$$

With ABEC7 bearings being commercially available with a maximum eccentricity tolerance of 50 μin, it can be expected that a set can be matched to within 10 μin. It can also be assumed that the location of the high spot can be marked and installed within ±7° total tolerance. With an eccentricity of 40 μin. one shaft end and 30 μin. on the other end and $\delta = 7^\circ$, the effective eccentricity becomes 11 μin. With a 7.5 inch span between bearing locations this is an angular error of 0.60 $\widehat{\text{sec}}$ (peak-to-peak). It can also be possible to determine the rotational center of the gimbal axis by autocollimating on a mirror placed on the gimbal. In relation to this rotational axis the peak-to-peak values vary from +.30 $\widehat{\text{sec}}$ to -.30 $\widehat{\text{sec}}$.

Shaft eccentricity between bearing locations is sometimes considered as a component of the overall bearing error. Using duplex DF bearing pairs with the degree of eccentricity within tolerable limits, this eccentricity can then be

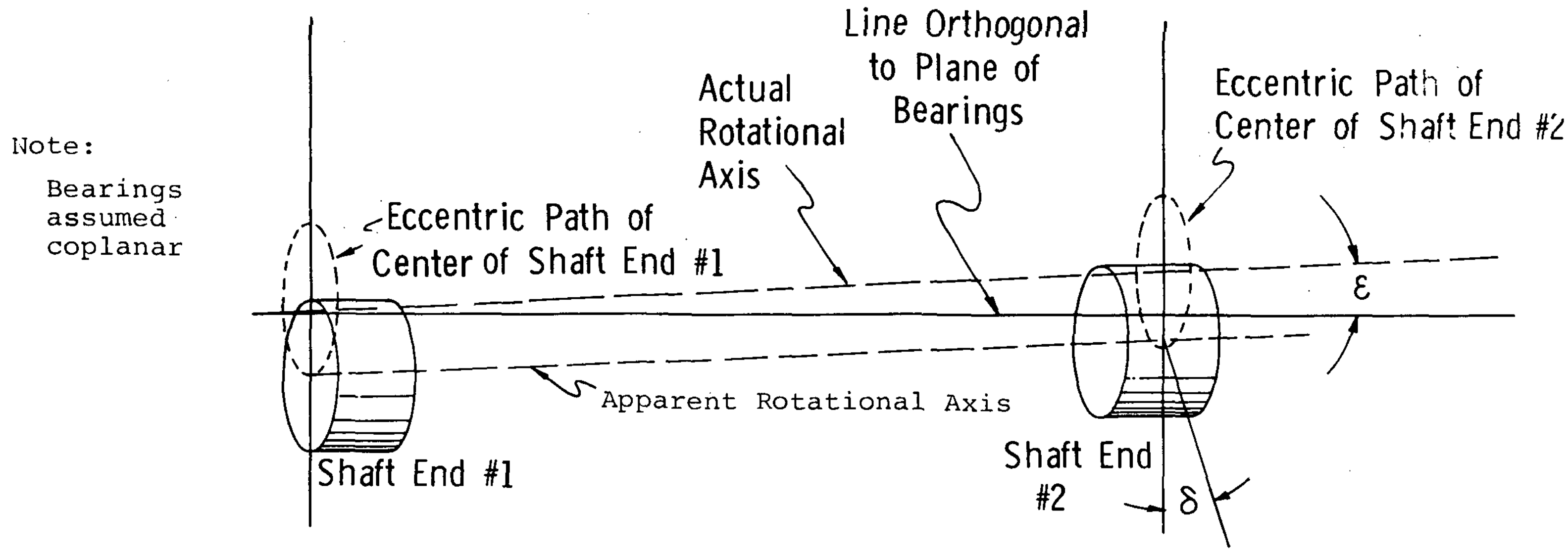

It is assumed that the planes of bearings #1 & #2 are parallel. δ is the rotational displacement of the bearing high spots, in the plane of the bearings, and will vary with time. ε is the orthogonality error due to shaft eccentricity, varying with time, and given by

$$\varepsilon = \left[(\varepsilon_1 \sin \delta)^2 + (\varepsilon_1 \cos \delta - \varepsilon_2)^2 \right]^{1/2}$$

Figure 3-4 Bearing Eccentricity Errors

interpreted as an orthogonality error and examined on this basis (see previous section).

Bearing uncertainty errors - With the exception of ball-to-ball diameter variations, which is controlled by the bearing manufacturer, the uncertainties in bearing performance are due to environmental conditions. The standardized contribution quantities which are normally used are: particle size of bearing contaminate, brinelling effects due to launch environment and bearing changes due to thermal gradients. The RMS value of these factors for the proposed IARU is 0.6 $\widehat{sec}$.

3.3.2.1.3 Gyroscope Instrument Error Model - The TGG-G1A unit is the latest in a family of floated, single-degree-of-freedom, inertial rate integrating gyros developed by the Inertial Gyro Group of the MIT/Charles Stark Draper Laboratory.

Many gyro design concepts proven in earlier generation instruments were used as a foundation upon which to build the new design, which incorporates several advanced concepts tested and proved in experimental units.

This third generation instrument has shown performance of bias drift uncertainty better than 0.01 meru and has a performance goal of bias instability in a zero-g environment of 0.0001 meru.

Even though the performance is significantly better than that required for EOS/SIMS, this level of performance ensures a soundness of build and thus the high reliability needed for this long-duration mission.

To meet the objectives of EOS/SIMS system, the TGG unit could operate at two synchronous wheel speeds if necessary. The higher wheel speed would be used during launch to safely survive any large acceleration shocks such as during stage separations. For the remainder of the mission, the gyro would operate at the lower wheel speed $\left(H = 25\times10^{-4} \frac{gm\text{-}cm^2}{sec}\right)$, with a resultant lower power consumption.*

Life tests on ball bearing versions of the TGG unit have demonstrated an MTBF of 100,000 hours with 99.4% confidence. Similar or better life experience is expected for the gas bearing instrument.

A more extensive description of the gyro was provided in the first interim report, ref. 85, pp 2-33 to 2-37.

Two TGG gyroscopes have been modeled by MIT/DL for a NASA/GSFC study. This testing determines very low frequency power spectral density characteristics. The present model describing the measured noise characteristics is:

$$\sigma^2 = \left[(1\times10^{-10})\Delta t^2 + 1\times10^{-4}\right] \widehat{sec}^2 \text{ (gimbaled)} \quad (3\text{-}4)$$

$$\sigma^2 = \left[(1\times10^{-10})\Delta t^2 + 8\times10^{-4}\right] \widehat{sec}^2 \text{ (strapdown, 0.1 sec quantization)} \quad (3\text{-}5)$$

where Δt is the time since the last stellar update in seconds. This model is valid for frequencies greater than 10^{-4} hz. and represents an approximate error of $\sigma = 0.04\ \widehat{sec}$ after a one hour period in the gimbaled case, or $0.05\ \widehat{sec}$ in the strapdown case. The non-time dependent terms shown represent torquing loop quantization assuming uniform distribution.

*R. A. Harris reports that in present plans to incorporate a TGG aboard a military Comsat the use of the single, lower wheel speed is the more probable approach.

3.3.2.1.4 Overall Error Allocation - The complete error allocation for the proposed three-axis gimbaled configuration is shown in Table 3-6. This table shows that the expected overall attitude uncertainty (1σ) over a ninety minute interval is about two $\widehat{sec}$ per axis.

3.3.2.2 Detailed Layout of IARU

3.3.2.2.1 Layout Drawing - A layout definition drawing of the IARU is shown in Figure 3-5. This three-axis gimbal assembly has unlimited motion about the inner axis (Pitch) and $\pm 5^{\circ}$ motion about the middle and outer axes. Mounted on the stable member are three TGG-G1A gyros.

The three inter-gimbal readout devices shown are equivalent to seven inch diameter inductosyns. Associated with this layout are thirty cubic inches of stable member-mounted electronics including instrument temperature control, pre-amplifiers, wheel and suspension supplies, the readout excitation and a signal multiplexer.

Also, attached to the stable member is an optical cube which will define the three gimbal axes for alignment and calibration purposes.

The stable member is supported in the middle gimbal through two sets of preloaded duplex pairs of bearings. The assembly at one end of the axis contains the readout device and a slip ring with approximately 34 circuits.* The other end of the axis has a D.C. Torque Motor and a Gyro Error Resolver.

The Middle Gimbal is supported in the Outer Gimbal and the Outer Gimbal in the Case through similar assemblies, except that no Gyro Error Resolver is required and the Slip Ring Assembly is replaced by flexible wires.

---

* This number is expected to be reduced by multiplexing. See subsection 3.3.2.3.

Table 3-6 Overall Three-Axis Gimbaled System Error Allocation

BD (Less than 90 minutes)	1.0 $\widehat{sec}$
Gimbal Readout (360°)	2.0 $\widehat{sec}$
accuracy	2.0 $\widehat{sec}$
quantization (25 Bits)	0.2 $\widehat{sec}$
Gimbal Orthogonality	1.0 $\widehat{sec}$
Gimbal Readout (±5°)	1.0 $\widehat{sec}$
accuracy	1.0 $\widehat{sec}$
quantization	0.2 $\widehat{sec}$
Gimbal Servo Error (standoff or stiction)	0.85 $\widehat{sec}$

Expected BD Stability (TGG Instrument)	=	0.01 meru (1σ) 0.00015°/Hr (1σ)
Expected 360° Readout	=	2.0 $\widehat{sec}$ (1σ)
Expected ±5° Readout	=	1.0 $\widehat{sec}$ (1σ)
Gimbal Orthogonality	=	1.0 $\widehat{sec}$ (1σ)
Gimbal Servo Error	=	0.85 $\widehat{sec}$ (1σ)

<u>GIMBALED SYSTEM ACCURACY</u>

	Pitch IGA	Yaw MGA	Roll OGA
GYRO BD (90 Min)	1.0 $\widehat{sec}$	1.0 $\widehat{sec}$	1.0 $\widehat{sec}$
Gimbal Servo Error	0.85 $\widehat{sec}$	0.85 $\widehat{sec}$	0.85 $\widehat{sec}$
Gimbal Readout Over 360°	2.0 $\widehat{sec}$	-	-
IGA to MGA Orthogonality	-	1.0 $\widehat{sec}$	1.0 $\widehat{sec}$
MGA to OGA Orthogonality	-	-	-
Gimbal Readout Over ±5°	-	1.0 $\widehat{sec}$	1.0 $\widehat{sec}$
OVERALL ATTITUDE ERROR/AXIS	2.4 $\widehat{sec}$	1.9 $\widehat{sec}$	1.9 $\widehat{sec}$

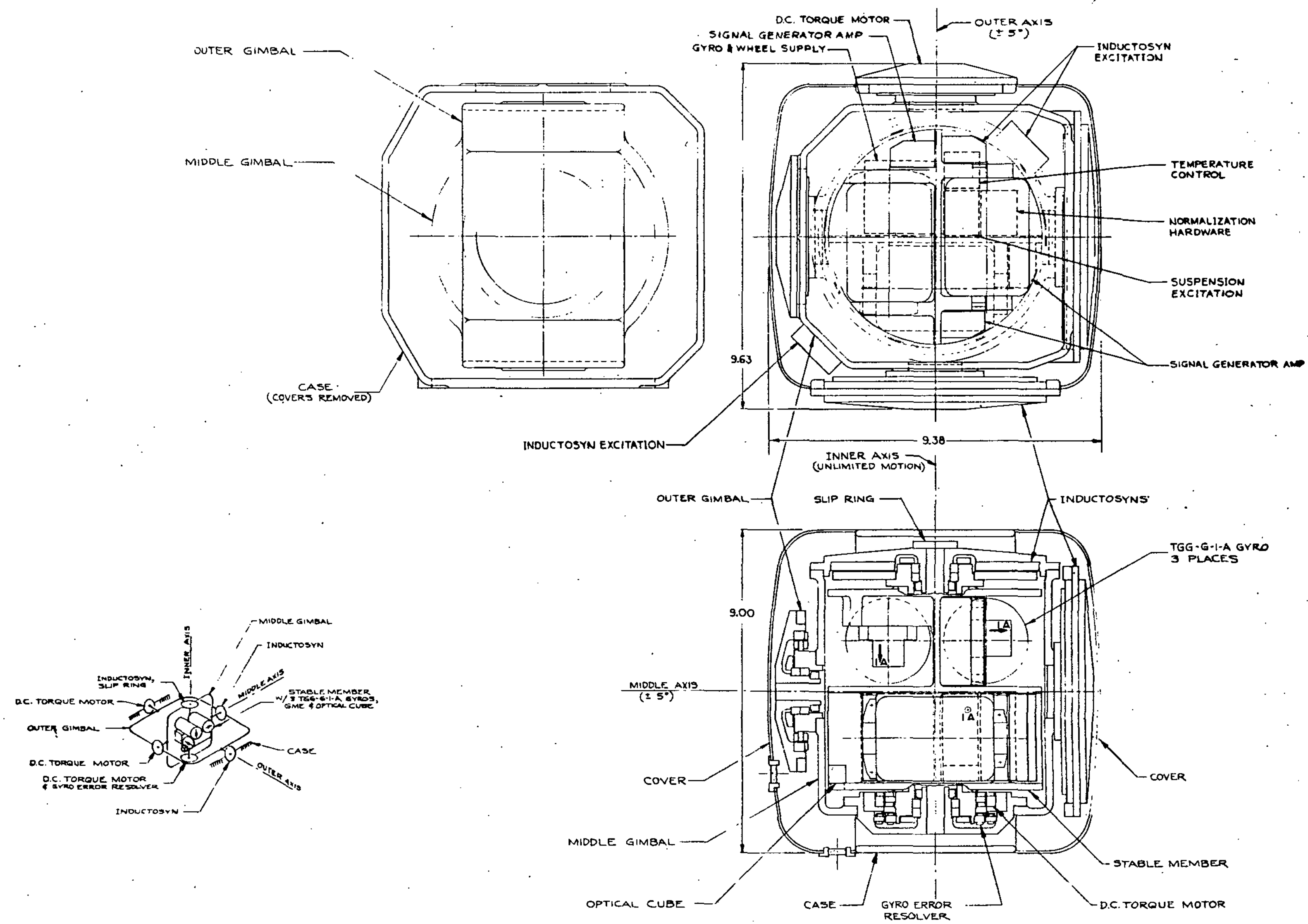

Figure 3-5 Layout of Three-Axis Gimbaled IARU

3.3.2.2.2 Readout Devices - It is presently expected that either the multispeed resolver or inductosyn could be expected to attain accuracies in the two $\widehat{sec}$ region over 360° of mechanical motion. The multispeed resolver is presently favored for this application for the reasons detailed below.

3.3.2.2.2.1 Resolvers - Both Clifton and Bendix have made resolvers with the intent of meeting high accuracy requirements (i.e., in the area of two $\widehat{sec}$). Size and geometry constraints dictate a reasonable maximum of 128 poles. Mounting misalignments and dynamic assymetries affect the overall accuracy. Measurement confidence for these error sources in the area of one $\widehat{sec}$ is believed possible. Experience indicates that a reliable resolver could be produced subject to the following conditions.

a) Design optimization
b) Rigid quality and process control
c) Advanced testing techniques
d) Improved mounting and thermal environment

The resulting device would have the advantage of good electrical characteristics and high reliability. The rigid mechanical structure provides for good repeatibility of performance, and successful calibration and correction by error modeling filter techniques should be expected.

3.3.2.2.2.2 Inductosyns - These devices as manufactured by Farrand and others have been used in the larger sizes in gyro test tables and similar applications for the accurate measurement of angles. They are electrically similar to resolvers except that the inductive elements are printed on an appropriate substrate. The same limitations apply as with resolvers: accuracy is determined by quality of element placement and by alignment effects.

An added problem is the low signal level which tends to complicate the digitizing and encoding problem. The mechanical configuration leads to mounting requirements which reduce the stability and repeatability of the device in equipment exposed to the adverse environments experienced during launch.

3.3.2.2.2.3 MIT/DL Inductosyn Design for an Accelerometer Application - This variation of the Inductosyn design improves the geometry and placement of the inductive elements on the substrate. This improvement factor may be required in order that the diameter of an acceptably accurate device can be reduced to be consistent with the IMU design.

The design improvement is accomplished by individual placement of the pattern elements using a one quarter $\widehat{sec}$ reference table. The accuracy and uniformity of the pattern tends to simplify the electronic problems implicit in the low signal level.

3.3.2.2.2.4 Readout Electronics - It is believed that all of the readout devices considered above will require similar readout electronics design. For the EOS application, a phase-lock loop electronics design is preferred. The capability which can be obtained in this technology would include:

1) one part in 2^{20} (~1 ppm) encoding accuracy for the least significant bit, and

2) random access to whole angle readings with access times less than one hundred microseconds.

3.3.2.2.3 Gimbal Thermal Design Considerations - In the past, as on the Apollo spacecraft, temperature gradient control was accomplished with use of a liquid-cooled gimbal outer case, where the coolant supply is temperature controlled. This was a convenient and practical solution since liquid cooling was available and necessary for other cooling requirements in the spacecraft.

Liquid cooling is not always available nor necessarily desirable in applications such as the EOS satellite, for reasons of weight, power and system reliability. Mission duration alone would suggest that pumps for liquid coolant and fans for convection heat transfer should be avoided.

Since the inertial component temperature is fixed at 135 deg F and the liquid coolant cannot be assumed available, a gimbal design with an internal thermal resistance which is relatively small is necessary.

The Draper laboratory has over the last 3 years expended considerable effort in the development of new internal arrangements for gimbal assemblies whose function is specifically to reduce this thermal resistance and thereby allow outer cases to remain at significantly higher temperatures. Such a design would allow the elimination of the typically-required liquid coolant on the case.

Typical EOS structural temperatures might likely go to 85 deg F under the hot condition at a point removed from the average gimbal case. This means that the average gimbal case would be hotter than the 85 deg F structural maximum. It is observed that the extra temperature rise could be made as small as possible by merely adding mass for conduction between these points, but such an approach has obvious limitations for space vehicles.

The problem simply-stated is to provide adequately low thermal resistance so that the inertial components at 135 deg F can operate into an average case which is untypically hot, say on the order of 100 deg F.

The most effective solution to this problem thus far analyzed is a technique which has been named "close-gap gimbals". This technique requires that the gimbal be filled with a gaseous medium like helium which has a thermal conductivity of about 6 times that of air. It further requires that the gimbals themselves be constructed so that the space between the adjacent gimbals is very small (on the order of 0.020 inch) and that the internal core of the gimbals be filled with a material such as a metal honeycomb which acts as a thermal short-circuiting material through the gimbal.

This concept has been designed and analyzed for two different gimbal assemblies in the past several years and the results indicate that the internal resistance of these gimbals can be reduced to a phenominally low value which allows the average case to exist at temperatures as high as 120 deg F.

Possible added advantages of this low resistance concept are that transient heat transfer problems are greatly minimized since they are closer to their final temperatures at initialization, and the role of active cooling devices such as pumps and fans as necessary supporting machinery with their power and reliability penalties are completely eliminated.

3.3.2.2.4 Gyro Thermal Gradient Attenuation - The Laboratory has pioneered the development and fabrication of a passive device for essentially eliminating the temperature gradients in the gyro floation fluid due to external thermal causes. Test results on an 18 IRIG obtained in 1970 indicate marked improvement in drift rate stability under the shielding influence of this device when the gyro was exposed to forced temperature differences. The measured thermal drift sensitivity was reduced from 0.78 meru/deg F to 0.060 meru/deg F when this thermal smoothing device was incorporated around the outer housing of the gyro.

This device is referred to as a "smoothing sleeve" since its configuration is that of a thin cylindrical sleeve which fits over the outer housing of the gyro and because, in effect, it reduces the temperature variations experienced on the inside of the sleeve as compared to those imposed on its outer surface, thereby attenuating the external gradients as felt by the gyro and its internal flotation fluid.

The smoothing sleeves fabricated to date are composed of alternate layers of highly conducting and highly insulating materials. From a thermal standpoint this alternate layering causes the heat to readily spread around the device through the "conductor" with minimum temperature variation, while impeding the flow of heat through the next adjacent layer of "insulator". It should be noted that a sleeve of typical geometry constructed solely of a highly thermally-conducting metal would cause virtually no temperature attenuation, nor would one constructed solely of the best available thermal insulator. It is this unique alternate layering that allows the device to work so effectively.

The construction of this device has been simplified by the use of a wrapping technique also devised by the laboratory. This technique has as its basis the use of silver metal foil several thousandths of an inch thick and Kapton plastic film in similarly-dimensioned tape form. In the construction process a number of layers of insulating tape are wound on a supporting cylindrical ring. This is terminated after an appropriate thickness is built up and it is followed by an identical number of layers of metal foil. In this way the composite structure is developed until the final outer layer is wound. Performance is critically dependent on the number of alternate layers, the thermal conductivity ratio of the metal to the insulator and the total thickness available for the space occupied by the device. Certain optimum designs exist with respect to these variables and with respect to the relative importance of space or weight.

A newly-developed technique indicates that greater performance levels can be achieved by fabricating the device from solid cylindrical rings of metallic conductor material separated mechanically by supporting layers of low-density, low-thermal conductivity foam material. The Laboratory is presently constructing a prototype of this improved version for testing purposes.

3.3.2.3 Interface Requirements

The external electrical interface requirements for the three-gimbaled IARU are shown in Figure 3-6. The internal IARU interface is shown in Figure 3-7. It is presently estimated that, using multiplexer capability, less than fifteen slip ring assignments or flexleads will be required along any gimbal axis.

3.3.2.4 IARU Characteristics

The overall weight, power and size estimates are:

Weight = 25 lbs.
Size = 9.6" × 9.4" × 9"
Power = 49.5 watts

A detailed breakdown of the electronics characteristics is shown in Table 3-7.

3.3.3 SIMS-D2 SINGLE-AXIS PLATFORM/HYBRID

Many of the discussions associated with the SIMS-D1 configuration are equally applicable to this system. Specifically,

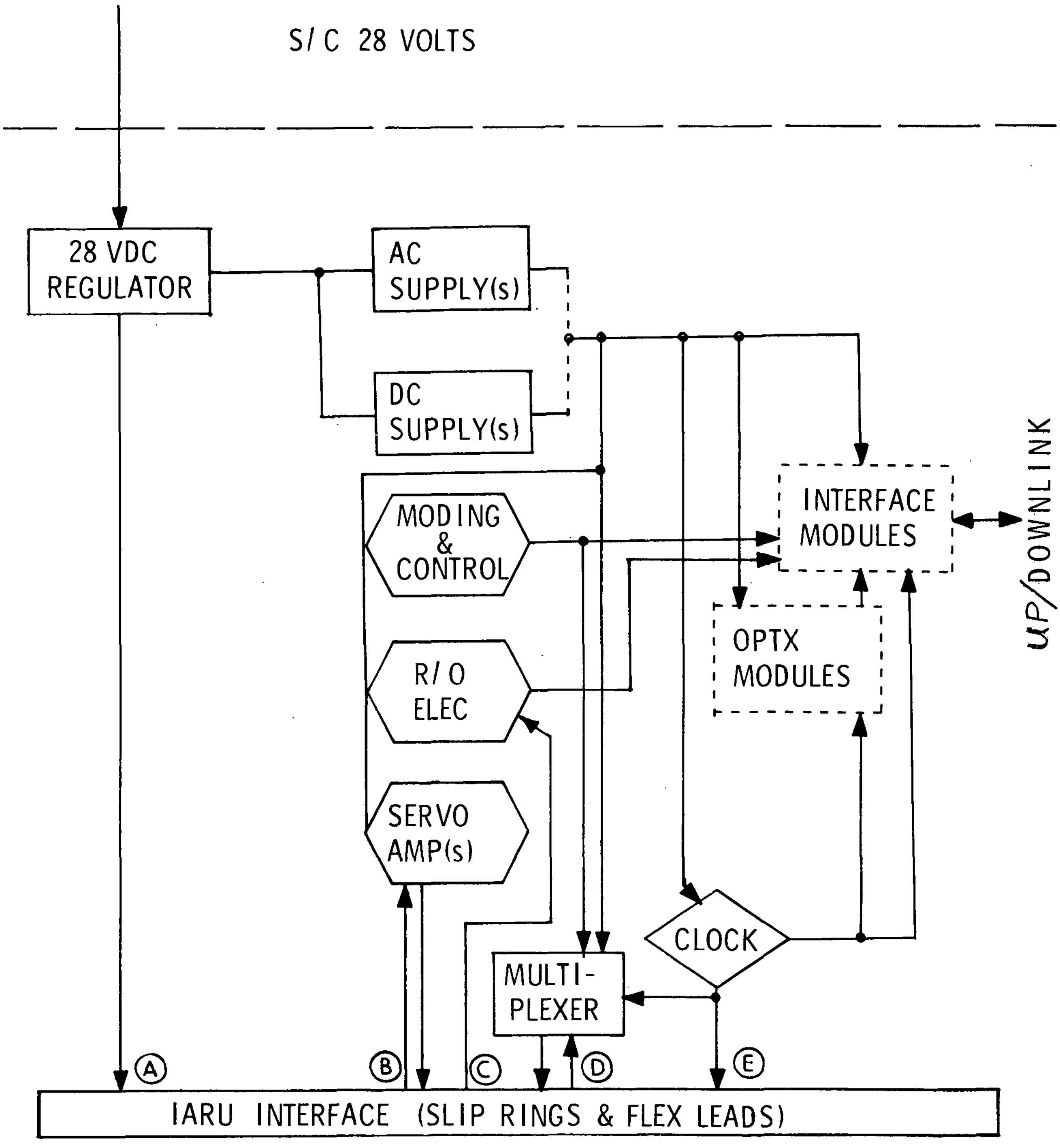

Figure 3-6 Three-Axis Gimbaled IARU External Electronics

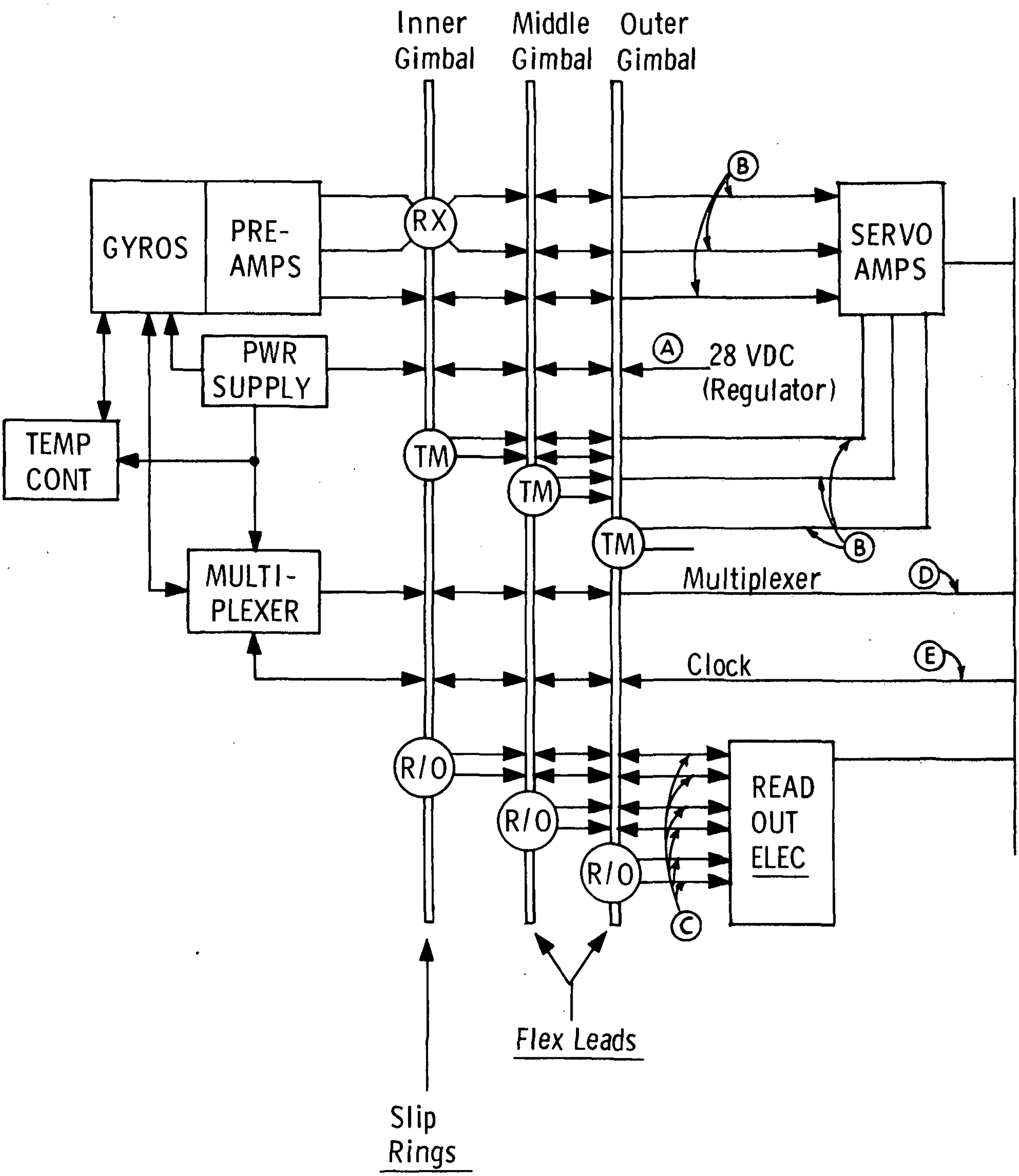

Figure 3-7 Three-Axis Gimbaled IARU Interface

Table 3-7

Three-Axis Gimbaled System - Electronics Characteristics

POWER SOURCE	POWER(w)	VOLUME(in^3)	WEIGHT
Gyro Wheel Supply	8.3 (Note 1)	10 (Note 3)	
Suspension Excitation	0.5	3 (Note 3)	
Normalization Hardware	0.1	1	
Signal Generator Amplifier	0.1	2	
Inductosyn Excitation	1.0	6 (Note 3)	
Temperature Control	2.0	2 (Note 3)	
Servo Amplifier	1.5 (Note 2)	7	
Inductosyn Readout	3.0	6	
	16.5 watts/axis	21 in^3 (Note 3) +16 in^3/axis	1.2 lbs/axis

Summary (Notes 3,4)

Power: 16.5×3 = 49.5 watts
Volume: 69 in^3 (30 in^3 on SM)
Weight: 3.6 lbs

Notes

1. The TGGs will use 5.0 watts for each wheel. To provide 0.1% power supplies, about 60% efficiency is achievable. The wheel supplies will be included on the stable member.

2. The servo amplifiers are external to the IARU.

3. This estimate includes all three axes.

4. These estimates include all the electronics but do not include any mounting or support structure.

the discussions concerning thermal control, readout requirements and gyro characteristics apply.

3.3.3.1 IARU Error Allocation

Most discussions on system error allocations shown in the previous SIMS-D1 description are valid for this system also. It will be noted that gimbal non-orthogonality errors do not appear in the SAP/Hybrid configuration. (Indeed, this is one of the reasons for consideration of the SAP for SIMS-D.) The overall SAP/Hybrid error allocation is given in Table 3-8.

3.3.3.2 Detailed Layout of IARU

The layout definition drawing for this configuration is shown in Figure 3-8. The inner member of this layout is identical to the stable member and inner axis assembly of the three-axis gimbal layout except for changes in the electronics packaging. The gyro error resolver has been removed and the middle gimbal assembly replaced by the gimbal mounting case.

3.3.3.3 Interface Requirements

The external electrical interface requirements for this configuration are shown in Figure 3-9 and the internal electrical interface requirements in Figure 3-10.

3.3.3.4 IARU Characteristics

The overall weight, power and size estimates are:

Weight	=	15 lbs.
Size	=	8.3" × 7" × 7"
Power	=	35 watts

A detailed breakdown of the electronics characteristics is shown in Table 3-9.

Table 3-8

Overall SAP/Hybrid System Error Allocation

SF Stability (90 min)	0.9 sec
Alignment Uncertainty (Short Term Instability)	2.0 sec
BD Gyros (90 min)	1.0 sec
Gimbal Servo Error	0.85 sec
Gimbal Readout Error	2.0 sec

Expected SF Stability = 20 ppm (1σ)

Expected Strapdown Gyro IA Alignment = 2.0 sec (1σ)

SAP/HYBRID SYSTEM ACCURACY

	Pitch Axis	Yaw Axis	Roll Axis
SF Stability (90 min)	-	0.9 sec	0.9 sec
Alignment Uncertainty	-	2.0 sec	2.0 sec
BD Gyros (90 min)	1.0 sec	1.0 sec	1.0 sec
Gimbal Servo Error	0.85 sec	-	-
Gimbal Readout Error	2.0 sec	-	-
OVERALL ATTITUDE ERROR/AXIS	2.4 sec	2.4 sec	2.4 sec

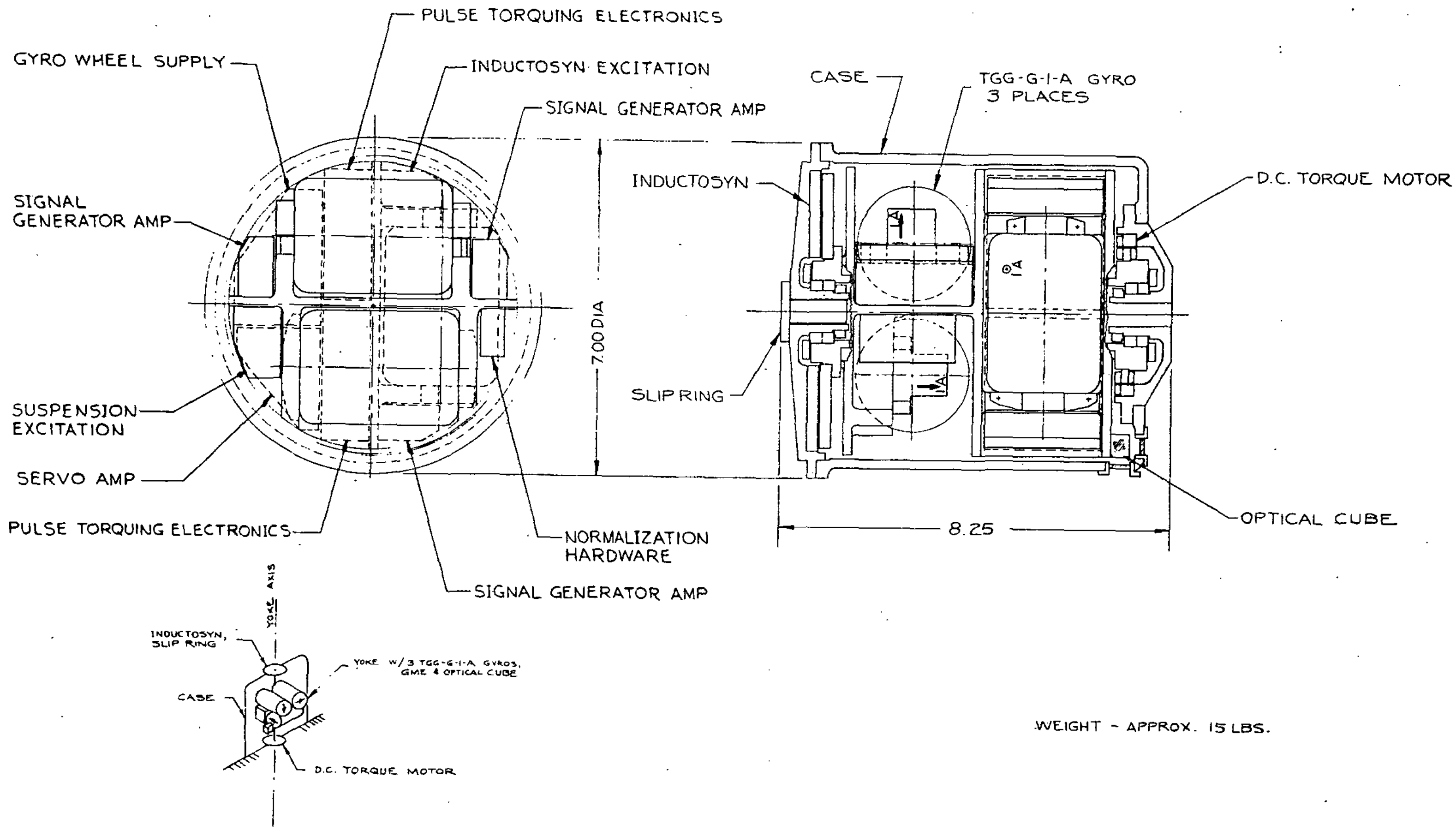

Figure 3-8 Layout of Single-Axis Platform/Hybrid IARU

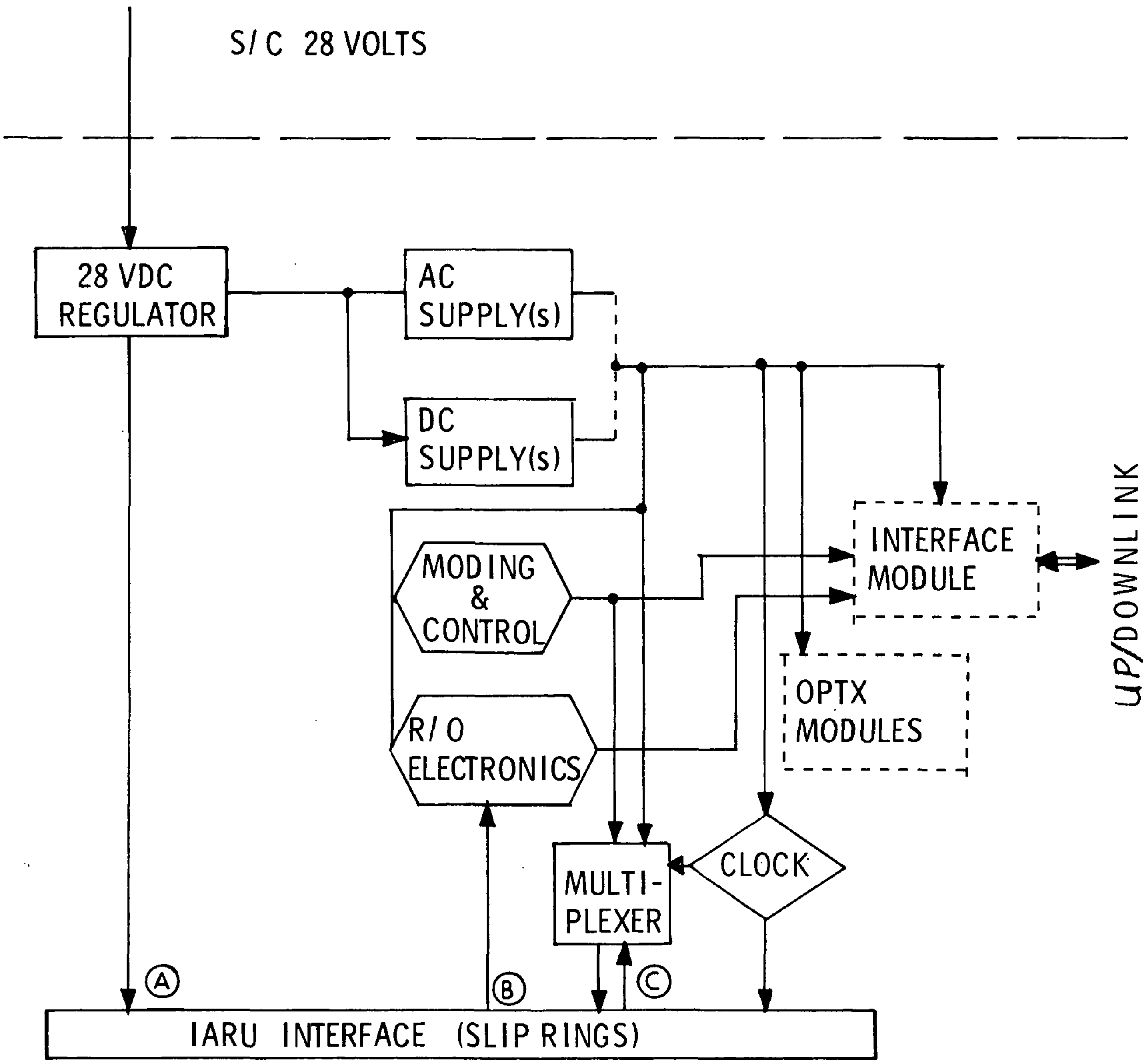

Figure 3-9 SAP/Hybrid External Electronics

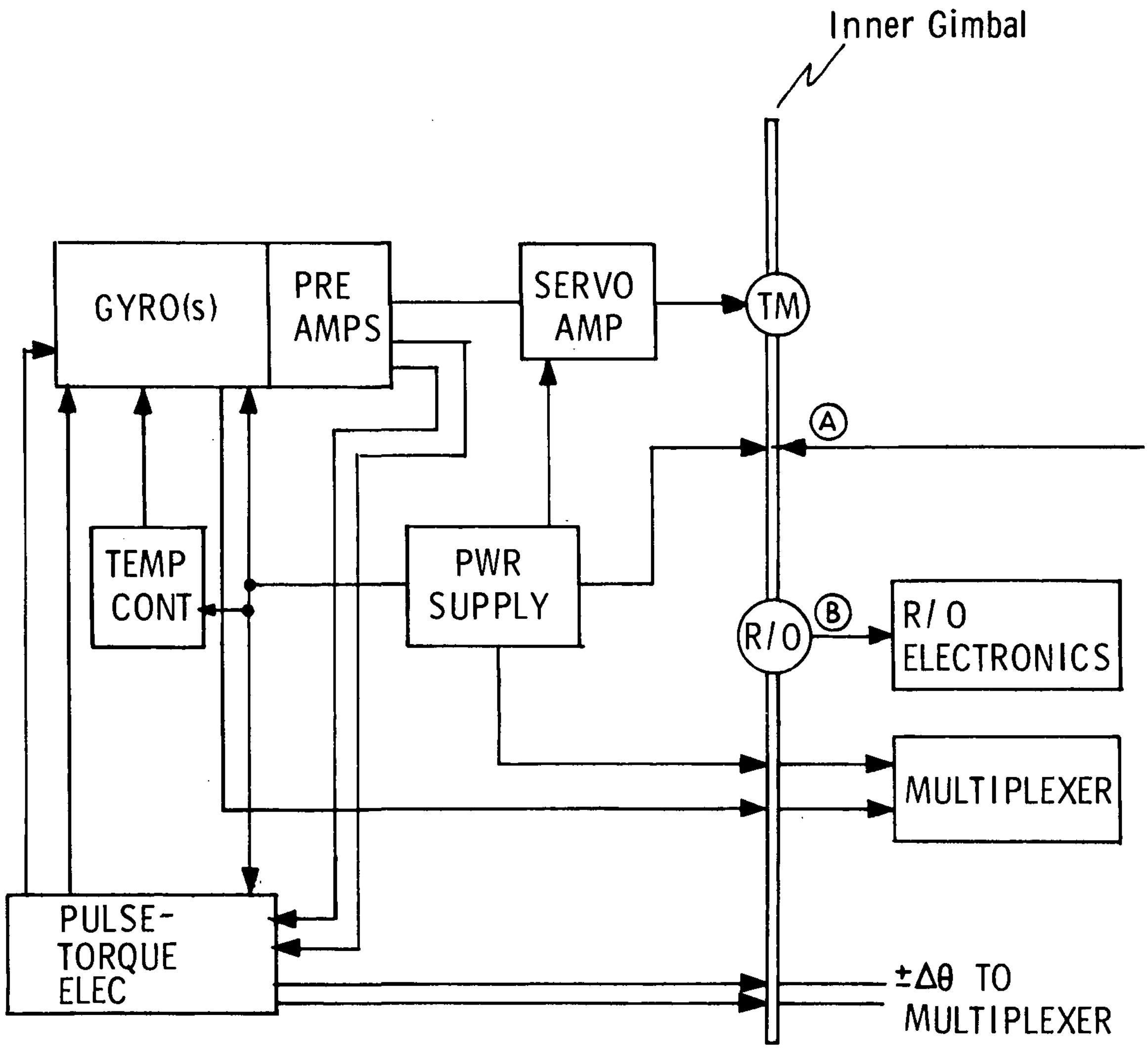

Figure 3-10 SAP/Hybrid Platform Interface

Table 3-9

SAP/Hybrid System - Electronics Characteristics

POWER SOURCE	POWER (w)	VOLUME (in^3)	WEIGHT
Gyro Wheel & Supply	8.3	10 (Note 3)	
Suspension Excitation	0.5	3 (Note 3)	
Normalization Hardware	0.1	1 (Note 3)	
Signal Generator Amplifier	0.1	2	
Pulsed Torquing Electronics	1.3 (Note 1)	7 (Note 4)	
Servo Amplifier	1.5 (Note 2)	7 (Note 5)	
Inductosyn Excitation	1.0 (Note 2)	2 (Note 5)	
Inductosyn Readout	3.0 (Note 2)	6 (Note 5)	
	14.5 watts (one axis) +10.3 watts (ea. of two axes)	36 in^3 +2 in^3 on ea. of 3 axes	1.2 lbs/axis

Summary (Notes 3,6)

Power: 10.3 × 2 + 14.5 = 35.1 watts

Volume: 42 in^3 (Note 7)

Weight: 3.6 lbs

Notes

1. There are two axes with pulse-torque electronics.
2. There is one axis with the Servo Amp and Inductosyn R/O Electronics.
3. This estimate includes all three axes.
4. This estimate includes the two strapdown axes.
5. Single-axis only.
6. These estimates include all the electronics* but exclude mounting or support structure.
7. For this configuration all the listed electronics are part of the inner package.

* Temperature Control electronics are not included here. Power, volume and weight are expected to be approximately the same as for SIMS-D1 (see Table 3-7).

3.4 IARU RELIABILITY CONSIDERATIONS

Information in this subsection is used to address the three year minimum expected operating life requirement identified in the introduction. Since little actual reliability information has been available in this study, certain assumptions will be defined to introduce a preliminary estimate of the IARU reliability requirements for a minimum three year operating life. The primary system reliability will be based upon expected gyroscope axis reliability estimates only, since the support electronics hardware or redundancy electronic mechanization requirements are presently not known. It will be assumed here that the failure detection and isolation capability will be implemented on the ground, and that the ability to change status of the airborne redundant system configuration can be accomplished by uplink command with perfect reliability.

Figures 3-11 through 3-16 are graphs of the reliability of various inertial measurement unit configurations (one triad, two triads, three triads, and a Hexad with either two or three failures allowed) for gyro axis MTBF's of 10,000, 50,000 and 100,000 hrs. In Figures 3-11 through 3-13 it is assumed that all systems in any one configuration are operating concurrently. Due to power constraints this is not expected for EOS/SIMS application. In Figures 3-14 through 3-16 it is assumed that the redundant triads or gyro axes (for the Hexad) are on standby with infinite MTBF, and are switched in using externally-derived information only when a failure occurs.

The reliability (i.e., probability of mission success) in Figures 3-11 through 3-13 was calculated using the results of Reference 96. The reliability in Figures 3-14 through 3-16 was calculated using the following formula found in Reference 97. (See Reference 97 for a "physical" explanation of the formula.)

$$P\ (\text{system failure}) = \int_0^t F_2(t-u) f_1(u)\,du \qquad (3\text{-}6)$$

where

P = probability of system failure,

$f_1(t)$ = failure probability density function of operating system, and

$F_2(t)$ = failure probability distribution function of standby system when it is operating.

The reliability, R, is given by

$$R = 1 - P \qquad (3\text{-}7)$$

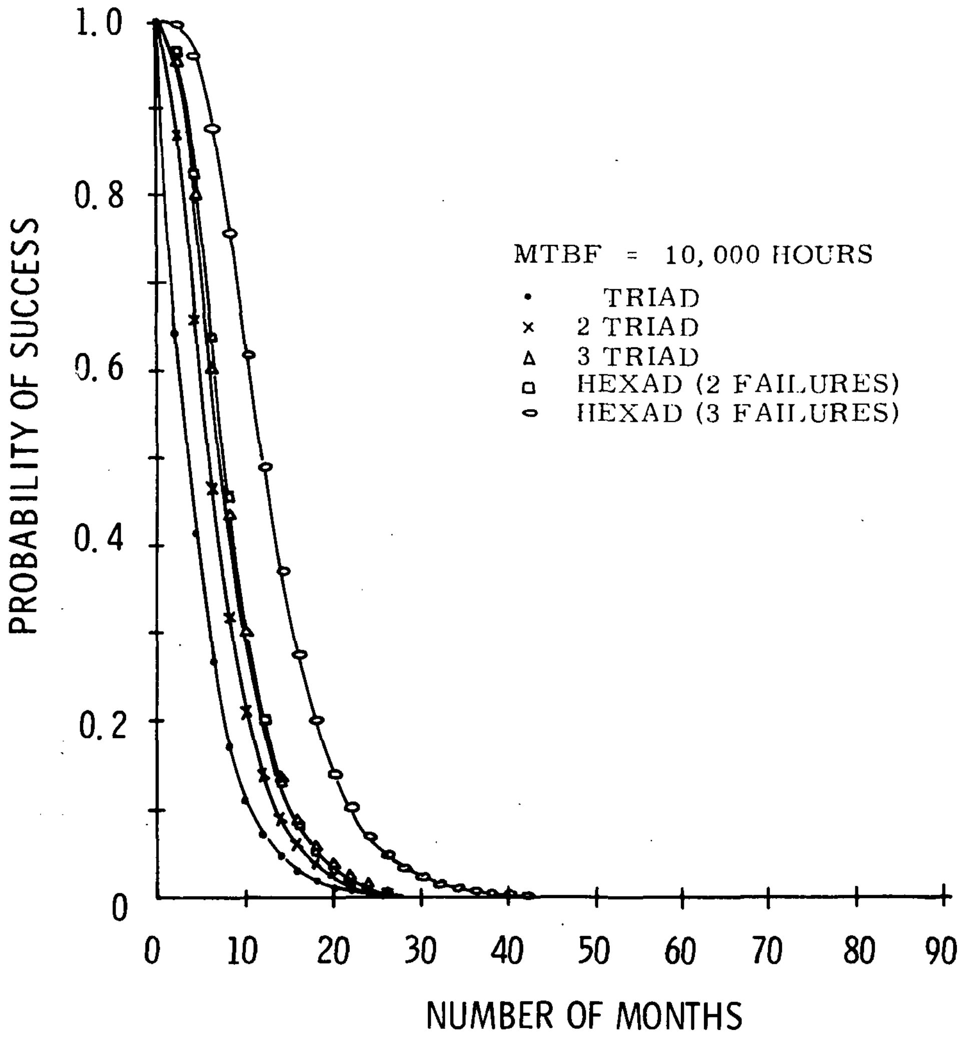

Figure 3-11 Mission Success Probability (Gyro Loop MTBF = 10,000 Hrs.)

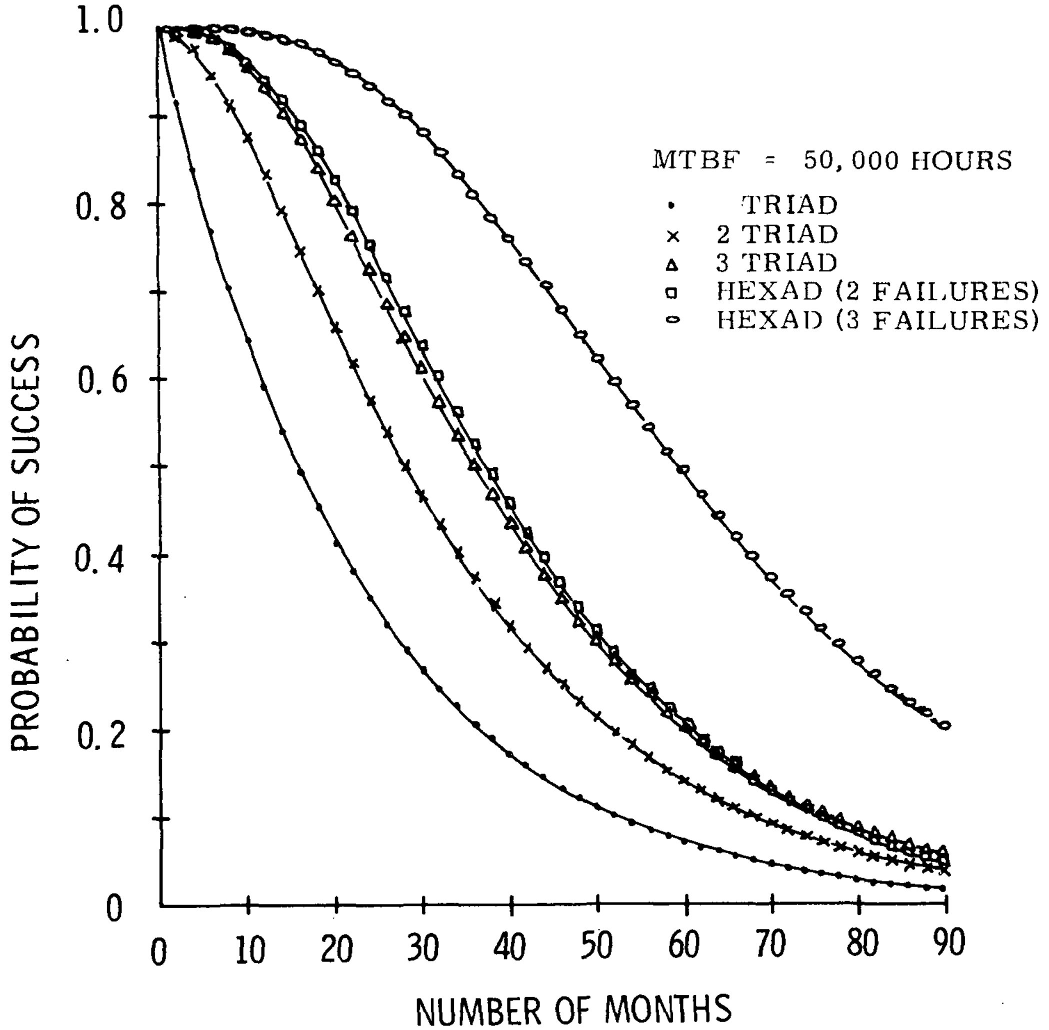

Figure 3-12 Mission Success Probability
(Gyro Loop MTBF = 50,000 Hrs.)

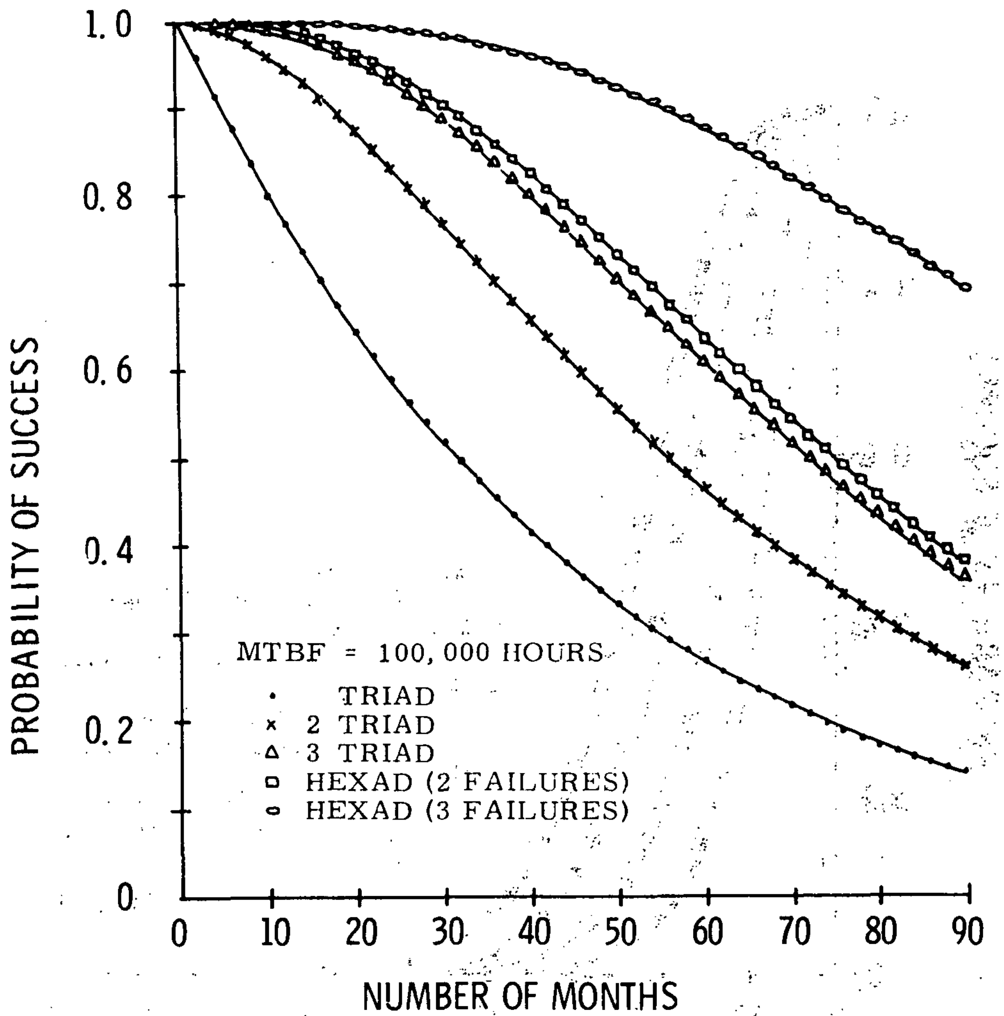

Figure 3-13 Mission Success Probability (Gyro Loop MTBF = 100,000 Hrs.)

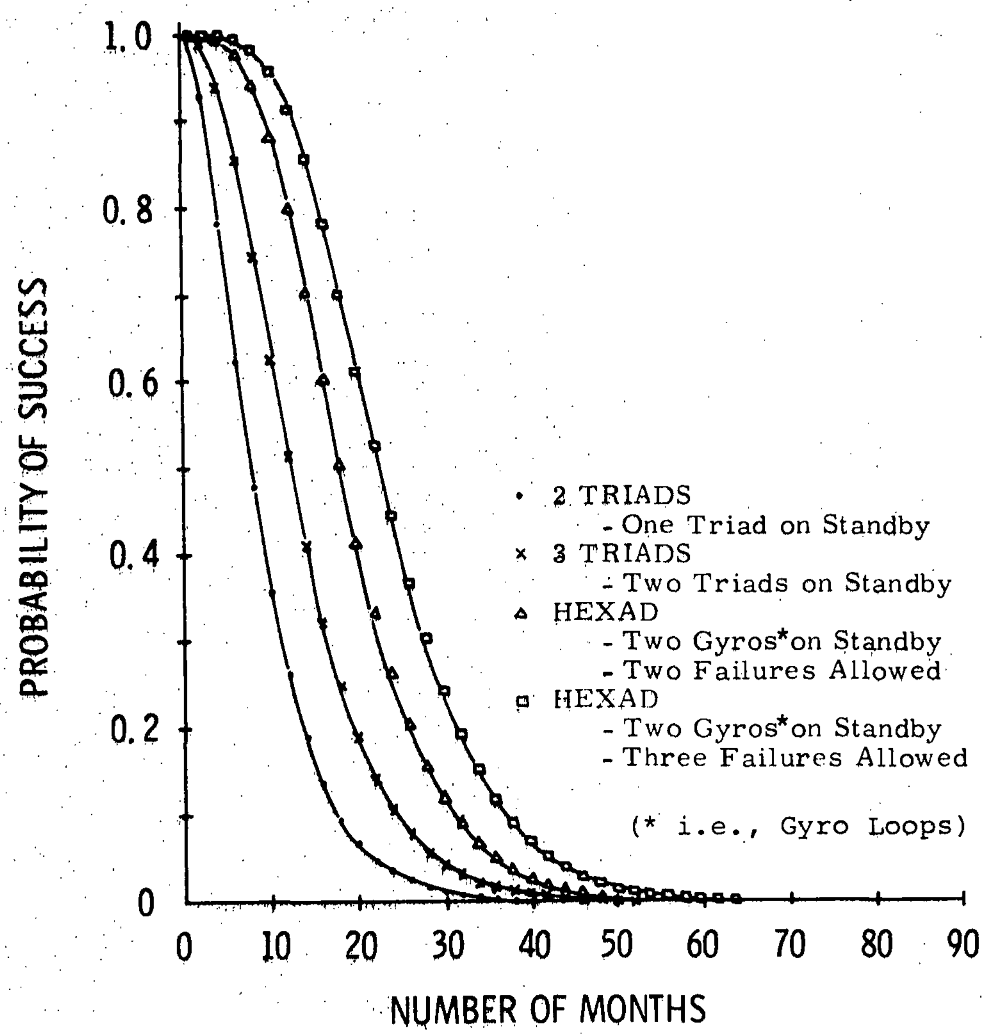

Figure 3-14 Mission Success Probability
(Gyro Loop MTBF = 10,000 Hrs.)

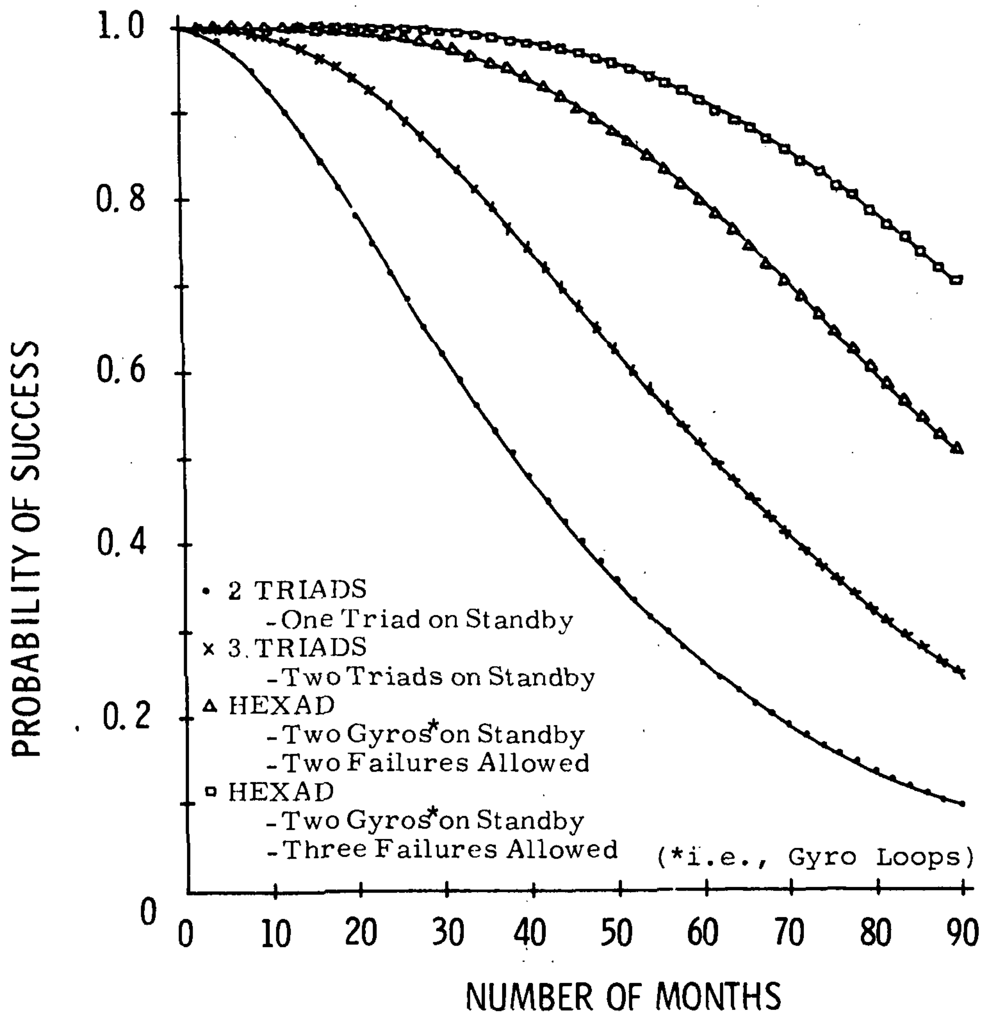

Figure 3-15 Mission Success Probability (Gyro Loop MTBF = 50,000 Hrs.)

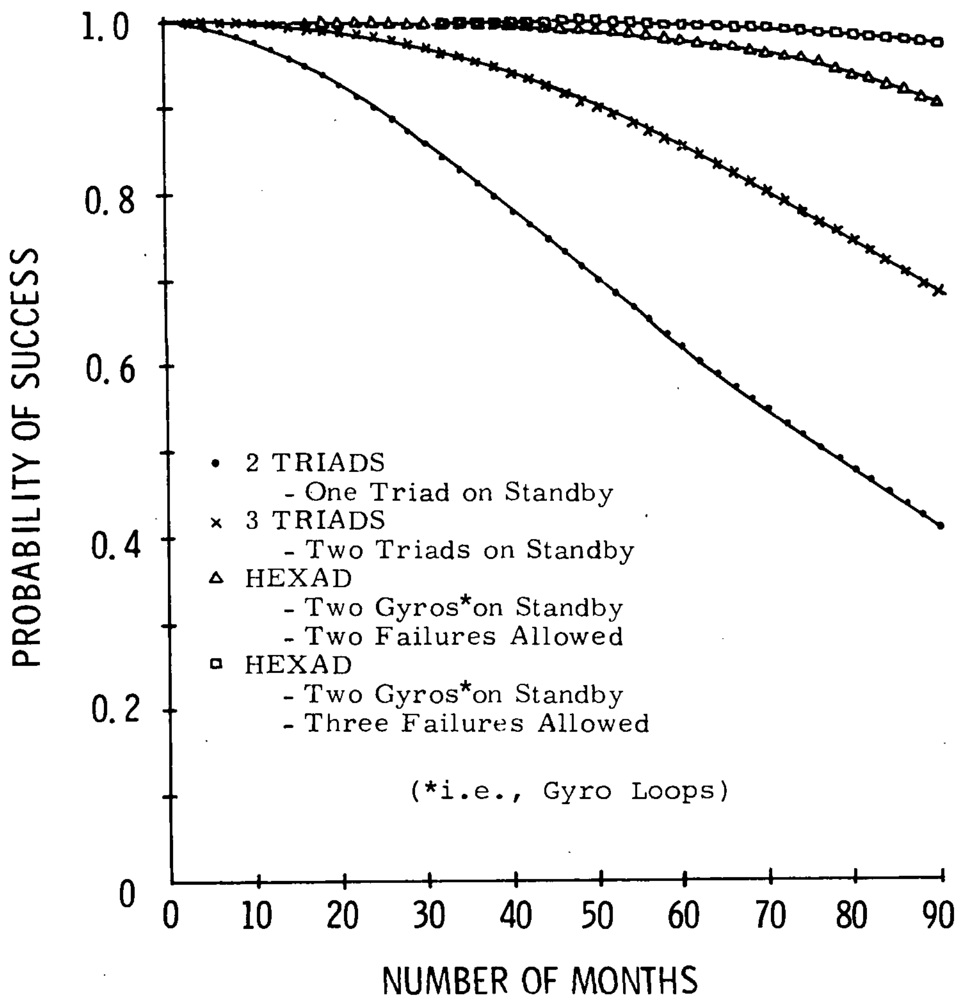

Figure 3-16 Mission Success Probability
(Gyro Loop MTBF = 100,000 Hrs.)

3.5 FUTURE DIRECTION OF IARU EVALUATION

3.5.1 THE SIMS-D CANDIDATE

It has become apparent during the study of the above candidate IARU mechanizations that the strongest candidates are the fully-strapdown and fully-gimbaled configurations. The SAP/Hybrid system was proposed originally to eliminate the additional scale factor uncertainties which are propagated in a fully-strapdown mechanization because of the constant orbital rate. If the fully-strapdown configuration uses the adaptive torque-to-balance loop suggested in Appendix A, the sensitivity to scale factor uncertainty is greatly reduced. Further, it is believed that gimbal orthogonality errors can be held to 2 $\widehat{\text{sec}}$, which eliminates another principal reason for consideration of the SAP/Hybrid. For these reasons IARU candidate D-2 will be eliminated from further study.

The single, remaining (three-axis gimbaled) SIMS-D IARU candidate will be studied further from the standpoint of system moding, initialization and both laboratory and in-flight calibration capabilities.

3.5.2 THE SIMS-A CANDIDATE

The SIMS-A (SPARS-like) configuration will be investigated in greater detail to determine actual hardware performance and problem areas.

3.5.3 THE SIMS-B CANDIDATE

Limited evaluation of the torque-to-balance loop mechanization is planned, using data to be supplied by Nortronics at TRW and GSFC request.

SECTION 4

STAR SENSOR STUDIES

4.1 INTRODUCTION

In this section, each SIMS Star Sensor candidate is examined in a common manner starting at the sensor input, examining each subassembly for function, error contributions, and trade parameters. The error contributions are assembled into an error model and the trade parameters are listed in summary, both to the extent of completion at this stage of the project.

4.1.1 STAR SENSOR CLASSIFICATION

Two classes of instruments for obtaining inertial attitude information from star sightings are being considered in this study. One class is generically referred to as star tracker. The basic star tracker requires two degrees of freedom in line-of-sight, optics to form a proper star image, a reticle at the image surface with either mechanical or electrical modulation, a photodetector, a servo-mechanism for using the demodulated star signal to align the optical or electronic boresights or both with the star line-of-sight, and appropriate angle readout provision. The other class is generically referred to as star mapper. The basic star mapper has optics to form a proper star image, a pattern of slit reticles in the image surface which is caused to move in some manner usually in conjunction with the optics so as to scan a portion of the star field, a photodetector to sense the star signals transmitted through the slits, and electronics for estimating the time of some meaningful feature of the star transit signal (hereinafter referred to as star transit time).

4.1.2 NASA DIRECTIVES

NASA/GSFC (NASA) has suggested that MIT/CSDL study a SPARS-like star mapper as the Star Sensor candidate for the SIMS-A configuration; the characteristics of the SPARS system are discussed in subsection 2.2 of ref. 85.

NASA has directed MIT to study the PPCS/PADS star tracker with appropriate modifications suitable to achieve a SIMS Star Sensor for the SIMS-B configuration. PPCS/PADS is the acronym for the Precision Attitude Determination System of the Precision Pointing Control System which is under development by TRW Systems Group (TRW) for NASA/GSFC (see subsection 2.3, ref. 85).

NASA had directed MIT to study the STARS concept as a Star Sensor package for the SIMS-C configuration. STARS is the acronym for the Stellar Tracking Attitude Reference System conceived by Hughes Aircraft Company, Space and Communications Group (Hughes) (see subsection 2.4, ref. 85). No further effort by MIT is planned in regard to the definition of a SIMS-C configuration, nor on the applicability of the STARS to such a purpose, nor on the evaluation of the STARS approach itself. MIT documentation of this decision is found in subsection 2.4 of ref. 85 and in the fourth monthly report from MIT to NASA under the present contract, ref. 86. NASA has not directed MIT to the further consideration of STARS, nor to consideration of any other techniques within the SIMS-C definition, nor to further consideration of the SIMS-C concept itself.

NASA has directed MIT to select and study a suitable gimbaled or hardmounted star sensor for application to the SIMS-D configuration (see subsection 2.5, ref. 85).

4.1.3 MIT SIMS-D STAR SENSOR

At the beginning of this study, in-depth considerations and establishment of specifications of the frequency of stellar-referenced updates required by the SIMS-D IARU candidates were not available. Therefore, MIT determined to prepare a sufficient number of star sensor approaches to respond at any level of SIMS-D IARU requirement.

A SIMS-DA Star Sensor (see subsection 2.5, ref. 85) designation is in the class of star mapper. It would be best suited for low frequency of update requirements at SIMS accuracy levels. The abbreviated notation SIMS-DA refers to the same star mapper in both the complete SIMS-D1A and SIMS-D2A configurations (see ref. 85 for notation).

A SIMS-DB2 Star Sensor (see subsection 2.5, ref. 85) designation is in the class of star tracker. It would have one degree of mechanical freedom about the spacecraft roll axis and a limited raster FOV with two degrees of electrical freedom. It would execute a scanning search with the mechanical degree of freedom. The spacecraft orbital pitch rate will advance the scanned segment in pitch direction. The FOV would be greater than for SIMS-DA and this candidate would meet higher frequency-of-update requirements at SIMS accuracy levels than a SIMS-DA. The abbreviated notation SIMS-DB2 refers to the same star tracker in both the complete SIMS-D1B2 and SIMS-D2B2 configurations (see ref. 85 for notation).

A SIMS-DB1 Star Sensor (see subsection 2.5, ref. 85) designation is in the class of star tracker. It would have one degree of mechanical freedom about the spacecraft roll axis which would be commanded from a limited on-board star catalog, and a limited FOV raster search with two degrees of electrical freedom. The catalog would contain approximately twenty or thirty stars and would be updated from an extensive ground-based catalog once or twice per week to account for orbital precession. The DB1 FOV is the greatest of the three SIMS-D approaches, as is the frequency of update. The abbreviated notation SIMS-DB1 refers to the same star tracker in both the complete SIMS-D1B1 and SIMS-D2B1 configurations (see ref. 85 for notation).

The frequency of stellar-referenced updates required by the SIMS-D IARU candidate has now been established to be very low. Therefore, a SIMS-DA star mapper is chosen as the suitable candidate of least mechanical complexity and greatest reliability of the three approaches.

No further development of the SIMS-DB1 and SIMS-DB2 star tracker candidates will be undertaken beyond those considerations documented in subsections 4.3.2 and 4.3.3 of this report.

4.1.4 SIMS-E DISPOSITION

The SIMS-E concept was presented in ref. 85, subsection 2.6, for formal completeness as an alternative to trade against the SIMS-C. For reasons set forth in ref. 85, on pp 2-52 and 2-53, MIT will not study SIMS-E further.

4.1.5 PROJECT ACTIVITIES

Project activities have included or will include: the acquisition and assimilation of documents and reports pertaining to SPARS (unclassified sections only), PPCS/PADS, Kollsman Instrument Corporation (KI) star trackers and star mappers, ITT Aerospace (ITT) star trackers and mappers, Honeywell Aerospace (HA) and Honeywell Radiation Center (HR) star trackers and mappers, American Science and Engineering (ASE) star trackers and mappers, Applied Physics Laboratories (APL) star trackers and mappers, Ball Brothers (BB) star trackers and mappers, and numerous publications and symposia reports; telephone conversations and correspondence with representatives of HA, HR, TRW, ITT, KI, ASE, APL, BB and NASA/GSFC-SIMS Study Group; trips to KI, HR, ASE, ITT, TRW and NASA; visits from representatives of KI and HR; the assemblage and evaluation of the material gathered through these activities; and the initial formulation of an MIT SIMS-D star mapper using a photomultiplier as a photodetector. These activities are further amplified in the following subsections dealing with the individual SIMS categories.

4.1.5.1 SIMS-A Star Sensor Activities

The documents listed as reference Nos. 98,99,100,101, 102,103,104,105,106,107 and 108 were drawn from the SPARS program and were obtained from HA. These documents plus telephone discussions were major inputs to the SIMS-A SPARS-like star mapper presentation required by NASA and discussed in subsection 4.2.2 of this report. Activities related to the SIMS-DA star mapper definition are providing important background information which is an aid to the evaluation of the SPARS-like SIMS-A star mapper candidate set forth by HA, especially in areas where direct SPARS information is classified.

4.1.5.2 SIMS-B Star Sensor Activities

The PPCS Technical Reports (ref's 27-32) prepared by TRW for NASA under contract No. NAS 5-2111, and excerpts from a TRW compilation, "PPCS/PADS, a Collection of Papers on Precision Attitude Determination and Control", (ref's 33-35) for presentation at the AIAA Guidance, Control and Flight Mechanics Conference, Hofstra University, Hemstead, New York, August 16-18, 1971, are the basic sources of written information utilized in the evaluation of the PADS star sensor for its adaptation to the SIMS-B Star Sensor. Contact has been maintained with TRW in order to incorporate the most current features of PADS and particularly TRW-initiated "SIMS-B - specific" modifications.

Activities related to the specifications of the SIMS-DB1 and SIMS-DB2 Star Sensors have provided additional insight into the SIMS-B Star Sensor.

4.1.5.3 SIMS-DA Star Sensor Activities

In subsection 4.1.3 it was stated that MIT determined to prepare a sufficient number of star sensor approaches to respond at any level of SIMS-D IARU requirement. For the same reason the update frequency required from a SIMS-DA star mapper was initially upper-bounded by our first estimates of SIMS-A requirements (since, presumably, the unstable error rates of the gimbaled, SIMS-D IARU should be less than those in SPARS). Industry was invited to participate (see attachment to fifth monthly progress report, ref. 87) with candidate star mappers. Several organizations have participated or indicated imminent participation, namely - KI with a silicon star mapper, HR with a silicon star mapper, and ASE with a photomultiplier star mapper (PSM).

With the relaxation of the SIMS-D IARU stellar update rate requirement it became evident that the SIMS-D candidate star sensor should be a star mapper. MIT/CSDL is conducting an intensive, brief, study to ascertain whether or not MIT should specify its own PSM candidate within the time remaining in this study. The rationale for initiating this study is based on several factors. First, since MIT is defining the SIMS-D candidate, MIT ought to specify all functions and components to the extent that it can do so from a position of ability and confidence. MIT/CSDL is not actively engaged in state-of-the-art research and development of gimbaled star trackers or solid state sensors that can be readily translated into SIMS capability as a competitive, strong, star sensor candidate. On the other hand, MIT/CSDL has no lack of ability to generate a strong, competitive PSM. There are no apparent fundamental physical or technical reasons why a PSM could not be developed to meet SIMS requirements. However, no organization has attempted to do so, in so far as we have ascertained to date (including discussions with NASA/GSFC personnel). The contemporary industry response to our request for specification of a PSM candidate does not indicate availability to NASA of an established technical R&D base that is significantly more advanced than that of MIT/CSDL in this development area.

4.1.5.4 SIMS-DB Star Sensor Activities

The SIMS-DB1 and SIMS-DB2 star tracker concepts were outlined by MIT and industry was invited to participate in proposing star sensor implementation.

Positive response toward participation was received from TRW. Cooperation to the extent of replying to inquiry is possible with ITT, but they have chosen not, at this time, to generate an in-house document specifying all trade parameters and system design. Since MIT has now concluded that a star mapper approach is appropriate for the SIMS-D star sensor MIT has informed TRW that no further response or activity on either SIMS-DB1 or SIMS-DB2 star sensors will be sought. However, MIT has indicated to TRW that it may incorporate into a SIMS-B any aspects of the SIMS-DB1 and -DB2 approaches that TRW may deem a useful modification.

4.1.6 PRESENTATION OF MATERIAL

Subsection 4.2 contains discussions of subjects as required by NASA for each star mapper candidate input made available in the course of this study (or reference to pertinent information in ref. 85) i.e., SIMS-A, SIMS-DA-KI, SIMS-DA-HR, SIMS-DA-HA, SIMS-DA-M, and SIMS-DA-ASE. (KI = Kollsman, HR = Honeywell Radiation Center, HA = Honeywell Aerospace, M = MIT/CSDL, ASE = American Science and Engineering) In this way, an attempt will be made to represent, fairly, all of the responses from industry. Many subsections in this report are presently deficient, but will be completed by the Final Report. The general format is prescribed in this report and is intended to also pertain to the final Report, i.e., subsections 4.2._.1; Optics, 4.2._.2; Photodetector, 4.2._.3; Electronics, 4.2._.4; GSE, 4.2._.5 Error Model, and 4.2._.6; Trade Parameters. A description of the contents assigned to each of these subsections is given in subsection 4.2.1.

Similarly, subsection 4.3 contains discussions of subjects as required by NASA for the star tracker candidate input made available in the course of this study (or reference to pertinent information in ref. 85). Essentially, this is the TRW input on SIMS-B and a brief commentary on the SIMS-DB concepts, in view of the MIT decision to choose a star mapper approach to SIMS-D. The general format prescribed in this report is again planned to also pertain to the Final Report, i.e., subsections 4.3.1.1; Optics, 4.3.1.2; Photodetector, 4.3.1.3; Modes and Electronics, 4.3.1.4; Gimbals, 4.3.1.5; Encoders, 4.3.1.6; Signal Processing, 4.3.1.7; GSE, 4.3.1.8; Error Model, and 4.3.1.9; Trade Parameters.

4.2 STAR MAPPERS

All of the star mappers considered for SIMS-A and SIMS-DA star sensors have body-fixed optical boresights and body-fixed reticles (hereinafter referred to as slit patterns or slits). The star field is imaged by the optics onto the slit surface. The orbital pitch rate causes the star images that enter the field-of-view to transit the several slits. A photodetector or photodetectors behind the slits converts the star radiant power transmitted through each slit into an electrical signal. The electronics following the photodetector amplify and filter the star signals, and measure the time of occurrence of some feature or features of the filtered star signals. These measurements have been loosely designated in the literature as star transit times, where it is to be understood that this means the time of occurrence of some meaningful feature (e.g., filtered star pulse centroid) and not the time interval taken to transit a slit by the actual star image.

There are two basic requirements that must be met by any star mapper used to bound unstable errors of an IARU. The mapper measurement must be suitably accurate and suitably frequent. It is relatively easy to achieve either of these requirements separately, but considerably more difficult to achieve them together. Accuracy can be achieved, with a reasonable aperture, by selecting the few brightest stars. Then, a frequent star measurement requirement will dictate a large field-of-view, which imposes severe tolerances on the fabrication of the optical components, slits and assembly and on the stability of the mechanical structure and supports, while also increasing thermal sensitivity, and increasing susceptibility to bright objects and stellar background. Frequency of stellar measurement can be achieved with reasonable fields-of-view by detecting the more populous dimmer stars. This dictates increasing the size of the aperture, or the sensitivity of the detector, or both; a larger aperture increases the sunshade problem, and imposes a weight penalty that increases, roughly, as the cube of the diameter of the aperture.

Photoconductive cadmium sulfide and photovoltaic silicon are the only solid state photodetectors considered in this study. Application of a photomultiplier is also considered and an S-20 photocathode is considered as an example. Cadmium sulfide has been used extensively by HA in the SPARS program. It is discussed in subsections 4.2.0 and 4.2.2 of this report. Silicon is being considered as an alternate photodetector for SPARS-like applications by HR, KI and HA. It is discussed in subsections 4.2.0, 4.2.3, and 4.2.4 of this report. The S-20 photocathode surface has been employed in a number of star tracker image dissectors, for example, the ITT F4004 and F4012 considered for application in the TRW PPCS/PADS (see Subsection 4.3 of this report). Other photocathode materials will be covered in the final report.

4.2.0 STAR MAPPER PERFORMANCE CHARACTERISTICS

The two performance characteristics required of a SIMS/EOS star mapper are sufficient attitude accuracy and sufficiently-frequent stellar measurements. A large number of parameters enter into the design considerations: aperture, field-of-view, spectral transmissivity of optical components, off-axis imagery, focal length, slit width, slit length, slit number, slit pattern, photodetector type, photodetector spectral response and efficiency, detector noise, detector response time, and signal processing. In addition there are the gross characteristics of size, weight, power, reliability, cost and lifetime.

Based on the three photodetectors which are to be considered, certain preliminary relationships between the parameters, bounded by the SIMS performance characteristics, can be established.

Given a photodetector and its preamplifier, and assuming, for the moment, that suitable fabrication of the optics and slits can be implemented, the list of remaining parameters can be lumped into an effective aperture area, a , the field-of-view (or swath width), W, and the noise bandwidth, B.

The effective aperture and bandwidth or bandpass determine the signal-to-noise ratio of the specific photodetector and preamplifier for each star (i.e., for each combination of stellar magnitude and spectral class). For silicon and the photomultiplier the photoresponse is fast and these detectors will follow the variation in radiant power as the star transits the slit. Cadmium sulfide (CdS) has a slow response. If the star image is equal to the slit width, the CdS response will continue to increase after the star image centroid has passed the slit centerline until the stellar radiant power has decreased to the point where the detector's potential static response is reduced to equal the slowly increasing real response. Thus, variations in transit time of star images due to variations in spacecraft attitude rates will affect the time of occurrence of the signal peak with respect to the actual time of coincidence of the star image centroid and slit centerline. This point will be examined in more detail in subsection 4.2.2.2.

For silicon and the photomultiplier the S/N is sufficient to establish the effective noise - equivalent transit time uncertainty. For CdS the transit time uncertainty contains both the noise-equivalent transit time uncertainty and the aforementioned angular error rate dependent uncertainty in occurrence of peak response.

The swath width and boresight offset from the orbital plane determine the total field-of-view scanned per orbit. The true anomalies of stars up to 6.5 visual magnitude have been assembled as a function of orbital orientation, swath width and detector response magnitude (see subsection 5.3.5 of this report). From this data the interval distributions between measurements of usable stars can be examined in detail.

4.2.0.1 Stellar Interval Evaluation

The stellar update performance required by a SIMS-A may be on the order of three-axis information every ten minutes.* Therefore, if the orbital period is approximately one hundred minutes, a new usable star must transit the star mapper within a 36° interval of true anomaly from the previous usable star transit. The anomaly interval in excess of 36° is designated a star-poor gap (SPG). A typical representation of SPG distributions is shown in Figure 4-1 drawn from the MIT star availability studies. From the star availability study certain empirical relations are discerned. Figure 4-2 shows the average number of usable stars per orbit for any limiting detector magnitude and swath width. The detector boresight is assumed to be in the orbital plane in Figure 4-2. The differential translations of the three detector scales is a result of the distribution of spectral classes of all the stars used in assembling the catalog. Presumably, if all stars were of the AO reference type, all of these magnitude scales would coincide. An approximate relationship between the average sum of SPG per orbit, $\overline{SPG}$, expressed as a percent, and the average number of usable stars per orbit was discerned and is shown in Figure 4-3.

---

* See subsections 5.1, 5.5, and 3.1.1.1.

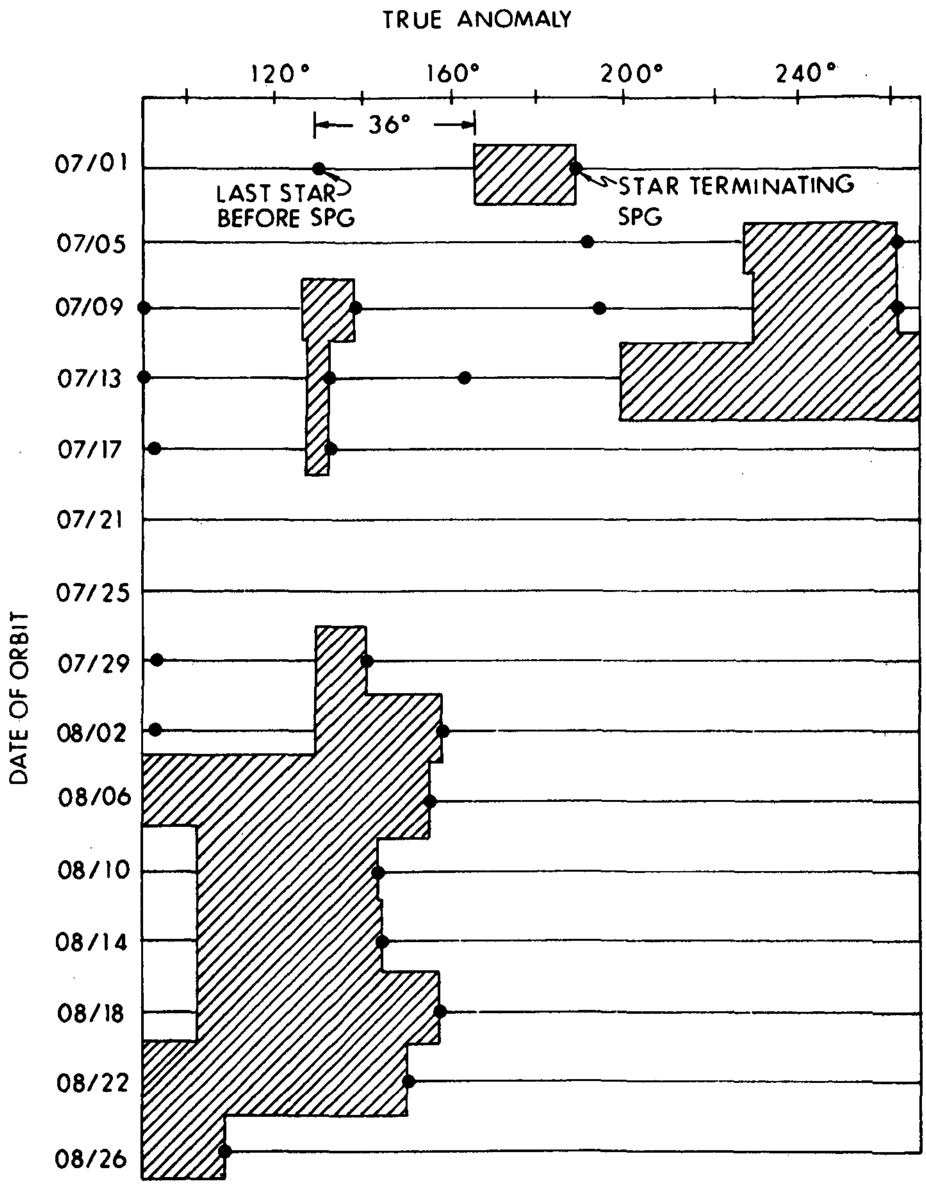

Zenith-directed boresight. 4^{o} Field-of-View.
Silicon detector. Usable stars brighter than 3.6^{M}(Si).

Figure 4-1 SPGs for Daylight Segments of a Few 9:00AM Sun-synchronous Orbits.

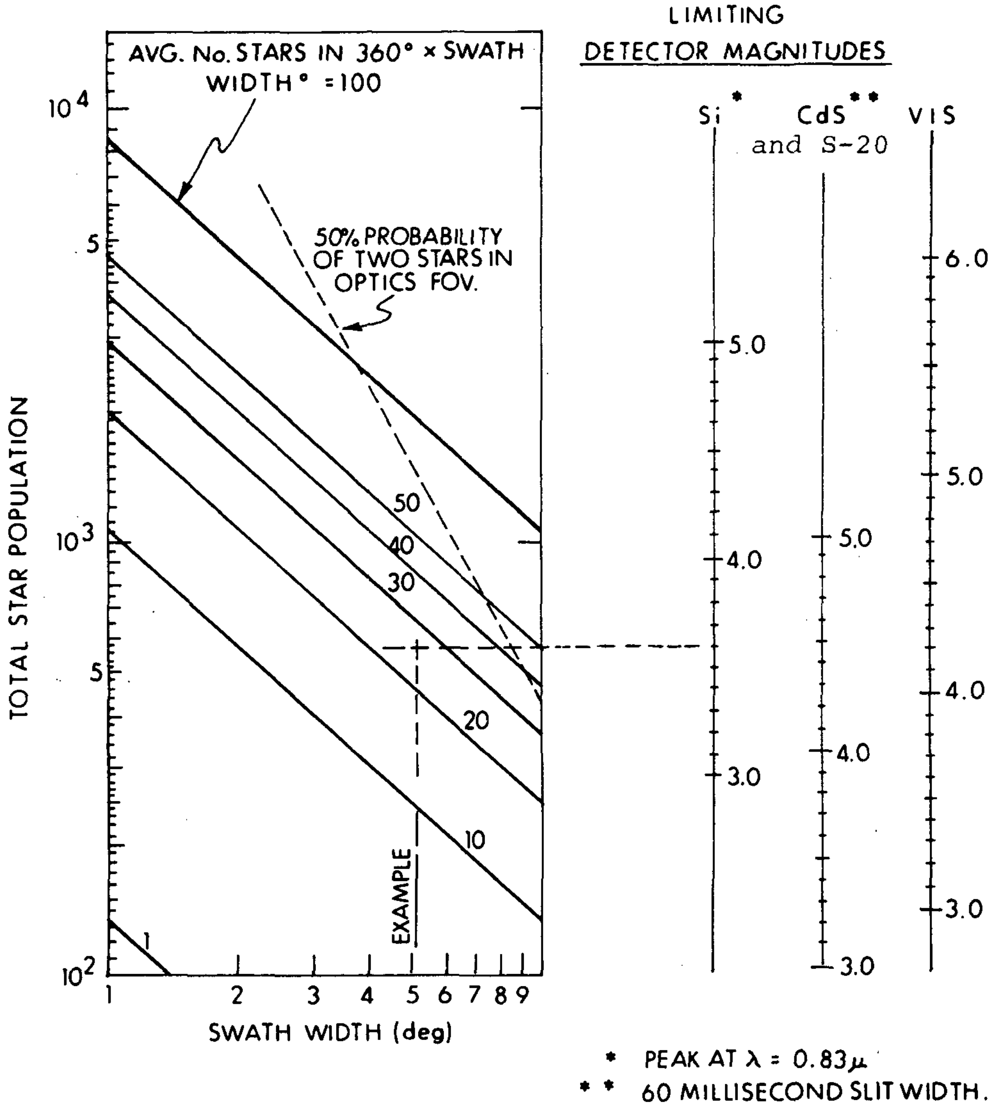

Figure 4-2 Loci of Constant Average Number of Usable Stars Per Orbit in the Plane Defined by Swath Width and Limiting Detector Magnitude.

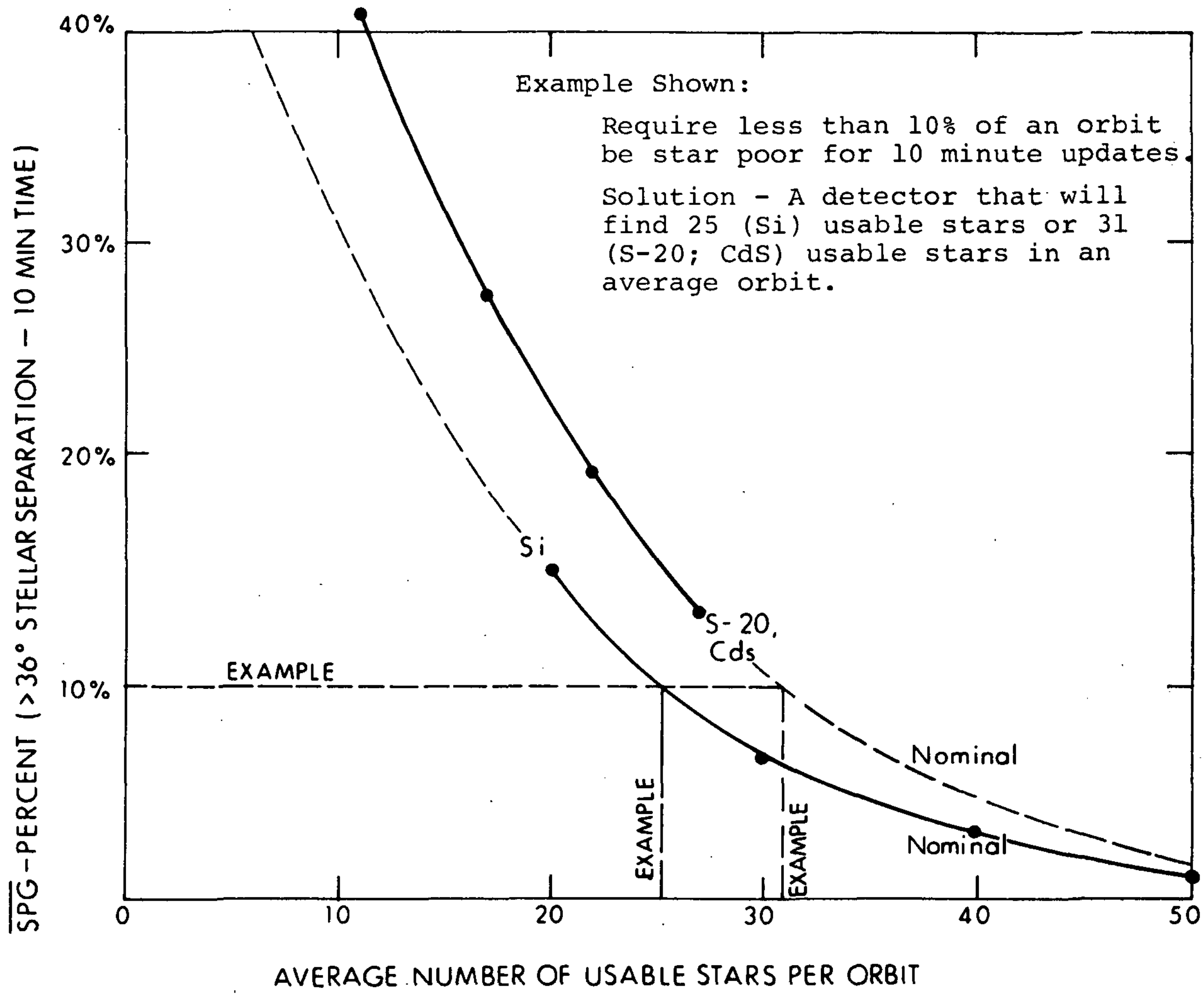

Figure 4-3 An Empirical Relation Between $\overline{SPG}$ and Average Number of Usable Stars Per Orbit

Figures 4-2 and 4-3 are of particular value because they establish a relationship between limiting detector magnitude and swath width when performance characteristics are specified. For example, if adequate stellar update for SIMS-A is required 90% of the time, i.e., $\overline{SPG}$ = 10%, then from Figure 4-3 the average number of usable stars for a silicon detector is 25. This determines the relationship between limiting silicon magnitude and swath width in Figure 4-2. If the detector magnitude is specified from other considerations (e.g., an aperture compromise between weight and S/N) as, say, 3.6^M, then the swath width (optics field-of-view) should exceed 5^O. If the swath width is specified from other considerations (e.g., limitations in optical tolerances for off-axis imagery) as, say, 5^O, then the detector limiting magnitude must exceed 3.6^M.

Knowledge of the distribution of SPGs can also be important. For example, with the requirement $\overline{SPG}$ = 10%, ten SPGs may occur in any orbit, each only 3.6^O. Then the intervals between acquisition of usable stars is eleven minutes which might still be quite acceptable. Figure 4-4 shows typical distributions of SPGs.

4.2.0.2 Signal and Noise Evaluation

The dependencies of the responses of various photodetectors on stellar magnitude and spectral class have been obtained from several sources and are presented in Figure 4-5. Response of silicon and S-20 were extracted from reference 109, designated by the abbreviation LPL in Figure 4-5.

The silicon response designated HR SPARS is claimed by HR[110]. At this time MIT has not seen documented data. This data will be sought for inclusion in the final report.

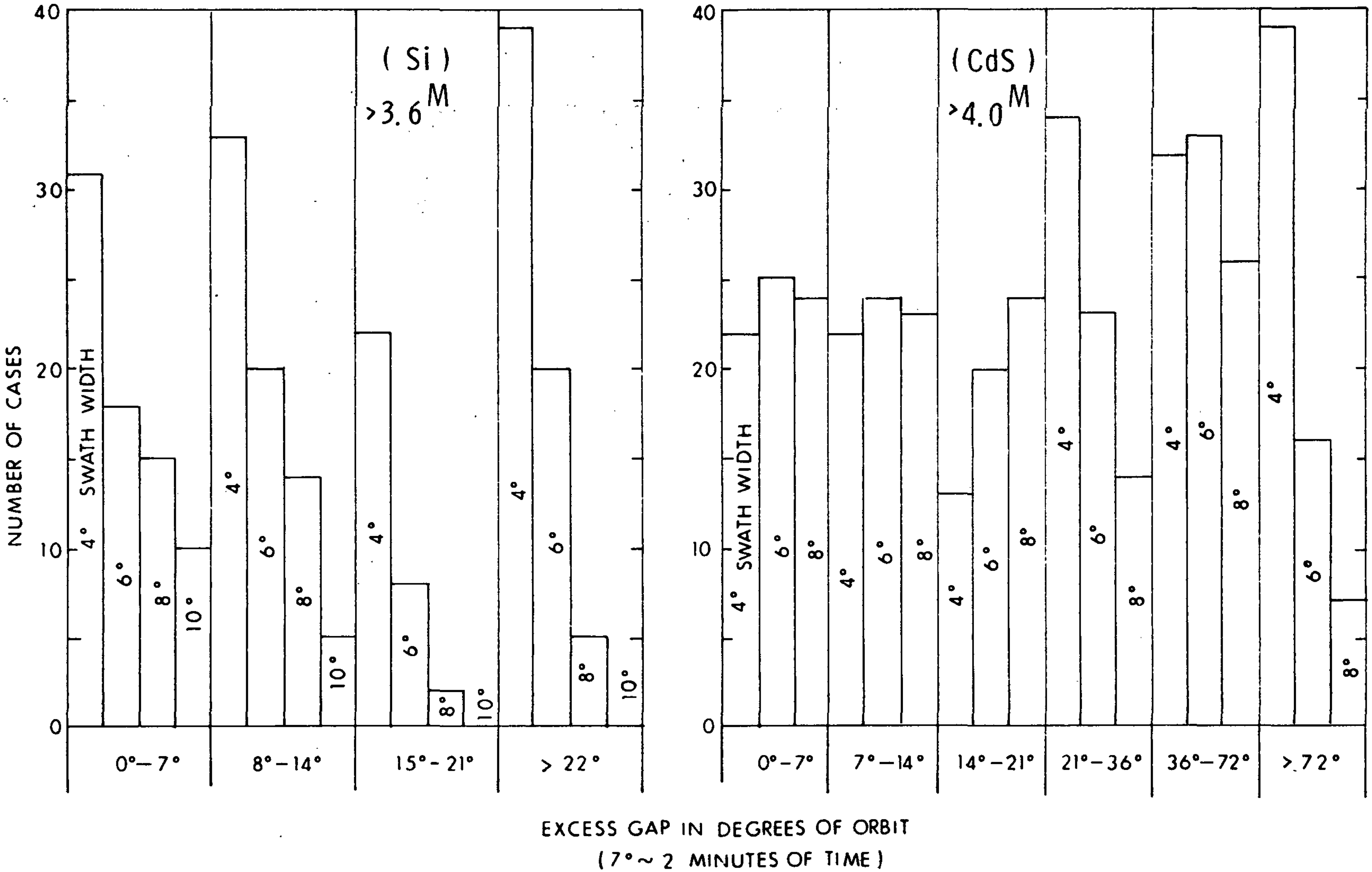

Figure 4-4 Some Typical SPG Distributions

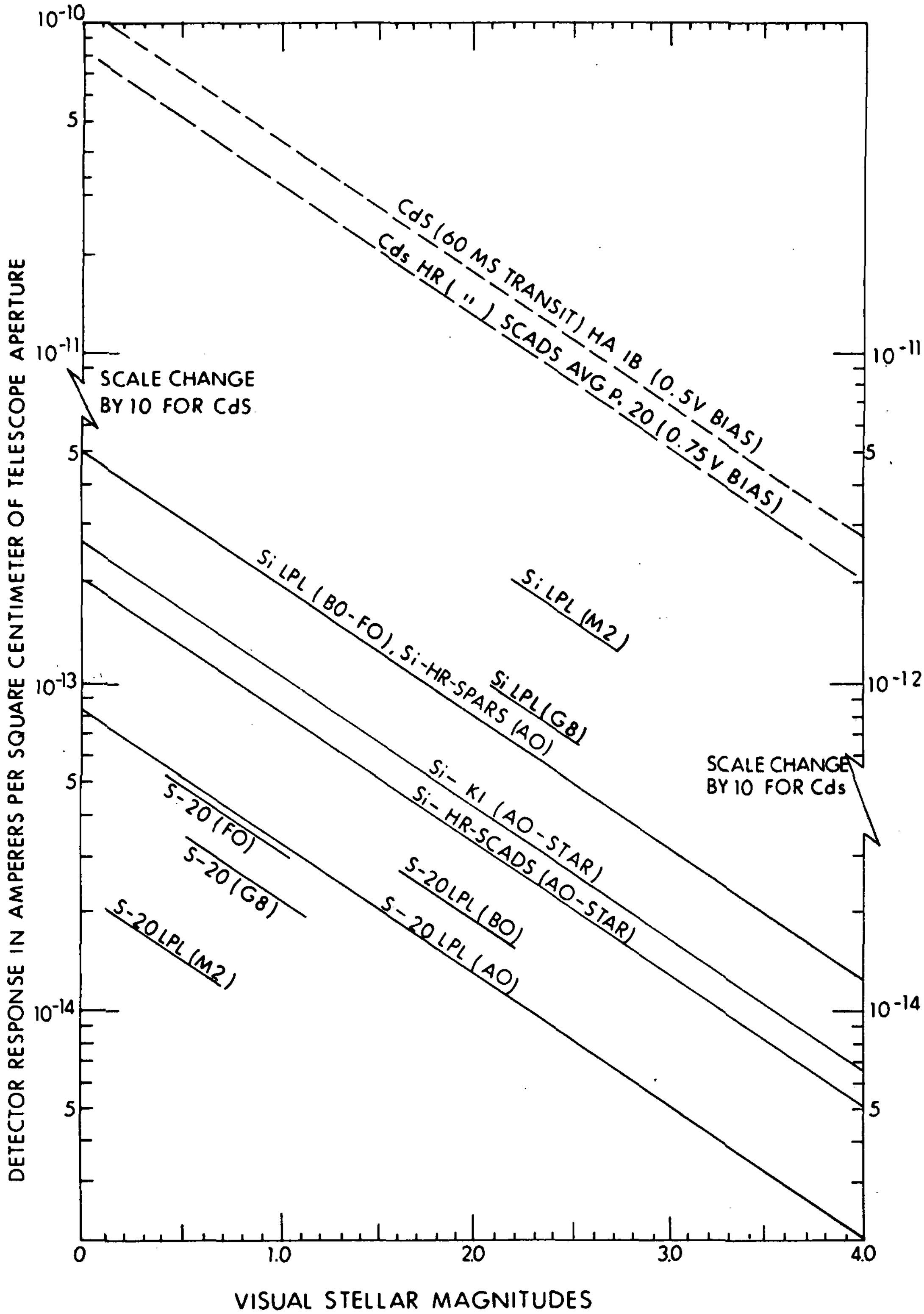

Figure 4-5 Estimates of Detector Responses Interpreted from Data Contained in Sources Referenced in the Text.

The silicon response designated HR-SCADS was calculated from data in reference 111. The silicon detectors referenced were fabricated by HR.

The silicon detector designated KI has been fabricated by Texas Instrument Company for KI. Insufficient data was supplied in reference 112 to accurately locate the Si-KI line in Figure 4-5. Its location relative to Si-HR-SCADS is based on the quoted peak responsivities in references 111 and 112. Additional data will be sought for analysis and inclusion in the final report.

The differences in response of the silicon reported from the four sources is dependent on the manufacturing processes and goals. Comparison of the spectral response curves in references 109 and 111 show a longer wavelength at peak response, broader spectral response, and higher peak response for LPL than for HR-SCADS. Silicon can be fabricated to achieve a specific peak wavelength. It is possible to increase the responsivity at longer peak wavelengths. The peak responsivities were ~0.3 amperes/watt for HR-SCADS, >0.35 a/w for KI, 0.46 a/w for LPL and ~0.5 a/w for HR-SPARS. The peak wavelengths as known are ~7000Å for HR-SCADS, ~8000Å for HR-SPARS and 8300Å for LPL.

The CdS response designated HR-SCADS was calculated from data in reference 111. The CdS detectors referenced were fabricated by HR. The response shown in Figure 4-5 is an average over the cell length corrected to a 60 millisecond star transit using a response versus transit time relationship found in reference 111.

The CdS response designated HA IB was estimated from data in reference 24, supplied by HA.

Representative noise-equivalent inputs given in or estimated from data in references 24, and 109 to 112 inclusive are:

Si-HR-SCADS	$N = 1.55\times10^{-14}$ a/Hz$^{1/2}$
Si-KI	$N = 1.23\times10^{-14}$ a/Hz$^{1/2}$
Si-HR-SPARS	$N = 0.4\times10^{-14}$ a/Hz$^{1/2}$
CdS-SCADS	$N = 1.06\times10^{-12}$ a/Hz$^{1/2}$

The noise arises principally from cell leakage current, I, and preamplifier feedback resistor, R, where

$$N^2 = \frac{4kT}{R} + 2eI \quad .$$

The extent of excess low frequency noise has not been fully assessed for all of these detectors. It is an important consideration that will be included in the final report.

Noise in the case of a photomultiplier arises chiefly from background illumination. In order to represent the S-20, the effect of sunlight at the sunshade design angle is assumed to be 0.15 pico ampere of S-20 response per square centimeter of effective aperture. The number used by KI in evaluating their solid state photodetector was 64 pico amperes for approximately 73 square centimeters of effective aperture (ref. 112). The KI number is reduced by a factor of 6 (see Figure 4-5 for estimating relative response of Si-KI and S-20-LPL assuming sunlight is in the G5 spectral class) yielding 0.15 pa/cm^2. The noise with a two inch diameter effective aperture is $N = 0.106\times10^{-14}$ a/[Hz(No. of slits)]$^{1/2}$.

Figure 4-6 summarizes the information collected on response and white noise, including stellar magnitude scales

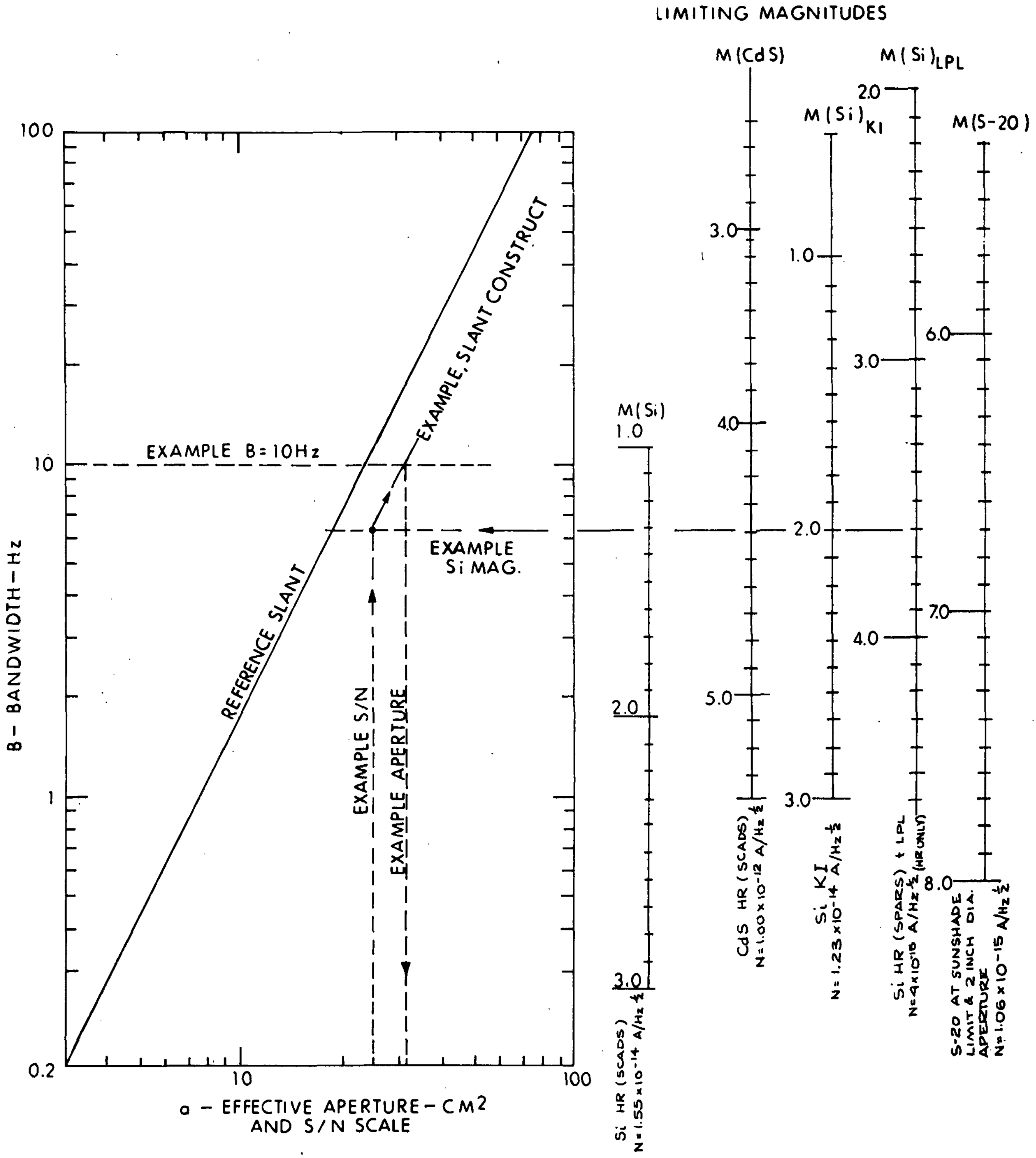

Figure 4-6 A Relationship Between S/N and Detector Limiting Magnitude, Noise Bandwidth and Effective Aperture.

of detector response. These magnitude scales were located by noting the visual magnitude in Figure 4-5 at which the detector response per unit aperture equaled the equivalent noise input per root bandwidth. The visual magnitudes were then corrected to detector magnitudes according to the empirical mean spectral class found in compiling Figure 4-2.

One important feature of a diagram in the form of Figure 4-6 is that a relationship is formed between the noise bandwidth, the effective aperture and the limiting detector magnitude. If the example used in Figure 4-2 is continued from the point-of-view that a 5° swath width is chosen to meet optical tolerances, then the limiting silicon magnitude satisfying the 10% average $\overline{\text{SPG}}$ requirement is 3.6M (Si-LPL). A relationship exists between bandwidth, signal-to-noise ratio and the transit time uncertainty. If the result of solving that exercise indicates a noise bandwidth of 10, and a signal-to-noise ratio of 25 (1σ), the effective aperture is read from Figure 4-6 as 31 cm^2 for a Si-HR (SPARS) detector system. Assuming 70% optical efficiency, the aperture diameter is 3 inches.

Figure 4-6 cannot be used with the S-20 magnitude scale for any aperture other than the 20 cm^2 which was used in the noise calculation. The S-20 scale was only included for comparative purposes. To illustrate, assume S-20 instead of silicon was used in the preceding example; the limiting magnitude is 3.98M(S-20). Then, for a bandwidth of 10 Hz, the signal-to-noise ratio is found as 135 (the construct extends out of the diagram).

4.2.0.3 Signal Shape Effects

The star signal output of the preamplifier is filtered by a narrow pass-band filter with a high cutoff frequency, f_H, (usually in the range of 10 Hz) and a low cutoff frequency, f_L, (usually less than 1.0 Hz).

The high frequency cutoff affects the star signal in four undesirable ways:

- Delays the star signal
- Distorts the star signal
- Decreases the star signal
- Decreases the leading edge slope of the star signal

This sacrifice is tolerated in some optimal compromise in order to achieve a reduced noise bandwidth.

The low frequency cutoff introduces three desirable features:

- Signal shaping
- Partial elimination of excess noise
- Elimination of D.C. bias shifts

A complete analysis of each of the filter outputs of real star transit situations for each candidate star mapper is a major task beyond the scope (in level of activity and funding) of the present task. However, a simple example can be displayed which will give order-of-magnitude answers and coarse functional dependencies.

Assume the stellar input to the photodetector is a symmetrical, triangular signal, Figure 4-7, of half-width T seconds of time (i.e., the time for the centroid of the star image to transit the slit from edge to edge), and amplitude A. Assume a high frequency cutoff characterized by a time constant $\tau > T$ for the system. The peak of the system response occurs at a time t_{pc} after the peak of the triangular input signal, where

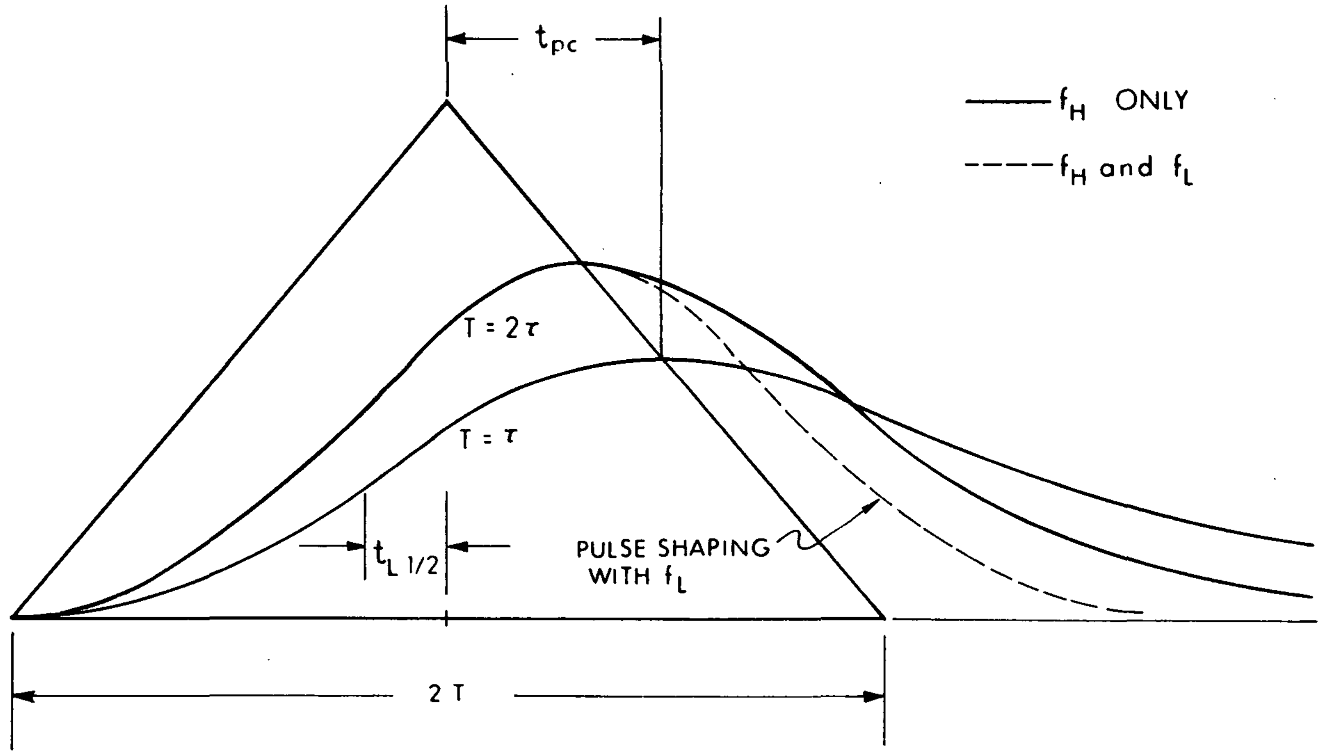

Figure 4-7 Response of a Linear Filter with Time Constant τ to a Triangular Signal

$$t_{pc} = \tau \; \ell n\left(2e^{T/\tau} - 1\right) - T \quad , \tag{4-1}$$

and the peak value of response is

$$R_p = A\left[1 - \frac{\tau}{2T}\; \ell n\left(2e^{T/\tau} - 1\right)\right] \quad . \tag{4-2}$$

The effect of T or τ on t_{pc} for small variations is

$$\delta t_{pc}\Big|_{\tau} = \left[\frac{2}{2-e^{-T/\tau}} - 1\right]\delta T \quad , \text{ and} \tag{4-3}$$

$$\delta t_{pc}\Big|_{T} = \frac{T}{\tau}\left[\frac{2}{2-e^{-T/\tau}} - \frac{\tau}{T}\; \ell n\left(2e^{T/\tau} - 1\right)\right]\delta\tau . \tag{4-4}$$

The time constant τ is determined by the electronic filters with silicon and photocathode detectors; but as the time constant of the CdS cell before filtering it is larger than T, it must be considered as the first important shift of signal peak, comparable in effect to the second shift imparted by the electronic filters.

If the peak angular error velocity in spacecraft attitude rate is .0017 deg/sec (1σ) (see Ref. 85, subsection 1.1.1), and the orbital rate is .06 deg/sec, then $\delta T/T \approx 0.03$. For silicon, with typical filter time constant ($\tau = 0.1$ sec) and a $10\widehat{''}$ slit width (i.e., T = 0.046 sec):

$$\frac{\delta t_{pc}}{T}\Big|_{\tau} = \left[\frac{2}{2-e^{-0.46}} - 1\right]0.03 = .0138$$

$$\delta\theta \simeq 0.138\widehat{''} \; (1\sigma) \quad \text{for a } 10\widehat{''} \text{ slit}$$

$$[0.235\widehat{''} \; (1\sigma) \quad \text{for a } 17\widehat{''} \text{ slit}]$$

For CdS, with typical cell time constant ($\tau = 0.3$ sec.) and a $10\widehat{''}$ slit width:

$$\frac{\delta t_{pc}}{T}\bigg|_{\tau} = \left[\frac{2}{2-e^{-0.153}} - 1\right] 0.03 = .0225$$

$$\delta\theta \simeq 0.225'' \ (1\sigma) \quad \text{for a } 10'' \text{ slit}$$

The effect of blur circle spectral influence will be evaluated in the Optics Subsections, i.e., 4.2._.1.

The effect of slit edge variability will be evaluated in the Photodetector Subsections, i.e., 4.2._.2.

4.2.1 GENERAL DESCRIPTION OF SUBSECTIONS

Subsection 4.2.2 describes the SPARS-like SIMS-A star mapper. The remaining subsections, 4.2.3 to 4.2.7 inclusive, define alternative approaches to implementing a SIMS-D star mapper. Subsections 4.2.3 and 4.2.4 represent silicon detector approaches suggested by KI and HR respectively. They differ significantly in the optics and electronics implementations. Subsection 4.2.5 is a modification of the SPARS-like SIMS-A, using CdS, and differs principally in FOV from SIMS-A in order to meet relaxed SIMS-D update requirements. Subsection 4.2.6 introduces a third possible sensor, the photomultiplier. The optics and electronics will have substantial differences from those used with solid state detectors. Subsection 4.2.7 is a response from AS to the photomultiplier approach to a SIMS-D and constitutes a modification to the star mappers developed for the X-ray Explorer Experiment (SAS-A).

Each of the subsections 4.2.2 to 4.2.7 are further divided into four subdivisions describing major components or functions and two subdivisions tabulating and summarizing the error and trade parameter items identified in the first five subdivisions. The general character of these subdivisions is as follows:

- Optics - the type of optics is identified, i.e., reflective, refractive, catadioptric; the configuration and dimensions are displayed; the blur circle or shape is examined as a function of wavelength and temperature throughout the field-of-view; the effects of temperature gradients are noted; the optics are diagnosed as part of the system by examination with Figs. 4-2, 4-3 and 4-6, to determine $\overline{SPG}$ relative to SIMS-A; comments on sunshading are given.

- Photodetector - the type of photodetector is identified, i.e., CdS, Si, PMT; the slit configuration and dimensions are displayed; characteristics of the detector response are examined including uniformity along the slit; characteristics of detector noise, i.e., white noise and excess noise, are examined; degradation factors and reliability are discussed; level bias drift and hysteresis effects are noted; power requirements are identified; bright object protection is noted.

- Electronics - the characteristics of the preamplifiers and filters are examined as to function, signal effects, noise contribution and noise bandwidth; the measurement function is examined and star detection time uncertainty contributory factors are identified and assessed; star mapper output format is identified; estimates of power, reliability and redundancy are given.

- GSE - identification of equipment required for incorporation of the star mapper into the SIMS and pre-flight calibration.

- Error Model - all the error contributions identified in the preceding four subdivisions are summarized in tabular form with comment; comment will place the error mechanism in a spectrum from true white noise type of uncertainty (e.g., Johnson and shot noise) through a semi-white noise (e.g., edge roughness, the grosser features of which may be calibratable and hence with large amounts of ground processing this effect could be reduced) to strong bias factors (e.g., shifts in star detection time associated with spectral color class or uniform temperature of the optics).

- Trade Parameters - weight, size, power, reliability, cost, accuracy, field-of-view required and simplicity of design will be summarized.

This is an ambitious program to be completed by the final report. A sizeable fraction of these areas is not yet completed in this second interim technical report. This is noted in subsection 4.4.

4.2.2 SIMS-A STAR MAPPER, FUNCTIONAL DESCRIPTION

A SIMS-A star mapper, derived from the experience and technology of the SPARS program (HA), is designated SPARS-like and consists of:

- A concentric catadioptric optical system.
- Six narrow-strip, cadmium sulfide, photoconducting detectors mounted in a spoke-like array on a curved substrate.
- Electronics to produce a narrow one-shot pulse and a slit identification signal associated with a star transit.
- A timing unit which encodes and records the time of the one-shot pulse and the slit identification.

A block diagram of the Star Sensor Assembly Electronics Function is shown in Figure 4-8 (from Ref. 24). The response time of cadmium sulfide is roughly 300 msec. For reasons related to the large time to respond (discussed in subsection 4.2.2.2), the shape of the leading edge of the star signal output from the photodetector is the most consistent feature of the signal relative to the actual time of star transit. The leading edge slope is close to maximum at half-amplitude. A time measurement of occurrence of the half-amplitude point of the leading edge is chosen which nearly minimizes the noise-equivalent transit time uncertainty. Therefore, as indicated in Fig. 4-8, the signal must be delayed until the peak response is measured, from which a half-amplitude threshold can be set.

The gate detector indicated in Fig. 4-8 permits processing of star signals that do not exceed the dynamic range of the electronics, and excludes processing of stronger signals.

Other star mappers are being developed (HR, HA, KI) as alternative approaches to SPARS-like application. These will be designated ASPARS in this report. Since none of the ASPARS have been developed within a total system context such as SPARS, discussion of ASPARS will only appear in the subsections 4.2.3, 4.2.4, 4.2.5, 4.2.6, and 4.27 describing SIMS-DA star sensor candidates.

4.2.2.1 SIMS-A Star Mapper Optics

A concentric catadioptric f/1.14 optical system (Fig. 4-9) was developed for use with a CdS slit array and is described in references 11, 15, 17, 24, 99, 100, 101, 104 and 105.

This type of optics practically eliminates coma and astigmatism throughout the field of view.

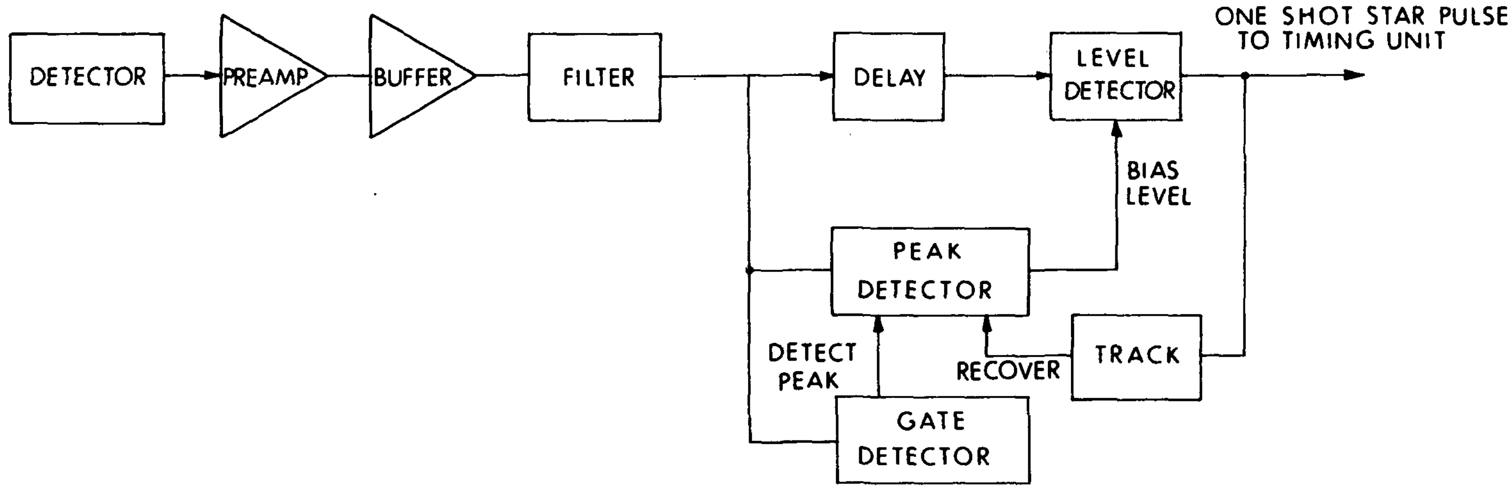

Figure 4-8 Block Diagram of Star Sensor Assembly Electronics Function

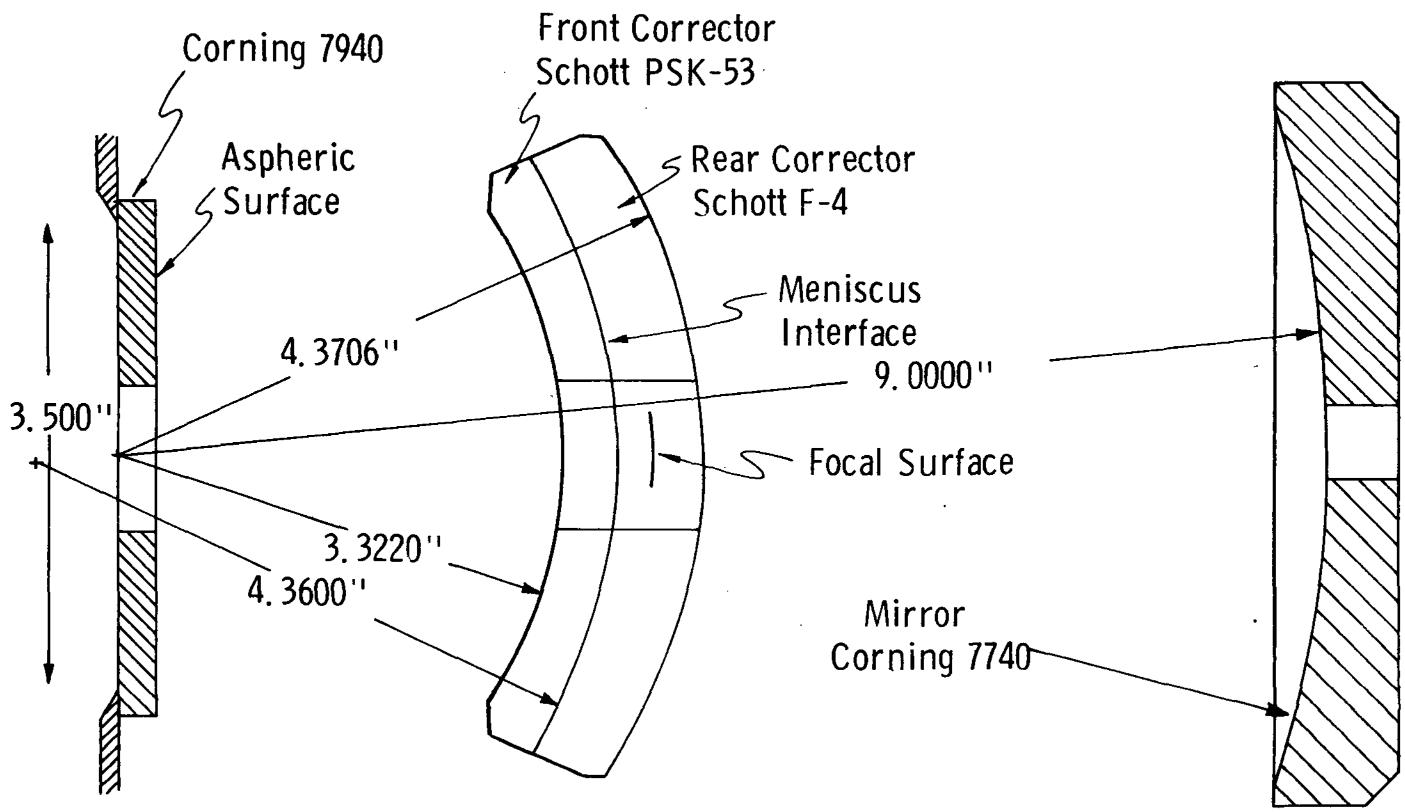

Figure 4-9 SPARS-Like Optical System

The housing is fabricated from invar to minimize thermal expansion and distortion. The design temperature is 72°F. Figure 4-10 shows a blur circle multiplication factor as a function of uniform temperature (inferred from ref. 104).

A plot of blur circle to slit width ratio (slit width .0003 inches) as a function of wavelength was generated from performance data shown in Fig. 13 of Ref. 17 at the design temperature of 72°F and is displayed in Figure 4-11.

HA cautions that a 3° F temperature gradient across the optics housing will cause sufficient mirror tilt relative to the meniscus interface to destroy accuracy.

The field-of-view achieved with the optics shown in Fig. 4-9 is 4°, the unobstructed portion of aperture is 57 cm^2, the transmission is assumed at 76% (a loss of 4% at each interface), and, therefore, the effective aperture is 43.4 cm^2. Then, from Fig. 4-6, with a noise bandwidth of 15 Hz (subsection 4.2.2.3), the limiting magnitude to achieve a S/N of 20 is 4.75^M(CdS). From Fig. 4-2, the average number of stars per orbit is 28. From Fig. 4-3, the $\overline{SPG}$ is 13%, i.e, attitude update can be maintained,with a SPARS-like IARU, throughout 87% of the mission.

Figure 4-12 compares the CdS-Optics color integral spectrum (Ref. 100) with the spectral irradiance of AO and KO stars (approximated by blackbodies at effective temperatures 10,700°K and 4900°K respectively). From Figs. 4-12 and 4-11, 35% of the CdS detector's response to an AO star is contributed by energy at wavelengths associated with blur circles greater than one slit width when the optics is at a temperature of 72° F.

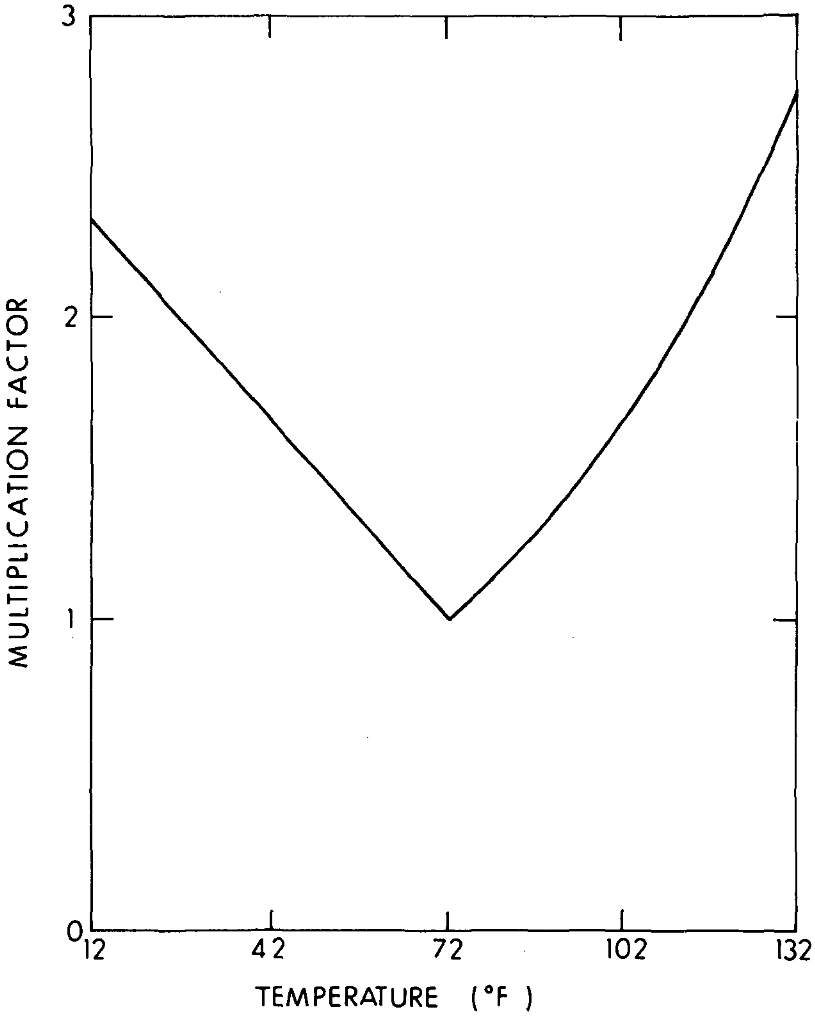

Figure 4-10 Blur Circle Multiplication Factor

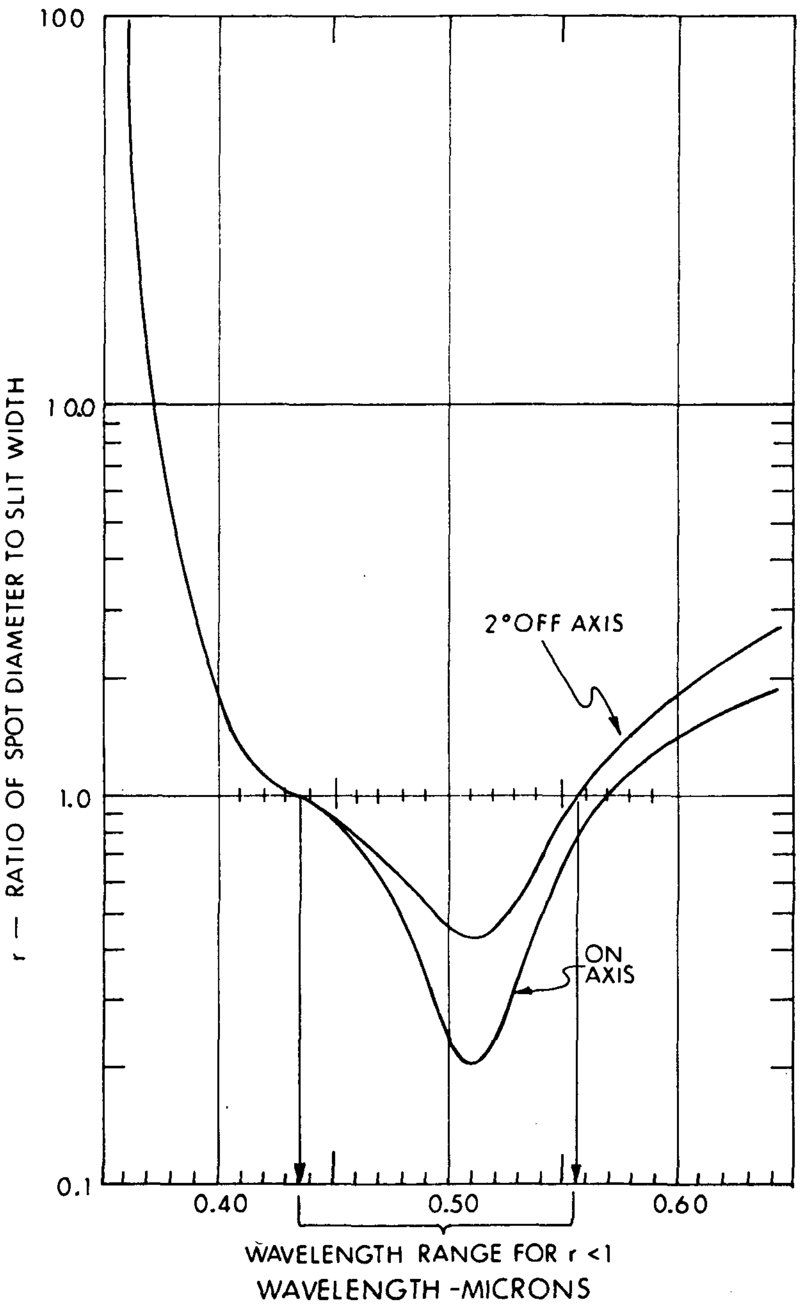

Figure 4-11 Ratio of Spot Diameter to Slit Width as a Function of Wavelength

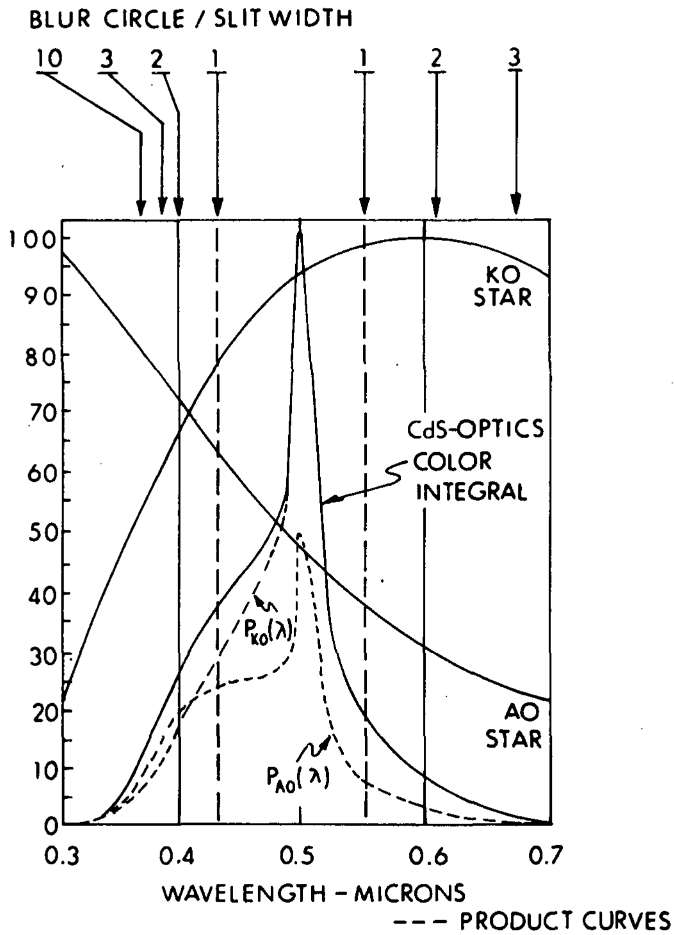

Effective Spectral Irradiance of AO and KO Stars Shown in Comparison

Figure 4-12 Response of the Integrated Subsystem - Optics and CdS - as a Function of Wavelength

The intensity in a spot is distributed as

$$I = I_0 \left[\frac{2\, J_1(x)}{x} \right]^2$$

where x is the radial distance from the center of the spot, J_1 is the Bessel function of order 1, and I_0 is the central intensity. Eight four percent of the incident radiant power is contained within a radius x_0 where x_0 is the first zero of $J_1(x)$. Thus, for any $x < x_0$ the fraction of radiant power between x and x_0 can be shown to be

$$f(x) = \frac{\int_x^{x_0} \frac{[J_1(x)]^2}{x}\, dx}{\int_0^{x_0} \frac{[J_1(x)]^2}{x}\, dx}$$

Set $x = x_0/\gamma$, where γ is the spot size to slit-width ratio. Then a plot of x as a function of λ can be generated in the range $0.360\mu \le \lambda \le 0.435\mu$ by using values of γ from Fig. 4-11. Similarly, a plot of x can be established in the range $0.556\mu \le \lambda \le 0.65\mu$. Having established these relationships, the integrals can be evaluated and the fraction of spectral radiant power outside a <u>circle</u> one slit width in diameter will be found as a function of λ,

$$F(\lambda) = f[x(\lambda)] \quad .$$

A geometrical correction factor $g(\gamma)$ must be calculated to determine the ratio of effective area in the slit and outside the <u>circle</u> containing this spectral radiant power to that area of the circle excluded from the slit. Then $G(\lambda) \equiv 1-g[\gamma(\lambda)]$, and

$$\mathfrak{T}(\lambda) = G(\lambda)F(\lambda)$$

where $\mathfrak{T}(\lambda)$ is the fraction of the spectral radiant power at wavelength λ that is outside the slit. Finally, the product curves, that combine the spectral irradiance of the star and CdS-optics color integral, shown as $P(\lambda)$ for the AO and KO stars in Fig. 4-12, must be integrated with $\mathfrak{T}(\lambda)$ to obtain the total radiant power excluded from the slit when the star image is centered in the slit. From this an estimate of the signal width and amplitude can be achieved. Then, application of equation 4-3 in subsection 4.2.0.3 to each star class will reveal the range in time uncertainty arising from the characteristics of the SPARS-like optics and CdS photodetector.

It is likely that a few representative calculations of these types can be achieved for the final report. A very crude estimate, by inspection of the product curves in Fig. 4-12 referenced by blur circle indicators at the top of the figure, and assuming $\overline{\mathfrak{T}}(\lambda) \simeq 3/4$, gives 12% radiant power outside the slit when an AO star image is centered and 8% for the KO star, at an optics temperature of $72^{\circ}F$. If the slit width is $10''$ the shift in half-amplitude point on the leading edge will be about $0.13''$ for the AO star relative to the KO star at $72^{\circ}F$. It is estimated that an additional bias of $0.2''$ can be added for each $4^{\circ}F$ displacement of uniform temperature from the design value of $72^{\circ}F$. A more exact solution should be presented in the final report.

A bright object sensor, shutter and sunshade will be required weighing approximately 5.0 pounds and adding 12 inches to the unit.

Total weight of optics, sunshade, shutters and electronics is estimated at 15 pounds.

SUMMARY

f/No.	1.14	
FOV:	4^{o}	
Sun Angle:	$>30^{o}$	
Size:	6" × 22"	including sunshade
Weight:	15 pounds	including sunshade
Accuracy:	0.13"	stellar spectrum bias
	0.20"	temperature bias ($\Delta temp \approx 4^{o}F$)
	0.34"	per $1^{o}F$ temperature diff. across optics housing if mounting flange at meniscus
	0.07"	per $1^{o}F$ ΔT across optics housing if flange at mirror
$\overline{SPG}$	13%	

4.2.2.2 SIMS-A Star Mapper Photodetector

The detector developed for the Phase IB SPARS star mapper was developed by Allen-Bradley Corporation (AB). It is a thin film of CdS deposited on a glass substrate. The substrate surface is a portion of an eight inch diameter sphere. An electrical mask is placed over the CdS film. This mask defines the slit array and provides the electrical contacts. The geometry and dimensions of the slit array are shown in Fig. 4-13.

Because of the substrate curvature it has not been possible to use photographic etching techniques to fabricate the slit. A stretched wire is used to shadow-mask the CdS film during deposition of the metal mask. The edge roughness is quoted in ref. 17 as 10 to 20 μ inches. If the slit edge roughness has

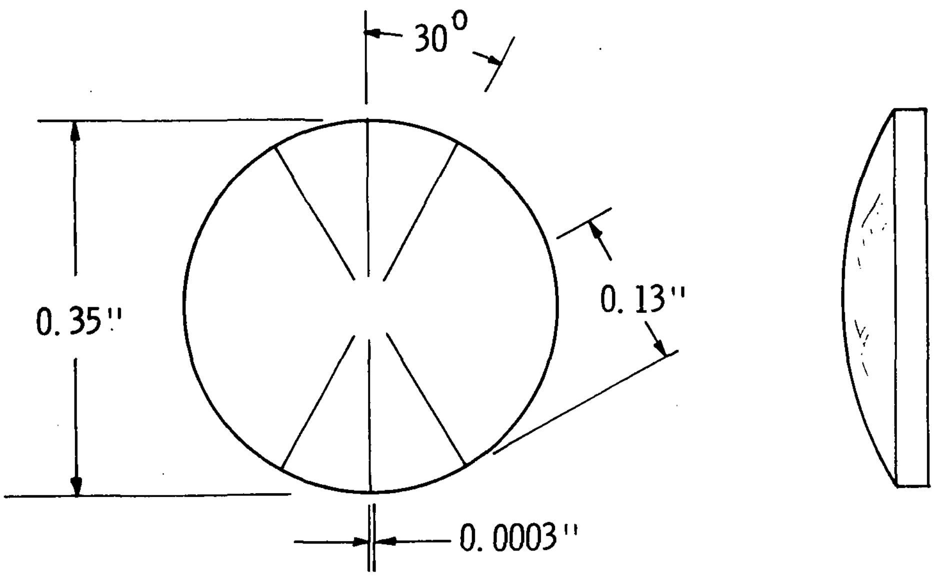

Figure 4-13 Slit Geometry and Dimensions in a SPARS-Like CdS Detector.

the same dimensional variability along the slit as across it, the effective uncertainty in the slit centerline location, ΔT_c, is the product of $\sqrt{2}$, the slit edge roughness (expressed as an equivalent time, ε milliseconds), and the ratio of slit edge roughness to blur circle diameter (also expressed as an equivalent time, γT, where γ is the ratio of blur circle diameter to slit width). Thus,

$$\Delta T_c = \sqrt{2}\,\frac{\varepsilon^2}{\gamma T} \simeq 0.16 \text{ milliseconds } (1\sigma)$$

and

$$\Delta\theta_c \simeq \pm.026'' \text{ or } .052'' \; (1\sigma) \;,$$

which is negligible.

If the edge roughness were mostly extended waviness (where the average spatial wavelength along the slit is large compared to a blur circle diameter), the effective slit width is changed to $T \mp \varepsilon$. The approximate uncertainty in time and angle would be

$$\Delta T_c \simeq \pm 2.2 \text{ milliseconds}$$

$$\Delta\theta_c \simeq \pm 0.36'' \text{ or } 0.72'' \; (1\sigma)$$

There is a variability of response associated with position along the slit. Statistics are given in refs. 24 and 108 on the distribution of amplitude of responses. Considerably better uniformity of response is shown in these references than can be inferred from data in the SCADS reference 111 (see MIT memo, ref. 113). A typical distribution from ref. 108 is reproduced here in Fig. 4-14.

An attempt will be made to determine, and record in the final report, whether a large variability of response time also exists along a slit, since this could be serious in terms

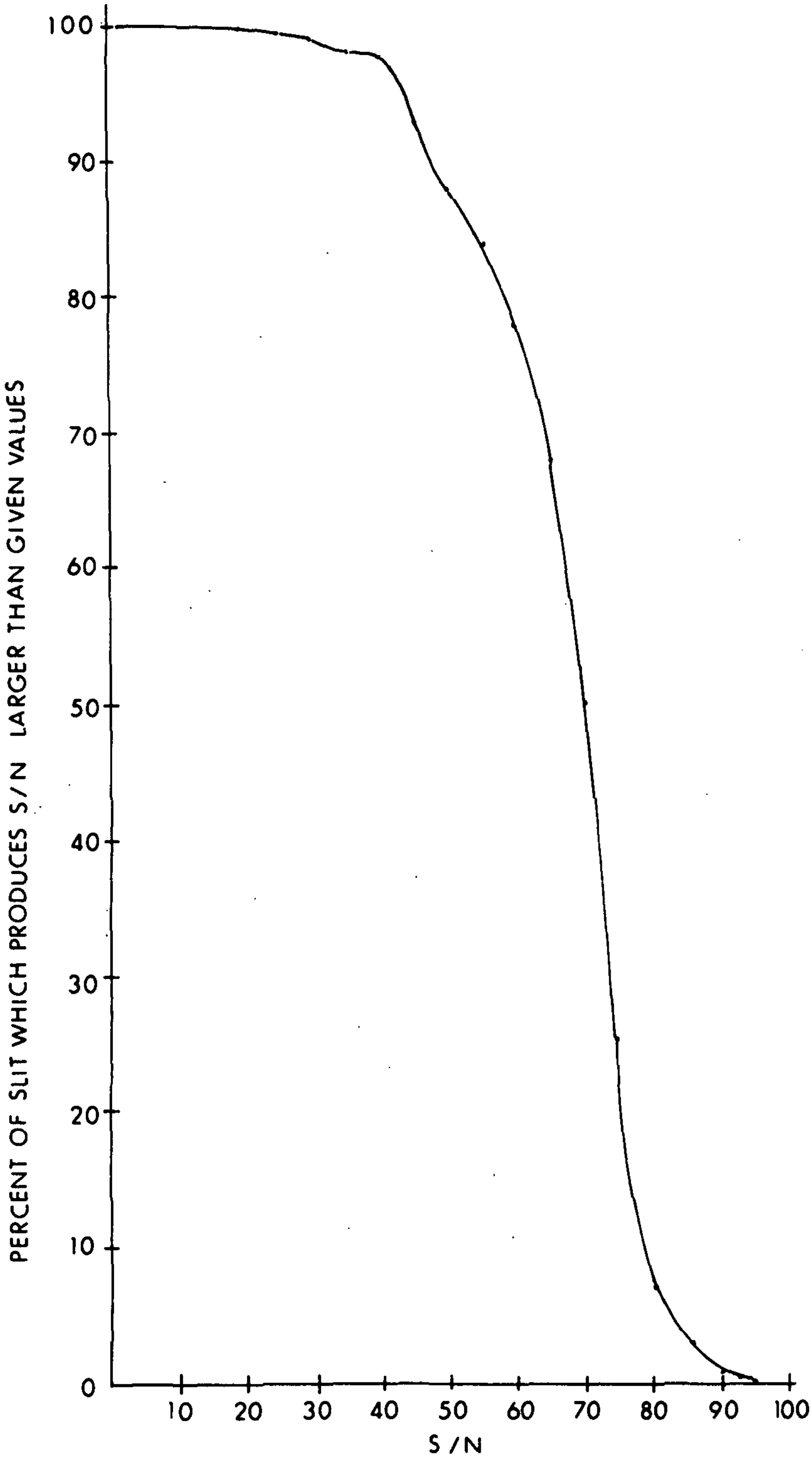

Figure 4-14 Typical CdS Response Variability Along the Slit (Detector #5, Ref.108)

of the SIMS/EOS accuracy requirement (typically $0.1''$ per 10% change in τ).

It is difficult to separate the detector and preamplifier noise contributions. A combined estimate of noise will be given in subsection 4.2.2.3.

The bias lighting of the CdS slit and bias voltage of 0.5 volts produce a DC leakage current of approximately 1.5×10^{-7} amperes. Then $(2eI)^{1/2} \approx 2.2\times10^{-13}$ amps/Hz$^{1/2}$ (estimated from ref. 98). If the allowable background of 1.5×10^{-6} amperes is taken into account, $(2eI) \approx 6.6\times10^{-13}$ amps/Hz$^{1/2}$, maximum.

The time constant of CdS is approximately 300 milliseconds which requires baseline level following to account for integrated effects of noise stars (see electronics subsection 4.2.2.3).

Information is being sought on the spectrum of excess (flicker) noise associated with CdS detectors and electrode interfaces for inclusion in the final report.

Information is being sought on degradation and failure factors for inclusion in the final report.

<u>SUMMARY</u>

Mat'l:	CdS
Slit width:	.0003 inch ($10''$)
Slit Length:	.13 inch (2°)
$\Delta\theta_c$:	$.035''$ (1σ) granular edge $.480''$ (1σ) wavy edge
Noise:	7.3×10^{-13} amps/Hz$^{1/2}$ (bias light and maximum background)

4.2.2.3 SIMS-A Star Mapper Electronics

Figure 4-15 is a partial block diagram extracted from ref. 98, where the purpose of each block is explained and signals are followed through the system.

Only the detector and preamplifier are mounted at the focal surface within the optics. The main electronics package is wrapped around the optics housing. (Transresistance ~10^9 volts/amp.)

The differential buffer provides rejection of common-mode noise between the preamplifier and external electronics package. The DC detector bias current is capacitively isolated at this point.

The low-pass filter is a two-pole Butterworth, with a 5 Hz cutoff. The corner frequency for noise roll-off (18 db/octave) with preamplifier and filter in tandem is 15 Hz.

The delay filter consists of two two-pole Butterworth sections in tandem, each with a cutoff of 7 Hz.

The peak detector normally tracks the signal. When the hold signal is applied, it will detect and hold the peak value of the signal pulse.

The peak value and baseline values are averaged and a 50% of the difference threshold level is generated for the image detector.

To estimate the effect of the signal-to-noise ratio on transit time uncertainty the slope at the half-amplitude point of the leading edge is assumed to be approximately one half of that of the signal slope at half maximum of the signal at the

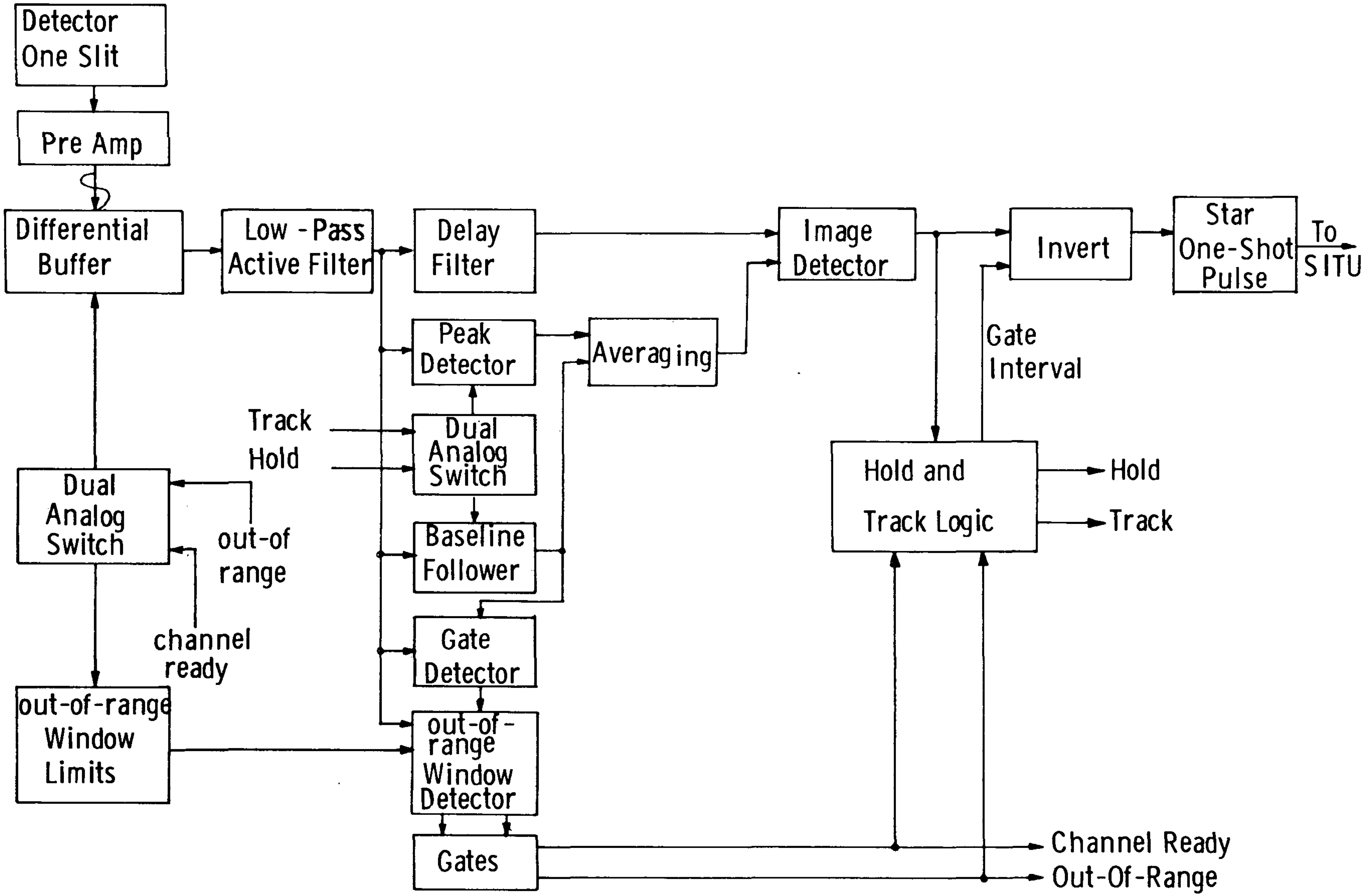

Figure 4-15 Block Diagram of SIMS-A Star Mapper Electronics

output of the preamplifier (i.e., essentially the delay filter has stretched the signal in time by a factor greater than 2).

The slope at half-amplitude of the delayed signal is

$$m_{D\frac{1}{2}} \approx \left(\frac{1}{2}\right)\left[\frac{S}{2T}\left(12\right)\right]\left\{1 - e^{-1/6}\right\} \quad ,$$
$$= 0.462\ S/T$$

where S is the signal amplitude and T is the time for the star image centroid to transit the slit (~46 milliseconds for a $10''$ slit).

The transit time uncertainty in the presence of noise of amplitude N (1σ) is

$$\Delta t = 2\frac{N}{m} = \frac{2T}{.462\ S/N} \quad ,$$

where the factor of 2 is introduced to account for the uncertanty in the presence of noise of the peak value. Then, for a $10''$ slit and a given S/N,

$$\Delta\theta_{N_0} = \frac{4.23''}{(S/N)_0}\ (1\sigma) \quad .$$

The electronics is designed to operate over a dynamic range of 98:1 and introduce less than 0.5 millisecond error (i.e., less than $0.10''$ shift with magnitude. Tests in ref. 106 seem to verify this capability.)

Typically, 50% of all S/N measurements along a slit are within a factor of two. Thus, if S/N is nominally 20, the (1σ) value of noise-equivalent angle uncertainty is

$$\Delta\theta_N\ (1\sigma) = 0.42''$$

The power consumption for the SIMS-A electronics is estimated at 5 watts.

A tentative estimate of SIMS-A electronics reliability (non-redundant per slit) assuming standard space-qualified electronics, is:

Time Elapsed	No. of Slits in Operation		
	1 Slit	4 Slits	6 Slits
2 years	.990	.960	.940
3 years	.985	.941	.914
4 years	.980	.924	.888
5 years	.975	.903	.856

This estimate will require additional inputs to become more realistic. It assumes 70 transistors per slit electronics and a maximum failure rate of .0007%/1000 hours per transistor (specifications for Minuteman guidance and control, vintage 1964).

4.2.2.4 SIMS-A Star Mapper Ground Support Equipment

No information on GSE has been obtained at this time. This information will be sought for inclusion in the final report.

4.2.2.4 SIMS-A Star Mapper Error Model

Contributor	Error	Comments
Angular Error Velocity	$0.23''$ (1σ)	Dynamic T effect (subsection 4.2.0.3)
Optics: Stellar Class	$0.13''$	Blur size -spectrum bias
Uniform Temp.	$0.20''$	Periodic ±4°F temp. change
Temp. Gradient ΔTemp=1°F	$0.34''$	Mounting flange at miniscus
	$0.07''$	Mounting flange at mirror
Slit Edge Roughness	$0.052''$ (1σ)	Granular edge variability*
	$0.72''$ (1σ)	Wavy edge variability
Effective slit edge straightness--to be determined		
NEA**	$0.42''$ (1σ)	Noise contributions at 4.75^M (CdS)
RSS White noise factors:	$0.48''$ (1σ)	Granular edge*
	$0.86''$ (1σ)	Wavy edge
RSS including stellar class:	$0.49''$ (1σ)	Granular edge*
	$0.87''$ (1σ)	Wavy edge
Max. Bias:	$0.54''$	With Meniscus-mount location
	$0.27''$	With Mirror-mount location
Worst-case RSS (White noise and max bias)	$0.73''$ (1σ)	granular edge } to 4.75^M (CdS) star
	$1.03''$ (1σ)	wavy edge } to 4.75^M (CdS) star

Attitude update - 87% (10 min. requirement)

---

*Granular edge most likely

**Noise-Equivalent Angle

4.2.2.6 SIMS-A Star Mapper Trade Parameters

Cost:	To be determined
Accuracy:	0.75" (1σ) @ 4.75^M (CdS)
Attitude Update:	87%
Weight:	15 pounds (not finalized; should decrease)
Power:	5 watts
Size:	6 inches diam × 22" long (inc. sunshade)
Aperture:	3.5 in. Dia.
FOV:	4^o
Nominal Temp:	72^oF
Sun Angle:	$>30^o$
Simplicity of Design:	Curved focal plane and low f/No. impose severe tolerances on elements and alignment.
Reliability:	Preliminary estimates on page 4-46, in subsection 4.2.2.3. Better estimates to be determined.
Cost of GSE:	To be determined
Availability:	Developed through Phase IB

4.2.3 SIMS-DA-KI STAR MAPPER, FUNCTIONAL DESCRIPTION

The SIMS-DA-KI star mapper candidate is designated a "Strapdown Solid State Star Sensor (S5) - Kollsman KI-494A" by KI in reference 112. This document will be forwarded to NASA as supplementary material in the SIMS/EOS study.

The KI star mapper employs design techniques developed for the U.S. Air Force under contract F33615-71-C-1159, and consists of:

- A catadioptric optical system composed of a large corrector element, a Mangin primary mirror, and a field corrector element.

- Six narrow-strip silicon photodiode detectors mounted in a spoke-like array on an optically-flat substrate, operating in a photovoltaic mode.

- Electronics to generate a negative signal whenever a fixed threshold is exceeded by the star signal.

- Logic to measure the time of the threshold signal, identify the slit, and store or transfer this information.

A functional diagram is shown in Figure 4-16 (from ref. 112). The response of silicon detectors is fast (microseconds) and in the absence of noise the output signal from the preamplifier would closely follow the radiant power level in the slit. The combined signal and noise output of the preamplifier are filtered, to reduce noise, and amplified again. The resulting signal is applied to a fixed-threshold detector and produces a negative output when the threshold is exceeded. The output of the threshold detector is interrogated at some high frequency, say 2000 Hz, and the time noted as that of the first interrogation pulse after the threshold detector goes negative. A lockout feature assures that only the first pulse after threshold is read by preventing further interrogation for a fixed interval.

The dynamic range of the electronics is 16:1 or from 4.2^M to 1.2^M (Si) stars.

4.2.3.1 SIMS-DA-KI Star Mapper Optics

The SIMS-DA-KI Optics is a catadioptric, f/1.25 system employing a Mangin primary mirror with refractive corrector elements, which permits both a large field-of-view and a broad spectral response. Figure 4-17 is a design layout from Ref. 112 showing the dimensions of optical elements and sunshade.

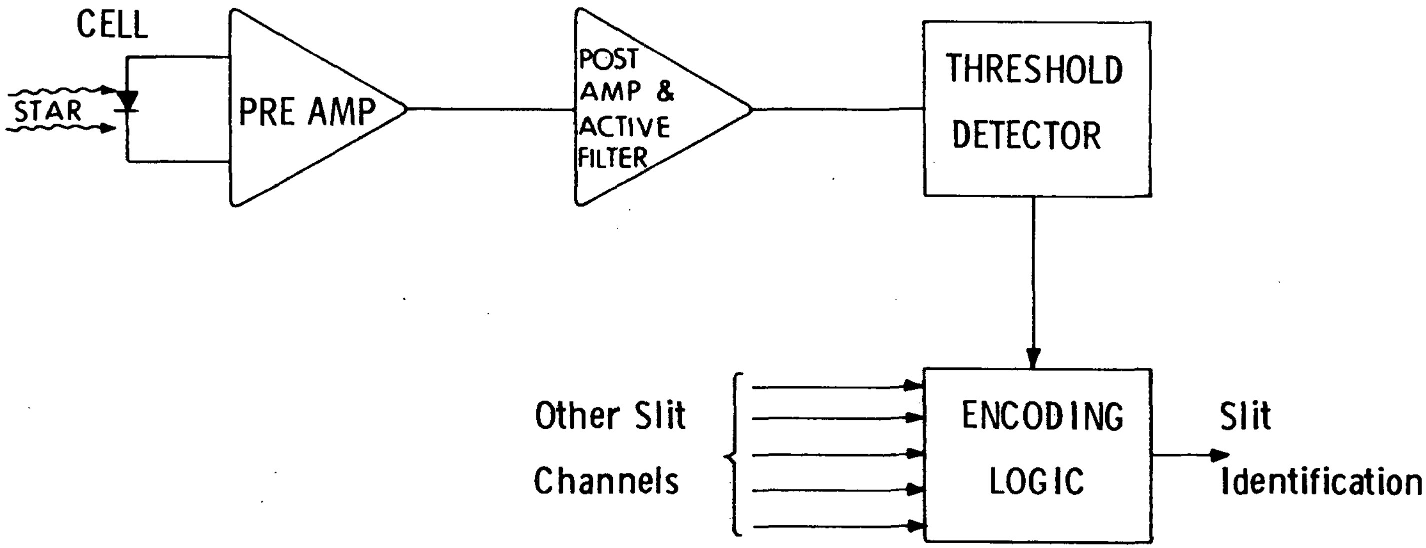

Figure 4-16 Block Diagram of the Electronic Functions (From Fig. 3-1, Ref. 112)

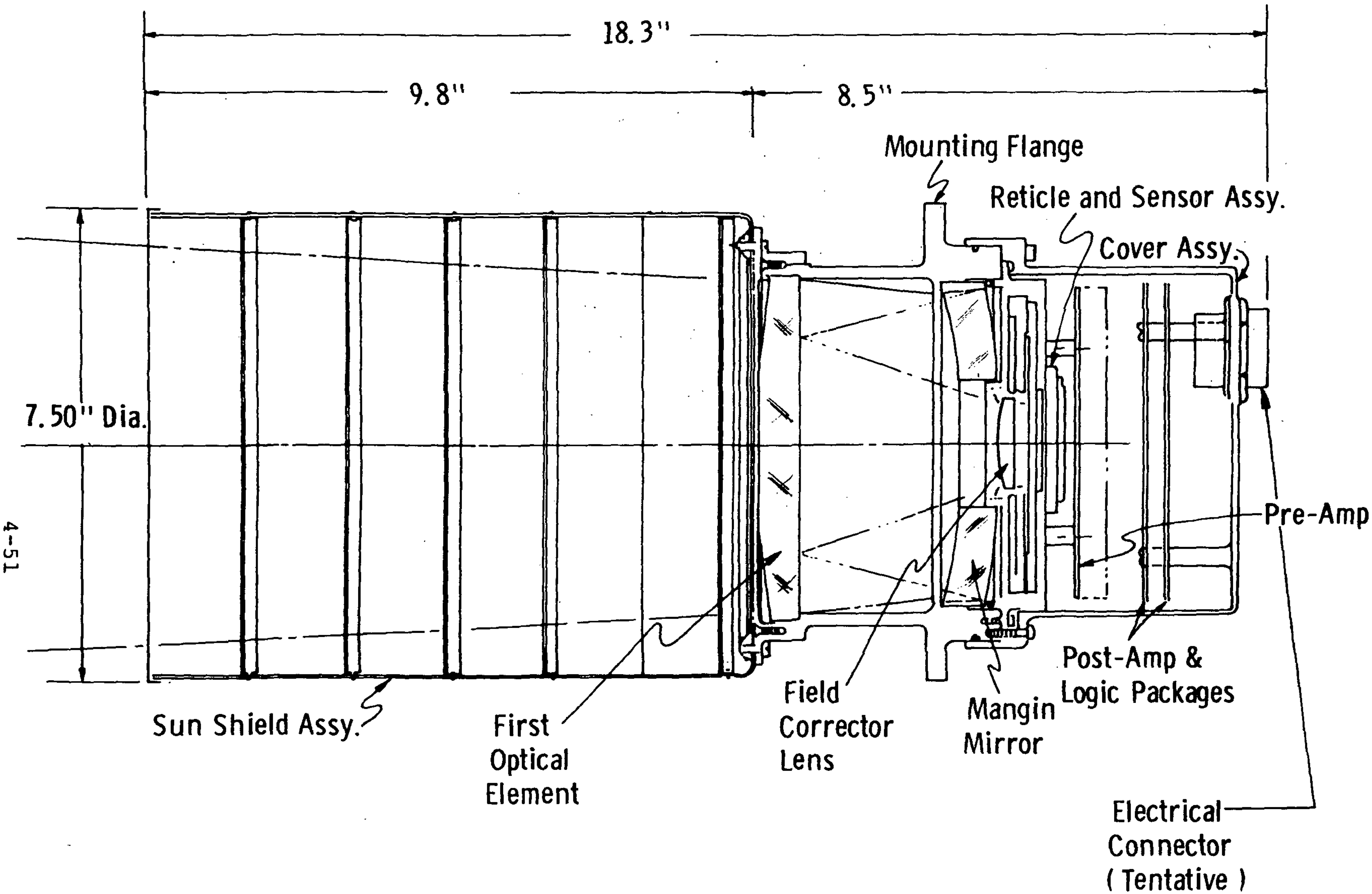

Figure 4-17 Design Layout Showing Optics, Sunshade, Optics Housing and Electronics Compartment(From Fig.5-1, Ref.112)

Since the detector slits (section 4.2.3.2) are arranged radially from the center of the image format, the tangential (radial) spread of the image is not important, while a change in sagittal spread with image position is to be avoided. Therefore, this system has been designed such that the image is permitted to be astigmatic with the sagittal image held in focus on a flat focal plane. Representative blur shapes shown in Ref. 114 illustrate this. However, it is essential to obtain more quantitative detail of star signal shape than is shown in these spot diagrams, since the spot diagrams show complex distributions of energy which might affect star signal shape as a function of off-axis position and star spectral class. This information will be sought for inclusion in the final report.

The optical elements are housed in a lightweight cylindrical beryllium housing, with the Mangin primary centrally-located at the mounting flange.

Transient temperature distributions within the telescope were calculated for a 99^o inclination orbit, with orbital period of 100 minutes, and spacecraft structure temperature periodic between $+23^oF$ and $+113^oF$. The coefficient of expansion of beryllium and the optical glass are closely matching, so that uniform temperature changes should not introduce severe problems of focal plane shifting relative to the detector plane. Theoretical calculations indicate less than one micron shift. Beryllium has high thermal conductivity which is important in reducing gradients across the telescope.

The field-of-view achieved with the optics is 6^o; the effective collecting aperture area is 73 cm^2 (within a 5.33 inch diameter entrance). From Fig. 4-6, with a noise bandwidth of 9.1 Hz (subsection 4.2.3.3), the limiting magnitude to achieve a signal-to-noise ratio of 10 is 4.0^M (Si). From Fig. 4-2, the average number of stars per orbit is 50 (49 if the stars brighter than 1.2^M are excluded). From Fig. 4-3, the $\overline{SPG}$ is 1.0% for a SIMS-A, i.e., attitude update can be maintained, with a SPARS-like IARU through 99% of the mission. For a SIMS-D1 IARU, this number is effectively 100%.

The aluminum sunshade is designed for a 30° sun angle. No bright object sensor or shutter is required. The maximum background noise spectral density generated will be $.205 \times 10^{-28}$ $amps^2/Hz$.

The weight breakdown, including all electronic elements associated with the optics housing, is

Lens	1.3 pounds
Mangin Mirror	1.2 "
Field Lens Assembly	0.7 "
Main Housing	1.3 "
Lens Retainer and Sun Shield Interface	0.2 "
Sun Shield	1.4 "
Subtotal	6.1 pounds
Preamp and Detector Assembly	0.4
Postamp and Threshold Detector	0.4 "
Logic and Power Supply	0.6 "
Rear Cover	0.8 "
Electrical Connector	0.3 "
Misc. Hardware and Wire	0.4
Total	9.0 pounds

SUMMARY

f/No.:	1.25
FOV:	6^{o}
Aperture	5.33 in. O.D.
Obscuration:	42% by secondary
Loss:	13% by surface reflection
Eff. Aperture Area:	11.3 in^2 ($73 cm^2$)
Sun Angle:	$>30^{o}$
Size:	7.5" dia×18.3" long (including sunshield)
Weight:	9.0 pounds (including sunshield)
Accuracy:	Unspecified; assign $0.5\widehat{''}$ temporarily for possible star signal off-axis bias. $I_{NB}^2 = .205 \times 10^{-28}$ amp^2/Hz at sunshade angle.
$\overline{SPG}$:	1.0% for SIMS-A.

4.2.3.2 SIMS-DA-KI Star Photodetector

The silicon detectors for a SIMS-DA-KI star mapper will be similar to cells developed by Texas Instruments (TI) for Kollsman as part of the Advanced Star Sensor study performed for the Aeronautical Systems Division of the Air Force Systems Command in June of 1971. The silicon chips are approximately 0.006 inch wide and 0.370 inch long. Six are mounted on an optically-flat substrate in a 30^{o}-between-spokes array similar to the SPARS star mapper pattern. These chips are overlayed with a slit-defining mask that is .0006 inch ($17.3\widehat{''}$) wide and 0.366 inch (3.1^{o}) long. The slits are formed by a photo-etch process that produces a worst-case edge definition of .00003 inch (3σ) and a slit straightness of .00005 inch. If the slit edge graininess has the same dimensional character parallel and perpendicular to the slit edge, the effective uncertainty in slit centerline location (see subsection 4.2.2.2) is

$$\Delta T_c \simeq 0.163 \text{ milliseconds } (3\sigma)$$

and

$$\Delta\theta_c \simeq .016'' \text{ (1}\sigma\text{) granular edge}$$

$$\Delta\theta_{BIAS} \simeq 1.36'' \text{ (slit straightness)} \quad .$$

($\Delta\theta_c$ is quite negligible.) If the edge variability is mostly an extended edge waviness (i.e., predominant spatial wavelengths along slit edge large compared to the slit width), then

$$\Delta T_c \simeq 3.3 \text{ milliseconds } (3\sigma)$$

and

$$\Delta\theta_c \simeq 1.1'' \text{ (1}\sigma\text{) wavy edge.}$$

Silicon slit detectors usually display good uniformity of response along the slit (e.g., see ref. 111).

The silicon detector operates in a near-zero bias mode and acts in a photovoltaic mode as a current source whose strength is proportional to the incident radiant power. The peak radiant sensitivity of typical TI silicon supplied to KI is greater than 0.35 amps/watt. Leakage current across the silicon surface driven by a FET unbalance of 0.1 volt is stated as less than 10^{-10} amperes or $\sqrt{2eI} = 5.65\times10^{-15}$ amp/Hz$^{1/2}$. It is difficult to separate the detector and preamplifier noise contributions. A combined estimate will be given in subsection 4.2.3.3.

Information is being sought on the spectrum of excess (flicker) noise associated with silicon detectors for inclusion in the final report.

Radiation environment at the EOS 1000 kilometer orbital altitude is expected to degrade silicon performance less than 2% per year.

No bright object protection is required.

SUMMARY

Mat'l:	Silicon (TI)
Slit width:	0.0006 inch (17.3")
Slit length:	0.366 inch (3.1°)
$\Delta\theta_c$:	{ .016" (1σ) granular edge 1.1" (1σ) wavy edge
$\Delta\theta_{BIAS}$:	1.36" slit straightness (calibratible)
Peak Sensitivity:	0.35 amps/watt
Degradation:	< 2%/year
Leakage noise spectral density:	0.32×10^{-28} amps^2/Hz

4.2.3.3 SIMS-DA-KI Star Mapper Electronics

Figure 4-18 is a schematic diagram of the pre-amplifier, postamplifier and threshold detector for a single slit. The preamplifier is designed to provide a relatively low impedance load to the photodiode so that the photodiode in the photovoltaic mode acts as a current source. The cell resistance is 1000 MΩ, the amplifier input impedance appears as the feedback resistor (200 MΩ) divided by the loop gain (2390) or 83.6 KΩ. The feedback resistor thermal noise accounts for 91% of the mean square noise current spectral density, and the input FET and Op-Amp contribute the remainder;

$$I_{NA} \simeq 0.953 \times 10^{-28} \text{ amp}^2/\text{Hz}.$$

If the worst-case FET unbalance is assumed to be 0.1 volt (assuming a worst-case temperature of 40°C) the leakage

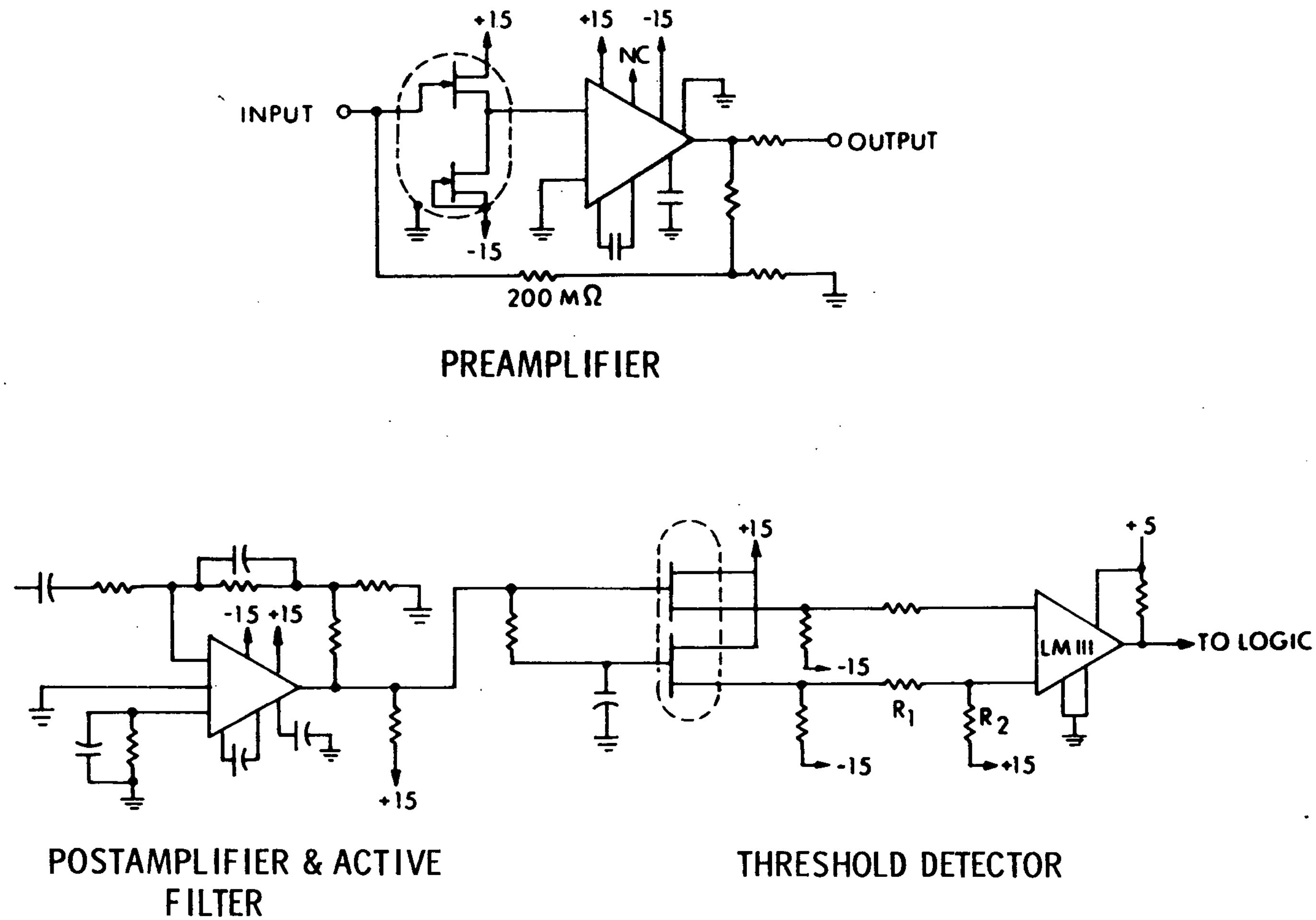

Figure 4-18   SIMS-DA-KI Star Mapper Electronics

current in the photodiode contribution to the mean-square noise current spectral density is

$$I_{FET}{}^2 = 0.32\times10^{-28}\ \mathrm{amp}^2/\mathrm{Hz}$$

The offset voltage to the photodiode must be low to ensure photovoltaic operation. The input to the preamplifier is a pair of FETs, matched for a maximum differential gate source voltage of 5 millivolts. At worst-case temperature, the offset should not exceed 20 millivolts which is small compared to the cell leakage test level of 100 millivolts.

The preamplifier transresistance is 2.5×10^9 volts/ampere. The upper cutoff frequency of 360 Hz is reached when the reactance of stray shunt capacitances equals the resistance of the feedback resistor. The preamplifier will have a negligible effect on system response since the active filter in the postamplifier has a cutoff at 6 Hz.

The postamplifier is designed to have a voltage gain of 800. The active filter cuts off below 0.029 Hz and above 5.8 Hz. The noise bandwidth is $(\pi/2)(5.8) = 9.1$ Hz.

The threshold level in the threshold detector is achieved by selection of resistors R_1 and R_2 (in Fig. 4-18) which act as a voltage divider. The operational amplifier in the postamplifier will cause a variable baseline offset voltage to exist. Thus, an LM111 voltage comparator is used in the threshold detector to extract the star signal differentially with common mode rejection of the DC part of the offset voltage. The variable part of the offset is integrated and stored on the input capacitor to the lower FET of the source-follower pair. During a star signal input, this integrator produces a 2% error in the threshold level for the dimmest star. Since, the threshold level is fixed at 360 millivolts, a bright star will trigger the threshold detector sooner than a dim star. The threshold is set at 60% of the peak response of the dimmest usable star (i.e., 4.2^M). The crude model based on a triangle input predicts a shift of 61 milliseconds or $13''$. The analysis in Ref. 112 (Fig. 4-1 thereof) shows about $8''$. Thus, ground-based computation is required to correct the threshold time for star magnitude. Furthermore, it may be necessary to calibrate the detector slits against every real star listed in the catalog. The alternative is to increase the onboard electronics to contain a peak detector or to detect leading plus trailing edge. These possible modifications will be explored with KI and the disposition indicated in the final report.

The remaining electronics are a logic block which permits an onboard computer or recorder to interrogate the star mapper for time of threshold and slit identification and which informs the computer when it is ready for interrogation (i.e., a dead zone is present, after a successful interrogation, to permit the star to complete transit of the slit and the threshold detector to return to a ready condition). The logic contributes, at most, a 0.5 millisecond uncertainty or $0.11''$ (3σ).

The power dissipation of the electronics including the power supplies is (for 6 channels)

Preamplifier	108 mw
Post amplifier and threshold detector	237 mw
Logic	100 mw
Total	445 mw

If additional detection, such as trailing edge or peak will be required, the threshold detector and logic will need to be increased another 250 mw. The total dissipation is then about 700 mw.

At 30% conversion efficiency the input power required is 1.5 watts (2.3 watts, modified).

Redundancy is included in the power supplies to the extent of full redundancy in the 5 volt digital supply (all six channels will operate if one power supply failed) and half-redundancy in the ±15 volt power supply (3 channels would operate if one supply failed).

KI predicts a MTBF for the star mapper of 222,568 hours and a failure rate of $4.493/10^6$ hours.

<u>SUMMARY</u>

$\overline{I_N^2} = 1.273 \; 10^{-28} \; \text{Amp}^2/\text{Hz}$

Noise bandwidth:	9.1 Hz
Angle bias range:	$8''$ for 4.2^M to 1.2^M (with leading edge threshold detection only)
Quantization Error:	$.06''$ (1σ)
Power:	1.5 watts (leading edge detection only)
	2.3 watts (leading and trailing or peak detection implemented)
λ:	4.493 failures/10^6 hours
NEA:	$1.22''$ (1σ) leading edge det. only $.87''$ (1σ) leading and trailing edge det.

4.2.3.4 <u>SIMS-DA-KI Star Mapper Ground Support Equipment</u>

Four different circuit testers will be used to support each of the circuit board subassemblies and to provide interface to commercial test equipment.

A fixture will be required to facilitate focus and alignment of optics, housing and sensor.

An electronic interface box will be required for final testing. It would provide 28V. DC power and control signals, and all required readout provisions.

Equipment will be required to align and calibrate the optics boresight and slit pattern relative to the instrument mounting structure (IMS) on the spacecraft.

Further definitions of GSE and cost will be sought for inclusion in the final report.

4.2.3.5 SIMS-DA-KI Star Mapper Error Model

Contributor		
Angular Error Velocity:	0.15" (1σ)	Dynamic ΔT effect (subsection 4.2.0.3)
Optics:	0.50" off-axis bias	(Temporary assignment based on appearance of off-axis sagittal blur distribution)
Slit Edge Roughness:	0.016" (1σ) 1.1" (1σ)	granular edge wavy edge
Slit Edge Straightness:	1.36" bias	(can be calibrated)
NEA:	1.22" (1σ) 0.87" (1σ)	Leading edge only 4.00^M (Si) with S/N=10 Leading and trailing edge
Quantization Error:	0.06" (1σ)	At 2000 Hz logic interrogation rate
Max Bias Range:	8"	Leading edge only, fixed threshold for stars from 1.2^M to 4.00^M; (can be calibrated)

(Cont'd on p. 4-62)

RSS uncertainty:	1.24″	lead. det only.	granular edge
	0.90″	lead. and trail. det.	
	1.65″	lead. det. only	wavy edge
	1.41″	lead. and trail. det.	
Max. Bias with no calibration:	9.86″	leading edge det. only	
	1.86″	leading and trailing edge detection	
Total RSS with no bias calibration:	2.07″	granular	leading and trailing edge detection.
	2.33″	wavy	
			4.0″ (Si)

Attitude update, SIMS-D: - 100%
(SIMS-A: - 99%)

4.2.3.6 SIMS-DA-KI Star Mapper Trade Parameters

Cost: $30,000/unit
$300,000 non-recurring cost (approximate, due to lack of definitive statement of work)

Accuracy:
- Capable of 0.90″ (1σ) with additions suggested by MIT and calibration of biases
- Capable of 2.07″ (1σ) with additions suggested by MIT and no calibration of biases
- ~ 10″ (1σ) as found in Ref. 112

Attitude Update: 100% (SIMS-D)

Weight: 9.0 pounds

Power:
- 2.3 watts with additions suggested by MIT
- 1.5 watts as found in Ref. 112

Size: 7.5 inch dia. $\times$ 18.3 inches long

FOV: 6°

Sun Angle: $> 30^{\circ}$

Simplicity of design: Flat focal plane relaxes slit-fabrication problems. Tight tolerances required by fast optics. Design is conceptually simple.

Reliability: λ = 4.493 failures/10^6 hours (KI estimate)

Cost of GSE: To be determined

Availability: To be determined

4.2.4 SIMS-DA-HR STAR MAPPER, FUNCTIONAL DESCRIPTION

The SIMS-DA-HR star mapper candidate is based on the experience and technology of HR in developing alternate photodetector approaches for SPARS-like applications. The SIMS-DA-HR consists of:

- A catadioptric optical system with two corrector elements, and a primary and secondary mirror on a single element.
- Six narrow-strip silicon photodiode detectors mounted in a spoke-like array on an optically-flat substrate, operating in a photovoltaic mode.
- Electronics to: generate a one-shot pulse marking the estimate of the time of coincidence of the star image centerline with a slit centerline, identify the slit, and supply star amplitude if required.

A functional diagram is shown in Figure 4-19. The response of silicon detectors is fast (microseconds); in the absence of noise the output signal from the preamplifier would closely follow the radiant power level in the slit. The signal and noise output of the preamplifier are filtered to reduce the noise bandwidth. The filter is designed to preserve star signal symmetry. The filtered star signal is applied to a threshold detector; the latter generates a pulse to initiate a timing count at a fixed detection level of the leading edge, and generates a second pulse to terminate the count at the same detection level of the trailing edge. The count is divided by two in the timing logic to estimate the time of coincidence of star image centerline with slit centerline.

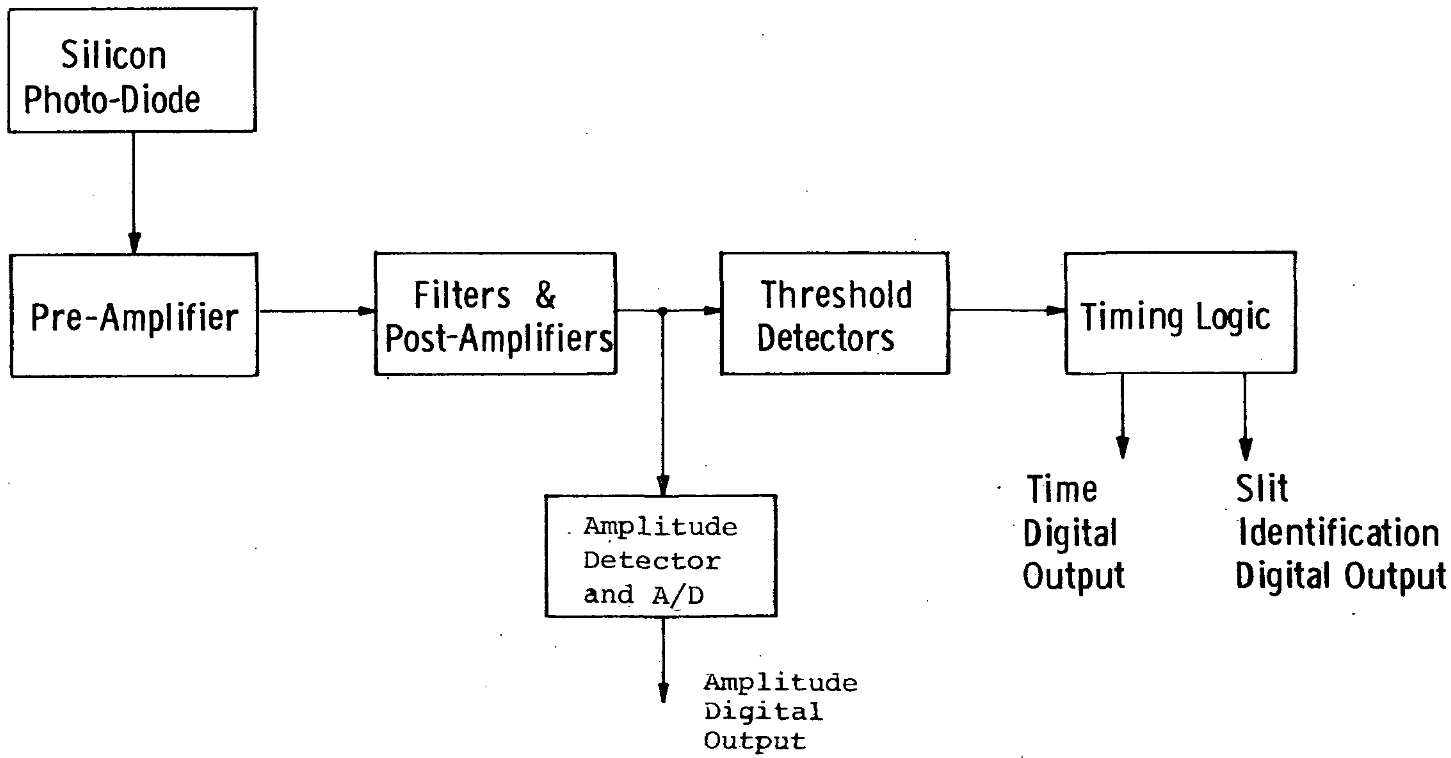

Figure 4-19 Functional Block Diagram of SIMS-DA-HR Star Mapper

4.2.4.1 SIMS-DA-HR Star Mapper Optics

The SIMS-DA-HR star mapper optics is a catadioptric, f/2.0 system employing two corrector elements and a single quartz element with a primary and secondary mirror (Figure 4-20a). The housing in Fig. 4-20b will contain the optics, photodetector slits and preamplifiers. The sunshade, not shown, will add 6 inches of length , will be 3.5 inches in diameter, and is designed for a 45° minimum sun angle. Assuming 0.88 pa/cm^2 and an effective collecting aperture area of 20cm^2, $I_{NB}{}^2=5.63\times10^{-30}$ amp^2/Hz.

No information is presently available on blur image behavior off-axis and at different wavelengths. Astigmatism will definitely exist but is of no concern, since the slits will be radially deployed. An estimate of the degree of sagittal spread should be available for the final report, as its variation with star spectral class and off-axis location will affect the signal slope and amplitude, hence the noise-equivalent transit time uncertainty.

The mounting flange is located at the quartz mirrors element. This, coupled with a larger f/No., the low thermal expansion coefficient of quartz and the ability to mount the detector head against the quartz element, imply less thermal sensitivity for this optics design than for the two star mappers considered in the preceding sections. An analysis of the effect of uniform temperature changes and of cross-optics gradients will be sought for inclusion and evaluation in the final report.

The field-of-view is 8°; the effective aperture area is 20 cm^2 (within a 2.5 in. dia. entrance). From Fig. 4-6, with a noise bandwidth of 15 Hz (subsection 4.2.4.3), the limiting magnitude to achieve a signal-to-noise ratio of 10 is 3.9^M (Si).

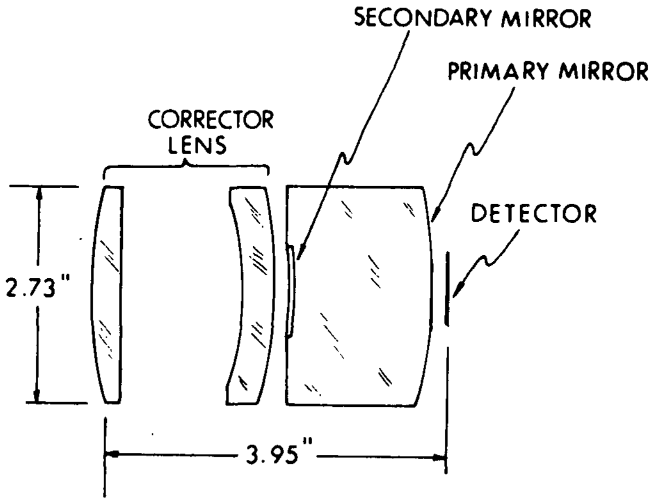

Figure 4-20a Solid Catadioptric Optical System in SIMS-DA-HR Star Mapper

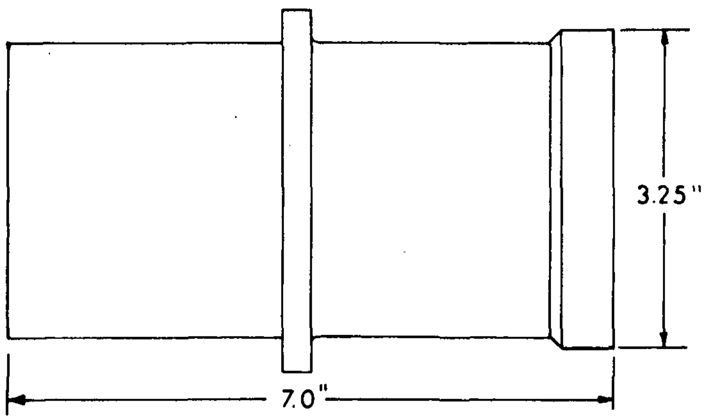

Figure 4-20b Optical/Mechanical Head Housing, SIMS-DA-HR Star Mapper

From Figure 4-2, the average number of usable stars per orbit is approximately 60. Update is achieved for 100% of a SIMS-D1 IARU and 99.7% for a SIMS-A IARU. The limiting magnitude recommended by HR is 3.2^M (Si). This yields an average of 25 usable stars per orbit and an $\overline{SPG}$ of 10% for a SIMS-A IARU, but still effectively 0% for a SIMS-D1 IARU.

SUMMARY

Weight:		
	Optical/Mechanical head	3.0 pounds
	Sunshade	1.0 pound
Overall dimensions:	3.5 in. dia.×13 in. long (including sunshade)	
Aperture:	2.5 in. dia	
Effective transmission:	63%	
Effective aperture area:	20 cm^2	
F/No.:	2	
FOV:	8^o	
Accuracy:	Unspecified (est <0.5$\widehat{"}$)	
$I_{NB}{}^2$:	5.63×10^{-30} amp^2/Hz	

4.2.4.2 SIMS-DA-HR Star Mapper Photodetector

The silicon detectors for a SIMS-DA-HR star mapper will be similar to cells developed by HR as alternative SPARS-like detectors. The silicon cells are mounted behind slits whose dimensions are approximately .00045 in. wide (16$\widehat{"}$) by 0.4 in. long (4^o). Six silicon cells are mounted on an optically-flat substrate in a 30^o-between-spokes array similar to the SPARS star mapper pattern. The slits are formed by a photoetch process that produces edge definition better than 30μ in. (1σ). The edges are of a granular nature;

$$\Delta\theta_c \leq 0.10'' \ (1\sigma)$$

The silicon responsivity quoted is quite high, 0.5 amp/watt. Part of this improvement comes from a SiO_2 anti-reflection coating.

The leakage current from a FET unbalance of 0.10 volts is stated as 4×10^{-12} amps, or $2eI = I_{NL}{}^2 = 1.28\times10^{-30}$ amp^2/Hz. It is difficult to separete the detector and preamplifier noise contributions. A combined estimate will be given in subsection 4.2.4.3.

SUMMARY

Mat'l:	Silicon (HR)
Slit width:	0.00045 inch (16")
Slit length:	0.400 inch (4°)
$\Delta\theta_c$:	0.10" (1σ) granular edge
Peak Responsivity:	0.5 amp/watt
Degradation:	2%/year
Leakage noise spectral density:	1.28×10^{-30} amp^2/Hz

4.2.4.3 SIMS-DA-HR Star Mapper Electronics

MIT has been requested at this time to not publish, here, the nature of the HR preamplifier, which is held by HR to be proprietary at this time. The noise current spectral density of the cell-preamplifier combination is quoted as 16×10^{-30} amp^2/Hz. This, combined with the background maximum contribution (section 4.2.4.1), produces

$$I_N = 4.65\times10^{-15} \text{ amp/Hz}^{1/2}$$

Two MIT tracings of MIT photographic enlargments taken from oscilloscope photographs of real star transits supplied by HR are shown in Figures 4-21 and 4-22. The star signals were recorded at the output of the preamplifier with a bandpass of 0.2 to 100 Hz. Figure 4-23 is an original-size oscilloscope photograph of a star transit (similar in magnitude and spectral class to the star in Fig. 4-21) but with a bandpass of 0.2 to 20 Hz. The data in Fig's 4-21 through 4-23 were taken with unshielded optics, during a full moon. (From the relative positions of Cassiopeia and a full moon in the autumn, the angle between moon line-of-sight and optics boresight would be on the order of 90°.)

The total power required is 2.0 watts.

A threshold adjust on command is available.

Outputs consist of:

- One-shot pulses marking thresholds (leading and trailing edges)
- Slit identification
- Amplitude of signal if required

The outputs of the electronics are fed to timing logic that estimates the time-of-coincidence of star image center and slit centerline from the two threshold pulses.

The signal-to-noise ratio for a 3.2^M (Si) star and noise bandwidth of 15 Hz is estimated from Figures 4-21 and 4-22 as approximately 17, and the transit time uncertainty at orbital rate is $3.15/\sqrt{2}$ milliseconds or

$$\Delta\theta_c \simeq 0.48\hat{''} \ (1\sigma)$$

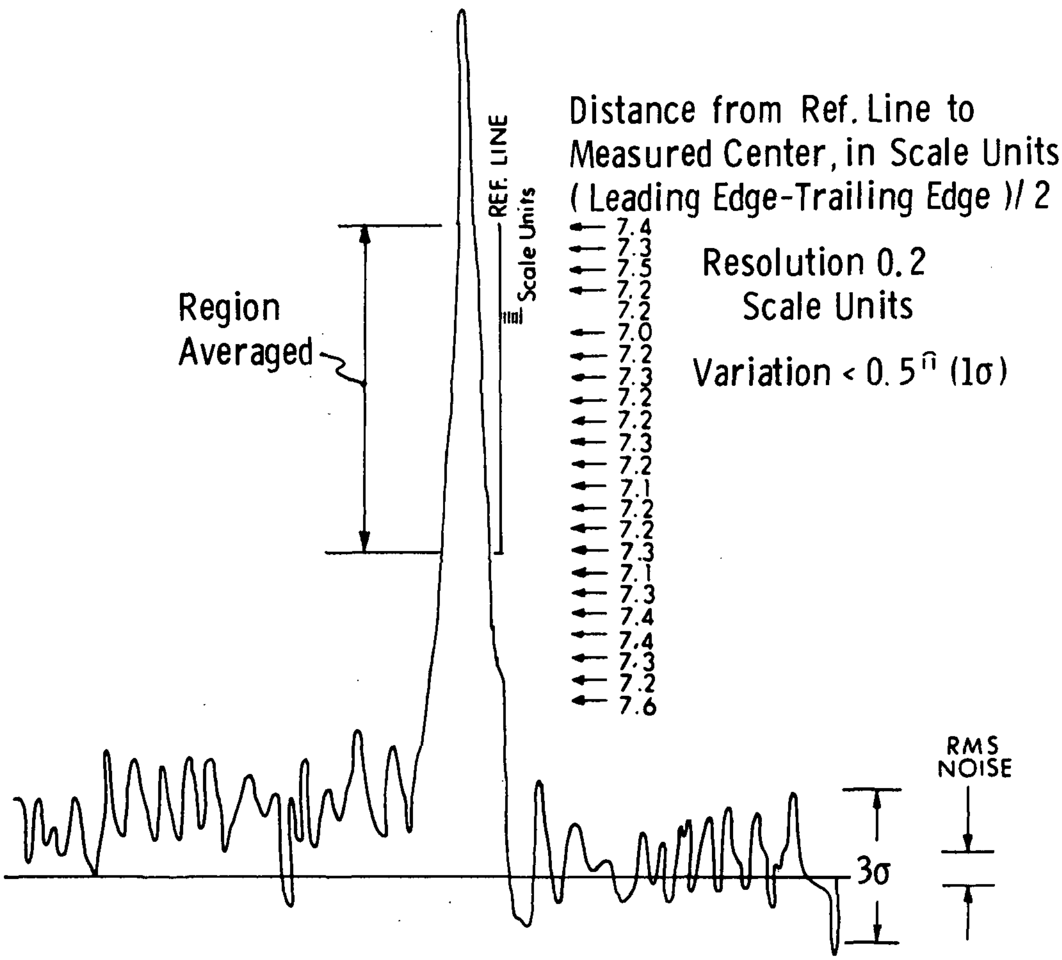

2.5^M(Si); Bandwidth - 100 Hz; 1.0 scale unit =
2.4 milliseconds (~2.4"); Slit Width 16";
S/N ≈ 26 (1σ) Estimate; S/N ≈ 23.6 (1σ) calculated.

Figure 4-21 Real Star Transit (Photoenlarged); β-Cassiopeia

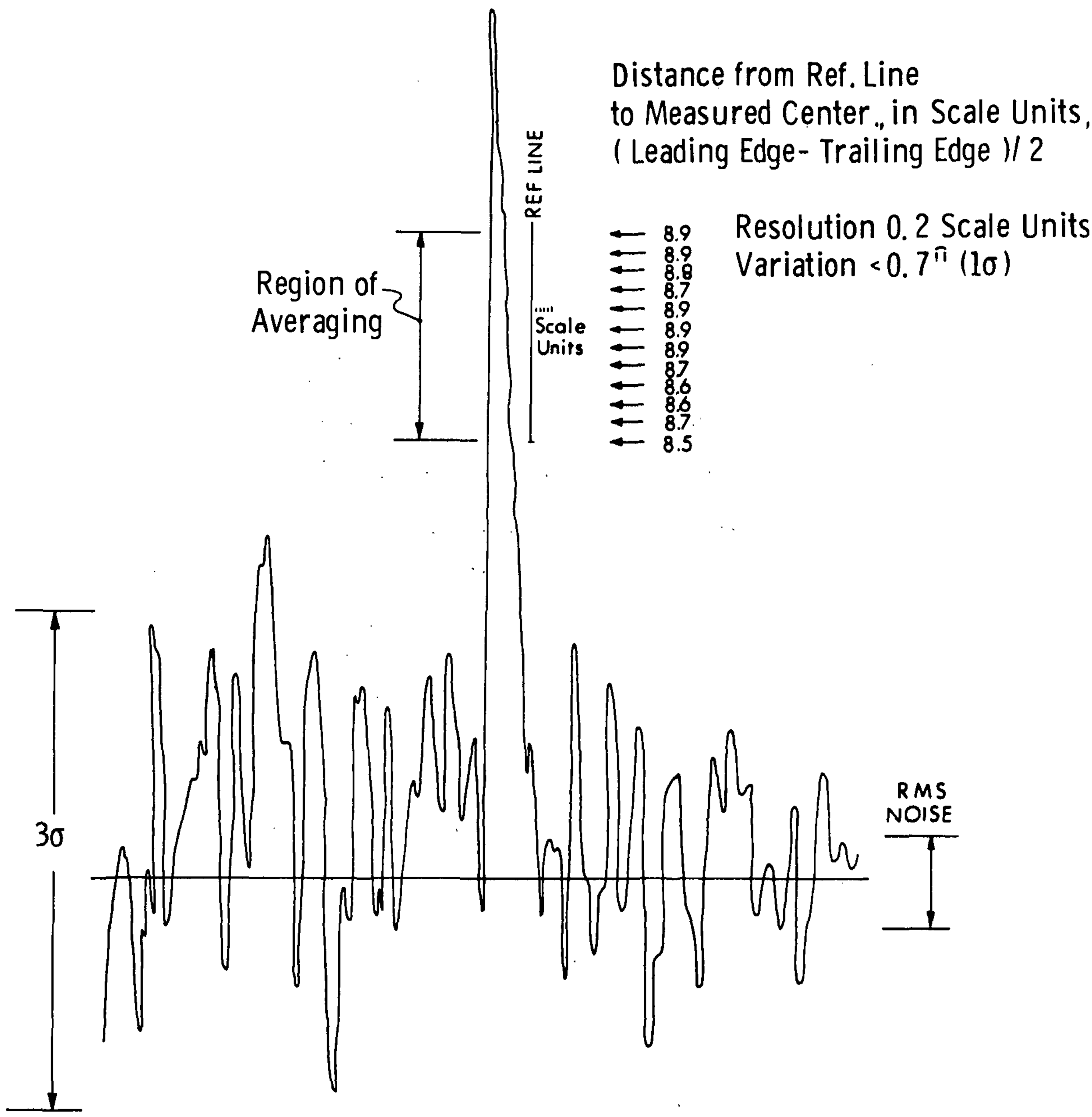

4.0^M(Si); Bandwidth - 100 Hz; 1.0 scale unit = 2.8 milliseconds (~2.8"); Slit Width 16"; S/N ≃ 9.4 (1σ) estimate; S/N ≃ 12 (1σ) calculated.

Figure 4-22 Real Star Transit (photoenlarged); η-Cassiopeia

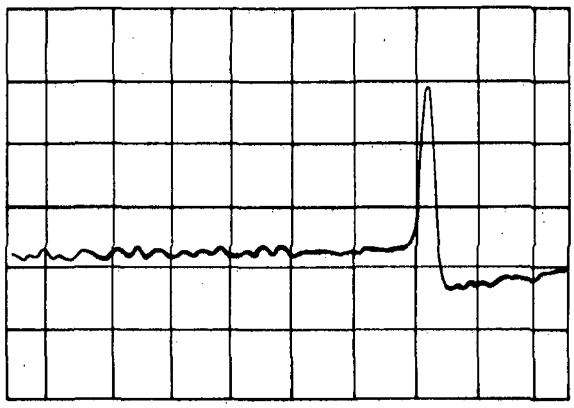

2.7^M (Si); Bandpass - 0.2 to 20 Hz. The improvements in S/N due to decreased bandwidth, and in signal symmetry are evident in comparison with Figure 4-21 (a star of roughly the same magnitude and spectral class).

Figure 4-23 Real Star Transit; Polaris

SUMMARY

I_{ND}^2:	16×10^{-30} amp^2/Hz
Noise Bandwidth:	15 Hz
Quantization Error:	0.05" (1σ)
NEA:	0.48" (1σ) , 3.2^M (Si)
Total Power:	2.0 watts
Reliability:	0.99, 4 slits, 3 years

4.2.3.4 SIMS-DA-HR Star Mapper Ground Support Equipment

No information on GSE has been obtained to date. This information will be sought for inclusion in the final report.

4.2.4.5 SIMS-DA-HR Star Mapper Error Model

Contributor	Error	Comments
Angular Error Velocity:	0.14" (1σ)	Dynamic ΔT effect (subsection 4.2.0.3)
Optics:	< 0.50" (1σ)	(Temporary estimate)
Slit Edge Roughness:	0.10" (1σ)	Granular edge
Slit Edge Straightness:	To be determined	
NEA	0.48" (1σ)	3.2^M (Si)
Quantization Error:	0.05" (1σ)	
RSS uncertainty:	0.72" (1σ)	
Attitude update, SIMS-D:	100%	3.2^M(Si)
[Sims-A:	90%	3.2^M(Si)]

4.2.4.6 SIMS-DA-HR Star Mapper Trade Parameters

Cost:	HR marketing has not responded at this time
Accuracy:	~ 0.72" (1σ)
Attitude Update:	100% SIMS-D
Weight:	7.0 pounds
Power:	2.0 watts
Size:	3.5 in. dia.×13 in. long (opto/mech head and sunshade) 4.5 in.×6.0 in×3 in (signal processing)
FOV:	8^{o} swath width
Sun Angle:	$>45^{o}$
Simplicity of Design:	Single-element quartz, with two mirrored surfaces and ability to mount detector head against the element, provide excellent mechanical and thermal stability.
Realiability:	0.99 for four slits for three years
Cost of GSE:	To be determined
Availability:	Pre-qualification stage. Sensor head built and undergoing tests at NASA. Electronics in breadboard and rack.

4.2.5 SIMS-DA-HA STAR MAPPER, FUNCTIONAL DESCRIPTION

The SIMS-DA-HA will be functionally similar to the SIMS-A. Differences will be allowable in the FOV and aperture. See subsection 4.2.2 for a general functional description.

The considerations in sections 4.2.5.1 to 4.2.5.6 are preliminary; further investigation into detail will be required, and will be reported on in the final report.

4.2.5.1 SIMS-DA-HA Star Mapper Optics

A significantly smaller field-of-view can be accepted for SIMS-D than was used in SIMS-A. With a two degree field-of-view and a limiting magnitude of 4.0^M (CdS) the average number of usable stars per orbit will be about 6 and never less than 3.

A reduction by ½ in the length of the CdS slits (with no reduction in slit width) can be achieved. This will reduce the leakage current across the cell by a factor of 2 and the bias current from the background lighting by a factor of two. This should affect a reduction of $\sqrt{2}$ in the noise-equivalent input (NEI).

The reduction in requirement for limiting magnitude and the decreased NEI permit a decrease in the effective collecting aperture area to 18 cm^2. This is a factor of 2.4 less than the effective area in the SIMS-A star mapper and suggests a straightforward 1/1.55 scaling of the diameter of all optical elements in the SIMS-A design while leaving the lengths and radii of curvatures untouched. Allotting 5 pounds to the optics, including sunshade, and retaining the weight assessed to the electronics in SIMS-A, yields an estimated star mapper weight of 7 pounds. The overall dimensions would be about 5.0 in. dia by 20 in. long. This reflects reducing the length of the sunshade by a factor of 1.55 and increasing the length of the housing by 2 in. to accommodate the space lost to the electronics in the diameter reduction.

No loss in mechanical or thermal stability should result from these changes, and perhaps a slight improvement in spectral blur circle performance can be achieved due to more optical material closer to the axis.

4.2.5.2 SIMS-DA-HA Star Mapper Photodetector

The SIMS-DA-HA photodetector is essentially the same as the SIMS-A photodetector (see subsection 4.2.2.2). The length of the CdS slits can be reduced by a factor of two while the widths are held the same.

If the limiting magnitude is 4.0^M (CdS), the noise bandwidth is 15 Hz (subsection 4.2.5.3), and the minimum (slit-averaged) S/N is 20; the effective aperture is 18 cm^2 (can be found from Fig. 4-6 by using either $B=15/\sqrt{2}$ or shifting the CdS magnitude scale to reflect the $\sqrt{2}$ decrease in NEI).

4.2.5.3 SIMS-DA-HA Star Mapper Electronics

The SIMS-DA-HA star mapper electronics are essentially the same as the SIMS-A star mapper electronics (see subsection 4.2.2.3).

4.2.5.4 SIMS-DA-HA Star Mapper Ground Support Equipment

The SIMS-DA-HA star mapper GSE is essentially the same as the SIMS-A star mapper GSE (see subsection 4.2.2.4).

4.2.5.5 SIMS-DA-HA Star Mapper Error Model

Contributor		Error	Comments
Angular Error Velocity		0.225" (1σ)	Dynamic ΔT effect (subsection 4.2.0.3)
Optics:	Stellar Class	0.10"	Blur size-spectral class bias
	Uniform Temp.	0.20"	Periodic ±4°F
	Temp. Gradient ΔT=0.25°F	0.17"	mtg. flange at meniscus
		0.03"	mtg. flange at mirror
Slit Edge Roughness		0.037" (1σ)	granular edge*
		0.72" (1σ)	wavy edge
NEA		0.42" (1σ)	noise contributions at 4.0^M (CdS)

(Cont'd on page 4-77)

*Most likely case

RSS white noise factors: [4.0^M (CdS)]	0.44" (1σ) with granular edge* 0.65" (1σ) with wavy edge
RSS including stellar class:	0.45" (1σ) with granular edge* 0.66" (1σ) with wavy edge
Max. Bias:	0.37" with meniscus mount location
Min. Bias:	0.23" with mirror mount location
Worst-case RSS, 4.0^M(CdS) (white noise and max. bias)	0.58" (1σ) with granular edge* 0.76" (1σ) with wavy edge

Attitude update - 100% (SIMS-D)

4.2.5.6 SIMS-DA-HA Star Mapper Trade Parameters

Cost:	To be determined
Accuracy:	0.60" @ 4.0^M (CdS)
Attitude Update:	100% (SIMS-D)
Weight:	7 pounds (including sunshade)
Power:	5 watts
Size:	5.0 in. dia×20 in. long (including sunshade)
FOV:	2°
Sun Angle:	$>30^\circ$
Simplicity of Design:	Same Comment as for SIMS-A (subsection 4.2.2.6) with some relief on tolerances anticipated due to smaller FOV.
Reliability:	Same comment as for SIMS-A (subsection 4.2.2.6).
Cost of GSE:	To be determined
Availability:	Remodeling of SIMS-A Phase IB star mapper is required

4.2.6 SIMS-DA-M STAR MAPPER, FUNCTIONAL DESCRIPTION

The SIMS-DA-M star mapper candidate is put forth by MIT to examine the performance characteristics of a photomultiplier-based SIMS star mapper. This mapper will contain:

*Most likely case

- Refractive optics, taking advantage of the excellent image properties available with small fields-of-view, and the reduced thermo-mechanical sensitivity associated with slower optics.

- A six-slit reticle in a SPARS-like array, photo-etched on a metallic-coated glass substrate, with anti-reflection coatings on the clear surfaces, and mounted at the focal plane.

- A second lens system to defocus the stellar radiant power transmitted by the slits and spread it over a large portion of the photocathode.

- A photomultiplier detector with an optimum photocathode material (the choice must be based on a study of comparative merits and will be accomplished, time permitting, in the last phase of the SIMS Trade study program).

- Standard, space-qualified, electronics to amplify, filter, and estimate star coincidence time.

Advantages of a photomultiplier over a solid-state detector include:

- Built-in, essentially noise-free amplification, reducing the severe noise limitation considerations that must go into fabrication of solid-state detectors and preamplifiers.

- Background-limited operation, as contrasted against the detector noise mechanisms in solid-state detectors (leakage currents and thermal noise).

(Cont'd)

This advantage implies a combination of:

- smaller fields-of-view with higher stellar magnitudes,
- smaller apertures,
- and, therefore, a smaller weight.

• Higher signal-to-noise ratio on sufficient stars for SIMS-D accuracy and update.

• Less susceptible to EMI.

Disadvantages of a photomultiplier include:

• Single sensor - star mapper failure with catastrophic failure of photocathode; lack of slit identification (although this is not required for SIMS-D).

• Thermal sensitivity of photocathode; irreversible degradation requires lower operating temperatures than silicon, and bright-object protection.

High-voltage operation and magnetic shielding have not been included in the disadvantage list. Qualified high voltage hardware is a demonstrated technology with many hours in space. Extensive magnetic shielding is only required in image dissector applications.

A functional block diagram of a SIMS-DA-M star mapper is shown in Figure 4-24.

4.2.6.1 SIMS-DA-M Star Mapper Optics

A high quality refractive optical system developed as a replacement for the Apollo Sextant Telescope (i.e., equivalent to the Wild-Herzbrug T-2 theodolite optics) is shown in Figure 4-25, adapted to the SIMS-D application.

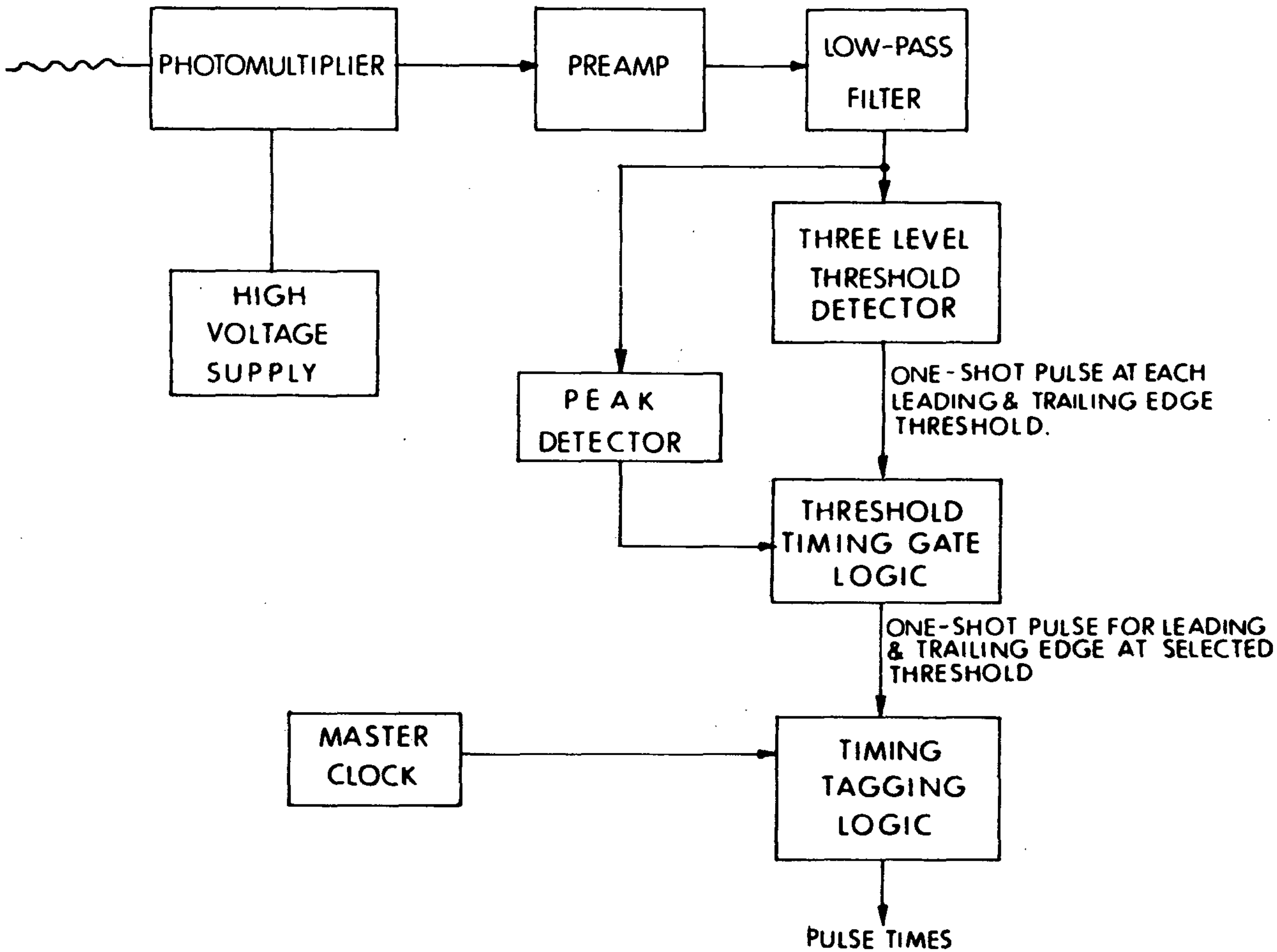

Figure 4-24 A Functional Block Diagram Concept For the SIMS-DA-M Star Mapper

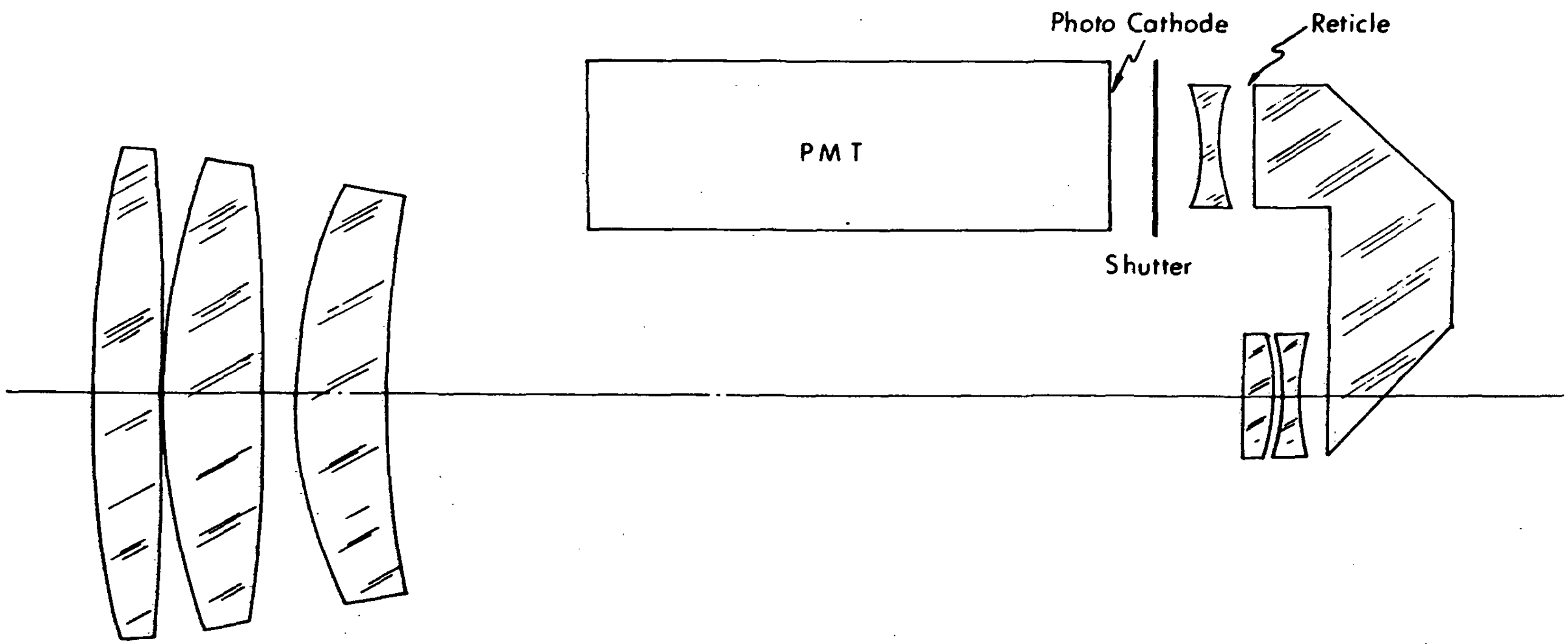

(2 × SCALE)

Figure 4-25 Concept for a SIMS-DA-M Optics Design

The optics housing would be fabricated from beryllium, which insures good thermo-mechanical stability of the image surface relative to the slit reticle, and minimum weight.

Aperture:	1.6 in. dia.
f/No.:	f/5.5
Blur Circle:	$10''$ at 1° off-axis
Size:	2 in.×3 in. × 12 in., including sunshade (6 in. long), PMT electronics housing, and redundant HV power supply.
Weight:	Estimate under 6 pounds

Pending a more thorough analysis, and based on similar experience, a tentative error budget of $0.5''$ (1σ) will be assigned to the optics.

4.2.6.2 SIMS-DA-M Star Mapper Photodetector

An S-20 photocathode is evaluated as an example. An optimum choice of photocathode type has not been considered, yet. Even so, the performance of an S-20 is more than adequate. Assuming a photocathode response of 0.30×10^{-12} amp/cm^2 (0.15×10^{-12} reduced by a factor of 3 to account for field-of-view difference from example in section 4.2.0.2 and multiplied by 6 to account for all six slits transmitting to single detector) at minimum acceptable sun angle, an effective optical aperture area of 10 cm^2, and a noise bandwidth of 50 Hz;

$$\sqrt{2eI_B} = 0.982\times10^{-15} \text{ amp/Hz}^{\frac{1}{2}}$$

$$\sqrt{2eI_B B} = 6.94\times10^{-15} \text{ amp}$$

$$I_S = 80\times10^{-15} \text{amp for } 5^M(v) \text{ AO star}$$

and

$$S/N = 11.5 \text{ for } 5^M(v) \text{ AO star} \quad .$$

There are a sufficient number of stars brighter than 3.5^M to guarantee three updates of the SIMS-D IARU in the worst orbit; the S/N for these cases is

$$S/N = 61 \text{ for } 3.5^M(v) \text{ AO star.}$$

The reticle slits would be formed by photoetching, and edge definition should be comparable to that occurring in the other SIMS-D candidates examined in the preceding sections.

SUMMARY

NEA:	$<0.14''$ (1σ) at 3.5^M / $0.68''$ (1σ) at 5.0^M — worst sun angle
Edge Roughness:	$0.10''$ (1σ) granular edge
Slit Width:	$10''$ (.0005 inch)
Photocathode Signal:	0.80×10^{-13} amps at 5.0^M AO star
	4.15×10^{-13} amps at 3.5^M AO star
Photomultiplier Output:	0.08 μ amperes at 5.0^M AO star
(at gain of 10^6)	0.42 μ amperes at 3.0^M AO star

4.2.6.3 SIMS-DA-M Star Mapper Electronics

The electronics will consist of standard electronics; i.e., an AC-coupled preamplifier, a low-pass filter, threshold detectors, and time-tagging logic.

The AC-coupled preamplifier would have the following characteristics:

Transresistance:	1.25×10^5 volts/amp
Dynamic Range:	30 db
Band-pass:	1.0 - 500 Hz
AC-coupled follower input	
ENI:	$<7\times10^{-9}$ amp/Hz$^{1/2}$

The AC coupling can be accomplished with a photomultiplier where it is impossible with solid-state detectors that must operate at ultra-low noise levels ($\sim 10^{-12}$ to 10^{-14} amp/Hz$^{\frac{1}{2}}$). The dynamic range is chosen to accommodate a range of star magnitudes and spectral classes from 5.0^M AO to 0.0^M AO. The low cut-off frequency at approximately 1.0 Hz eliminates DC bias shifts, attenuates low frequency excess noise and helps pulse shaping of the signal trailing edge. The high cutoff frequency is chosen high enough not to affect system response.

The low-pass filter would have a high frequency cutoff at approximately 33 Hz, defining a noise bandwidth of 50 Hz.

The threshold detector can be set at a single level corresponding to the half amplitude of a 5.0^M AO star. Because of the large dynamic range and the amplification of pulse asymmetry at low threshold levels it may be desirable to include several threshold levels with a peak detector and logic to decide which threshold level should be used.

The threshold detector measures the time of occurrence of the leading and trailing edges at the threshold level. There is no need for on-board processing to determine the centroid. Both leading and trailing edge pulses will be time tagged, recorded and transmitted to ground.

4.2.6.4 SIMS-DA-M Ground Support Equipment

No information on GSE has been obtained to date. This information will be sought for inclusion in the Final Report.

4.2.6.5 SIMS-DA-M Star Mapper Error Model

Contributor	Error	Comments
Angular Error Velocity:	$<0.05''$ (1σ)	Dynamic ΔT effect (subsection 4.2.0.3)
Optics:	$<0.50''$ (1σ)	(Temporary estimates)
Slit Edge Roughness:	$0.10''$ (1σ)	
NEA:	$0.14''$ (1σ) $0.68''$ (1σ)	3.5^M AO 5.0^M AO with worst-case sun angle of 45°
Quantization Error:	$0.06''$ (1σ)	
RSS:	$<0.53''$ (1σ) $<0.86''$ (1σ)	3.5^M AO 5.0^M AO with worst-case sun angle of 45°
Attitude Update:	100% (SIMS-D)	

4.2.6.6 SIMS-DA-M Star Mapper Trade Parameters

Cost:	To be determined
Accuracy:	$<0.52''$ (1σ) with worst-case sun angle
Attitude Update:	100% (SIMS-DA)
Weight:	6.0 pound preliminary estimate
Power:	2.0 watt preliminary estimate
Size:	2 in. × 3 in. × 12 in. (including sunshade)
FOV:	2° swath width
Sun Angle:	$>45^\circ$
Simplicity of Design:	Additional complexity of folding prism before reticle plane offset by decrease in thermo-mechanical sensitivity due to larger f/No. Bright object sensor and shutter required.
Reliability:	Estimates to be acquired on PMT catastrophic failure probability at launch; otherwise, with bright object shuttering, reliability should be competitive with solid-state.
Cost of GSE:	To be determined
Availability:	Conceptual design stage

4.2.7 SIMS-DA-AS STAR MAPPER CONSIDERATIONS

Due to the lateness of approach by MIT to AS&E, a full response adequate for inclusion in this report has not been assembled, and will have to be deferred to the final report. Tentative indications were that AS&E would employ minimal modifications to their basic technique used in SAS technology. AS employs a superfarron 76 mm f/0.87 lens (F.L.=50 mm) which produces star images <1.0 minute of arc, and an N-shaped reticle, and would consider an EMR-05 photomultiplier. Weight without sunshade is on the order of 10 pounds including redundant HV and redundant LV power supplies and electronics. Power required is 0.65 watts.

4.3 STAR TRACKERS

Only the SIMS-B star tracker using TRW PPCS/PADS technology is considered in detail since the SIMS-D IARU requirements tend to show the adequacy of a star mapper for the SIMS-D star sensor. The SIMS-DB1 and SIMS-DB2 concepts are briefly outlined for the purpose of project activity documentation only.

4.3.1 SIMS-B STAR TRACKER, FUNCTIONAL DESCRIPTION

The star sensor specified by NASA/GSFC for use in the SIMS-B configuration is based upon the Star Tracker Assembly (STA) under development for the PPCS/PADS (Precision Attitude Determination System of the Precision Pointing Control System) by TRW Systems Group. This STA consists of a Star Sensor Unit (SSU) mounted in a two-degree-of-freedom Sensor Gimbal Unit (SGU). The SSU can be considered as being comprised of optical, detector and electronics subassemblies, while the SGU is made up of the SSU, the inner gimbal, the outer gimbal, and the associated motor drive and angle encoding subsystems and electronics. References 27 through 35 are TRW publications which define the PPCS, and thus the STA. The following subsections include the major differences (as known at this time) between the STA described in the referenced publications and that which TRW would probably propose for use in the SIMS-B.

4.3.1.1 SIMS-B Star Tracker Optics

Type:	Cassegrain-Barlow
Focal Length:	84.5 cm
Detector FOV:	$0.5^{\circ} \times 0.5^{\circ}$
Effective Aperture:	42 cm^2
Instantaneous FOV:	84"
Star Image Blur Circle:	~5 to 7"
Star Sensitivity	>+3.5 Mag (S-20)
Size:	~12 cm dia × 50 cm length (includes sunshade and detector)

The electronic processing of the STA detects the centroid of a star image; thus the overall STA is not diffraction limited. The Cassegrain-Barlow optical design, using beryllium for the mechanical mounting components is similar to a design MIT proposed to NASA/MSC in an Apollo Optics Unit Assembly Improvement Study; such an optical design approaches the optimum for a star tracker.

Error sources contributed by the optics can be considered negligible during the star tracking function. i.e., Optical distortion is negligible along the boresight axis; the reflective optics design eliminates chromatic aberrations; and alignment biases can be removed by calibration. Mechanical and thermal stability will be considered separately as an error source in succeeding sections.

4.3.1.2 SIMS-B Star Tracker Photodetector

Image Dissector PMT:	ITT 4004
Aperture:	0.010 in
IPD:	0.014 in
Deflection:	Magnetic
Focusing:	Magnetic
Sun Protection:	Required
Star Sensitivity:	>+3.5 Mag (S-20)

Error sources contributed by the photodetector itself can be listed as detector photocathode nonuniformity, nonlinearity of electron beam deflection coils and star intensity bias. The RSS value of these errors appears to be less than $0.07''$ (again, because of near-null operation) and become negligible when combined with the electronics section.

4.3.1.3 Modes and Electronics

The star tracker primary modes are:

1. Cage: for launch environment protection
2. Acquire: external signals drive tracker LOS to within $\pm 0.25^{\circ}$ of estimated star position; internally-generated scan search covers acquisition FOV until star is acquired.
3. Track: star is tracked until commanded by signal to acquire different star.

(4. Self-Calibration: not presently a mode of the STA, but should be considered for SIMS-B in order to compensate for alignment shifts during launch and long-term shifts during operation.)

The STA electronics appear to be basically what is required for star tracker operation in SIMS-B and to be of an excellent design.

The primary error sources for the SSU (which includes the optics, detector, electronics and mechanical components) are:

Bias stability:	
Electronic	$< 0.6''$
Thermo-mechanical	$< 1.3''$
Initial Misalignment:	$< 0.3''$
Total Bias Uncertainty (RSS)	$< 1.5''$
Electronic Noise (NEA)	$< 1.5''$

4.3.1.4 <u>SIMS-B Star Tracker Gimbals</u>

The gimbal design with flexure supports for single-ball bearing suspensions appears excellent, especially with regard to alignment accuracy and mechanical and thermal stability. The flexure supports are very stiff radially, but relatively soft axially. This allows the gimbal shaft length to change (due to temperature changes) by moving the flexures axially while maintaining gimbal angular accuracy. Symmetry (thermal and Mechanical) in design has resulted in a very stable gimbal structure. The primary error sources for the gimbals are static misalignment bearing noise, bearing runout, and thermo-mechanical stability. The static misalignment is removed during calibration. The bearing runout errors (which are functions of the sine of the gimbal rotational angles), and the bearing noise errors are made quite small by precision machining of the ball bearings. The primary gimbal error source is thermo-mechanical stability, which is $< 0.5''$ (1σ).

4.3.1.5 SIMS-B Star Tracker Encoders

The gimbal angle encoders use the sine/cosine amplitude data of two-speed inductosyns (air core resolvers) mounted on each gimbal structure. The amplitude data is converted by the encoders into digital position output, each encoder being mechanized as a pair of trigonometric phaselock loops. A unique design for the phase shift circuit has resulted in a substantial stability improvement over conventional phase shifting circuits. The inductosyns used for angle readouts are a 1-speed/360-speed pair. No error sources originate in the 1-speed resolver, as it has a resolution of better than $1/4^{\circ}$, which is well within the tolerance required to determine the correct cycle of the 360-speed resolver. Error sources within the 360-speed inductosyns are caused by mechanical misalignment, electronics and readout quantization. The RSS of these error sources indicates that the error contribution of the gimbal encoders is $<1.0''$ (1σ).

4.3.1.6 SIMS-B Star Tracker Signal Processing

All signal processing is done internally within the STA. STA outputs are discretes giving mode, star magnitude, star presence, bright object presence; and digital outputs giving gimbal angles and SSU LOS position error angles. Computer requirements will depend upon STA operational requirements (e.g., random stars or on-board star catalog). Error sources which can be attributed to the signal processing have been collected under the encoder summation.

4.3.1.7 SIMS-B Star Tracker GSE

GSE requirements will be that equipment required for incorporation of the STA into the overall SIMS-B system. This would include such items as star collimators, theodolites, stable bases, etc.

4.3.1.8 SIMS-B Star Tracker Error Model

Operating Specifications -

Gimbal Freedom:	±45° Roll (outer) ±15° Pitch (inner)
Gimbal Rates:	4°/sec, Peak ~0 to 0.10°/sec, Tracking
Acquisition FOV:	0.5° × 0.5°
Acquisition Time:	≤ 0.5 sec after star enters FOV
Accuracy:	Better than 2.7"/axis (1σ) for star mag (S-20) ≤3.5
Sun Angle Constraint:	Tracking accuracy must be achieved with SSU boresight within 45° of sun
Temp. Range:	-10° to +55° C.

Error Model -

	RSS (1σ)	
SSU Bias Uncertainty	< 1.5"	
Electronic Noise (NEA)	< 1.5"	
Gimbal thermo-mechanical stability	< 0.5"	O.G.
	< 0.5"	I.G.
Gimbal Encoder Uncertainty	< 1.0"	O.G.
	< 1.0"	I.G.
	RSS < 2.7"	

4.3.1.9 SIMS-B Star Tracker Trade Parameters

Accuracy:	RSS < 2.7"/axis (1σ)
Total FOV:	±45° Roll (O.G.) ±15° Pitch (I.G.)
Acquisition FOV:	0.5° × 0.5°

(Cont. on page 4-92)

Sun Angle Constraint:	Tracking accuracy will be met with SSU boresight within 45° of sun
Weight:	41 lb (Beryllium Construction)
Power:	26w
Cost:	$210K (recurrent basis)
GSE Cost:	$75K
Availability:	Engineering model now in final assembly, will be tested by 1 July 1972. Flight HW avail. by 12 - 15 mo. after receipt of order.
Simplicity of Design:	The STA is a state-of the-art system, and the design appears not to be overly conservative. In order to meet the overall accuracy requirements, any star tracker needs the utmost in mechanical and thermal stability. The STA appears to be of reasonable simplicity, considering the accuracy and stability requirements.

4.3.2 SIMS-DB STAR TRACKER CONCEPT

Both the SIMS-DB1 and SIMS-DB2 Star Tracker mechanical configurations are discussed, briefly, below. The telescope and sensor package are body-fixed with the single axis of (sealed) mechanical rotational freedom aligned parallel to the spacecraft roll axis. The telescope entrance is attached by a vacuum-tight flange to the prism housing. The prism housing contains limited-angle-of-rotation annular gimbals with the prism output face (facing the telescope) framed in the rear annulus. Torquers are mounted on each gimbal (for thermal symmetry) and an angle encoder is mounted on the forward gimbal. The input face of the prism is attached to the sunshade by a flange. The prism and sunshade are rotated around the telescope axis as a single unit. Vacuum-tight sealing of the prism housing is accomplished by a flexible bellows-type boot which is attached at one end to the sunshade flange and at the other end to the prism housing. The prism housing can be mounted with a zenith-pointing boresight (at unrotated prism position) for 9:00AM and twilight orbits, or with a 45^{o} offset for noon orbits. The prism housing and telescope housing will contain low-pressure nitrogen gas. In this way, no rubbing parts or lubricants will be exposed to vacuum and a three to five year reliability is made a much more realistic goal.

The SIMS-DB1 differs from the SIMS-DB2 in the star-search mode.

The SIMS-DB1 searches for stars from a very limited on-board catalog (20 or 30 stars). Digital increments are stored by time address. Each increment represents the nominal roll angle at which a particular star is expected to transit the plane defined by the nominal pitch and yaw axes. As the onboard clock cyclic count coincides with a storage address, the digital increment is compared with the digital output of the angle encoder and the error drives the torquer to seek a null. At null the star tracker mode switches to a limited-mechanical-step scanning search (approximately $\pm 1.5^{o}$) to acquire the star within the limit of spacecraft attitude error. The 0.5^{o} wide (in roll) electronic raster search field-of-view is stepped in 0.5^{o} increments at the completion of each 0.25^{o} raster pitch search (in the forward portion of the available $0.5^{o} \times 0.5^{o}$ raster field). The raster search field, advanced by the spacecraft pitch rate, overlaps the raster search field of the previous mechanical search cycle by an amount sufficient to avoid gaps at the extremes of attitude angular velocity rate error. When a star is acquired its electrical roll signal is used to drive the gimbals to a null so that the spacecraft pitch rate will cause the star to transit the star tracker boresight, where rate and position data are recorded for ground processing. The onboard star catalog digital increments will be automatically adjusted twice a day (i.e., at a fixed value of increment change per update) in order to follow orbital precession. When a star angle is incremented beyond the gimbal limits it is automatically erased from the catalog and a new star position increment and address may be added from a ground command.

The internal optical, mechanical, sensor and tracking electronic configurations associated with the telescope would be identical to those of the PPCS/PADS telescope, sensor and tracking elements.

SIMS-DB2 has no onboard star catalog. Its search mode is mechanical-step scanning in a $\pm 15^{\circ}$ roll direction to acquire stars of opportunity. The aperture in the image dissector (i.e., the instantaneous field-of-view) would likely be increased and the raster points decreased so that the $0.25^{\circ} \times 0.5^{\circ}$ search field can be stepped mechanically at a sufficient rate to overlap the previous scanning cycle. This entails some loss in accuracy. After acquisition the signal is processed and the gimbal commanded in exactly the same manner as in the SIMS-DB1 star tracker.

4.4 SUMMARY

Table 4-1 summarizes the estimated values of parameters associated with each SIMS star mapper at the present level of iteration.

The gaps in Table 4-1 indicate that the data has either not been received or not assimilated or both. All gaps

(...cont'd on page 4-100)

Table 4-1 SIMS Star Mapper Parameters

	SIMS-A	SIMS-DA-KI	SIMS-DA-HR	SIMS-DA-HA	SIMS-DA-M
OPTICS:					
Type	Concentric Catadioptric	Catadioptric; Mangin Primary	Catadioptric	Concentric Catadioptric	Refractive
Swath Width	4°	6°	8°	2°	2°
Entrance Aperture	3.5 in.	5.33 in.	2.5 in.	2.26 in.	1.6 in.
Effective Aperture Area	43.4 cm^2	73 cm^2	20 cm^2	18 cm^2	10 cm^2
f/No.	1.14	1.25	2.0	1.76	5.5
Housing	Invar	Beryllium		Invar	Beryllium
Sunshade Angle	>30°	>30°	>45°	>30°	>45°
Design Temperature	72° F			72° F	
DETECTOR:					
Type and No.	CdS, 6	Si, 6	Si, 6	CdS, 6	PMT S-20, 1
Slit Width	0.0003 in. (10")	0.0006 in. (17.3")	0.00045 in. (16")	0.0003 in. (10")	(10")
Array	SPARS-like	SPARS-like	SPARS-like	SPARS-like	SPARS-like
Bias	0.5 V and Background Light	Photovoltaic Mode	Photovoltaic Mode	0.5 V and Background	High Voltage Dynodes

Table 4-1 SIMS Star Mapper Parameters (Cont.)

	SIMS-				
	-A	-DA-KI	-DA-HR	-DA-HA	-DA-M
ELECTRONICS:					
Type	Leading Edge at 1/2 Peak Ampl.	KI: Leading Edge at Fixed-Thresh. (MIT: Lead. and Trail.)	Leading and Trailing Edge, Fixed-Thresh. (Command Adjust)	Leading Edge at 1/2 Peak Amplitude	Leading and Trailing Edges at One of Three Levels
Preamp Transresistance	$\sim 10^9$	2.5×10^9	$>2.0 \times 10^9$	$\sim 10^9$	1.25×10^5
Dynamic Range	98:1	16:1 (4.2^M ro 1.2^M)	Not Specified	98:1	30 db
Noise Bandwidth	15 Hz	9.1 Hz	15 Hz	15 Hz	50 Hz
Bandpass	? - 7.0 Hz	0.028 - 5.8 Hz	? - 7.0 Hz	? - 7.0 Hz	1.0 - 32.8 Hz
Output	One-Shot Pulse; Slit ID	Goes Negative At Thresh.; Slit ID	Digital Time; Slit ID; Amplitude	One-Shot Pulse; Slit ID	Pos. Leading Edge Pulse; Neg. Trailing Edge Pulse

Table 4-1 SIMS Star Mapper Parameters (Cont.)

	SIMS-				
	-A	-DA-KI	-DA-HR	-DA-HA	-DA-M
ERROR, (1σ):					
Angular Error Velocity	0.23"	0.15"	0.14"	0.23"	0.23"
Edge Roughness (Statistical)	0.05"	0.016"	0.10"	0.05"	0.10"
Noise-Equivalent Angle	0.42" @ 4.75^M (CdS)	KI - 1.22" @ 4.00^M (Si) (MIT - 0.87" @ 4.00^M)	0.48" @ 3.2^M (Si)	0.42" @ 4.00^M (CdS)	0.14" @ 3.5^M (S-20) 0.68" @ 5.0^M (S-20)
Quantization Error		0.06"	0.05"		0.05"
RSS	0.48" @ 4.75^M	1.24" (0.90") @ 4.00^M	0.51" @ 3.2^M	0.48" @ 4.0^M	0.29" @ 3.5^M (S-20); 0.73" @ 5.0^M (S-20)

Table 4-1 SIMS Star Mapper Parameters (Cont.)

	SIMS-				
	-A	-DA-KI	-DA-HR	-DA-HA	-DA-M
ERROR, BIAS					
Optics Spectral Class	0.13"			0.10"	
Optics Uniform Temp.	0.2"/Δ°F (from 72°F)	<0.5" (Estimate)	<0.5" (Estimate)		<0.5" (Estimate)
Optics Temp. Cross-Gradient	0.07"/Δ°F (Mirror Mount) 0.34"/Δ°F (Meniscus Mount)			0.03"/0.25Δ°F (Mirror Mount) 0.17"/0.25Δ°F (Meniscus Mount)	
Dynamic Range Shift	<0.10"			<0.10"	
Slit Straightness		1.36"			1.25"
Stellar Magnitude Shift	<0.10"	8" KI (<0.1" MIT)		<0.10"	
(1σ) (Max Bias^2 + RSS^2)$^{1/2}$ With 4°F ΔT <u>UNCALIBRATED</u>	(Incomplete) 1.49" (Mirror Mount) 2.54" (Meniscus Mount) @ 4.75^M (CdS)	(Incomplete) 9.75" (9.70") @ 4.00^M(Si)	(Incomplete) 0.71" @ 3.2^M(Si)	(Incomplete) 0.64" (Mirror Mount) 1.09" (Meniscus Mount) @ 4.00^M (CdS)	(Incomplete) 1.48" @ 3.5^M (S-20) 1.62" @ 5.00^M (S-20)

Table 4-1 SIMS Star Mapper Parameters (Cont.)

	SIMS-				
	-A	-DA-KI	-DA-HR	-DA-HA	-DA-M
$\overline{\text{SPG}}$	13% SIMS-A	0% SIMS-D (1% SIMS-A)	0% SIMS-D (0.3% SIMS-A)	0% SIMS-D	0% SIMS-D
WEIGHT	15 Pounds (Not Optimized)	9.0 Pounds	4.0 Pounds	7 Pounds	<6 Pounds
SIZE	6 in. Dia. x 22 in. Long, Including Sunshade	7.5 in. Dia. x 18.3 in. Long, Including Sunshade	3.5 in. Dia. x 13 in. Long, Including Sunshade	5 in. Dia. x 20 in. Long, Including Sunshade	2 in. x 3 in. x 12 in., Including Sunshade
POWER	5 Watts	1.5 Watts (2.3 Watts)	2.0 Watts	5 Watts	2.0 Watts
COST		\$300,000 Non-recurring. \$30,000/unit			
AVAILABILITY	Through Phase 1B (SPARS)			Modified Phase 1B (SPARS)	Conceptual Design Stage
RELIABILITY		MTBF 222,568 Hr. = $4.493/10^6$ Hr.	0.99, 4-Slits, 3 Years		

should be filled in or discussed by the final report. The data shown in Table 4-1 ranges from acquired and quoted material to a best estimate at present.

Since only a single star tracker is considered as the SIMS-B star tracker candidate, a summary (such as Table 4-1) is not necessary here. All parameters are found in section 4.3.1.

SECTION 5

ERROR STUDIES

5.1 GENERAL APPROACH TO PROBLEM

The objective of the present error studies is to determine the accuracy of attitude determination for three SIMS candidates which are fairly representative of today's technology and are briefly identified as follows:

SIMS Candidate	Chief Characteristics
A	Strapped-Down Gyros and Star Sensor
B	Strapped-Down Gyros; Gimbaled Star Sensor
D1-A	Gyros Fully Gimbaled; Strapped-Down Star Sensor

Each of the above candidates contains a gimbaled or strapped down set of gyros to provide short-term wide-bandwidth attitude information, and a gimbaled or strapped down star sensor to bound the long-term attitude errors.

Attitude determination in the present case implies determination, on the ground, of the inertial attitude of some spacecraft reference block at an arbitrary epoch using gyro and star measurement data received before and after that epoch. This is often referred to as "after-the-fact" attitude determination and involves the mathematical problem of smoothing.

The attitude accuracy desired by NASA is 0.001 deg (1σ) per axis. The extent to which any of the SIMS candidates meet this requirement is one of the primary objectives of this study. In the present case it is important to note that the ability of a given candidate includes not only the equipment on board the spacecraft but also the ground technique used to process the data. There are a number of techniques for smoothing and processing the data. Many of these, like the one being used in this study, generate a solution in the least squares sense, and make use of a priori knowledge of the system errors. However, the performance of any of these techniques will be limited by how well they model the system and its error sources. Each SIMS candidate possesses a number of error sources, some of which are more important than others. Consequently, two of the first steps required in the error studies are: (1) to determine the error sources associated with each candidate, and (2) to identify, on the basis of engineering judgment and preliminary calculations, those sources which are the major contributors to the error in attitude determination.

In the present effort, the statistics of all significant random-type error sources have been modeled in the data smoothing technique since this is considered essential in this type of application. However, in the case of bias-type errors, only the bias drift of each gyro has been modeled in the smoothing process for the following reasons:

1) Gyro bias drift is by far the most significant bias-type error in any of the candidates.

2) To account for a bias-type error in the smoothing process, one must usually include it as an additional parameter to be estimated along with spacecraft attitude. Since this results in a significant increase in computation, the number of biases handled in this way should be kept to a minimum. In the present instance it is felt that the inclusion of other biases in the state

estimate would result in a computational effort which is beyond the scope of the present effort.

3) By including bias drift in the smoothing estimates, one has also accounted, to some extent, for gyro scale factor bias and gyro misalignment bias which look very much like gyro bias drift for the small librations in attitude anticipated in this type of mission.

With the exception of gyro bias drift, and, to some extent, gyro scale factor and misalignment bias, the other bias errors in each candidate have not been accounted for in the smoothing process. However, the effect of these other bias errors will be considered to some extent in this study. Although the other bias errors do not cause an attitude error that increases with time as do those mentioned for the gyros, they do affect the accuracy of attitude determination in one way or another. None of these bias errors causes an error in attitude that exceeds the bias error itself and many have even less effect because of the nature of the data processing.

It is obvious that the manner in which the data will be processed in this study does not completely determine the accuracy of attitude determination for each candidate since this is subject to many factors such as the extent to which the system errors are modeled in the data processing technique. However, it is felt that the approach will give a fairly good idea of the accuracy obtainable with each candidate and, what is probably more important in terms of trade considerations, it will give a very good indication of the relative performance of these systems. One would expect very little change in the relative performance of these systems if the same errors were modeled in some other type of smoothing process. It should be noted, however, that there may be one shortcoming in the present analysis of SIMS-A and -B which is the omission of the gyro scale factor and misalignment biases as separate parameters to be estimated in the smoothing process. Although these biases can be accounted for to some extent in the estimation of gyro drift bias because of the small attitude librations, they may still require separate estimation in any smoothing technique used to support a real mission. This would probably require the estimation of 9 new parameters (i.e., 3 for scale factor bias and 6 for misalignment). In the case of a fully-gimbaled gyro system, such as SIMS-D1-A, this would not be necessary since these errors do not affect this type of system.

In the error studies an effort will also be made to determine the sensitivity in overall performance of each SIMS candidate to certain key error sources and other factors such as data interval size. This information can be useful in establishing the accuracy required of certain system components in order to achieve a desired system performance. The manner in which the sensitivity data will be obtained is by repeated operation of the smoothing technique for different values of the particular parameter.

The star availability studies, which are essentially complete and are reported in Section 5.3, represent an important step in the error studies. The manner in which these studies were conducted was considered essential in order to obtain realistic performance values for each SIMS candidate in the error studies. Real star distributions were generated for each candidate, taking into account the spectral response of the detector and the spectral characteristics of each star. The results enable one to select for error studies those star distribution cases which are representative of the "worst" and "typical" situations. Although various sun-synchronous orbits are being considered in the EOS application, only the 9 PM - 9AM orbit was analyzed in the present case since it was considered sufficient for the purpose of this study.

5.2 BASIC MATHEMATICAL DESCRIPTION OF CANDIDATES

5.2.1 COORDINATE SYSTEMS COMMON TO ALL CANDIDATES

This section defines the reference coordinate systems or frames used in the error studies and simulations that are common to all candidates. These primary reference frames are the following:

Basic Inertial (I-frame)
Orbit-Oriented Inertial (O-frame)
Body-Fixed (B-frame)

Other coordinate systems apply to particular candidates and are defined in the appropriate sections.

5.2.1.1 Basic Inertial Coordinate System (I-frame)

The coordinate axes for this system are defined in Figure 5-1. The axes X_I and Y_I both lie in the equatorial plane with X_I pointing towards the vernal equinox. Axis Z_I points along the north polar axis of the Earth. Star catalogs normally give the directions of stars in this coordinate system.

5.2.1.2 Orbit-Oriented Inertial Coordinate System (O-frame)

This system of axes is also defined in Figure 5-1. The coordinate system is oriented relative to the basic inertial coordinate system through the angles Ω and i. The first angle is the right ascension of the orbit ascending node, and the angle i is the orbit inclination. This orbital plane does precess slowly about the earth's rotational pole due to oblateness of the earth. However, the orbit-oriented coordinate system is defined herein to be an inertial frame since, in our simulations , orbit plane rotation due to precession is ignored as

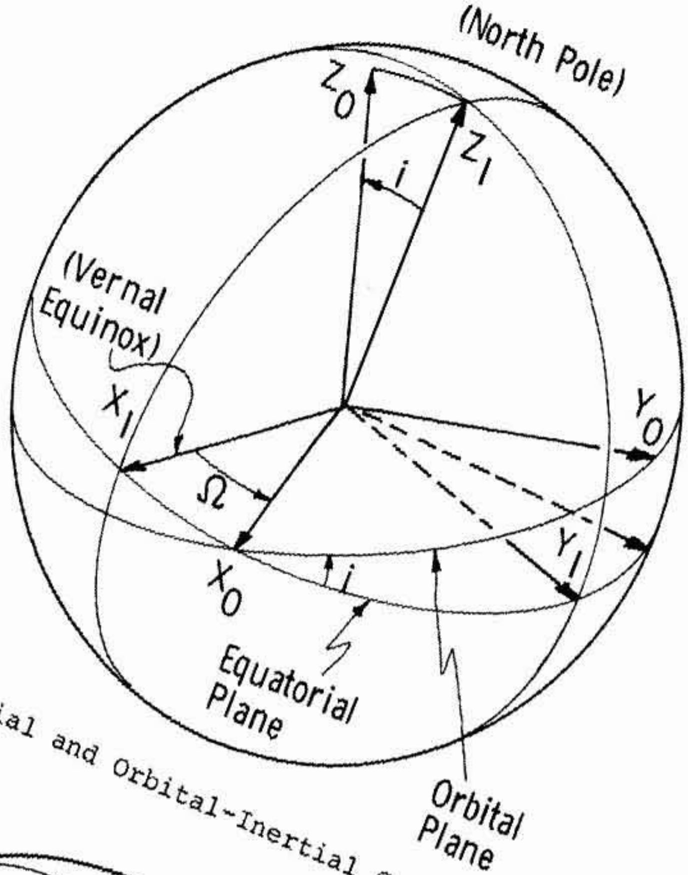

Figure 5-1 Inertial and Orbital-Inertial Coordinate Systems

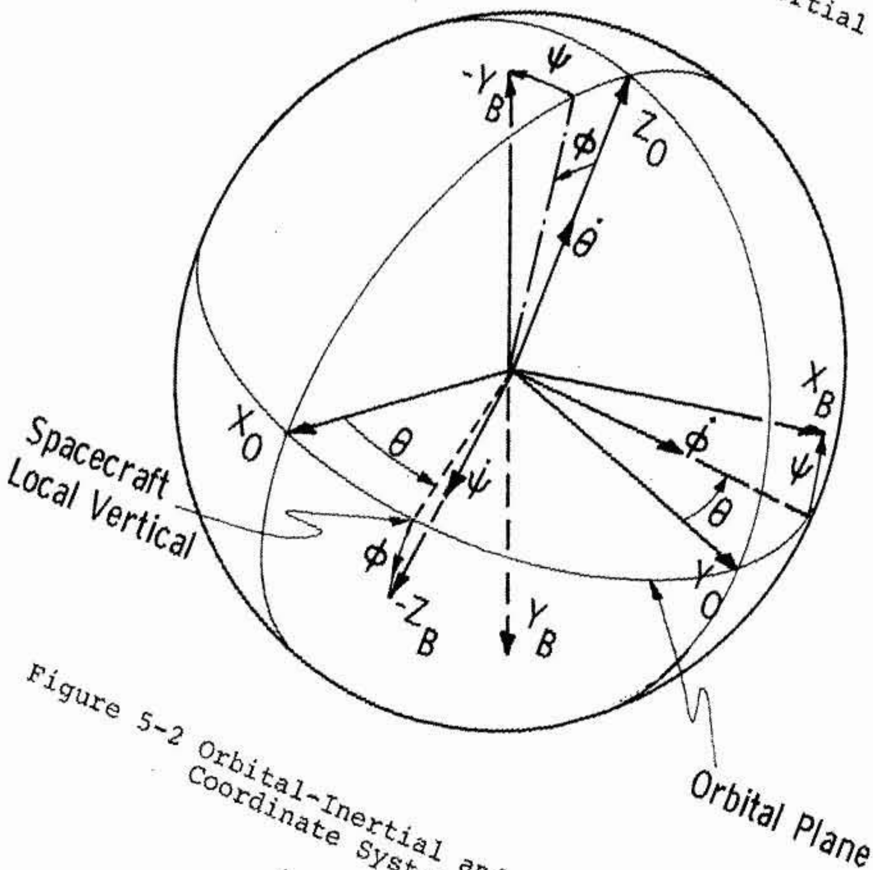

Figure 5-2 Orbital-Inertial and Body-Fixed Coordinate Systems

being irrelevant to the SIMS configuration comparison. Since real rotation of the EOS orbit plane is a small fraction of a degree over the course of a typical simulation (≈3 hours), the distribution of available stars is not affected by such precession. The transformation matrix T_{OI}, from basic inertial to orbit-oriented inertial coordinates is given by:

$$T_{OI} = \begin{bmatrix} 1 & 0 & 0 \\ 0 & ci & si \\ 0 & -si & ci \end{bmatrix} \begin{bmatrix} c\Omega & s\Omega & 0 \\ -s\Omega & c\Omega & 0 \\ 0 & 0 & 1 \end{bmatrix} \tag{5-1}$$

when c denotes cosine, and s denotes sine. Thus a star vector $\underline{s}_O$ in the orbit-oriented frame can be computed, given the star vector $\underline{s}_I$ in basic inertial coordinates.

$$\underline{s}_O = T_{OI}\, \underline{s}_I \tag{5-2}$$

5.2.1.3 <u>Spacecraft Body-Fixed Coordinate System (B-frame)</u>

The axes of this system are such that X_B, Y_B, and Z_B are respectively the roll, pitch and yaw axes of the spacecraft. The nominal orientation of these axes is as follows:

X_B - is along the projection of the spacecraft velocity vector onto the local horizontal plane

Y_B - is normal to the orbital plane

Z_B - is along the local nadir

The orientation of the B-frame with respect to the O-frame is shown in Figure 5-2. The transformation from the O-frame to the B-frame is through the Euler angle sequence of pitch (θ), roll (ϕ), and yaw(ψ) as shown in Figure 5-2 and expressed by:

$$T_{BO} = \begin{bmatrix} 0 & 1 & 0 \\ 0 & 0 & -1 \\ -1 & 0 & 0 \end{bmatrix} \begin{bmatrix} 1 & 0 & 0 \\ 0 & c\psi & s\psi \\ 0 & -s\psi & c\psi \end{bmatrix} \begin{bmatrix} c\phi & 0 & -s\phi \\ 0 & 1 & 0 \\ s\phi & 0 & c\phi \end{bmatrix} \begin{bmatrix} c\theta & s\theta & 0 \\ -s\theta & c\theta & 0 \\ 0 & 0 & 1 \end{bmatrix} \tag{5-3}$$

The input axes for the strapped down gyros, which both SIMS candidates -A and -B possess, are ideally colinear with the spacecraft body-fixed axes, so that $X_g = X_B$, $Y_g = Y_B$ and $Z_g = Z_B$.

Other coordinate systems apply to the gimbaled gyro systems or to the star sensors (either star mapper or star tracker). These will be described in the following sections.

5.2.2 SIMS-A

Both SIMS-A and -B have strapped down gyro systems. The problem of computing body attitude with such gyros should be considered here.

5.2.2.1 Attitude Computation

With strapped down gyros, spacecraft attitude relative to some inertial reference is continuously computed using gyro output pulses and an algorithm to update the attitude matrix. This matrix may be either a nine-element direction cosine matrix or a four-element quaternion. The simplest or 1st order algorithm used to update the direction cosine matrix is as follows:

$$C(t + \Delta t) = C(t) + C(t)W(t)\Delta t \tag{5-4}$$

where the second term on the right represents the incremental attitude information obtained from the gyro loops. C(t) is the direction cosine matrix at time t. $C(t + \Delta t)$ is the computed matrix at time $t + \Delta t$, one update interval later.

W(t) is the following skew-symmetric matrix containing the measured body rates $\omega_x(t)$, $\omega_y(t)$ and $\omega_z(t)$:

$$W(t) = \begin{bmatrix} 0 & -\omega_z(t) & \omega_y(t) \\ \omega_z(t) & 0 & -\omega_x(t) \\ -\omega_y(t) & \omega_x(t) & 0 \end{bmatrix} \qquad (5\text{-}4A)$$

The order of the algorithm used to update the attitude matrix directly affects the accuracy of the attitude computations. The error in attitude computation is a function of the input rates to the gyros and of the update interval. With a first-order algorithm this error can be relatively large; however, reduction in update interval can reduce the attitude error. But if a 2nd-or 3rd-order algorithm is used, the associated attitude error is greatly reduced. With all SIMS candidates the attitude computation together with implementation of the required algorithm will be carried out on the ground. Hence there will be no impediment to using a sufficiently high order algorithm to minimize the effects of orbital angular rate and of attitude librations on attitude computation.

5.2.2.2 Kinematic Equations

Equations are presented that relate the Euler angle rates, $\dot{\phi}$, $\dot{\theta}$, and $\dot{\psi}$, to the spacecraft body rates, ω_x, ω_y, ω_z, that are measured by the strapped down gyros. The latter rates are measured about body-fixed axes relative to inertial space. The required equations are as follows:

$$\begin{bmatrix} \dot{\theta} \\ \dot{\phi} \\ \dot{\psi} \end{bmatrix} = \begin{bmatrix} s\psi/c\psi & -c\psi/c\phi & 0 \\ c\psi & s\psi & 0 \\ s\phi s\psi/c\phi & -s\phi c\psi/c\phi & -1 \end{bmatrix} \begin{bmatrix} \omega_x \\ \omega_y \\ \omega_z \end{bmatrix} \qquad (5\text{-}5)$$

Since the spacecraft will be stabilized about the local vertical, the angles ϕ and ψ will be small angles, but θ will lie anywhere between 0 and 360 degrees. For the case where $\phi = \psi = 0$, we have:

$$\dot{\theta} = -\omega_y$$
$$\dot{\phi} = \omega_x \qquad (5\text{-}6)$$
$$\dot{\psi} = -\omega_z$$

5.2.2.3 Star Mapper Measurement Equations

The star mapper uses relatively small-FOV concentric optics (4 deg. FOV) to focus the star field onto the detector surface. The detector consists of several photo sensitive elements called slits. The error simulations assumed one star mapper with three slits with the optical axis of the mapper oriented directly overhead.

The basic star sensor measurement is the time at which a star image crosses one of the slits. Ideally each detector slit lies in a single plane containing the telescope optical axis. The orientation of each slit plane is defined in body-fixed coordinates by a unit normal vector, $\underline{n}_B$.

At the time of star transit, a measure of the attitude error is obtained by the following dot product:

$$\text{DOT} = \underline{n}_{B_j} \cdot \left[T_{BO} \, T_{OI} \, \underline{s}_I \right] \qquad (5\text{-}7)$$

where j denotes the jth slit and $\underline{s}_I$ is the unit vector of the cataloged star in basic inertial coordinates which is transformed to body-fixed coordinates using T_{BO} and T_{OI}, where T_{BO} has been computed for the time of transit and T_{OI} is assumed to be fixed. Ideally DOT should be zero if the vehicle attitude expressed in T_{BO} is correct. Since DOT is a small quantity for the level of attitude errors expected in this type of mission, it can be interpreted as being the attitude error in radians about an axis which is normal to $\underline{n}_{B_j}$ and the star direction.

5.2.3 SIMS-B

Because SIMS-B has strapped down gyros like SIMS-A, the presentation in the previous section on attitude computation and on kinematic equations also applies here. SIMS-B also has a gimbaled star tracker with inner and outer gimbal axes. The discussion here is concerned with the star tracker coordinate system and the measurement equations.

The star tracker coordinates (X_T, Y_Y, Z_T) are defined in Figure 5-3 relative to body-fixed axes. As shown, Z_T is directed outward along the tracker optical axis, and Y_T is oriented along the tracker inner gimbal axis. The figure also shows the outer gimbal angle, Φ, which is about body roll axis, and the inner gimbal angle, θ_T, about "pitch". For the simulations the outer gimbal can rotate through $\pm$ 45°, the inner gimbal through $\pm$ 15°.

The transformation, T_{TB}, from body-fixed to tracker coordinates is given by:

$$T_{TB} = \begin{bmatrix} 1 & 0 & 0 \\ 0 & -1 & 0 \\ 0 & 0 & -1 \end{bmatrix} \begin{bmatrix} c\theta_T & 0 & -s\theta_T \\ 0 & 1 & 0 \\ s\theta_T & 0 & c\theta_T \end{bmatrix} \begin{bmatrix} 1 & 0 & 0 \\ 0 & c\Phi & s\Phi \\ 0 & -s\Phi & c\Phi \end{bmatrix}$$

$$T_{TB} = \begin{bmatrix} c\theta_T & s\theta_T s\Phi & -s\theta_T c\Phi \\ 0 & -c\Phi & -s\Phi \\ -s\theta_T & c\theta_T s\Phi & -c\theta_T c\Phi \end{bmatrix} \qquad (5\text{-}8)$$

For this tracker a star does not have to be exactly along the optical axis since two offset angles α_T and β_T are used to indicate the displacement of the star with respect to the axis as shown in Figure 5-4. Since α_T and β_T are always very small,

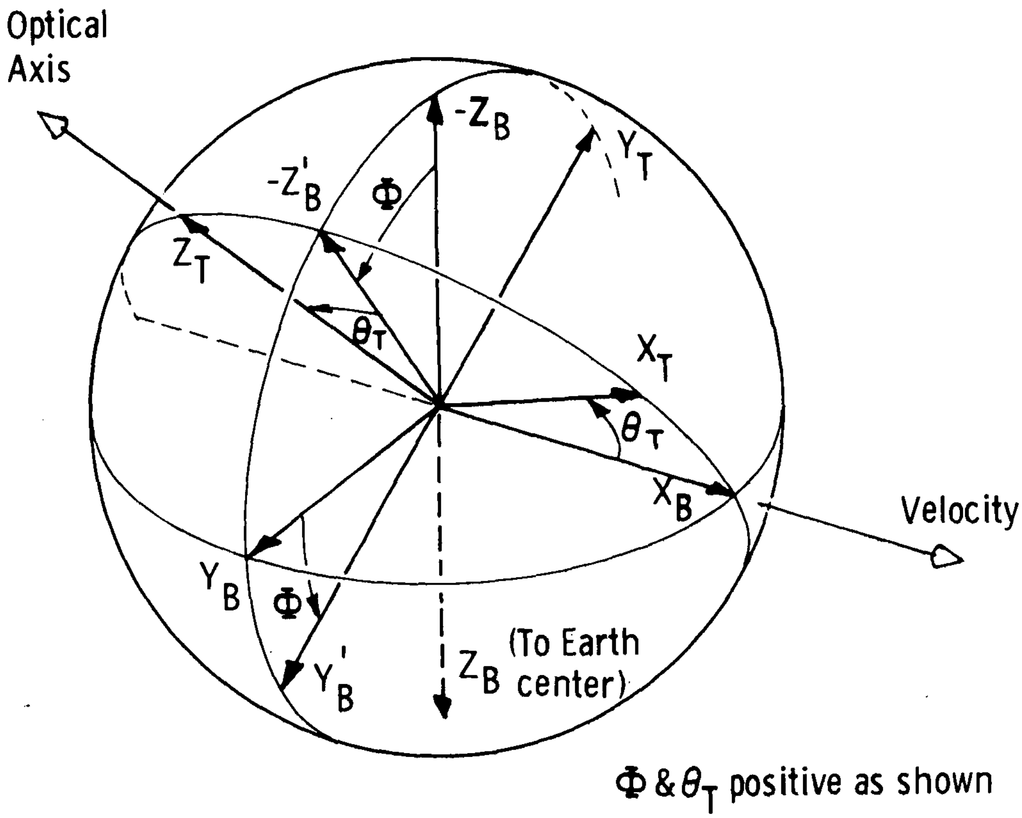

Figure 5-3 Star Tracker Coordinate System

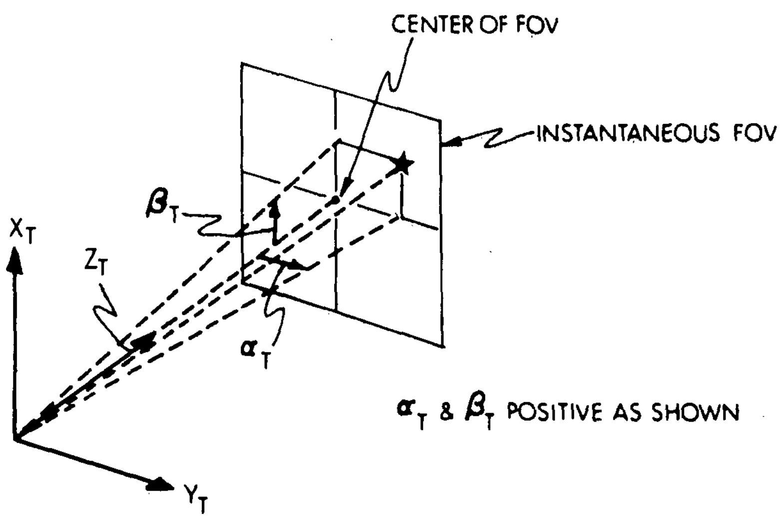

Figure 5-4 Star Location in Instantaneous FOV

the direction of the star in star tracker coordinates can be expressed by the vector $[\beta_T, \alpha_T, 1]$. The measured direction of the star in body-fixed coordinates can be expressed by the following vector $\underline{s}_B$:

$$\underline{s}_B = T_{BT} \begin{bmatrix} \beta_T \\ \alpha_T \\ 1 \end{bmatrix} = \begin{bmatrix} \beta_T c\theta_T - s\theta_T \\ -\alpha_T c\Phi + \beta_T s\theta_T s\Phi + c\theta_T s\Phi \\ -\alpha_T s\Phi - \beta_T s\theta_T c\Phi - c\theta_T c\Phi \end{bmatrix} \tag{5-9}$$

An estimate $\underline{s}'_B$ of the direction of the star in body-fixed coordinates, based upon knowledge of the vehicle inertial orientation, can be obtained as follows:

$$\underline{s}'_B = T_{BO}\, T_{OI}\, \underline{s}_I \tag{5-10}$$

where $\underline{s}_I$ is a unit vector of the known direction of the star in basic inertial coordinates. Except for measurement errors in $\underline{s}_B$, the angular difference between $\underline{s}_B$ and $\underline{s}'_B$ can be assumed to be due to incorrect knowledge of vehicle attitude. Since both vectors are essentially unit vectors, the measurement equations require only the first two components of each vector:

$$\begin{bmatrix} \beta_T c\theta_T - s\theta_T \\ -\alpha_T c\Phi + \beta_T s\theta_T s\Phi + c\theta_T s\Phi \end{bmatrix} = \begin{bmatrix} (s\psi s\phi c\theta - c\psi s\theta) & (s\psi s\phi s\theta + c\psi c\theta) & (s\psi c\phi) \\ (-c\psi s\phi c\theta - s\psi s\theta) & (-c\psi s\phi s\theta + s\psi c\theta) & (-c\psi c\phi) \end{bmatrix} T_{OI}\underline{s}_I \tag{5-11}$$

5.2.4 SIMS-D1-A

This candidate differs from the first two candidates in that it has a fully-gimbaled gyro system. Like SIMS-A it has a strapped down star mapper. Because the gyro platform is fully stabilized, the spacecraft attitude angles with respect to an inertial frame can be read off from the three platform gimbal angles.

For the purposes of this study it is assumed that the stabilized member (or platform) coordinate system coincides with the orbit-oriented coordinate system except for small misalignment angles α, β, and γ which are used in an Euler sequence as shown in Figure 5-5. The transformation from orbital to platform coordinates is given approximately by:

$$T_{PO} \cong \begin{bmatrix} 1 & 0 & 0 \\ 0 & 1 & \gamma \\ 0 & -\gamma & 1 \end{bmatrix} \begin{bmatrix} 1 & 0 & -\beta \\ 0 & 1 & 0 \\ \beta & 0 & 1 \end{bmatrix} \begin{bmatrix} 1 & \alpha & 0 \\ -\alpha & 1 & 0 \\ 0 & 0 & 1 \end{bmatrix}$$

$$T_{PO} \cong \begin{bmatrix} 1 & \alpha & -\beta \\ -\alpha & 1 & \gamma \\ \beta & -\gamma & 1 \end{bmatrix} \qquad (5\text{-}12)$$

The orientation of the body-fixed coordinate system with respect to the platform axes is given by the three platform gimbal angles I, M, and O, which are respectively the inner, middle, and outer gimbal angles. The sequence of gimbal angle transformations shown in Figure 5-6 was chosen so that I, M, and O would correspond to the Euler angles θ, ϕ, and ψ used previously in the strapped down gyro cases (SIMS-A and -B). If there were no misalignment between the platform and orbit-oriented coordinate systems, the angles I, M, and O would equal θ, ϕ, and ψ, respectively. The transformation from platform to body-fixed coordinates is given by:

$$T_{BP} = \begin{bmatrix} 0 & 1 & 0 \\ 0 & 0 & -1 \\ -1 & 0 & 0 \end{bmatrix} \begin{bmatrix} 1 & 0 & 0 \\ 0 & cO & sO \\ 0 & -sO & cO \end{bmatrix} \begin{bmatrix} cM & 0 & -sM \\ 0 & 1 & 0 \\ sM & 0 & cM \end{bmatrix} \begin{bmatrix} cI & sI & 0 \\ -sI & cI & 0 \\ 0 & 0 & 1 \end{bmatrix} \qquad (5\text{-}13)$$

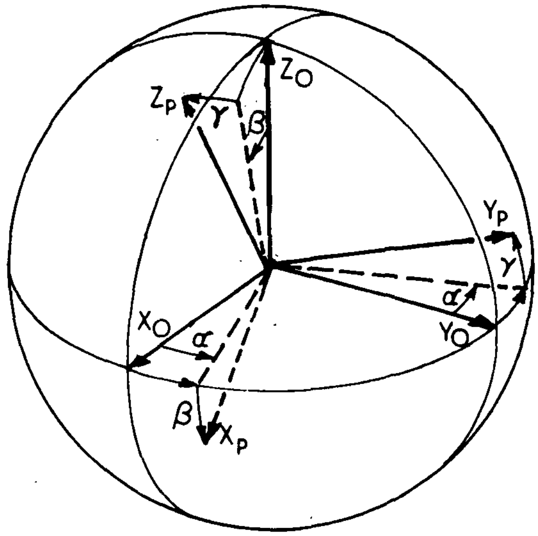

Figure 5-5 Platform and Orbital-Inertial Coordinate Systems

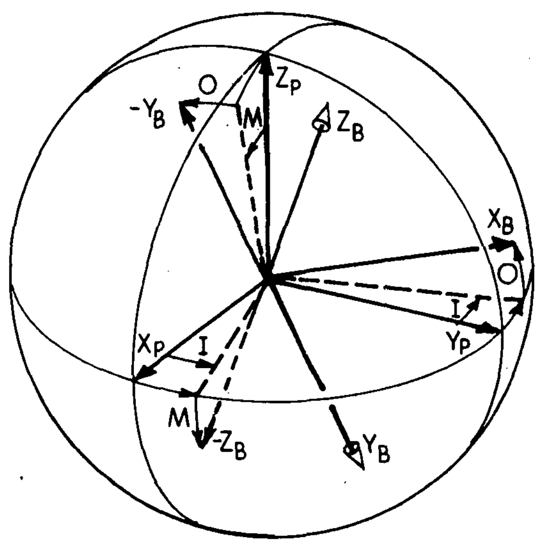

Figure 5-6 Body-Fixed and Platform Coordinate Systems

5.3 STAR AVAILABILITY STUDIES

5.3.1 INTRODUCTION

The objective of the star availability studies is to acquire spatial distribution data on stars for each detector being considered in order to be able to select representative and worst-case distributions for use by the error analysis programs. These programs require as input a swath catalog containing all stars, down to a designated limiting detector magnitude and listed in order of acquisition, that fall within the field-of-view of the particular SIMS condidate's star mapper or tracker for the specified orbit.

The general approach to the solution of this problem is to first obtain a general star catalog which contains a sufficient number of stars to include all stars down to the necessary limiting detector magnitude for any detector of interest. Then the detector magnitudes must be calculated and the detector star catalogs generated for each detector being considered. Finally these detector catalogs must be used in conjunction with the orbit specification and the characteristics of a particular SIMS candidate to generate statistical data and availability plots for visual inspection in order to make a selection of typical and worst cases for the error studies.

5.3.2 GENERAL STAR CATALOGS USED

There are two major requirements of a general star catalog that is to be used in generating the detector star catalogs needed for this study. The first is that the catalog contain stars distributed over the entire celestial sphere. This seems obvious but a few recent catalogs, although complete in all other respects, only cover a portion of the sphere, such as the northern hemisphere, presumably because the observations have so far been restricted to only one observatory. The second requirement is that the general catalog contain all stars down to the limiting magnitude for the detector under consideration. This requirement is most important for the silicon sensor, which is most sensitive in the red and infrared portions of the spectrum. For example, the silicon detector magnitude of a red M-type star may be 3 magnitudes brighter than the visual magnitude of that star, which means that in order to generate a catalog that includes all stars down to a silicon magnitude of 4.0, the input catalog must include all stars down to a visual magnitude of 7.0. The difference between the visual and detector magnitudes of a star is normally referred to as the "color index".

In order to meet these requirements and make use of the most recent data available, it was necessary to utilize several of the existing star catalogs, filling in the holes in one with information from another.

The thirteen-color narrow-band photometry done by Richard I. Mitchell and Harold L. Johnson at the University of Arizona[115] and continued by R. I. Mitchell at the University of Texas yields probably the most accurate specification of stellar output in the visible region yet performed. This catalog contains data for 945 northern stars and preliminary data for 139 southern stars down to about the sixth visual magnitude. The catalog lists narrow-band stellar output at wavelengths of .33, .35, .37, .40, .45, .52, .58, .63, .72, .80, .86, .99, and 1.10 microns. Stellar detector magnitudes can be computed directly from this data by convolving the detector spectral response with the spectral output for each star.

Data for many stars not included in the above catalog was obtained from the UBVRIJKL work (for ultra-violet, blue, visual red, and four regions in the infra-red) done earlier by the University of Arizona[116]. This catalog lists broad-band data for 1324 northern stars at wavelengths of approximately .36, .44, .55, .70, .90, 1.25, 2.2, and 3.4 microns and includes data for 301 stars not included in the 13-color catalog. The UBVRIJKL data can also be convolved with the detector's spectral responses to obtain the detector magnitudes.

In addition to the above stars, 7677 others were taken from the Yale University Observatory Catalog of Bright Stars[117] which includes 9091 stars down to about the seventh visual magnitude and distributed over the entire celestial sphere. Since this catalog only lists (as far as stellar output is concerned) the visual magnitude and spectral type for each star, the detector magnitude must be calculated from the detector color index function, as described in the following section.

5.3.3 DERIVATION OF DETECTOR MAGNITUDES AND COLOR INDICES

In order to compute any detector magnitudes, the detector spectral response must be known. The relative sensitivities for the S-20[118], cadmium sulfide[119], and silicon[120] sensors are shown in Figure 5-7.

For the 13-color photometry data the detector magnitudes can be directly computed from these relative sensitivities and the thirteen different color magnitudes. These magnitudes are specified as a magnitude at .52 microns (M52) and as difference magnitudes at the other wavelengths, such as M33-52 or M52-58. It is then simply a matter of adding or subtracting these difference magnitudes from M52 to obtain the narrow-band magnitudes M_i. The relative flux density for wavelength λ_i is

$$B_i = A_i \, 10^{-M_i/2.512} \tag{5-14}$$

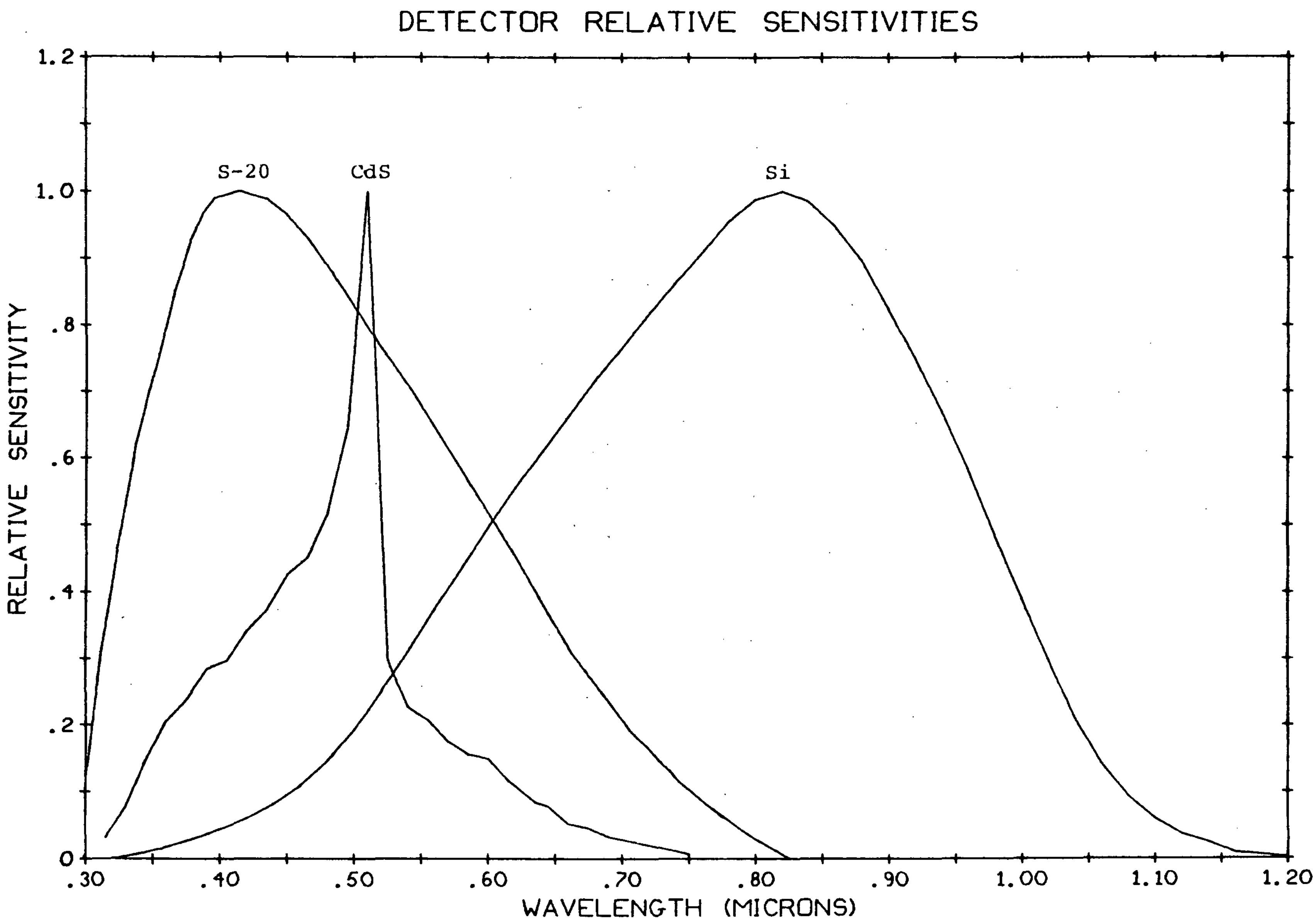
DETECTOR RELATIVE SENSITIVITIES
S-20
CdS
Si
RELATIVE SENSITIVITY
1.2
1.0
.8
.6
.4
.2
0
.30
.40
.50
.60
.70
.80
.90
1.00
1.10
1.20
WAVELENGTH (MICRONS)

Figure 5-7

where A_i is the absolute flux density calibrated for a zero magnitude AO V star for wavelength λ_i (see Table 5-1). The relative total flux is then

$$I = \sum_{i=1}^{12} RS_i \left(\frac{B_i + B_{i+1}}{2} \right) \tag{5-15}$$

where RS_i is the average detector relative sensitivity over the interval λ_i to λ_{i+1}. A reference relative total flux is computed for the zero magnitude AO V star from Equations 5-14 and 5-15 with the M_i's set to zero or equivalently by

$$I_{ref} = \sum_{i=1}^{12} RS_i \left(\frac{A_i + A_{i+1}}{2} \right) \quad . \tag{5-16}$$

The detector magnitude is then

$$M_d = -2.512 \log_{10} (I/I_{ref}) \tag{5-17}$$

For the UBVRIJKL data the computation is much the same, where M_i in Equation (5-14) now represents one of the broad-band magnitudes U, B, V, R, I, J, K, or L,and A_i is the absolute flux density calibration for the broad-band wavelength λ_i (see Table 5-2). However, in this case, the relative total flux is computed by

$$I = \sum_{i=1}^{8} RS_i \, B_i \tag{5-18}$$

or

$$I_{ref} = \sum_{i=1}^{8} RS_i \, A_i \tag{5-19}$$

Table 5-1

ABSOLUTE CALIBRATION FOR
13-COLOR PHOTOMETRY[121]

FILTER BAND	EFFECTIVE WAVELENGTH (μ)	ABSOLUTE FLUX DENSITY (ZERO MAG. AO V STAR)
33	.337	3.63×10^{-12} W/cm^{2}μ
35	.353	3.57 "
37	.375	4.89 "
40	.402	8.40 "
45	.459	6.67 "
52	.518	4.69 "
58	.583	3.36 "
63	.635	2.51 "
72	.724	1.73 "
80	.800	1.25 "
86	.858	1.02 "
99	.985	0.76 "
110	1.108	0.52 "

Table 5-2

ABSOLUTE CALIBRATION FOR
UBVRIJKL PHOTOMETRY[122]

FILTER BAND	EFFECTIVE WAVELENGTH (μ)	ABSOLUTE FLUX DENSITY (ZERO MAG. AO V STAR)
U	.36	4.35×10^{-12} W/cm^{2}μ
B	.44	7.20×10^{-12} "
V	.55	3.92×10^{-12} "
R	.70	1.76×10^{-12} "
I	.90	0.83×10^{-12} "
J	1.25	0.34×10^{-12} "
K	2.2	0.39×10^{-13} "
L	3.4	0.81×10^{-14} "

where RS_i is the average detector relative sensitivity in the wavelength interval over which the corresponding broad-band filter is effective (i.e., where it transmits 70% or more).

To compute the detector magnitude for stars from the Yale Bright Star Catalog the color index curve for that detector must first be calculated. The color index of a detector is the difference between the visual magnitude and the detector magnitude for some star,

$$C.I. = M_v - M_d \quad , \tag{5-20}$$

and is a function of stellar spectral type. It was shown in the previous discussion that the detector magnitude can be directly computed for all stars for which either 13-color or UBVRIJKL data is given. The visual magnitude and spectral type is also given for each of these stars so that an average color index can then be calculated for each spectral type. The color index versus spectral type function can then be fitted to a tenth-order polynomial to yield the color index curves of Figure 5-8. Using these curves and Equation (5-20) the detector magnitudes are easily obtained.

Color index can also be calculated using blackbody considerations and this was done to determine how much this method differed from the more realistic approach given above. The blackbody radiation is described by the Plank function

$$B(\lambda,T) = C1 \Big/ \lambda^5 \left(e^{C2/\lambda T} - 1 \right) \tag{5-21}$$

where

$$C1 = 3.7403 \times 10^8 \text{ watt } \mu^4/M^2$$
$$C2 = 1.43868 \times 10^4 \ \mu \ {}^oK$$

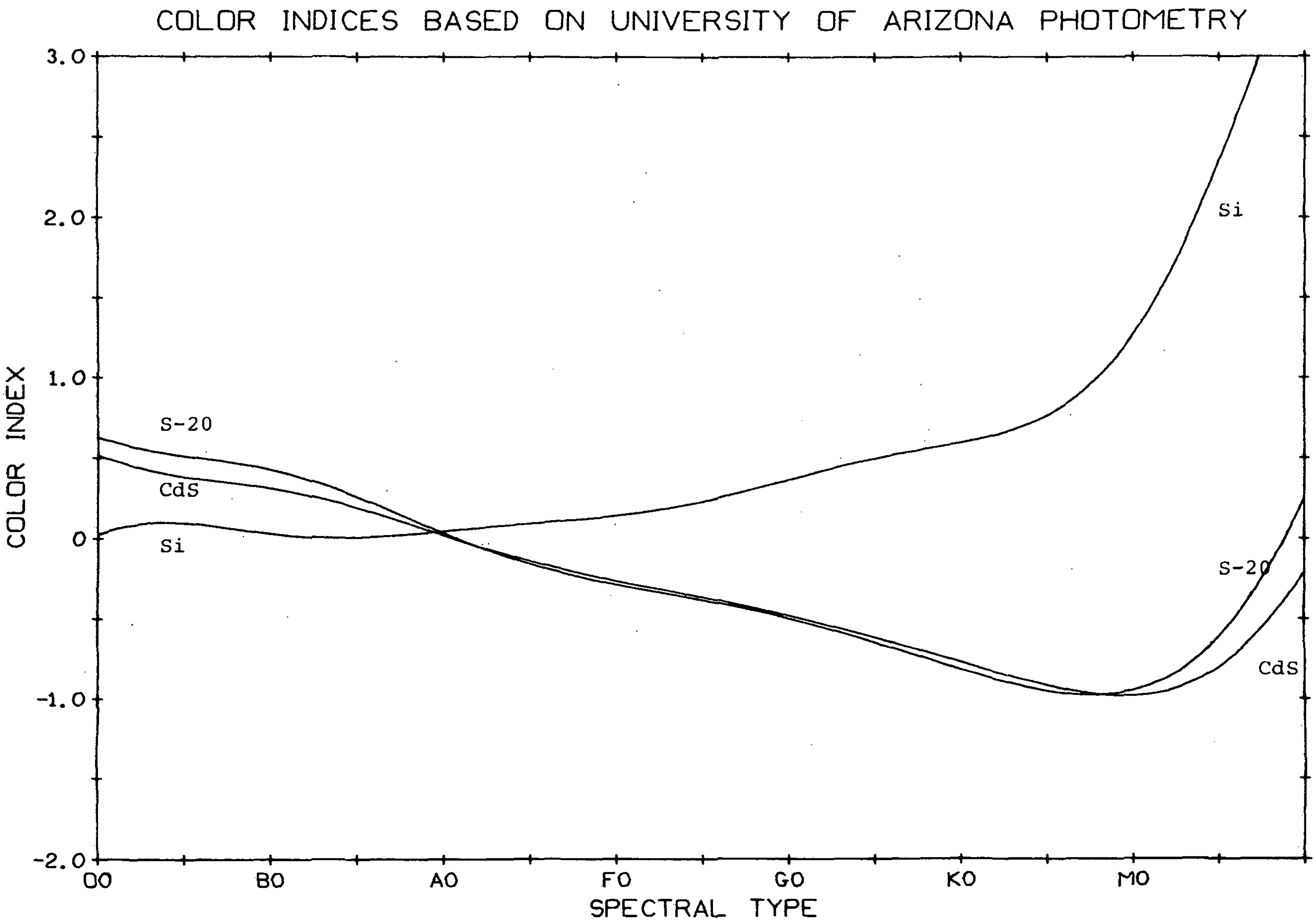
COLOR INDICES BASED ON UNIVERSITY OF ARIZONA PHOTOMETRY
3.0
2.0
1.0
0
-1.0
-2.0
COLOR INDEX
OO
BO
AO
FO
GO
KO
MO
SPECTRAL TYPE
S-20
CdS
Si
Si
S-20
CdS

Figure 5-8

λ = wavelength in microns
T = effective temperature in ^{o}K

The flux density at λ_i relative to that at .52 microns for a given effective temperature is then

$$B_i = B(\lambda_i, T)/B(.52, T) \quad (5\text{-}22)$$

and the relative total flux is again

$$I = \sum_{i=1}^{12} RS_i \left(\frac{B_i + B_{i+1}}{2} \right) \quad (5\text{-}23)$$

The relative detector magnitude is

$$M_d = -2.512 \log_{10} (I/I_{ref}) \quad (5\text{-}24)$$

where I_{ref} is computed from Equations (5-22) and (5-23) with T set to the effective temperature of an AO V star. The relative visual magnitude, M_v, can be calculated from Equations (5-23) and (5-24) with RS_i set to the relative sensitivity of a V (visual) filter. M_d and M_v computed in this way are relative magnitudes because no calibration has been performed. Calibration is not necessary here, however, since it is just the difference C.I. = $M_v - M_d$ that is of interest. Color index as a function of effective temperature, and therefore of spectral type, can easily be computed and is shown in Figure 5-9 only for comparison to Figure 5-8, which illustrates the more realistic approach which has been used in the generation of the detector star catalogs.

5.3.4 STAR CATALOGS FOR DETECTORS

Each of the general detector star catalogs contains for each star an identifier, which is the Yale Bright Star

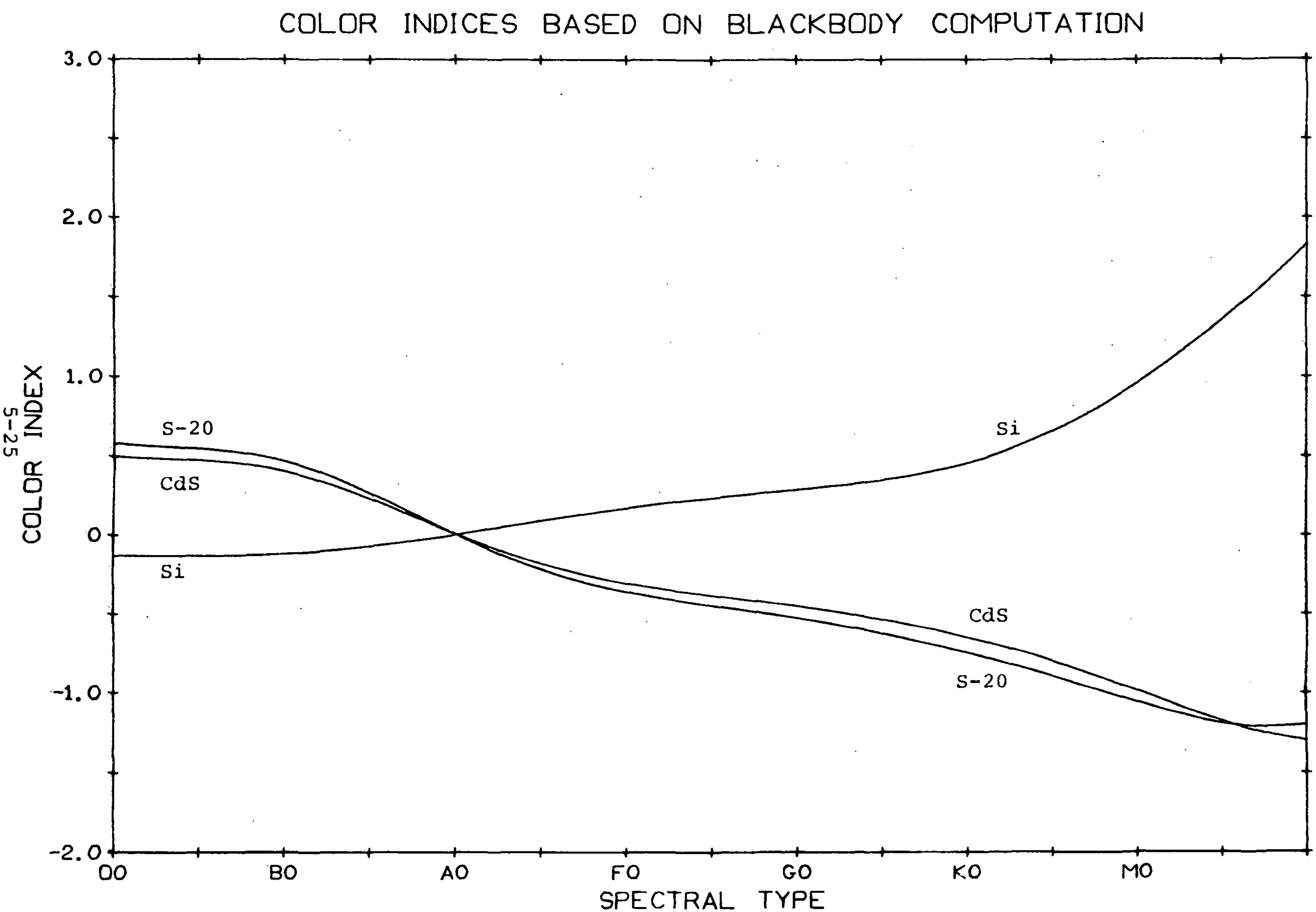
COLOR INDICES BASED ON BLACKBODY COMPUTATION
3.0
2.0
1.0
0
-1.0
-2.0
COLOR INDEX
S-20
CdS
Si
Si
CdS
S-20
OO
BO
AO
FO
GO
KO
MO
SPECTRAL TYPE
Figure 5-9

number, a unit vector in basic inertial coordinates, and the detector magnitude. The unit vector is computed from a linear interpolation to the year 1975 using the right ascensions and declinations given in the Yale Bright Star Catalog for the years 1900 and 2000. Each catalog contains all stars in the input catalog down to some specified limiting detector magnitude, subject to the qualifications of the following double-star criteria which is based on the double-star data in the Yale Bright Star Catalog.

> If the difference in detector magnitude (or in visual magnitude if the companion is not entered separately) is greater than 2.0, accept the brighter star. If the difference is less than 2.0, do the following:
>
> A. For a Star Mapper: If the angular separation is greater than 20 arc seconds, accept the brighter star, otherwise accept neither.
>
> B. For a Star Tracker: If the angular separation is greater than 100 arc-seconds, accept the brighter star, otherwise accept neither.

Appendix B lists the 961 stars whose magnitude for <u>any</u> detector is 4.0 or brighter. Note that in constructing the tables of this Appendix the star mapper double-star criteria were used. For a star tracker a few of the stars in these tables would be deleted due to the more stringent separation criterion.

Table 5-3 gives some statistical data on the number of stars that are brighter than a given detector magnitude for each detector.

Table 5-3

NUMBER OF STARS BRIGHTER THAN OR EQUAL TO A GIVEN DETECTOR MAGNITUDE

MAGNITUDE	STAR TRACKER DETECTOR S-20	STAR MAPPER DETECTORS S-20	CdS	Si
0.0	3	3	3	9
1.0	13	13	12	21
2.0	48	48	44	84
3.0	125	125	121	287
4.0	360	362	350	918
5.0	1093	1108	1083	2544
6.0	3337	3376	3316	6542

5.3.5 STAR DISTRIBUTION RESULTS

The primary purpose of the star distribution data is to indicate the distribution and number of stars available to the star mapper or star tracker at various times of the year for one of the sun-synchronous orbits being considered in the EOS mission. This data will enable one to select those cases which are considered to be most appropriate for system error analysis, such as the "typical" and "worst" cases. The orbit chosen for this purpose is a circular sun-synchronous orbit with an inclination of 99 degrees and the ascending node is always at local 9:00 PM. As the earth goes around the sun the orbit of the spacecraft rotates with respect to inertial space, completing one rotation each year.

The star distribution data are presented as star plots which show those stars that will be available to a star sensor for different orientations of the orbit during the year. The manner in which the star plots are generated for the star mapper is slightly different from that for the star tracker due to the significant difference in the size of the FOV for these two star sensors. In either case, however, additional data is generated showing the number and mathematical distribution of the stars available in each orbit.

5.3.5.1 Star Mapper Plots

The manner in which the star distribution plots were generated for the star mapper is shown in Figure 5-10. Assuming that the optical axis of the star mapper lies within the orbital plane, the stars which pass through the FOV of the star mapper will be those in a band (or swath) of the celestial sphere which is symmetrical with respect to the orbital plane. In other words, for a star mapper with a 4 degree FOV, the stars will be those within 2 degrees of the orbital plane. The position of each star with respect to the orbit can be essentially given by the true anomaly of the projection of the star's direction onto the orbital plane since its angle out of plane is small and unnecessary in the present instance. A line plot can therefore be used to show the star positions in accordance to their true anomalies as shown at the bottom of Figure 5-10. Various symbols are used in the plot to indicate the brightness of the stars in accordance with Table 5-4. The symbol (•) is used for stars below the acceptance limit of the star mapper down to two magnitudes below that limit. These weak stars are shown to illustrate possible noise sources.

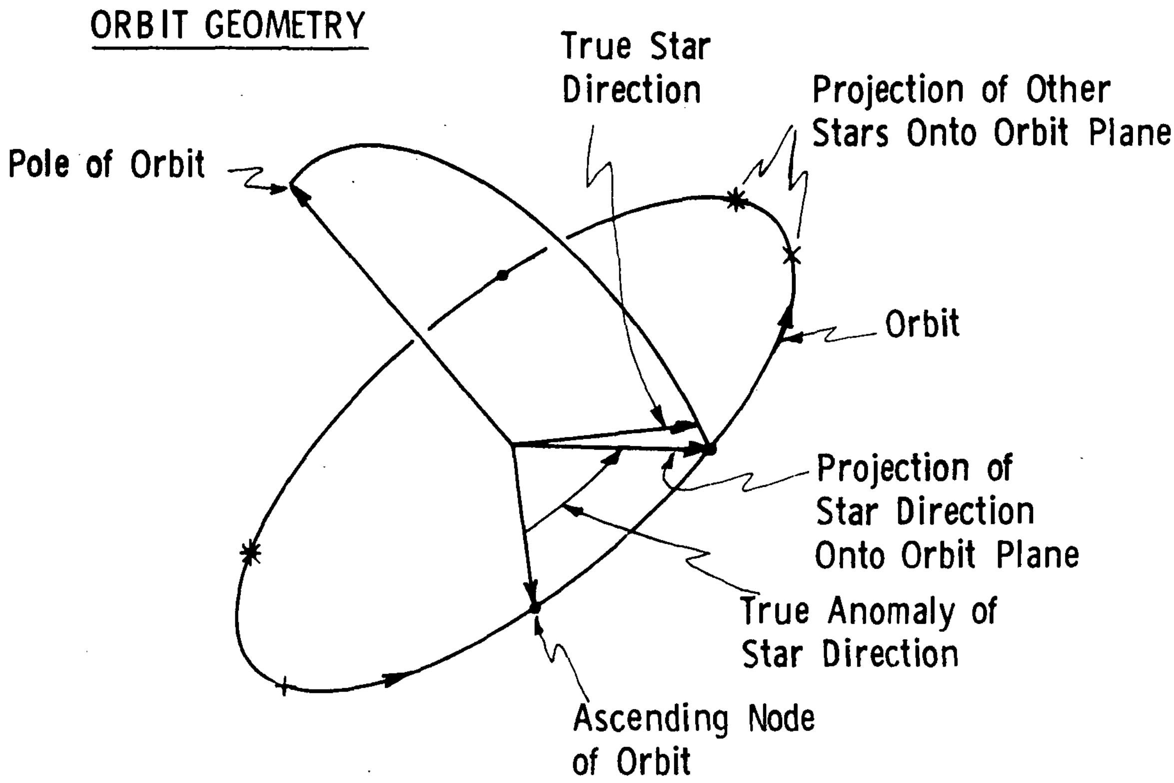

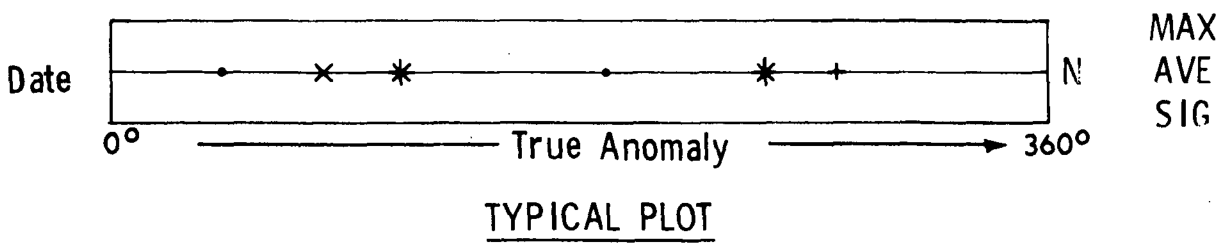

Figure 5-10 Basic Description of Star Mapper Plot

Table 5-4

Stellar Magnitude Ranges
Denoted by Various Symbols

SYMBOL	STAR TRACKER DETECTOR	STAR MAPPER DETECTORS		
	S20	S20	CdS	Si
*	$M \leq 2.5$	$M \leq 3.0$	$M \leq 3.0$	$M \leq 2.6$
×	$2.5 < M \leq 3.0$	$3.0 < M \leq 3.5$	$3.0 < M \leq 3.5$	$2.6 < M \leq 3.1$
+	$3.0 < M \leq 3.5$	$3.5 < M \leq 4.0$	$3.5 < M \leq 4.0$	$3.1 < M \leq 3.6$
•	$3.5 < M \leq 5.5$	$4.0 < M \leq 6.0$	$4.0 < M \leq 6.0$	$3.6 < M \leq 5.6$

Additional data is given on the left and right sides of the plot as shown in Figure 5-10. The month and day of the orbit for the year 1972 will be given on the left side. The parameters N, MAX, AVE, and SIG give various statistics for the stars which are above the acceptance limit of the star mapper. N is the number of such stars in the plot. MAX is the maximum separation, in degrees of true anomaly, between two adjacent stars. AVE is the average separation in degrees and is simply 360/N. SIG is the standard deviation of the N separations and is computed as follows:

$$SIG = \sqrt{\sum_{i=1}^{N} (S_i - AVE)^2 / N} \qquad (5\text{-}25)$$

where S_i is the angular separation between $star_i$ and $star_{i+1}$ (Note that $star_1$ follows $star_N$).

Star distribution plots were generated for the star mapper for four different fields-of-view (4,6,8, and 10 degrees) and three different detectors (CdS, Si, and S-20). As an example, the results for a star mapper with a 4 degree FOV and an S-20 photomultiplier detector are shown in Figure 5-11. The full set of plots is shown in Appendix C. Note that a star distribution plot is given for the orbit every 4 days for a period of 180 degrees to insure complete* coverage of that portion of the celestial sphere which can be seen by the star mapper during the year. In this case, it is assumed that the optical axis of the mapper lies within the orbital plane.

5.3.5.2 Star Tracker Plots

The manner in which the star distribution plots were generated for the star tracker is shown in Figure 5-12. In this case, the plots are two-dimensional with each star position being given by its true anomaly and its angle out of the orbital plane, which are analogous to the right ascension and declination of a star. The star plot shows all stars within ±45 degrees of the orbital plane which can be seen by a star tracker with an S-20 detector. Various symbols are used to indicate the brightness of the stars in accordance with Table 5-4. Statistical data again appear at the right side of the plot and MAX, AVE, and SIG are as before except that the angular separation of two adjacent stars (in terms of true anomaly) is the true angular separation. The quantities N_1, N_2, and N_3 at the right side of the plot indicate the number of detectable stars within ±15, ±30, and ±45 degrees of the orbital plane, respectively.

Star distribution plots were generated for the star tracker for the inertial orientation of the orbit every 30 days during a period of 180 days. Figure 5-13 shows the plot for July 1, 1972. The full set of plots is shown in Appendix C. Note in Figure 5-13 that no stars are shown within 45 degrees of the sun because of star tracker limitations. Also note

*i.e. virtually complete

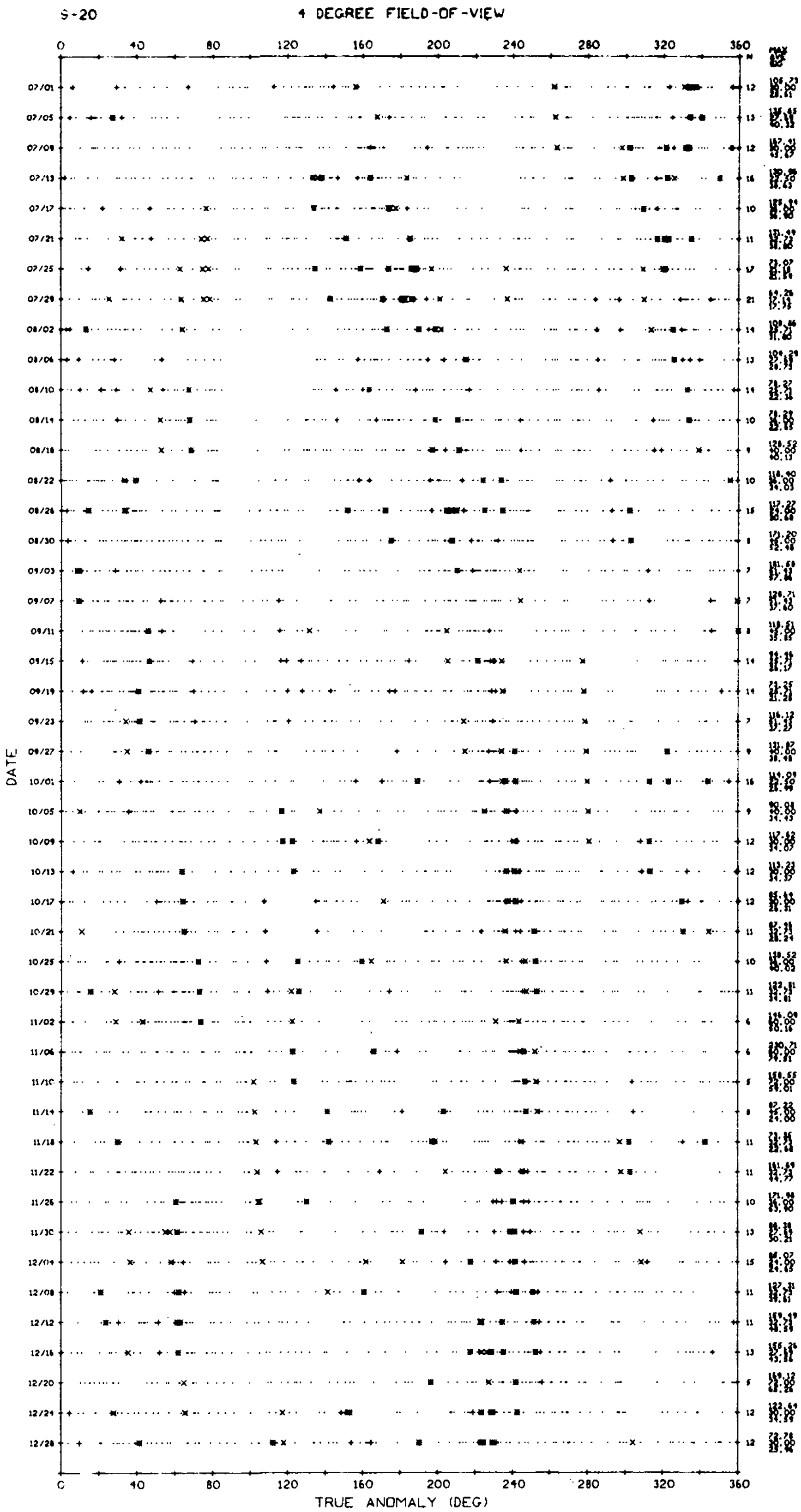

Figure 5-11 Star Distribution Plot for Star Mapper with 4° FOV and S-20 Photomultiplier Detector.

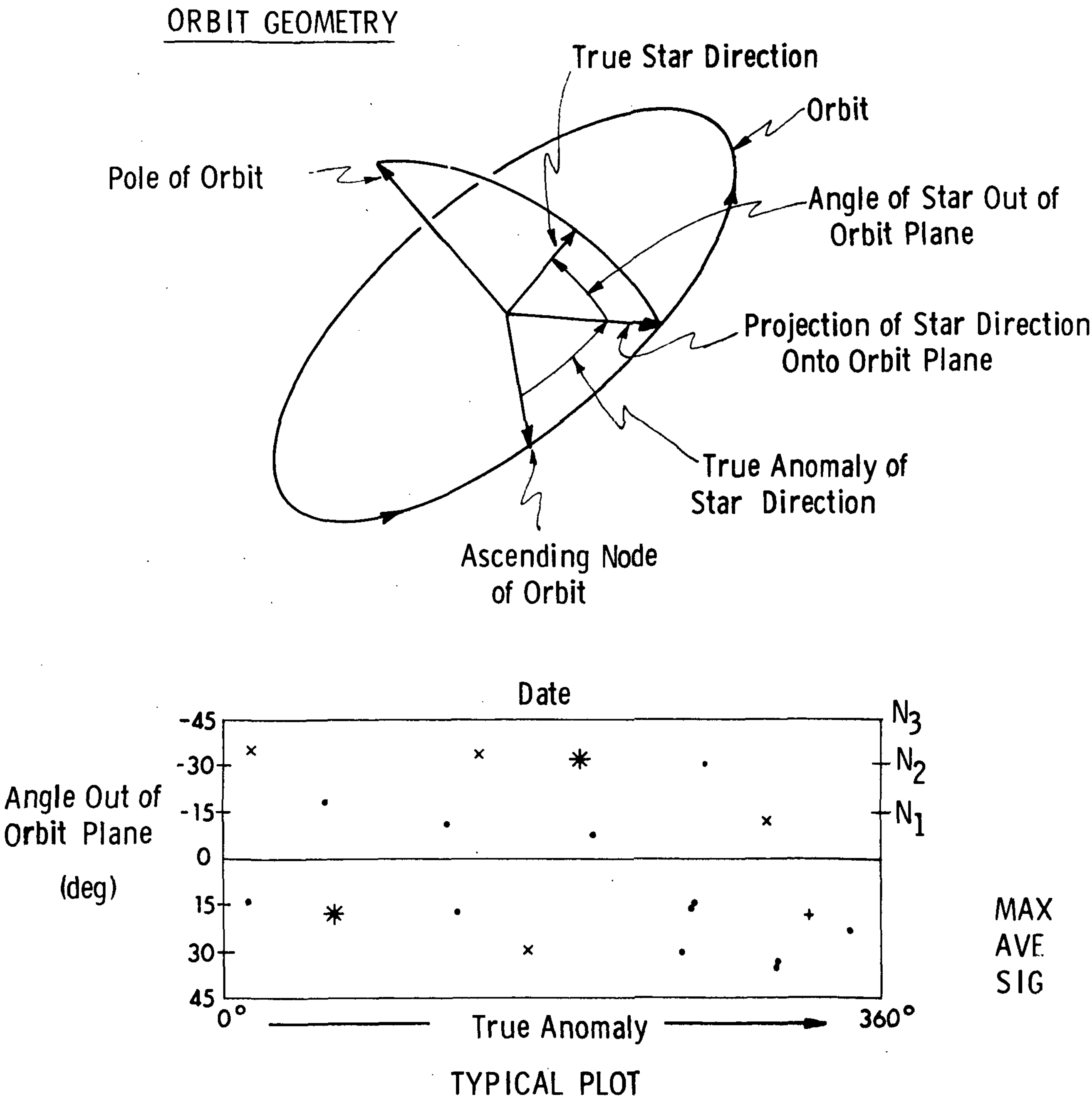

Figure 5-12 Basic Description of Star Tracker Plot

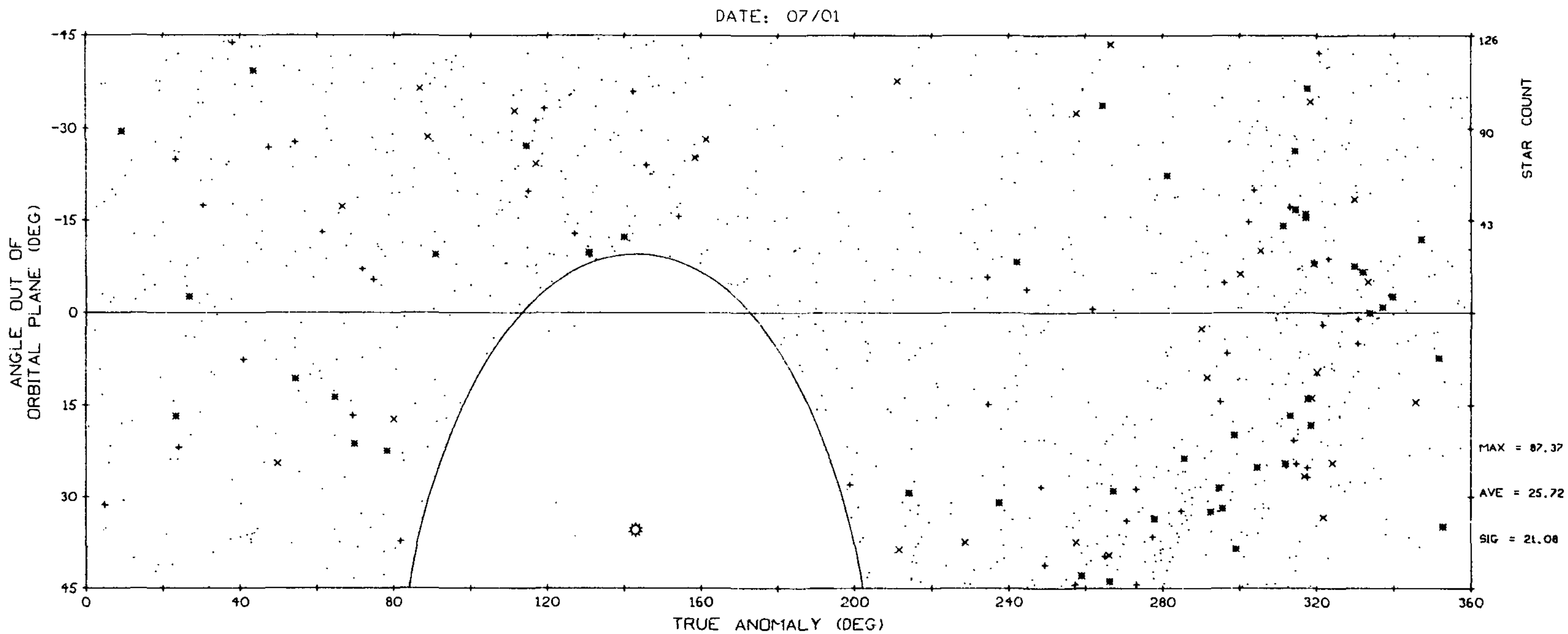

Figure 5-13 Star Distribution Plot for Star Tracker for July 1, 1972

that small dots are again used to represent noise stars that are within two magnitudes below the acceptance (or detection) limit of the star tracker.

In Figure 5-13 it is seen that a large number of stars may be used by the star tracker. To use all of these stars during each orbit for update purposes would not only result in an unnecessary amount of computation, but would also be operationally unfeasible. Consequently, a star selection method was adopted to establish some control over the number and regularity of star updates with the star tracker. Basically, this method periodically selects that star within the FOV which is furthest separated from the previous selection.

The star tracker gimbals permit the tracker to see stars within a rectangular portion of the sky centered at zenith, which extends out to 45 degrees either side of the orbital plane and extends 15 degrees ahead and behind in the orbital plane. This 30 by 90 degree window or FOV sweeps across the celestial sphere as the spacecraft moves along its orbit.

The manner in which the star selection is made is as follows: The first star selected is the one with the smallest true anomaly in the distribution plot. It is assumed that the spacecraft has the same true anomaly at that time. Afterwards, the spacecraft and its FOV are advanced by a fixed amount in true anomaly, and that star within the FOV, which is furthest separated from the previous selection, is selected. The spacecraft is again advanced by the same fixed amount in true anomaly and a new star is selected. This procedure is repeated until the end of the selection process. It can be seen that the repeated advance by a fixed amount in true anomaly can be regarded as establishing a fixed frequency of star updates in time.

The star selection method was applied to the previous star distribution data for the star tracker with step sizes in true anomaly of 8, 20, and 40 degrees, which correspond to 2, 5, and 10 minute update intervals for a 90 minute orbit. Figure 5-14 shows the results for an 8 degree step size in the orbit at July 1, 1972. The results for all of the cases are shown in Appendix C. In Figure 5-14 the circled stars are the ones selected. The numbers adjacent to these stars indicate the order of selection. Note that the dots representing noise stars were omitted for clarity. It should also be noted that the statistical data at the right side of the figure now applies to only those stars selected.

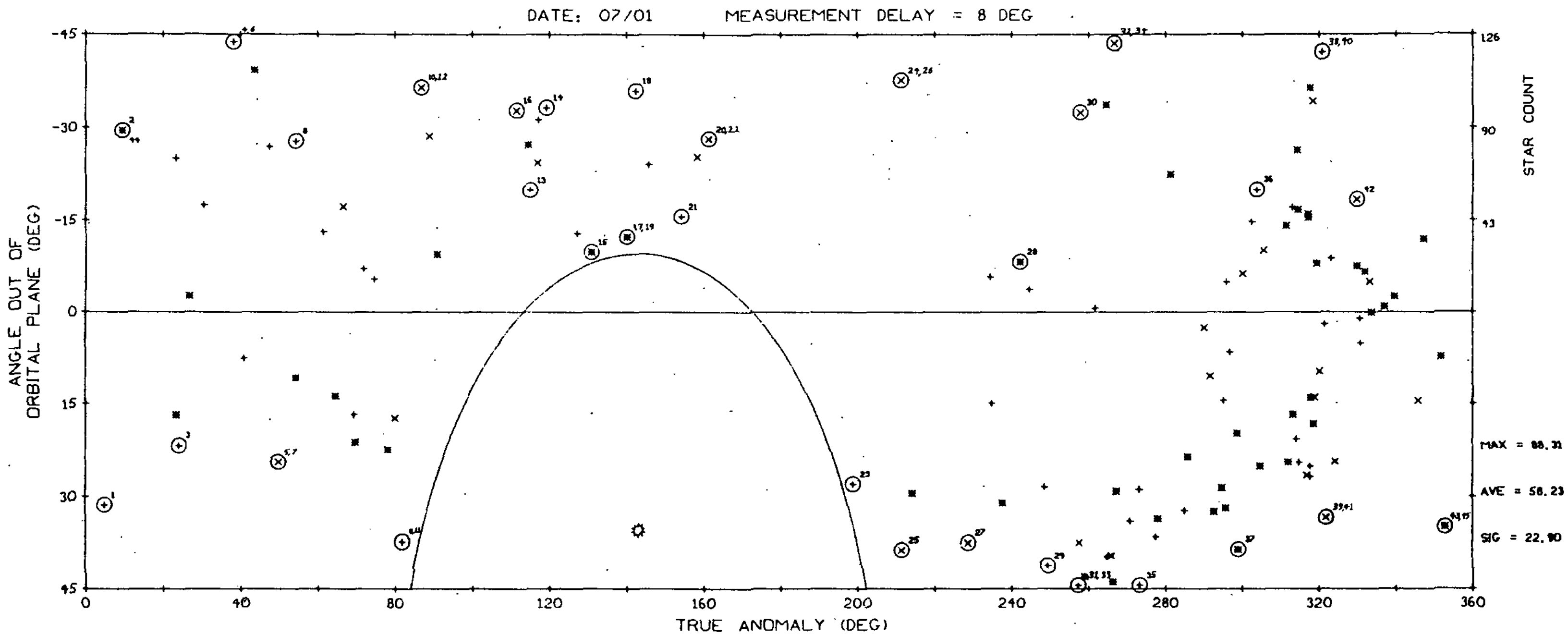

Figure 5-14 Star Distribution Plot Showing Star Selection for Star Tracker, for July 1, 1972 (8 Degree Measurement Interval)

5.4 METHOD OF DATA PROCESSING

The problem discussed in this section is that of how to obtain the best reconstruction of the time history of the spacecraft attitude given a post flight record of both inertial and stellar observations obtained during the period in which the attitude history is desired. Both the stellar and inertial measurements are corrupted by data noise, as are the estimates of spacecraft orbital position and any initial estimate of spacecraft attitude which may exist. Included in the information available for processing all these data is an estimate of the statistics of all the error sources and mathematical descriptions of the physical and measurement properties involved.

The purpose of this section is twofold: 1) to provide a short summary and comparison of the techniques available to use all these information sources to obtain the best reconstruction of the spacecraft attitude history, and 2) to document the method and specific equations used to perform the error studies on the SIMS candidates.

5.4.1 AVAILABLE DATA PROCESSING METHODS

The data processing methods which are potentially applicable to this problem fall into three broad categories: 1) filtering, which provides an estimate of the desired quantity at a given time based upon data up to and including that time 2) prediction, which provides an estimate of the desired quantity at a time which is in the future relative to the last data point available, and 3) smoothing, which provides an estimate of the desired quantity at a time which is in the past relative to the last data point available. Since the problem under consideration here is a data reduction situation, the method which should be used takes the form of a smoothing solution.

Smoothing solutions are available in three forms: 1) fixed interval smoothing, in which the data interval is fixed and an estimate of the desired quantity is obtained for all points within that interval 2) fixed point smoothing, in which the estimate of the desired quantity at a fixed point is obtained while the length of the data interval is increased, and 3) fixed lag smoothing, in which the length of the data interval increases while an estimate of the desired quantity is obtained at times which are a fixed length behind the latest data point. Since in the application under consideration here it is of interest to use all the available data to obtain estimates of the vehicle attitude at various times within the interval, the smoothing solution should be used in its fixed interval form.

Fixed interval smoothing solutions can be classified into four computational forms: 1) batch processing in which all the data is processed simultaneously to provide the least squares estimate of the quantity of interest at any time of interest within the data interval; 2) the solution to a two point boundary problem; 3) those that have a forward recursive pass over the entire data interval followed by a backwards recursive calculation to the time of interest; and 4) those that have a forward recursive pass over the data interval from the beginning up to the time of interest and a backward recursive pass over the data interval from the end back to the time of interest. When the system is linear, the noises involved are additive with Gaussian ensemble distributions and white time distributions, and the measure of optimality is either least squares or maximum likelihood, all these solutions are identical provided that the same information sources are used in each. It should be possible to linearize the system of equations for the application under consideration and place the problem in a form where all these constraints have been satisfied. This assumption has been made for the present error studies but should be verified for the actual data reduction task.

Each of these four computational forms will now be briefly discussed. This discussion will then be followed by a brief comparison of the latter two methods, which seem to be most applicable to the case under consideration.

5.4.1.1 Batch Processing

This method is the one originally devised by Gauss[123]. In fairness, we should probably admit that all the modern filtering, prediction, and smoothing schemes trace their lineage back to this solution. A discussion of batch processing may be found in Refs. 124 and 125 and will not be included here. Reference 125 provides a good summary of different ways of obtaining the solution by this method and concludes that for reasons of numerical accuracy a "square root" solution procedure is more desirable than the direct solution method. The solution of Golub[126] is especially useful for this purpose.

The batch processing mode is not recommended for this data processing application for several reasons: 1) experience at MIT/DL and elsewhere has shown that it can be cumbersome to use and program; 2) this same experience has shown that it can be subject to serious numerical errors (although these are less likely if the above mentioned square root solutions are used); and 3) it is not as easy to incorporate all the available information about the physical situation as in the modern forms.

5.4.1.2 Two Point Boundary Value Method

This method of solution is best suited for those applications where one can not obtain a set of linearized equations to describe the dynamical system or where the iterative solution* of the linearized equations does not converge well. In this application neither of these seems likely, hence this method should be considered only if one of the subsequent methods does not work. The details of this solution may be found in Ref. 127. Solution by this method can be expensive in terms of computer time due to the necessity for numerically solving the two point boundary problem. Research is necessary in most cases to find and tune the proper numerical solution procedure to the particular problem of interest.

5.4.1.3 Full Forward Sweep Smoother

Solutions of this form require sweeping recursion formulas over all the data from beginning to end, then recursively processing the result backwards to the point of interest. They are obtained from the general solution mentioned in the previous section by restricting the system to be linear (or a linearized nonlinear system). These fall into two computational forms. One has been documented by Bryson and Frazier[127] and Cox[128] while the other was published by Rauch[129] and Rauch, Tung, and Striebel[130]. Kaminski[125] develops square root forms for these and demonstrates the increased accuracy which is obtainable when the square root of the covariance matrix or information matrix is used instead of the covariance matrix or information matrix. These forms are easily programmed and can easily use all the

---

* An iterative solution is generally necessary if the partial derivatives involved in the Taylor series expansion are evaluated about the best available state estimate.

available information about the system and data. Like all smoothing schemes, they require a substantial amount of computer storage. Quantitative estimates of these requirements are provided in Section 5.4.1.5.

5.4.1.4 Two Filter Smoother

Solutions of this form make use of two "Kalman" filters[131], one of which processes the data forward from the beginning of the data interval to the point of interest, while the other works backward to this point from the end of the data. The boundary conditions on the backward filter require it to be written in information form; that is, it employs the inverse of the covariance matrix rather than the covariance matrix itself. These solutions are due to Fraser[132] and Fraser and Potter[133]. A similar form has been published by Mayne[134], except he does not identify his results as two separate filters. These forms have all the advantages of the forward sweep smoother forms plus they can be written in a form which reduces their sensitivity to numerical errors. Reference 132 contains both analytical and numerical demonstrations of the numerical superiority of these forms over the forward sweep forms. This decreased sensitivity is obtained at the expense of increased arithmetic.

As a final refinement one can square root these forms as demonstrated by Kaminski[125] and obtain still greater numerical accuracy with no additional storage or computation requirements. These square root forms work in the two filter mode except that they employ the square root of the covariance and information matrices. Kaminski also gives a way of reducing the arithmetic and increasing accuracy by replacing vector measurements with a sequence of scalar updates. This can be done even if the measurement covariance matrix is not diagonal.

5.4.1.5 Comparison of Smoothing Solutions

The following conclusions can be made for the application under consideration: 1) smoothing via the solution of the two point boundary value problem should only be used if linearization can not be made to work; 2) the recursive modern smoothing schemes described in the previous two sections are preferable to the batch processing methods; 3) the two filter smoother approach is more accurate than the forward sweep solutions; and

4) the most accurate forms are the square root recursive smoother forms.

It should be strongly emphasized that freedom from numerical errors is of paramount importance in a data reduction task of the size under consideration here due to the large amount of arithmetic necessary. Propagation of numerical errors through such a large number of arithmetic operations can easily lead to useless results. Only if adequate performance can be obtained with those solutions which are more prone to numerical errors should they be seriously considered. It would seem, however, that since the square root forms obtained by Kaminski provide square root type accuracy at little or no expense, they should be most seriously considered for the actual data reduction problem.

The remainder of this section is based upon data taken from Kaminski's Ph. D. dissertation[125] and can be used to evaluate the storage, arithmetic and time requirements for the following computational forms: 1) the Rauch forward sweep smoother; 2) the Bryson-Frazier forward sweep smoother; 3) the Fraser two filter smoother; 4) the Kaminski square root information smoother (SRIS); and 5) the Kaminski scalar SRIS. The latter two are two filter smoothers which work with the square root of the information matrix. The last uses the scalar measurement decomposition of Cholesky[135] which replaces an arbitrary vector observation with a sequence of scalar observations.

Table 5-5 compares these algorithms on the basis of storage; Table 5-6 provides the comparison on the basis of total number of arithmetic operations; and Table 5-7 shows the computation time for each on an IBM/360 Model 67-1 for a 10 dimensional state, a five dimensional driving disturbance, and a scalar measurement. All data are for a single computational cycle only. To obtain the totals for the entire data reduction task these numbers must be multiplied by $(N + 1)$ where N is the total number of data points in the interval. In computing the arithmetic operations shown in Table 5-6 the filter computations are assumed to be in square root form for the square root smoother, square root information form for the square root information smoother, and Joseph[136] form for all others. The Joseph form for the filter equations is the least sensitive to numerical problems of any filter schemes which work with the covariance matrix directly.

Table 5-5

SUMMARY OF FIXED INTERVAL SMOOTHER STORAGE REQUIREMENTS

Smoothing Algorithm	Storage Required per Stage
Rauch	$\frac{1}{2} n (n + 3)$
Bryson-Frazier	$\frac{1}{2} n (n + 3) + m$
Fraser Two-Filter	$\frac{1}{2} n (n + 3) + m$
Square Root Two-Filter	$\frac{1}{2} n (n + 3) + m$
SRIS	$\frac{1}{2} p (p + 3) + np$
Scalar SRIS	$2p + np$

n = dimension of state; m = dimension of measurement;

p = dimension of driving force

Table 5-6

APPROXIMATE NUMBER OF OPERATIONS FOR A SINGLE STAGE SMOOTHING COMPUTATION INCLUDING SINGLE STAGE FILTERING OPERATION

Smoothing Algorithm	Approximate Number of Operations	
	$P_{k/N}$ Not Computed	$P_{k/N}$ Computed
Rauch	$\frac{1}{6}[n(57n^2 + 51n + 30mn + 30m + 9pn + 12p + 18m^2) + m(6m^2 + 15m + 27)]$	$\frac{1}{6}[n(66n^2 + 54n + 30mn + 30m + 9pn + 12p + 18m^2) + m(6m^2 + 15m + 27)]$
Bryson - Frazier	$\frac{1}{6}[n(36n^2 + 46n + 32mn + 30m + 6pn + 12p + 18m^2) + m(6m^2 + 16m + 27)]$	$\frac{1}{6}[n(72n^2 + 72n + 36mn + 30m + 6pn + 12p + 18m^2) + m(6m^2 + 21m + 27)]$
Fraser Two Filter	$\frac{1}{6}[n(82n^2 + 50n + 33mn + 30m + 15pn + 12p + 18m^2) + m(6m^2 + 15m + 27)]$	$\frac{1}{6}[n(82n^2 + 60n + 33mn + 30m + 15pn + 12p + 18m^2) + m(6m^2 + 15m + 27)]$
Square Root Two Filter	$\frac{1}{6}[n(35n^2 + 16n + 25 + 42mn + 30m + 21pn + 6p) + 36m]$	$\frac{1}{6}[n(35n^2 + 30n + 25 + 42mn + 30m + 21pn + 6p) + 36m]$
Scalar SRIS	$\frac{1}{6}[n(14n^2 + 25n + 34 + 12mn + 24m + 36pn + 37p) + p(p + 18) + 6]$	$\frac{1}{6}[n(20n^2 + 42n + 34 + 12mn + 24m + 54pn + 66p) + 18p]$

$P_{k/N}$ = Smoother Covariance Matrix; n = dimension of state; m = dimension of measurement;

p = dimension of driving force

Table 5-7

COMPARISON OF NET SMOOTHING COMPUTATION TIME PER STAGE

Smoothing Algorithm	Computation Time (m sec)
Rauch	52
Bryson-Frazier	60
Fraser Two-Filter	81
Square Root Two-Filter	49
Scalar SRIS	44

n = 10, p = 5, m = 1

Examination of these tables together with the realization that the square root forms give the greatest numerical accuracy shows the reason for the above recommendation of the use of the square root forms for the actual data processing task.

5.4.2 SMOOTHER EQUATIONS USED IN ERROR STUDIES

5.4.2.1 General Comments

The Fraser two filter smoother formulation is being used in the error studies since it has been previously used at MIT/DL and provides the best tradeoff between numerical accuracy and programming time. Previous experience in software development makes it possible to generate a working program in a short period of time.

Due to the limited scope of the present effort and the relatively short time remaining to complete the study, certain steps have been taken to expedite matters. One of these is the computation of only the smoother covariance matrix of the state (but not the state itself) since this gives a statistical measure of the obtainable accuracy of a SIMS configuration. Another step taken to reduce computer computation time and storage requirements is to compute the smoother covariance matrix of state for only a few selected points in the data interval. These points will usually be chosen near the middle of the data interval where the best smoother performance is anticipated. The effect of data interval size and the number of star updates will also be investigated.

5.4.2.2 General System Equations of State and Measurement

Before presenting the equations associated with the Fraser two filter smoother formulation a brief review will be made of the general equations used to describe the state and measurements of a linear system, since these are fundamental to most methods of filtering, prediction, and smoothing. It is assumed that the reader is somewhat familiar with the standard equations presented in this section.

A linear system can be described by the following vector differential equation:

$$\dot{\underline{x}}(t) = F(t)\,\underline{x}(t) + G(t)\,\underline{u}(t) \qquad (5-26)$$

where $\underline{x}(t)$ is the state vector and $\underline{u}(t)$ is the driving force (which shall be assumed to be a random disturbance or noise). The state is propagated from one time, t_{k-1}, to the next, t_k, as follows:

$$\underline{x}(t_k) = [\Phi(t_k; t_{k-1})]\,\underline{x}(t_{k-1}) \tag{5-27}$$

where $\Phi(t_k; t_{k-1})$ is the state transition matrix which can be obtained by solving:

$$\frac{d}{dt}[\Phi(t; t_{k-1})] = F(t)[\Phi(t; t_{k-1})] \tag{5-28}$$

beginning with $\Phi(t_{k-1}, t_{k-1}) = I$.

A priori information about the initial statistics of the state estimate at t_o is given by the covariance matrix $P(t_o)$ where:

$$P(t_o) = \overline{[\hat{\underline{x}}(t_o) - \underline{x}(t_o)][\hat{\underline{x}}(t_o) - \underline{x}(t_o)]^T} \tag{5-29}$$

The covariance matrix of the state is propagated from one time, t_{k-1}, to the next, t_k, as follows:

$$P(t_k) = \Phi(t_k; t_{k-1})\, P(t_{k-1})\, \Phi^T(t_k; t_{k-1}) + V_k \tag{5-30}$$

where V_k is the expected covariance of the integrated effect of the driving noise $\underline{u}(t)$ from time t_{k-1} to time t_k, which is given by:

$$V_k = G(t_k)Q(t_k)G^T(t_k) = \int_{t_{k-1}}^{t_k} \Phi(t_k, t)\,G(t)\,Q(t)\,G^T(t)\,\Phi^T(t_k, t)\,dt$$

$$Q(t) = \overline{\underline{u}(t)\,\underline{u}^T(t)} \tag{5-31}$$

The measurements $\underline{z}(t)$ made by the system are related to the state vector $\underline{x}(t)$ by the following equation:

$$\underline{z}(t) = H(t)\,\underline{x}(t) + \underline{v}(t) \tag{5-32}$$

where $\underline{v}(t)$ is the noise in the measurements and H(t) is a geometry matrix of the partial derivatives relating perturbations in state to perturbations in measurement. A priori information about the statistics of the measurement noise is given by the covariance matrix R(t) where:

$$\overline{\underline{v}(t)\,\underline{v}^T(\tau)} = R(t)\,\delta(t-\tau) \tag{5-33}$$

5.4.2.3 Fraser Two Filter Smoother Formulation

As previously mentioned, this method consists of a forward recursive pass over the data interval from the beginning up to the time of interest and a backward recursive pass over the data interval from the end back to the time of interest. The results of these two passes at the time of interest are then combined in an optimal manner to obtain the smoothed results.

The manner in which the data is processed by this method will be presented separately for the forward filter, the backward filter, and the final smoother. As an example, let it be assumed that N discrete measurements occur in a data interval which starts at time t_o and ends at time t_N, the time of the last measurement. Also, let each measurement be denoted by a value of k (i.e., k = 1, 2, . . . , N).

5.4.2.3.1 Forward Filter

The forward filter is a standard Kalman filter which is used to process the data from t_o to some time of interest t_j using the following equations at each successive measurement time t_k:

$$P'_k = \Phi_{k,k-1}\,P_{k-1}\,\Phi^T_{k,k-1} + V_k \tag{5-34}$$

$$W_k = P'_k H^T_k (H_k P'_k H^T_k + R_k)^{-1}$$

$$P_k = (I - W_k H_k) P'_k (I - W_k H_k)^T + W_k R_k W^T_k$$

where the subscripts k and k-1 denote the times t_k and t_{k-1} of the present and previous measurements, respectively. The matrix I is the identity matrix and the remaining matrices are defined in Section 5.4.2.2. If t_j

is not a measurement time then the final value P_j is obtained using the above equation for P'_k.

The last two of Eqs. (5–34) are the Joseph form of the Kalman filter mentioned in Section 5.4.1.5. These can be reduced to forms which require less arithmetic but the results are more sensitive to numerical errors than the Joseph form.

5.4.2.3.2 Backward Filter

The backward filter is a Kalman filter in information form. The information matrix, U_k, is processed from time t_N back to the time of interest t_j. Starting at $k = N$ (N corresponds to the time of the last measurement) and the condition $U'_k = U'_N = 0$, a value of U_k is computed as follows:

$$U_k = U'_k + H_k^T R_k^{-1} H_k \tag{5-35}$$

Afterwards, the inverse of the covariance matrix at each successive earlier time of measurement, t_{k-1}, is computed as follows:

$$J_k = U_k G_k (G_k^T U_k G_k + Q_k^{-1})^{-1}$$

$$U'_{k-1} = \Phi_{k,k-1}^T [(I - J_k G_k^T) U_k (I - J_k G_k^T)^T + J_k Q_k^{-1} J_k^T] \Phi_{k,k-1} \tag{5-36}$$

$$U_{k-1} = U'_{k-1} + H_{k-1}^T R_{k-1}^{-1} H_{k-1}$$

After the last measurement has been processed with the above equations, a final value U'_j is computed at the time of interest t_j using the first two of the above equations. G_k and Q_k are defined in Sec. 5.4.3.1 for the SIMS-A and -B.

5.4.2.3.3 Smoother

The final smoothed estimate $P_{j/N}$ of the covariance matrix is obtained from the two filter estimates P_j and U'_j as follows:

$$P_{j/N} = (I - K_j U_j')P_j (I - K_j U_j')^T + K_j U_j' K_j^T \qquad (5\text{-}37)$$

where

$$K_j = P_j[(I - P_j U_j')^{-1}]^T \qquad (5\text{-}38)$$

5.4.3 LINEARIZED STATE AND MEASUREMENT EQUATIONS FOR SIMS-A AND -B

5.4.3.1 State Equation for SIMS-A and-B

The use of the Fraser two filter smoother formulation requires that the state and measurement equations be linear. Consequently, a linear set of equations must be derived for each SIMS candidate. In this report the equations being used for SIMS-A and-B will be given without showing the details of derivation. The equations associated with SIMS-D1-A will not be given at this time.

For SIMS-A and-B the state (or vehicle attitude) expressed by the angles θ, ϕ, and ψ results in a non-linear state equation. However, a linear state equation can be derived by using state vector elements which are perturbations from the non-linear values of the three attitude angles. If one also wishes to estimate gyro bias drift in the data processing then the corresponding elements required in the linearized state vector will be the perturbations in bias drift for the three gyros. The resulting linearized state vector can therefore be expressed as follows:

$$\underline{x} = \begin{bmatrix} \delta\theta \\ \delta\phi \\ \delta\psi \\ \delta B_x \\ \delta B_y \\ \delta B_z \end{bmatrix} \qquad (5\text{-}39)$$

It should be noted that the small attitude deviations with respect to nominal, which are expected in the present application, will have essentially no effect on the smoother estimates of the covariance matrix for the above state. Consequently, certain simplifications can be made in deriving the linearized state equation, such as setting the attitude angles ϕ and ψ to zero. This would probably not be advisable if other types of bias errors were to be included in the state vector since some of these do require attitude deviation from nominal in order to be reliably estimated. For example, a gyro scale factor bias error can not be distinguished from a gyro bias drift error unless there is some variation in the angular rate sensed by the gyro.

The linearized state equation derived from SIMS-A and-B is as follows:

$$\dot{\underline{x}} = \left[\begin{array}{ccc|ccc} 0 & 0 & 0 & 0 & -1 & 0 \\ 0 & 0 & -\omega_0 & 1 & 0 & 0 \\ 0 & \omega_0 & 0 & 0 & 0 & -1 \\ \hline & 0 & & & 0 & \end{array}\right] \underline{x} + \left[\begin{array}{ccc} 0 & -1 & 0 \\ 1 & 0 & 0 \\ 0 & 0 & -1 \\ \hline & 0 & \end{array}\right] \underline{u} \qquad (5\text{-}40)$$

where ω_0 is the nominal orbital rate which is assumed to be constant, $\underline{u}$ is the noise introduced by gyro random drift, etc., and the last matrix on the right is the matrix G(t) required in the smoother formulation.

The transition matrix for the case is:

$$\Phi_{k,k-1} = \left[\begin{array}{ccc|ccc} 1 & 0 & 0 & 0 & -\Delta t_k & 0 \\ 0 & c\xi & -s\xi & s\xi/\omega_0 & 0 & (1-c\xi)/\omega_0 \\ 0 & s\xi & c\xi & (1-c\xi)/\omega_0 & 0 & -s\xi/\omega_0 \\ \hline & 0 & & & I & \end{array}\right] \qquad (5\text{-}41)$$

where the subscripts k and k-1 correspond to the times t_k and t_{k-1} at which star tracker or star mapper measurements are made, $\Delta t_k = t_k - t_{k-1}$, $\xi = \omega_0 \Delta t_k$, and s and c are used to denote sine and cosine.

The matrices Q_k and G_k required in the smoother formulation are:

$$Q_k = q^2 \Delta t_k I \tag{5-42}$$

and

$$G_k = 6 \times 3 \text{ constant matrix} = \begin{bmatrix} 0 & -1 & 0 \\ 1 & 0 & 0 \\ 0 & 0 & -1 \\ \hline & 0 & \end{bmatrix} \tag{5-43}$$

where I in these equations is the 3 x 3 identity matrix. Equation (5-42) can be derived by substitution of $Q(t) = q^2 I$ and Eq. (5-41) into Eq. (5-31). q^2 represents the magnitude of the low frequency gyro drift power spectral density for each gyro. In the present case the gyro random drift rate is being treated as white noise, although there is still some consideration to using other models for gyro random drift error, which require the use of Δt_k^2 or Δt_k^3 in the matrix Q_k.

5.4.3.2 Measurement Equation for SIMS-A

The linearized measurement equation derived for the star mapper of SIMS-A is the following:

$$z_k = [H_\theta, H_\phi, H_\psi, 0, 0, 0] \underline{x}_k + v_k \tag{5-44}$$

where k denotes the star measurement at t_k, v_k is the noise in the measurement, and the matrix on the right is the matrix H_k required in the smoother formulation. The elements of the matrix H_k are scalars as follows:

$$H_\theta = \underline{n}_B^T \begin{bmatrix} -c\eta & -s\eta & 0 \\ 0 & 0 & 0 \\ s\eta & -c\eta & 0 \end{bmatrix} \underline{s}_O \tag{5-45}$$

$$H_\phi = \underline{n}_B^T \begin{bmatrix} 0 & 0 & 0 \\ -c\eta & -s\eta & 0 \\ 0 & 0 & 1 \end{bmatrix} \underline{s}_O \tag{5-46}$$

$$H_{\psi} = \underline{n}_B^T \begin{bmatrix} 0 & 0 & 1 \\ -s\eta & c\eta & 0 \\ 0 & 0 & 0 \end{bmatrix} \underline{s}_O \qquad (5\text{-}47)$$

where $\underline{n}_B$ is the unit vector normal to the slit plane in body-fixed coordinates, $\underline{s}_O$ is the unit vector to the star in orbit-oriented inertial coordinates, and $\eta = \omega_o t_k$, where t_k is the total time since $t = 0$. The time $t = 0$ corresponds to a time when the vehicle was at the ascending node of its orbit.

The covariance matrix of the measurement noise v_k is R_k, which is given as a scalar quantity for the star mapper.

5.4.3.3 Measurement Equation for SIMS-B

The linearized measurement equation derived for the star tracker of SIMS-B is the following:

$$\underline{z}_k = \left[\begin{array}{c|c|c|c|c|c} \underline{H}_\theta & \underline{H}_\phi & \underline{H}_\psi & \begin{matrix}0\\0\end{matrix} & \begin{matrix}0\\0\end{matrix} & \begin{matrix}0\\0\end{matrix} \end{array} \right] \underline{x}_k + A_k \begin{bmatrix} v_{\theta_T} \\ v_{\Phi} \\ v_{\alpha_T} \\ v_{\beta_T} \end{bmatrix} \qquad (5\text{-}48)$$

where the first matrix on the right is H_k, k denotes the star measurement at t_k, the v's are the noises associated with the star tracker measurement angles θ_T, Φ, α_T, β_T previously defined in Section 5.2.3, and A_k is a noise transformation matrix. The elements of the matrix H_k are two dimensional vectors as follows:

$$\underline{H}_\theta = \begin{bmatrix} -c\eta & -s\eta & 0 \\ 0 & 0 & 0 \end{bmatrix} \underline{s}_O \qquad (5\text{-}49)$$

$$\underline{H}_\phi = \begin{bmatrix} 0 & 0 & 1 \\ -c\eta & -s\eta & 0 \end{bmatrix} \underline{s}_O \qquad (5\text{-}50)$$

$$\underline{H}_{\psi} = \begin{bmatrix} 0 & 0 & 1 \\ -s\eta & c\eta & 0 \end{bmatrix} \underline{s}_O \qquad (5\text{-}51)$$

where $\underline{s}_O$ is the unit vector to the star in orbit-oriented inertial coordinates, and η is the angle previously defined in Section 5.4.3.2.

The noise transformation matrix A_k is:

$$A_k = \left[\begin{array}{c|c|c|c} -\beta_T s\theta_T - c\theta_T & 0 & 0 & c\theta_T \\ -s\Phi(s\theta_T - \beta_T c\theta_T) & c\Phi(c\theta_T + \beta_T s\theta_T) + \alpha_T s\Phi & -c\Phi & s\Phi s\theta_T \end{array}\right] \qquad (5\text{-}52)$$

where θ_T, Φ, α_T, and β_T are the star tracker measurement angles for the star at time t_k.

A covariance matrix R of the star tracker measurement noise can be given as:

$$R = \begin{bmatrix} \sigma_{\theta_T}^2 & 0 & 0 & 0 \\ 0 & \sigma_{\Phi}^2 & 0 & 0 \\ 0 & 0 & \sigma_{\alpha_T}^2 & 0 \\ 0 & 0 & 0 & \sigma_{\beta_T}^2 \end{bmatrix} \qquad (5\text{-}53)$$

where the principal diagonal elements are the variances of the angular measurement errors. To obtain the covariance matrix R_k, which is required in the smoother formulation, the following transformation is used:

$$R_k = A_k R A_k^T \qquad (5\text{-}54)$$

5.5 GYRO ERROR MODELS

The function defined for gyros in a stellar-inertial system depends on the point-of-view (or prejudice) of the individual doing the defining. An individual oriented towards optical sensors would consider gyros to provide continuity between star sightings by the prime sensors. On the other hand, individuals oriented towards inertial systems would adopt the point-of-view that the role of optical sensors is to compensate gyro drift. The argument is academic, of course, because the sensors provide complementary information. Relative to each other, optical sensors provide low frequency information while gyros provide high frequency information, with the "crossover" determined primarily by a combination of the high frequency noise characteristics and bandwidth of the optical sensors and the long-term drift characteristics of the gyros. Generally speaking, overall system operation is simplified directly with quality of the long-term drift characteristics of the gyros because practical constraints (e.g., stellar data requirements are relaxed. On the other hand, applications that could require very low bandwidth data, such as the fine pointing of an orbiting telescope used (for tracking stars) in an inertially non-rotating spacecraft, may not require gyro information.

The SIMS mission could require attitude information at frequencies up to 10 Hz and hence gyros are included in the prime system candidates. The star sensor determines the low end of the passband in which gyro data is required. SIMS-A and -D1-A use a star mapper so that gyro data may be required for intervals up to an hour ($\approx 3\times10^{-4}$Hz). SIMS-B uses a star tracker and hence should require information from the gyros down to frequencies of about 2×10^{-3} Hz.

The parameters used to model the gyros in steady orbital operation are drift, scale factor and input axis alignment. In turn, two components are identified with each of those parameters. The first is called "bias" and it represents the standard deviation of the constant error expected after the system enters steady-state operation in orbit and before any estimates are made; i.e., the biases represent initial conditions of the gyro parameters. The biases are due to such factors as errors in ground calibration, changes in parameters subsequent to calibration and differences between on-earth and in-orbit operation. The values used in the study are based primarily on ground data provided by the manufacturers and that obtained at MIT/CSDL. The second component characterizes the random behavior of the parameters and is based primarily on ground data obtained by MIT/CSDL.

The gyros used are as follows: the Honeywell GG334 for SIMS-A, the Nortronics GI-K7G for SIMS-B and the MIT/CSDL TGG for SIMS-D1-A.

5.5.1 DRIFT

The bias components of drift are based on the characteristics of the non-g dependent drift as published by Honeywell[137] and Nortronics[138] and as measured by MIT/CSDL on the 2FBG-6F-OAO gyro (an ancestor of the TGG[139]). It is reasonable to assume that the extent to which in-orbit data reflect these ground data will depend on how well the gyro's float is floated and temperature gradients are minimized during ground operation. The standard deviations of the expected change in drift between calibration during system acceptance tests and in-orbit operation are:

SIMS-A	(GG-334)	10 meru
SIMS-B	(GI-K7G)	10 meru
SIMS-D1-A	(TGG)	2 meru

The random drift components are expressed as angles and are based on power spectral density measurements made by MIT/CSDL for NASA/GSFC for the advanced OAO program[140]. Two points that pertain to these data are worth bringing out. First, these noise data apply to the limited passband required for the SIMS study and should not be used as a basis for comparing the long-term performance of these instruments. Second, although they represent the best data available, they are based on a first-effort and hence cannot at this time be considered a final, authoritative source on the relative performance of these gyros. Plots representing the power spectral densities measured on each of the gyros are shown in Figure 5-15. The variance of the noise is described as the sum of: 1) a function of time to represent the characteristic which dominates in the passband of interest; plus 2) a constant to represent the higher frequency torque loop and gyro noise. The values are shown in Table 5-8. These values are now being considered for the error studies.*

5.5.2 SCALE FACTOR

The methods used to measure scale factor are low frequency processes and hence the statistics of the random component of scale factor noise is usually described by the standard deviation of a time series of measurements only. Therefore, in the absence of data defining the spectral characteristics of scale factor noise and because the electronic components used in current sources are characterized by white noise, the scale factor noise is assumed to be adequately characterized

* Additional, considerably less optimistic information received from Honeywell and TRW on GG334A and GI-K7G gyro drift models too late for inclusion here, is now being evaluated.

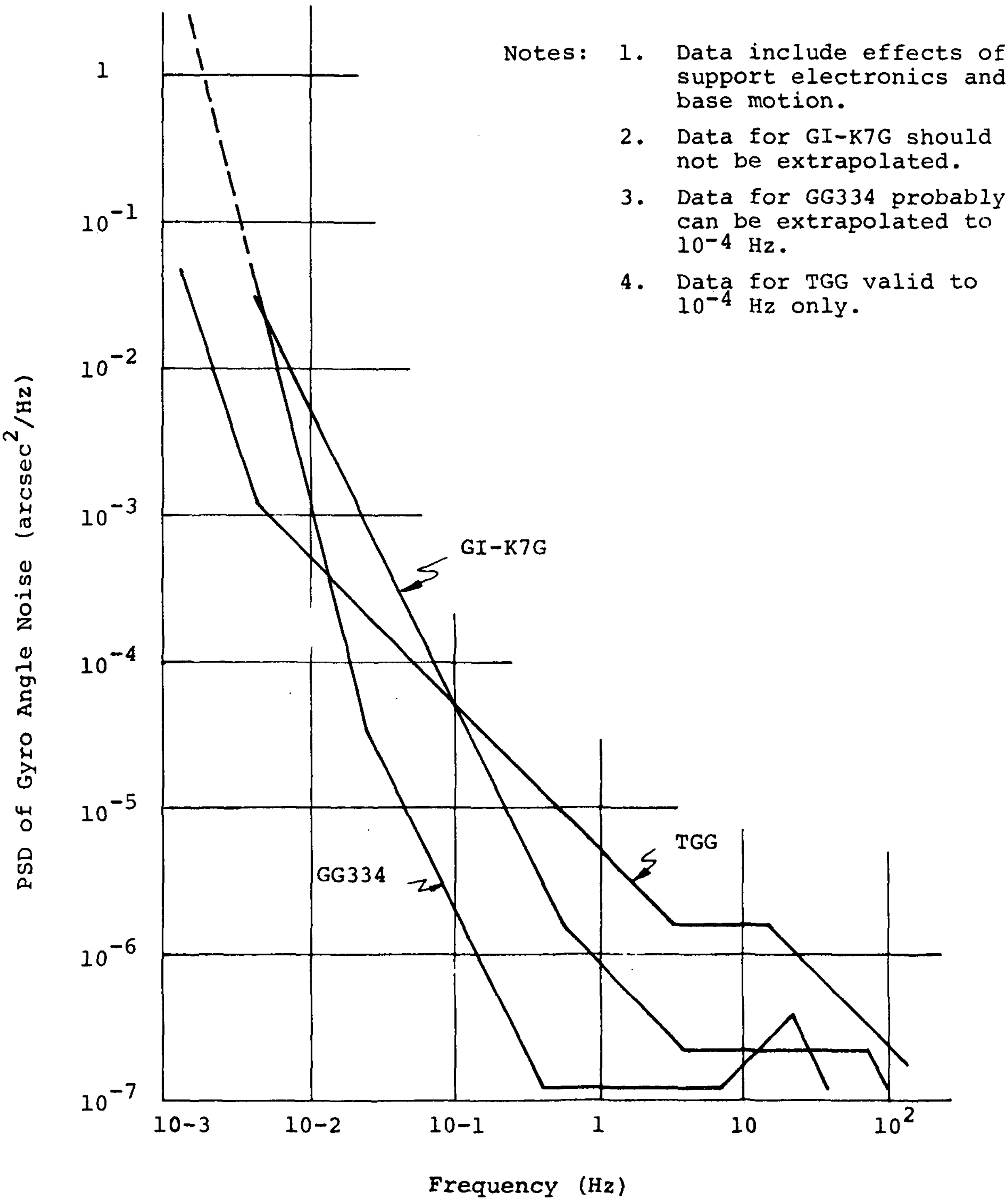

Figure 5-15 Power Spectral Density of Gyro Angle Noise

Table 5-8 Models of Gyro Random Drift

System Candidate	Gyro	Variance of Angle Noise ($arcsec^2$) (1)	Frequency Constraint
A	GG334	$6 \times 10^{-12} t^3 + 4 \times 10^{-4}$	$f > 10^{-4}$ Hz (2)
B	GI-K7G	$5 \times 10^{-7} t + 3 \times 10^{-3}$	$f > 10^{-3}$ Hz (3)
D1-A	TGG	$1 \times 10^{-10} t^2 + 10^{-4}$	$f > 10^{-4}$ Hz (4)

Notes:

(1) The unit of time (t) is seconds.

(2) The noise characteristic observed from 0.025 Hz to 0.003 Hz for the GG334 is consistent with random walk (markovian) torque processes used to describe long-term drift characteristics and therefore is extrapolated to 10^{-4} Hz with little reservation.

(3) The low frequency characteristic measured for the GI-K7G is consistent with a white torque process which is inconsistent with both the long-term drift characteristics of this gyro and "typical" long-term drift models. Therefore, these data should not be extrapolated below 10^{-3} Hz.

(4) Long-term drift tests of the TGG indicate that the noise process that dominates around frequencies of 10^{-4} Hz is significantly different from those shown in Figure 5-15. Therefore, a conservative, order-of-magnitude representation of drift data measured during long-term drift tests is used to model the TGG noise rather than extrapolation of the 10^{-3} Hz characteristic. However, even this 1/f torque model should not be used below frequencies of 10^{-4} Hz.

(5) The noise models are based on measurements that include noise due to support electronics and base motion in addition to instrument noise. The support electronics were typical of those used to test each instrument. The base motion could possibly contribute up to 50% of the noise described.

by a white process. Any significant deviations from this model probably will occur at very low frequencies so that their effects probably would be adequately included in drift compensation. This assumption is credible because the satellite maintains a constant attitide with respect to orbital rate and only low attitude control rates are encountered when precise attitude measurements are made. The values used are 10 ppm* for the standard deviation of bias and 5 ppm* for the standard deviation of the random component over a 30-day period.

5.5.3 INPUT AXIS ALIGNMENT

The stability of the angular displacement between the input axis of a gyro and an external reference frame depends on the signal generator and its readout electronics and the material and temperature stability of the gyro mounts. As with scale factor, the random characteristics of alignment are described by the standard deviation of a time series of measurements rather than spectrally. The model used here is white noise with the assumption that long-term changes will be accounted for by drift calibration. The values used are 10 arc sec for the standard deviation of the bias component and 1 arc sec for the random component.

---

* PPM is defined relative to the maximum rate capability of the gyro and torque loop, not to the measured rate.

SECTION 6

CONFIGURATION TRADES

6.1 SCOPE

Detailed information relative to the various trade criterions on the basis of which the SIMS configurations are to be evaluated has not yet been assembled to the extent necessary for presentation in a definitive manner. However, a method of assembling the information is in effect, and the format in which it will appear in the final report is evolving. Both the method and format are discussed in this section.

Also included in this section is an informal commentary on configuration trades. It is presented in the same vein as is the corresponding section (section 3) of the First Interim Report, ref. 85, and should be interpreted as a supplement to that section.

6.2 FORMAL PRESENTATION OF CONDENSED CONFIGURATION TRADE INFORMATION

The Final Report will contain the same section titles as does this report. However, Section 6 of the final report will be much broader. It will contain a condensation of all of the SIMS study results that are pertinent to comparisons between SIMS-A, -B and -D. Most of the results will be presented in charts or tables accompanied by commentary or reference to such commentary in earlier sections. Diagrams, sketches, graphs, etc. will also be employed or referred to if appropriate.

The Final Report will contain an Appendix A for which there is no counterpart in this report. That Appendix will consist of (or be derived from) worksheets covering each of the 11 trade criterions, at subsystem and/or at system level, for each of the three SIMS configurations that will be finally compared in detail, i.e., SIMS-A, -B and -D (where -D corresponds generically to SIMS-D1-A of ref. 85, but where its star mapper is yet to be specified). An example of a typical worksheet page heading is depicted below.

SYSTEM	CRITERION	SCOPE
B	Availability	Star Sensor

These worksheets will constitute the bulk of the reference material - in summary form - of Section 6. The table of contents of Appendix A of the Final Report appears below.

CONTENTS OF APPENDIX A (OF FINAL REPORT)

		SYSTEM								
	CRITERION	A			B			D		
1	COST	1	2	3	28	29	30	55	56	57
2	ACCURACY	4	5	6	31	32	33	58	59	60
3	WEIGHT	7	8	9	34	35	36	61	62	63
4	POWER	10	11	12	37	38	39	64	65	66
5	TELEMETRY REQUIREMENT	13			40			67		
6	TOTAL UNOBSTRUCTED FOV REQT.	14			41			68		
7	SIMPLICITY OF DESIGN, AND RELIABILITY	15	16	17	42	43	44	69	70	71
8	MODULARITY OF DESIGN, AND GROWTH POTENTIAL	18			45			72		
9	COST OF GSE	19	20	21	46	47	48	73	74	75
10	COMPLEXITY OF GROUND CONTROL/ COMMAND/DATA PROCESSING OPERATIONS	22	23	24	49	50	51	76	77	78
11	AVAILABILITY	25	26	27	52	53	54	79	80	81

LEGEND:

1. Numbers under system codes are Appendix reference numbers (page, para., etc.).

2. A three-compartment box under a system code signifies scope from left to right as: IARU, Star Sensor, System. In the same order the cognizant engineers are McKern, Coccoli, Ogletree, except for criterion #2 where the cognizant engineer for all compartments is White.

3. The cognizant engineer for criterions #5 and #8 is Ogletree, and for criterion #6 is Coccoli.

6.3 NEED FOR SIMS-A ERROR SIMULATION

Progress during the reporting period permits some of the consequences of gimbaling vs. structure mounting of components, as discussed in Section 3 of the First Interim Report, to be dealt with more concretely. That progress includes better knowledge of IARU and Star Sensor performance capabilities, and, because of completion of the star availability studies (see subsection 5.3), better knowledge of the performance required of the sensors. The claim of improved knowledge of performance requirements is not nearly as applicable to SIMS-A as to SIMS-B and -D, and for that reason the consequences of the aforementioned progress are discussed here only in relation to SIMS-B and -D. However, before proceeding with that discussion, the reason for omitting SIMS-A is clarified.

Knowing star availability for a star mapper does not of itself enable one to predict performance of SIMS-A. Dynamic simulations to determine error propagation in time are necessary because of the following considerations:

1) there are numerous sources of IARU error rate uncertainty in addition to gyro drift rate;

2) many IARU error rate bias terms must be estimated in addition to gyro drift rate;

3) stellar data is not acquired on command but rather when a star happens in the FOV of the star mapper;

4) the acquisition rate for useful stellar data is low both because of the small FOV and because the time between starlines of suitable angular separation is determined by orbital rate.

The problems of non-isotropic error sensitivity in the star mapper, the need to correct for spacecraft motion between star transits, and the potential corruption of data by background stars, while not as important as the items listed, further compound the difficulty of predicting performance without dynamic error simulations. Those simulations should eventually include gyro-output quantization so that the quantization level necessary to control non-commutativity errors is determined and the resulting hardware implications can be evaluated.

Even when SIMS-A simulations are completed there will remain some doubt as to the validity of the error models for scale-factor uncertainty and input axis alignment uncertainty. The efforts directed toward modeling those error sources do not appear to have reached the level of sophistication applied to gyro drift. Yet it is becoming apparent that gyro drift is of lesser importance.

Most of the material in this subsection is covered in greater detail in Section 3 of the First Interim Report. It is reiterated here merely to justify postponing comparisons of SIMS-A with SIMS-B and -D until error simulations indicate the kind of performance that can be expected of SIMS-A, or, alternatively, what kind of sensor performance would be required for SIMS-A to qualify.

6.4 SIMS-B vs. SIMS-D

SIMS-B also employs structure-mounted gyros, but its star tracker covers such a wide field ($30^{\circ} \times 90^{\circ}$) that a full (3-axis) IARU update is possible whenever a suitable pair of stars appears in the FOV. Since the star availability studies show that a suitable pair is present most of the time, the performance of the IARU is not nearly as critical a determinant of system performance as in SIMS-A. In fact, it is reasonable to state at this time that if the performance claimed for the SIMS-B tracker is valid, SIMS-B can meet the SIMS accuracy requirement.

SIMS-D also can meet that requirement. The supporting argument parallels that for SIMS-B, though with the complementary subsystem roles interchanged; that is, the superior IARU performance achievable with gimbaled gyros nullifies the effects of star mapper weaknesses. Just a few stars of suitable angular displacement per orbital revolution will suffice; and the star availability studies show that a good deal more than a few will be encountered in any orbit.

Assuming that the SIMS-B and -D subsystem error budgets are realizable (see sections 3 and 4), the foregoing remarks indicate that the choice between the two systems will be made on the basis of other criterions than accuracy. While it is not yet possible (for reasons given in Section 6.1) to compare SIMS-B and -D with regard to all criterions, four criterions for which the contrast is sharp are taken up below.

Total Unobstructed FOV Requirement

The SIMS-B FOV is almost two orders of magnitude greater than that of SIMS-D.

Simplicity of Design and Reliability

A number of reliability considerations, all of them favorable to SIMS-D, can be identified.

1) SIMS-D does not require a computer. SIMS-B requires a computer for directing the star tracker optical axis to the star-search sectors. Moreover, if the attitude algorithm computation is done on board the spacecraft, the necessary computation capacity will have to be included. There is a reliability penalty associated with the algorithm computation regardless of whether it is done on board the spacecraft or at a ground-based computer. This point is covered more fully in Section 3 of the First Interim Report.

2) The SIMS-D gimbals operate in a sealed, pressurized environment. The SIMS-B gimbals operate in the high vacuum of space thereby incurring special problems for rubbing parts and for heat transfer.

3) Since the basic reference in a SIMS is the star sensor it is desirable that that subsystem be as simple and reliable as possible. The star mapper for SIMS-D fulfills that objective much better than does the SIMS-B tracker. There will be orbits that provide enough stellar data to calibrate the SIMS-D IARU alignment and readout against long-

term changes, or shifts that occur during launch. Though an in-flight alignment and readout calibration procedure for the SIMS-B tracker can probably be devised it may not be as straightforward as for SIMS-D gimbals.

Modularity of Design, and Growth Potential

A number of systems employing the SIMS IARU data together with landmark data from the Thematic Mapper are discussed in Appendix B of the First Interim Report. Assessing the feasibility of those systems depends very much on the quality of the IARU assumed. For example, in one so-called landmark-inertial system the SIMS star sensor is omitted and the IARU is retained. Landmarks (together with the ephemeris data) then provide the data previously provided by the stars. Clearly, the fewer landmarks required the greater the assurance of feasibility. Therefore, the growth potential for a SIMS-D in relation to systems employing landmark data for attitude determination, orbit estimation, or both is greater than for a SIMS-B.

In the "NASA GSFC Phase A Final Report - EOS System Definition Studies" (Section 7.7.2) (ref. 89) it is stated that "a natural evolution of a precision attitude determination system (SIMS) would be a precision attitude control system to orient a high resolution sensor or sensors in real time". An accuracy goal of 0.01 degree is defined. For SIMS-B to provide real-time attitude indication the requirement for on-board attitude algorithm computation becomes essential, and, unless the IARU performance exceeds current expectations, stellar update of the IARU would also have to be computed on board. Yet a computer could still be unnecessary for SIMS-D. The additional hardware would depend on specific design requirements but would probably consist largely of three clocked registers whose contents are differenced with the IARU pitch, roll and yaw output registers. While differencing is a computation, the necessary hardware hardly qualifies as a computer.

Availability

The star tracker, which is the key subsystem of SIMS-B, has passed through the engineering prototype development phase. The IARU, which is the key subsystem for SIMS-D is merely in the conceptual design stage.

APPENDIX A

AN ADAPTIVE PULSE-TORQUING LOOP*

A.1 APPLICATION

The ideal strapdown implementation application occurs when no external environment is present. This application in practice, of course, would not use inertial technology. It is in this environment where the theoretical errors associated with gimbaled and strapdown implementation are similar and involve only time-dependent instrument errors. The ability of the strapdown implementation to compete in a specific application is based largely upon the understanding of the application and the design of the strapdown mechanization to handle the additional known error sources. It should be pointed out, however, if the additional error sources are understood and their errors minimized, strapdown offers many advantages in areas of simplicity, modularity and redundancy. We will now examine an application of precision attitude determination of a satellite in near-circular earth orbit where absolute attitude is periodically provided in three dimensions by use of a star tracker or mapper. The strapdown system mechanization is to provide incremental real-time attitude profiles where the gyroscope and its associated torque-to-balance loop will sense very small variations about a large, fixed (nominal) value of angular velocity.

---

*This torquer loop mechanization was conceived by R. McKern and H. Musoff of the MIT/DL staff and is believed to be a new and unique development for strapdown system mechanization. Its development during this study effort was motivated by a suggestion by Mr. Seymour Kant, NASA/GSFC, on 11 November 1971, that the deterministic nature of orbital rate should permit significant reduction of pitch axis scale factor error.

A.2 LIMITATIONS OF PRESENT PULSED TORQUING LOOPS

Present pulse torquing loop designs based upon digital timing to form the precisely-controlled current square waves into a gyroscope torque generator are limited in stability by factors that include:

a) instability of the current driver (PVR) (stability about 10 ppm/thousand hrs;)

b) changes in switching leakage currents;

c) pulse width instability and instability with high interrogation rates;

d) instability due to the torque transient during switching; and

e) heating effects during switching.

A.3 OPERATING PRINCIPLE OF ADAPTIVE LOOP

The block diagram shown in Figure A-1 illustrates the overall loop being proposed. There are two torquer currents during any one selected mode of torque loop operation. One is a large direct current (i.e., D.C. bias) that is selected from a number of fixed values and is used to cancel out the large nominal value of angular velocity due to the orbital input. The other is a sequence of small amplitude binary or ternary current pulses which account for the small angular velocity variations about the nominal value.

The selection of the direct current value is made as a function of measured plus or minus $\Delta\theta$ pulses generated by the fine resolution pulse torque loop. Discrete scaling changes of the D.C. bias are requested by $\Delta\theta$ accumulation

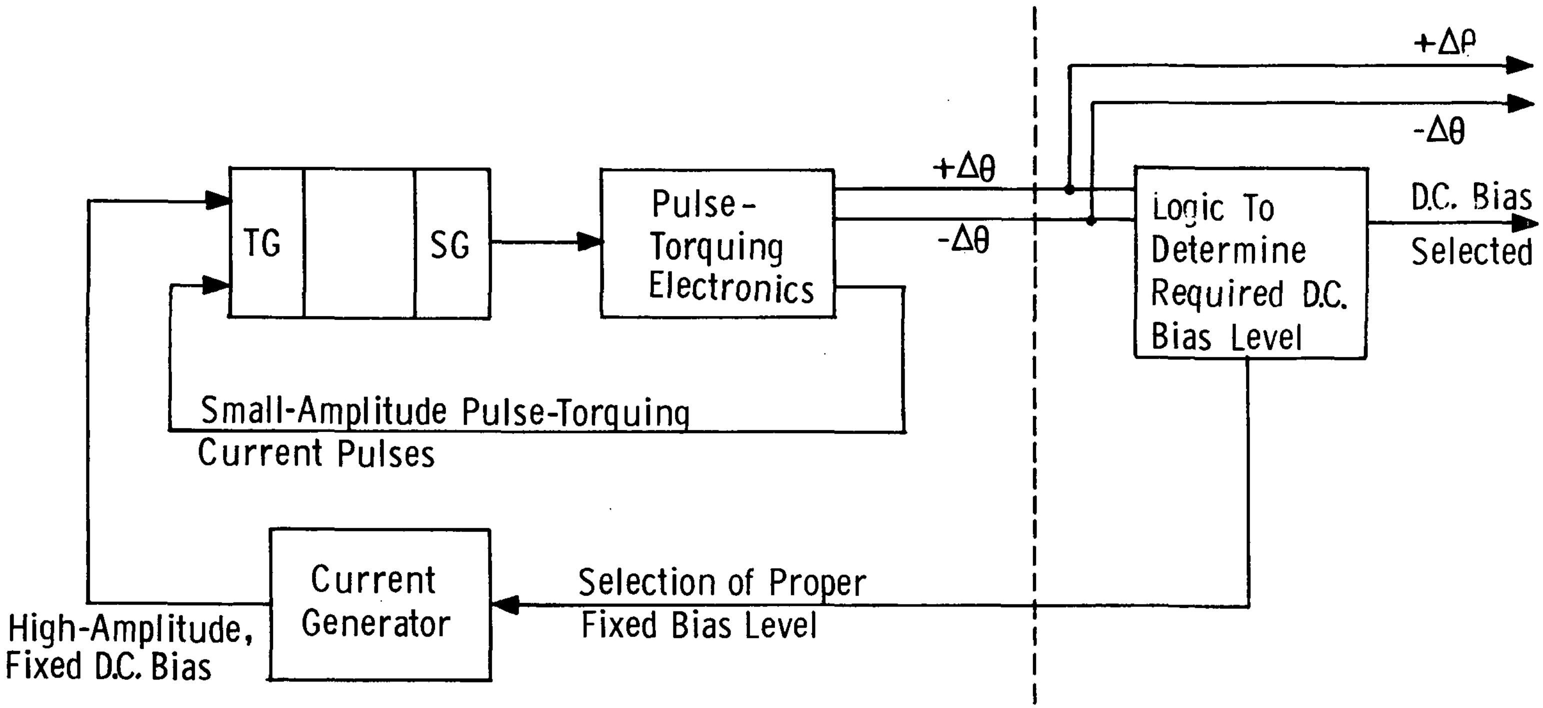

Figure A-1 Block Diagram of Adaptive Pulse-Torquing Loop logic circuitry just before the fine loop reaches saturation in either positive or negative directions.

A.4 ADVANTAGES OF THE ADAPTIVE LOOP

The main advantage of this loop in a constant input rate environment would be to maintain the best possible scale factor accuracy without jeopardizing fine attitude resolution. This is done by the adaptive loop with the following advantages:

a) Large transient effects are avoided;

b) Critical timing requirements are eliminated;

c) Possible large heating changes are eliminated;

d) D.C. biases can be maintained to at least 10 ppm/thousand hours; and

e) D.C. bias levels can be calibrated in earth orbit along with the non-g sensitive drift of the gyroscope, using the absolute attitude provided by the optics.

A.5 EXAMPLES OF POSSIBLE CIRCUIT IMPLEMENTATIONS

If separate torquer coils are available to implement both the D.C. bias and pulse-torquing loops, the overall implementation could be as shown in Figure A-2. Also, an alternative method could be implemented using several PVR levels.

If only a single torquer were used, the adaptive loop implementation might be as shown in Figure A-3.

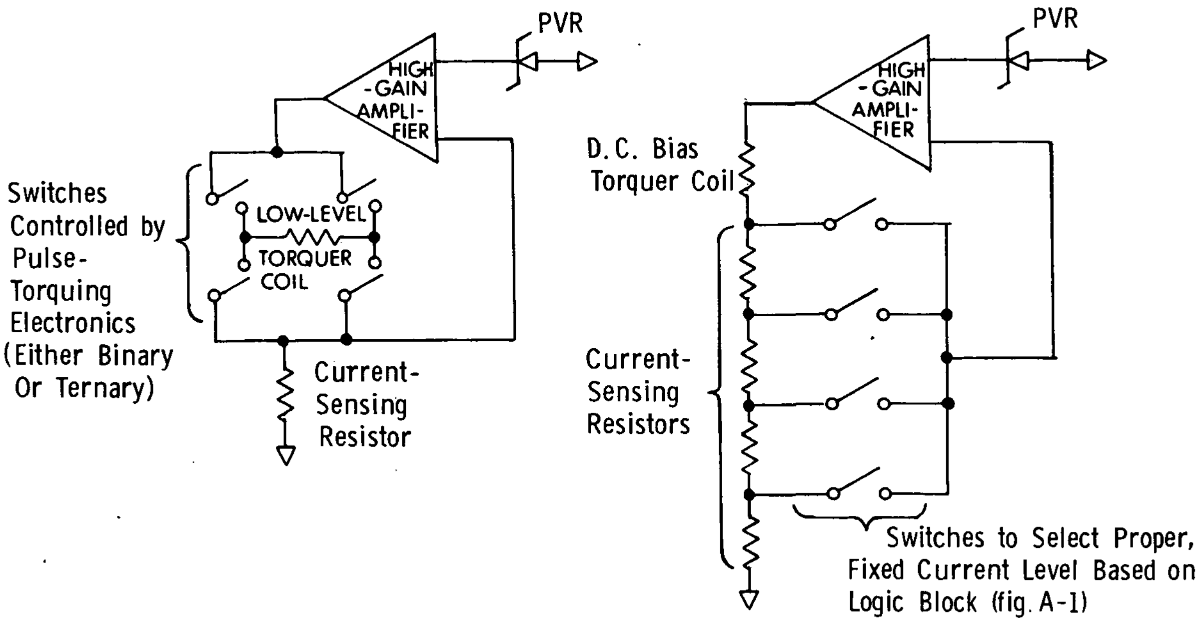

Figure A-2 Possible Adaptive Loop Mechanization (Dual-Torquer)

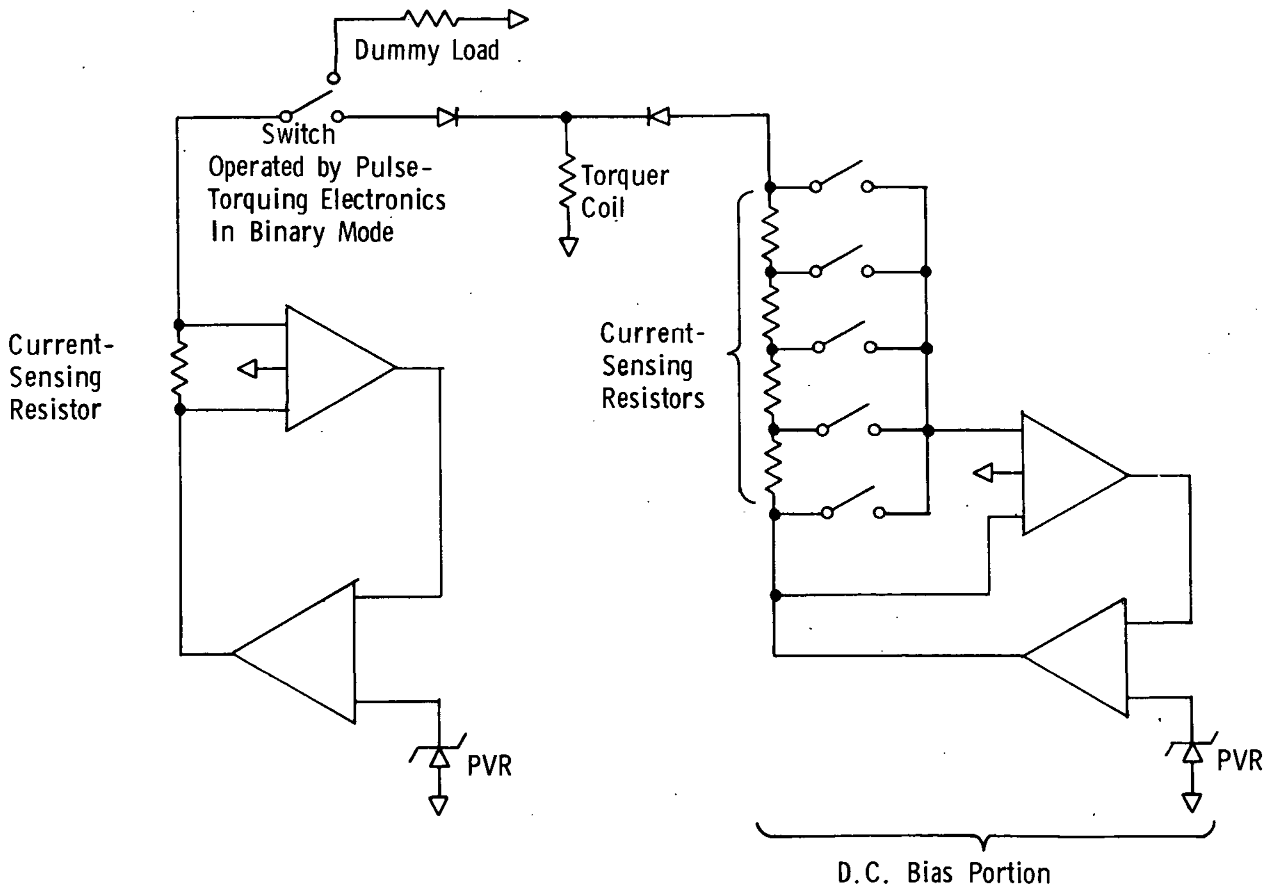

Figure A-3 Possible Adaptive Loop Mechanization (Single-Torquer)

APPENDIX B

CATALOG OF STARS OF MAGNITUDE 4.0 OR BRIGHTER AS SEEN BY ONE OR MORE DETECTORS

COLUMN HEADING	DESCRIPTION
YBS#	The Yale Bright Star Catalog number. A "D" following the number indicates that the star is a component of a double and satisfies the double-star criterion.
NAME	Generally the Bayer or Flamsteed designation taken from the Yale Bright Star Catalog. A numeral following a Greek letter is a superscript.
RA	The right ascension for 1975, interpolated linearly from the values given for the years 1900 and 2000 in the Y.B.S. Catalog.
DEC	The declination for 1975, interpolated as above.
S20	The S-20 detector magnitude
CDS	The cadmium sulfide detector magnitude.
SIL	The silicon detector magnitude
S	Source. If S=0, detector magnitudes are computed from the color index versus spectral type function =1, det. mags. are computed from UBVRIJKL photometry 2, det mags. are computed from 13-color photometry
VIS	Visual magnitude
SP.TYPE	Spectral type, taken from the Y.B.S. catalog

YBS#	NAME		RA	DEC	S20	CDS	SIL	S	VIS	SP.TYPE	
15D	ALF	AND	0.12	28.95	1.80	1.87	2.07	2	2.07	B8	III
21D	BET	CAS	0.13	59.01	2.54	2.53	2.08	2	2.27	F2	IV
25	EPS	PHE	0.14	-45.89	4.69	4.64	3.38	2	3.88	K0	III
39	GAM	PEG	0.20	15.05	2.27	2.40	2.85	2	2.83	B2	IV
45	CHI	PEG	0.22	20.06	5.76	5.78	3.49	2	4.81	M2	III
46D			0.22	- 7.92	5.94	6.05	3.29	0	5.13	M3	III
48	7	CET	0.22	-19.07	5.46	5.50	3.16	2	4.49	M1	III
74	IOT	CET	0.30	- 8.97	4.46	4.41	2.93	2	3.56	K2	III
77	ZET	TUC	0.31	-65.03	4.64	4.65	3.89	2	4.23	G2	V
85	T	CET	0.34	-20.20	5.62	5.81	2.66	0	5.00	M5	II
98	BET	HYI	0.41	-77.39	3.27	3.26	2.48	2	2.80	G2	IV
100	KAP	PHE	0.42	-43.82	4.12	4.11	3.88	2	3.94	A7	V
103	47	PSC	0.45	17.75	5.51	5.62	2.86	0	4.70	M3	III
105	ETA	SCL	0.44	-33.15	5.75	5.81	3.22	2	4.81	M4	III
130	KAP	CAS	0.53	62.80	3.95	4.06	4.07	2	4.17	B1	I
153	ZET	CAS	0.59	53.76	3.20	3.32	3.73	2	3.71	B2	V
163	EPS	AND	0.62	29.18	5.01	4.98	3.86	2	4.35	G8	III
165D	DEL	AND	0.63	30.73	4.24	4.20	2.59	2	3.30	K3	III
168D	ALF	CAS	0.65	56.40	3.13	3.08	1.67	2	2.24	K0	II
188	BET	CET	0.71	-18.12	2.90	2.85	1.56	2	2.09	K1	III
211	57	PSC	0.75	15.35	6.09	6.23	3.28	0	5.36	M4	
215D	ZET	AND	0.77	24.13	4.97	4.94	3.50	2	4.14	K1	II
219D	ETA	CAS	0.79	57.68	3.82	3.82	3.10	2	3.44	G0	V
224	DEL	PSC	0.79	7.45	5.44	5.44	3.48	2	4.47	K5	III
248	20	CET	0.86	- 1.27	5.75	5.76	3.71	2	4.77	M0	III
257			0.88	-63.00	6.26	6.45	3.30	0	5.64	M5	
259			0.90	24.43	6.53	6.81	3.29	0	6.19	M7	
264D	GAM	CAS	0.92	60.58	1.72	1.88	2.15	2	2.27	B0	IV
269D	MU	AND	0.92	38.36	4.01	3.99	3.83	2	3.88	A5	V
271	ETA	AND	0.93	23.28	5.12	5.08	3.92	2	4.40	G8	III
280	ALF	SCL	0.96	-29.50	3.99	4.05	4.27	1	4.27	B8	III
285			1.09	86.12	5.16	5.10	3.60	2	4.24	K2	III
294	EPS	PSC	1.03	7.75	5.02	4.98	3.74	2	4.28	K0	III
334	ETA	CET	1.12	-10.32	4.34	4.29	2.85	2	3.46	K3	III
337D	BET	AND	1.14	35.48	3.07	3.09	0.91	2	2.10	M0	III
338D	ZET	PHE	1.12	-55.38	3.72	3.78	3.93	0	3.94	B6	V
352	TAU	PSC	1.17	29.97	5.35	5.30	3.95	2	4.51	K0	III
377D	KAP	TUC	1.25	-69.00	4.65	4.64	4.00	0	4.25	F6	V
402D	THE	CET	1.38	- 8.31	4.47	4.42	3.10	2	3.65	K0	III
403	DEL	CAS	1.40	60.10	2.79	2.77	2.59	2	2.65	A5	V
424D	ALF	UMI	2.23	89.13	2.45	2.42	1.67	2	1.96	F8	I
429	GAM	PHE	1.45	-43.45	4.42	4.43	2.37	2	3.41	K5	II
434	MU	PSC	1.48	6.02	5.81	5.79	4.00	2	4.86	K4	III
437D	ETA	PSC	1.50	15.22	4.37	4.33	3.14	2	3.62	G8	III
440	DEL	PHE	1.50	-49.21	4.71	4.67	3.44	2	3.95	K0	III
458	UPS	AND	1.59	41.27	4.45	4.45	3.80	2	4.08	F8	V
464	51	AND	1.61	48.49	4.52	4.48	2.89	2	3.59	K3	III
472	ALF	ERI	1.61	-57.37	0.12	0.21	0.51	2	0.48	B5	IV
489	NU	PSC	1.67	5.36	5.41	5.38	3.64	2	4.46	K3	III
496	PHI	PER	1.70	50.56	3.65	3.79	3.95	2	4.09	B1	III

YBS#	NAME		RA	DEC	S20	CDS	SIL	S	VIS	SP.TYPE	
509	TAU	CET	1.72	-16.07	4.06	4.05	3.12	2	3.53	G8	V
510	OMI	PSC	1.73	9.02	5.01	4.96	3.77	2	4.26	G8	III
519			1.75	-50.94	6.29	6.40	3.64	0	5.48	M3	III
539	ZET	CET	1.84	-10.46	4.57	4.52	3.14	2	3.71	K2	III
542	EPS	CAS	1.88	63.56	3.02	3.10	3.38	2	3.37	B3	IV
544	ALF	TRI	1.86	29.46	3.76	3.76	3.16	2	3.41	F6	IV
551			1.89	40.56	5.19	5.15	3.68	0	4.32	K2	
553	BET	ARI	1.89	20.68	2.80	2.79	2.63	2	2.67	A5	V
555	PSI	PHE	1.88	-46.44	5.29	5.37	2.66	2	4.41	M4	III
566D	CHI	ERI	1.92	-51.72	4.35	4.33	3.24	2	3.69	G5	IV
580	50	CAS	2.02	72.30	3.97	3.97	3.94	2	3.95	A1	V
583	57	CET	1.98	-20.95	6.33	6.38	3.98	0	5.41	M1	
585	UPS	CET	1.98	-21.20	5.00	5.01	2.90	2	4.01	M1	III
587			1.99	- 8.64	6.12	6.31	3.16	0	5.50	M5	
591	ALF	HYI	1.97	-61.69	3.15	3.14	2.76	2	2.87	F0	V
602	CHI	PHE	2.01	-44.84	6.09	6.12	3.88	0	5.14	K5	
617	ALF	ARI	2.10	23.33	2.89	2.84	1.40	2	2.03	K2	III
622	BET	TRI	2.13	34.87	3.17	3.16	2.96	2	3.03	A5	III
631	15	ARI	2.15	19.38	6.57	6.68	3.92	0	5.76	M3	
649	XI1	CET	2.19	8.73	5.06	5.03	3.91	2	4.37	G8	II
674D	PHI	ERI	2.26	-51.63	3.36	3.41	3.60	2	3.57	B8	V
681D	OMI	CET	2.30	- 3.10	3.75	3.98	0.48	2	3.21	M6	
689	69	CET	2.34	0.27	6.14	6.22	3.65	0	5.27	M2	
699	65	AND	2.40	50.17	5.74	5.74	3.74	2	4.75	K4	III
721	KAP	ERI	2.43	-47.81	3.98	4.05	4.23	0	4.24	B5	III
750	15	TRI	2.57	34.57	6.26	6.37	3.61	0	5.45	M3	
758	R	TRI	2.59	34.16	6.03	6.17	3.22	0	5.30	M4	
779	DEL	CET	2.64	0.22	3.53	3.66	4.12	2	4.10	B2	IV
794	IOT	ERI	2.66	-39.96	4.89	4.85	3.56	2	4.11	K0	III
799D	THE	PER	2.71	49.11	4.45	4.46	3.86	2	4.12	F7	V
804D	GAM	CET	2.70	3.13	3.56	3.56	3.43	2	3.48	A2	V
811	PI	CET	2.72	-13.97	3.99	4.06	4.27	2	4.25	B7	V
824	39	ARI	2.77	29.15	5.38	5.33	3.94	2	4.52	K1	III
834D	ETA	PER	2.81	55.80	4.84	4.85	2.82	2	3.82	K3	I
838D	41	ARI	2.81	27.16	3.43	3.48	3.65	2	3.63	B8	V
841	BET	FOR	2.80	-32.52	5.23	5.19	3.96	2	4.46	G6	III
843	17	PER	2.83	34.96	5.55	5.56	3.46	2	4.58	K5	III
854D	TAU	PER	2.87	52.66	4.55	4.51	3.53	2	3.95	G5	III
867	45	ARI	2.91	18.23	6.43	6.66	3.32	0	5.94	M6	III
868	R	HOR	2.88	-50.00	4.34	4.62	1.10	0	4.00	M7	
874	ETA	ERI	2.92	- 9.00	4.72	4.68	3.32	2	3.89	K1	III
911	ALF	CET	3.02	4.00	3.52	3.55	1.23	2	2.56	M2	III
915D	GAM	PER	3.05	53.40	3.49	3.46	2.51	2	2.92	G8	III
921	RHO	PER	3.06	38.74	4.28	4.38	1.46	2	3.45	M4	II
935D			3.09	- 6.20	6.07	6.18	3.42	0	5.26	M3	
936D	BET	PER	3.11	40.85	1.97	2.02	2.10	2	2.15	B8	V
937	IOT	PER	3.12	49.52	4.46	4.46	3.72	2	4.03	G0	V
941D	KAP	PER	3.13	44.77	4.57	4.52	3.30	2	3.80	K0	III
951	DEL	ARI	3.17	19.64	5.16	5.11	3.83	2	4.35	K2	III
963D	ALF	FOR	3.18	-29.08	4.17	4.18	3.58	2	3.85	F8	IV

YBS#	NAME	RA	DEC	S20	CDS	SIL	S	VIS	SP.TYPE
999		3.31	28.96	5.49	5.50	3.50	2	4.49	K4 III
1003D	TAU4 ERI	3.31	-21.84	4.59	4.65	2.03	2	3.70	M3
1004		3.31	-24.21	6.47	6.55	3.98	0	5.60	M2
1008		3.32	-43.16	4.81	4.79	3.90	2	4.27	G5 V
1009		3.37	64.50	6.18	6.21	3.97	0	5.23	M0 II
1017	ALF PER	3.38	49.76	2.23	2.20	1.53	2	1.80	F5 I
1030	OMI TAU	3.39	8.95	4.31	4.27	3.16	2	3.61	G8 III
1035D		3.45	59.86	4.50	4.54	3.99	2	4.28	B9 I
1038	XI TAU	3.43	9.65	3.59	3.64	3.75	2	3.76	B8
1052	SIG PER	3.48	47.91	5.33	5.30	3.57	2	4.37	K3 III
1066	5 TAU	3.49	12.86	4.99	4.94	3.59	2	4.13	K0 II
1084	EPS ERI	3.53	- 9.55	4.39	4.35	3.21	2	3.71	K2 V
1087	PSI PER	3.58	48.12	3.95	4.03	4.18	2	4.24	B5
1122	DEL PER	3.69	47.70	2.74	2.82	3.05	2	3.04	B5 III
1131D	OMI PER	3.71	32.20	3.57	3.67	3.77	2	3.84	B1 III
1135D	NU PER	3.72	42.50	4.13	4.11	3.53	2	3.77	F5 II
1136	DEL ERI	3.70	- 9.85	4.23	4.19	3.06	2	3.53	K0 IV
1142	17 TAU	3.72	24.04	3.48	3.54	3.71	2	3.72	B6 III
1143D		3.70	-37.40	5.47	5.43	3.96	2	4.59	K2
1149	20 TAU	3.74	24.29	3.67	3.73	3.85	2	3.88	B7 III
1155		3.79	65.45	5.44	5.54	2.75	2	4.48	M1 III
1156	23 TAU	3.75	23.87	3.98	4.04	4.14	2	4.18	B6 IV
1162	PI ERI	3.75	-12.18	5.44	5.46	3.23	2	4.47	M2
1165D	ETA TAU	3.77	24.04	2.66	2.72	2.86	2	2.88	B7 III
1175	BET RET	3.73	-64.88	4.72	4.68	3.24	2	3.85	K0 IV
1178D	27 TAU	3.79	23.97	3.43	3.49	3.62	2	3.64	B8 III
1195		3.81	-36.27	4.89	4.85	3.72	2	4.17	G5 III
1203D	ZET PER	3.88	31.81	2.66	2.77	2.77	2	2.88	B1 I
1208	GAM HYI	3.79	-74.32	4.22	4.25	2.00	2	3.25	M0 III
1220D	EPS PER	3.94	39.93	2.32	2.47	2.90	2	2.90	B0.5 V
1228	XI PER	3.96	35.71	3.66	3.79	3.94	2	4.03	O7
1231D	GAM ERI	3.95	-13.59	3.94	3.95	1.81	2	2.96	M0 III
1239	LAM TAU	3.99	12.41	3.10	3.18	3.43	2	3.44	B3 V
1247	DEL RET	3.97	-61.47	5.53	5.56	3.34	2	4.55	M2 III
1251	NU TAU	4.03	5.93	3.89	3.89	3.86	2	3.87	A1 V
1256	37 TAU	4.05	22.02	5.20	5.15	3.81	2	4.36	K0 III
1264	GAM RET	4.01	-62.22	5.40	5.48	2.76	2	4.50	M5
1273	48 PER	4.11	47.65	3.83	3.91	4.02	2	4.07	B3 V
1298	OMI1 ERI	4.18	- 6.90	4.34	4.32	3.90	2	4.06	F2 III
1303D	MU PER	4.22	48.34	4.89	4.86	3.63	2	4.16	G0 I
1325D	OMI2 ERI	4.24	- 7.70	5.03	5.01	3.96	2	4.41	K1 V
1326	ALF HOR	4.22	-42.35	4.70	4.66	3.32	2	3.86	K1 III
1336D	ALF RET	4.23	-62.53	4.08	4.03	2.93	2	3.35	G6 II
1345		4.29	-20.78	6.73	6.87	3.92	0	6.00	M4
1346	GAM TAU	4.31	15.56	4.40	4.35	3.14	2	3.63	K0 III
1355D	EPS RET	4.27	-59.37	5.31	5.27	3.80	0	4.44	K2 IV
1373	DEL TAU	4.36	17.47	4.53	4.48	3.27	2	3.76	K0 III
1393	43 ERI	4.38	-34.07	4.94	4.93	3.05	2	3.96	M1 III
1409	EPS TAU	4.45	19.13	4.34	4.28	3.04	2	3.53	K0 III
1411	THE1 TAU	4.45	15.90	4.61	4.56	3.37	2	3.85	K0 III

YBS#	NAME		RA	DEC	S20	CDS	SIL	S	VIS	SP.TYPE	
1412	THE2	TAU	4.45	15.81	3.58	3.57	3.33	2	3.43	A7	III
1451	47	ERI	4.55	- 8.27	5.91	6.02	3.26	0	5.10	M3	
1453	UPS1	ERI	4.54	-29.82	5.18	5.15	3.97	1	4.50	G6	III
1454	58	PER	4.58	41.22	5.09	5.07	3.53	2	4.22	G5	I
1457D	ALF	TAU	4.57	16.45	1.89	1.90	-0.19	2	0.92	K5	III
1463	NU	ERI	4.58	- 3.40	3.40	3.53	3.96	2	3.94	B2	III
1464	UPS2	ERI	4.58	-30.62	4.56	4.52	3.36	2	3.82	K0	III
1465D	ALF	DOR	4.56	-55.10	3.06	3.11	3.28	2	3.27	A0	
1481D	53	ERI	4.62	-14.35	4.68	4.63	3.26	2	3.85	K2	III
1492D	R	DOR	4.61	-62.12	4.48	5.05	-0.09	2	4.50	M7	
1497	TAU	TAU	4.68	22.92	3.96	4.04	4.30	2	4.29	B3	V
1520	MU	ERI	4.74	- 3.30	3.66	3.75	4.03	2	4.02	B5	IV
1527			4.83	63.46	6.48	6.56	3.99	0	5.61	M2	
1542	ALF	CAM	4.86	66.29	3.94	4.07	4.21	2	4.31	09.5	I
1543	PI3	ORI	4.81	6.91	3.49	3.49	2.95	2	3.18	F6	V
1552	PI4	ORI	4.83	5.56	3.20	3.32	3.69	2	3.69	B2	III
1556	OMI1	ORI	4.85	14.21	5.53	5.64	2.88	0	4.72	M3	
1562	5	ORI	4.87	2.47	6.24	6.29	3.89	0	5.32	M1	
1567	PI5	ORI	4.88	2.41	3.24	3.36	3.75	2	3.74	B2	III
1577	IOT	AUR	4.92	33.11	3.72	3.71	1.85	2	2.72	K3	II
1580D	OMI2	ORI	4.92	13.46	4.99	4.95	3.48	2	4.12	K2	III
1601	PI6	ORI	4.95	1.68	5.46	5.43	3.72	2	4.48	K2	II
1603D	BET	CAM	5.02	60.41	4.74	4.70	3.59	2	4.03	G0	I
1605D	EPS	AUR	5.00	43.80	3.42	3.40	2.64	2	2.99	A8	I
1612	ZET	AUR	4.99	41.02	4.54	4.57	2.81	2	3.77	K5	II
1641	ETA	AUR	5.08	41.20	2.76	2.86	3.19	2	3.17	B3	V
1652D	GAM	CAE	5.06	-35.52	5.43	5.39	3.91	2	4.55	K3	
1654	EPS	LEP	5.07	-22.40	4.16	4.14	2.34	2	3.19	K5	III
1663	ETA2	PIC	5.07	-49.62	5.87	5.95	3.38	0	5.00	M2	III
1666	BET	ERI	5.11	- 5.12	2.90	2.89	2.72	1	2.79	A3	III
1679	LAM	ERI	5.13	- 8.78	3.73	3.86	4.28	2	4.27	B2	IV
1693			5.17	-11.88	6.17	6.40	3.06	0	5.68	M6	
1695			5.12	-63.43	5.83	5.97	3.02	0	5.10	M4	
1698D	RHO	ORI	5.20	2.84	5.34	5.29	3.83	2	4.45	K3	III
1702	MU	LEP	5.20	-16.23	3.04	3.10	3.29	2	3.28	B9	III
1707D	R	AUR	5.25	53.55	6.84	7.12	3.60	0	6.50	M7	
1708D	ALF	AUR	5.25	45.97	0.67	0.63	-0.36	2	0.04	G8	III
1713D	BET	ORI	5.22	- 8.23	-0.14	-0.04	0.11	2	0.16	B8	I
1722			5.27	42.77	6.36	6.50	3.55	0	5.63	M4	
1726D	16	AUR	5.28	33.34	5.34	5.32	3.78	1	4.54	K3	III
1735D	TAU	ORI	5.27	- 6.87	3.31	3.37	3.60	2	3.59	B5	III
1756	LAM	LEP	5.31	-13.21	3.63	3.78	4.32	2	4.30	B0.5	IV
1784	29	ORI	5.38	- 7.82	4.86	4.82	3.62	2	4.13	G8	III
1790	GAM	ORI	5.40	6.33	1.06	1.19	1.66	2	1.64	B2	III
1791	BET	TAU	5.41	28.58	1.38	1.45	1.69	2	1.68	B7	III
1829D	BET	LEP	5.45	-20.77	3.43	3.39	2.39	2	2.80	G5	III
1834D	31	ORI	5.47	- 1.10	5.63	5.59	3.99	0	4.70	K4	III
1845	119	TAU	5.51	18.57	5.36	5.50	2.62	2	4.41	M2	I
1852D	DEL	ORI	5.51	- 0.32	1.57	1.72	2.24	2	2.23	09.5	II
1855	UPS	ORI	5.51	- 7.33	3.93	4.09	4.64	2	4.62	B0	V

YBS#	NAME		RA	DEC	S20	CDS	SIL	S	VIS	SP.TYPE	
1862	EPS	COL	5.51	-35.50	4.74	4.69	3.32	2	3.87	K1	
1865D	ALF	LEP	5.53	-17.85	2.80	2.77	2.44	2	2.57	F0	I
1876	PHI1	ORI	5.56	9.47	3.86	4.01	4.40	2	4.40	B0	IV
1879D	LAM	ORI	5.56	9.92	2.79	2.94	3.38	2	3.40	O8	
1899D	IOT	ORI	5.57	- 5.93	2.12	2.28	2.81	2	2.80	O9	III
1903	EPS	ORI	5.58	- 1.22	1.12	1.27	1.71	2	1.72	B0	I
1907	PHI2	ORI	5.59	9.27	4.81	4.78	3.56	2	4.09	G8	III
1910	ZET	TAU	5.60	21.13	2.51	2.62	2.98	2	2.98	B2	IV
1922	BET	DOR	5.56	-62.50	3.84	3.83	3.10	0	3.40	F8	I
1931D	SIG	ORI	5.62	- 2.61	3.13	3.28	3.75	2	3.76	O9.5	V
1948D	ZET	ORI	5.66	- 1.96	1.13	1.29	1.76	2	1.77	O9.5	I
1956D	ALF	COL	5.65	-34.10	2.38	2.45	2.64	2	2.64	B8	V
1964			5.59	-73.75	6.51	6.65	3.70	0	5.78	M4	
1983D	GAM	LEP	5.72	-22.46	3.94	3.94	3.35	2	3.60	F6	V
1998	ZET	LEP	5.76	-14.84	3.63	3.63	3.50	1	3.56	A3	V
2004	KAP	ORI	5.78	- 9.67	1.54	1.68	2.06	2	2.08	B0.5	I
2011	UPS	AUR	5.82	37.31	5.77	5.80	3.56	2	4.80	M1	
2012D	NU	AUR	5.83	39.14	4.85	4.80	3.42	2	4.00	K0	III
2020	BET	PIC	5.78	-51.07	4.01	4.01	3.78	2	3.85	A3	V
2035	DEL	LEP	5.84	-20.87	4.50	4.46	3.21	2	3.75	G8	III
2040	BET	COL	5.83	-35.77	3.99	3.94	2.56	2	3.12	K2	III
2042	GAM	PIC	5.82	-56.16	5.34	5.30	3.89	0	4.50	K1	III
2061D	ALF	ORI	5.90	7.40	1.36	1.45	-1.19	2	0.39	M2	I
2063	U	ORI	5.91	20.15	5.57	5.90	2.21	0	5.40	M8	
2077	DEL	AUR	5.96	54.28	4.51	4.46	3.23	2	3.72	K0	III
2085	ETA	LEP	5.92	-14.17	3.97	3.97	3.59	2	3.74	F0	V
2088D	BET	AUR	5.96	44.95	1.97	1.96	1.91	2	1.92	A2	V
2091	PI	AUR	5.97	45.95	5.28	5.38	2.59	2	4.39	M3	II
2095D	THE	AUR	5.97	37.20	2.51	2.53	2.61	1	2.62	B9.5	V
2102			5.90	-63.09	5.54	5.50	3.97	0	4.64	K3	
2113			5.98	- 3.08	5.43	5.39	3.83	2	4.54	K2	III
2120	ETA	COL	5.97	-42.82	4.84	4.80	3.41	2	3.96	K0	III
2156	S	LEP	6.08	-24.20	6.49	6.72	3.38	0	6.00	M6	
2168	19	LEP	6.11	-19.16	6.18	6.26	3.69	0	5.31	M2	
2215	1	LYN	6.26	61.52	5.71	5.82	3.06	0	4.90	M3	
2216D	ETA	GEM	6.22	22.51	4.16	4.21	1.69	2	3.25	M3	III
2219	KAP	AUR	6.23	29.51	5.09	5.05	3.76	2	4.31	G8	III
2227D	GAM	MON	6.23	- 6.27	4.92	4.88	3.25	2	3.98	K3	III
2245	ETA2	DOR	6.19	-65.58	5.82	5.93	3.17	0	5.01	M3	
2256	KAP	COL	6.26	-35.12	5.10	5.07	3.81	0	4.36	G8	III
2273	7	MON	6.31	- 7.82	3.88	3.98	4.24	0	4.25	B2	V
2275			6.31	- 2.94	5.81	5.86	3.46	0	4.89	M1	
2282	ZET	CMA	6.32	-30.05	2.57	2.68	3.06	2	3.02	B2.5	V
2286D	MU	GEM	6.36	22.53	3.89	3.95	1.35	2	2.98	M3	III
2289	PSI1	AUR	6.38	49.30	5.95	5.98	3.74	0	5.00	M0	I
2294	BET	CMA	6.36	-17.94	1.38	1.52	2.01	2	2.00	B1	II
2296	DEL	COL	6.35	-33.42	4.36	4.34	3.45	0	3.84	G4	
2326	ALF	CAR	6.39	-52.67	-0.53	-0.55	-0.83	2	-0.73	F0	I
2343D	NU	GEM	6.46	20.23	3.89	3.96	4.18	2	4.17	B7	IV
2387D	XI1	CMA	6.51	-23.40	3.82	3.94	4.36	1	4.35	B0.5	IV

YBS#	NAME		RA	DEC	S20	CDS	SIL	S	VIS	SP.TYPE	
2421	GAM	GEM	6.60	16.42	1.98	1.97	1.94	2	1.95	A0	IV
2429	NU2	CMA	6.59	-19.23	4.79	4.74	3.44	2	3.97	K1	IV
2443	NU3	CMA	6.61	-18.21	5.31	5.26	3.86	2	4.45	K1	II
2450			6.64	-14.11	5.85	5.83	4.00	2	4.85	K3	III
2451	NU	PUP	6.62	-43.16	2.94	3.00	3.17	2	3.17	B8	III
2469			6.68	- 9.14	6.13	6.16	3.92	0	5.18	M0	
2473D	EPS	GEM	6.71	25.16	4.02	3.98	2.36	2	3.04	G8	I
2478D	30	GEM	6.71	13.26	5.40	5.36	3.89	2	4.52	K1	III
2484	XI	GEM	6.73	12.92	3.74	3.74	3.20	2	3.43	F5	IV
2491D	ALF	CMA	6.73	-16.68	-1.44	-1.43	-1.41	2	-1.42	A1	V
2506	18	MON	6.78	2.43	5.34	5.28	3.92	2	4.48	K0	III
2508			6.77	- 8.97	5.98	6.03	3.63	0	5.06	M1	II
2527			6.94	77.00	5.54	5.51	3.77	2	4.59	K4	III
2538	KAP	CMA	6.81	-32.49	3.59	3.69	3.95	0	3.96	B2	V
2540D	THE	GEM	6.85	34.00	3.76	3.75	3.58	2	3.64	A3	III
2550	ALF	PIC	6.80	-61.91	3.47	3.47	3.15	2	3.26	A5	V
2553	TAU	PUP	6.82	-50.59	3.73	3.69	2.33	0	2.92	K0	III
2554			6.82	-53.59	4.97	4.95	3.94	0	4.39	G3	
2574	THE	CMA	6.88	-12.02	5.06	5.04	3.21	2	4.10	K4	III
2580	OMI1	CMA	6.88	-24.17	4.85	4.85	2.97	1	3.92	K3	I
2608			6.93	-48.68	5.75	5.86	3.10	0	4.94	M1	
2609			7.48	87.06	5.94	6.02	3.45	0	5.07	M2	
2618D	EPS	CMA	6.96	-28.93	0.87	1.02	1.50	2	1.50	B2	II
2639			7.01	- 5.70	6.07	6.15	3.58	0	5.20	M2	
2646D	SIG	CMA	7.01	-27.90	4.31	4.33	2.24	1	3.43	M0	I
2650D	ZET	GEM	7.04	20.60	4.36	4.33	3.40	2	3.76	F7	I
2652			7.00	-51.38	5.72	5.77	3.37	0	4.80	M1	
2653	OMI2	CMA	7.03	-23.80	2.54	2.66	2.97	2	3.01	B3	I
2657	GAM	CMA	7.04	-15.60	3.84	3.91	4.12	2	4.12	B8	II
2693	DEL	CMA	7.12	-26.36	2.39	2.35	1.55	2	1.84	F8	I
2697D	TAU	GEM	7.16	30.29	5.33	5.28	3.73	2	4.40	K2	III
2703			7.19	51.47	6.33	6.44	3.68	0	5.52	M3	
2717	51	GEM	7.20	16.21	5.73	5.87	2.92	0	5.00	M4	III
2742			7.43	82.45	5.63	5.77	2.82	0	4.90	M4	
2747			7.24	8.04	6.53	6.67	3.72	0	5.80	M4	
2748D			7.21	-44.61	5.71	5.90	2.75	0	5.09	M5	
2749	OMG	CMA	7.23	-26.72	3.48	3.56	3.78	1	3.82	B3	IV
2763D	LAM	GEM	7.28	16.58	3.69	3.67	3.54	2	3.58	A3	V
2764D			7.26	-23.27	5.67	5.68	3.65	1	4.78	M0	
2766			7.26	-27.84	5.40	5.45	3.13	1	4.60	M3	
2773	PI	PUP	7.27	-37.05	3.67	3.69	1.66	2	2.70	K5	III
2777D	DEL	GEM	7.31	22.03	3.77	3.76	3.34	1	3.53	F0	IV
2795D	56	GEM	7.34	20.50	6.05	6.08	3.84	0	5.10	M0	
2802			7.33	-25.84	6.60	6.74	3.79	0	5.87	M4	
2803	DEL	VOL	7.28	-67.90	4.41	4.40	3.67	0	3.97	F8	II
2821	IOT	GEM	7.40	27.85	4.59	4.54	3.28	2	3.81	K0	III
2827	ETA	CMA	7.38	-29.25	2.14	2.22	2.36	1	2.41	B5	I
2845	BET	CMI	7.43	8.33	2.71	2.74	2.89	2	2.89	B7	V
2854D	GAM	CMI	7.45	8.98	5.28	5.27	3.43	2	4.32	K3	III
2864	6	CMI	7.47	12.07	5.49	5.44	3.88	2	4.55	K2	III

YBS#	NAME		RA	DEC	S20	CDS	SIL	S	VIS	SP.TYPE	
2878D	SIG	PUP	7.47	-43.25	4.18	4.15	2.47	0	3.23	K5	III
2902			7.54	-14.46	5.86	5.94	3.37	0	4.99	M2	I
2905	UPS	GEM	7.57	26.95	5.06	5.06	3.00	2	4.08	M0	III
2938	74	GEM	7.63	17.72	6.00	6.03	3.79	0	5.05	M0	
2943D	ALF	CMI	7.63	5.30	0.66	0.65	0.14	2	0.35	F5	IV
2970	ALF	MON	7.67	- 9.49	4.75	4.70	3.44	2	3.95	K0	III
2973	SIG	GEM	7.70	28.95	5.02	4.99	3.62	1	4.28	K1	III
2985D	KAP	GEM	7.72	24.46	4.32	4.28	3.13	2	3.60	G8	III
2990D	BET	GEM	7.73	28.08	1.92	1.87	0.62	2	1.14	K0	III
2993D	1	PUP	7.71	-28.34	5.45	5.46	3.43	1	4.58	K5	
2996	3	PUP	7.71	-28.89	4.07	4.07	3.79	1	3.95	A3	II
2999			7.75	37.58	5.99	6.10	3.34	0	5.18	M3	
3003	81	GEM	7.74	18.56	5.87	5.86	3.94	2	4.92	K5	III
3013D	PI	GEM	7.77	33.48	6.09	6.12	3.88	0	5.14	M0	
3017			7.74	-37.92	4.41	4.37	3.01	0	3.60	K	
3024D	ZET	VOL	7.70	-72.54	4.75	4.71	3.35	0	3.94	K0	III
3045D	XI	PUP	7.80	-24.80	4.16	4.13	2.72	1	3.35	G3	I
3055D			7.81	-46.30	3.68	3.80	4.08	0	4.10	B0.5	III
3080			7.86	-40.52	4.43	4.40	3.15	1	3.73	G5	III
3090			7.88	-48.05	3.83	3.94	4.21	0	4.23	B1	I
3102	11	PUP	7.93	-22.82	4.72	4.70	3.82	1	4.20	F8	II
3117	CHI	CAR	7.94	-52.92	3.09	3.19	3.45	0	3.46	B2	IV
3129D	V	PUP	7.96	-49.17	3.93	4.03	4.29	0	4.30	B2	
3141	28	MON	8.00	- 1.33	5.69	5.67	3.77	2	4.71	K4	III
3145			8.02	2.42	5.32	5.28	3.68	2	4.41	K2	III
3153			7.99	-60.53	6.11	6.14	3.90	0	5.16	M0	II
3165	ZET	PUP	8.05	-39.93	1.65	1.78	2.22	1	2.25	O5	
3170			8.05	-32.61	5.92	5.97	3.57	0	5.00	M1	
3185D	RHO	PUP	8.11	-24.23	3.15	3.14	2.62	1	2.82	F6	II
3187			8.10	-45.18	5.99	6.02	3.78	0	5.04	M0	
3188D	ZET	MON	8.12	- 2.91	5.10	5.06	3.88	2	4.35	G2	I
3206D			8.15	-47.27	3.90	4.00	4.23	0	4.24	B3	
3225			8.17	-39.54	5.25	5.21	3.85	0	4.44	K	
3243D			8.22	-40.27	5.30	5.26	3.79	0	4.43	K0	
3248	R	CNC	8.25	11.81	6.34	6.62	3.10	0	6.00	M7	
3249D	BET	CNC	8.25	9.27	4.55	4.53	2.66	2	3.56	K4	III
3275	31	LYN	8.35	43.28	5.27	5.27	3.28	2	4.28	K5	III
3282			8.34	-32.97	5.77	5.80	3.56	0	4.82	K1	III
3307	EPS	CAR	8.37	-59.42	2.69	2.65	1.29	0	1.88	K0	II
3314			8.41	- 3.83	3.89	3.90	3.91	2	3.91	A0	V
3318	ALF	CHA	8.32	-76.84	4.46	4.45	3.81	0	4.06	F6	IV
3319	27	CNC	8.42	12.73	6.31	6.42	3.66	0	5.50	M3	
3323D	OMI	UMA	8.47	60.80	4.04	4.01	2.95	2	3.39	G5	III
3340D	THE	CHA	8.36	-77.40	5.15	5.11	3.75	0	4.34	K0	III
3347	BET	VOL	8.42	-66.05	4.63	4.59	3.12	0	3.76	K2	III
3403	PI2	UMA	8.63	64.42	5.51	5.46	3.99	2	4.63	K2	III
3418	SIG	HYA	8.62	3.44	5.36	5.30	3.82	2	4.44	K2	III
3438D	BET	PYX	8.65	-35.21	4.62	4.60	3.49	0	3.98	G4	III
3445D			8.66	-46.56	4.14	4.12	3.65	0	3.82	F2	I
3447	OMI	VEL	8.66	-52.83	3.28	3.38	3.61	0	3.62	B3	III

YBS#	NAME		RA	DEC	S20	CDS	SIL	S	VIS	SP.TYPE	
3454	ETA	HYA	8.70	3.47	3.85	3.96	4.33	2	4.31	B3	V
3457D			8.67	-59.66	3.92	4.03	4.30	0	4.32	B1	III
3461D	DEL	CNC	8.72	18.24	4.80	4.75	3.40	2	3.97	K0	III
3468	ALF	PYX	8.71	-33.11	3.33	3.43	3.69	0	3.70	B2	III
3475D	IOT	CNC	8.75	28.86	4.73	4.69	3.51	1	4.02	G8	II
3477D			8.73	-42.56	4.70	4.68	3.57	0	4.06	G5	
3484D	12	HYA	8.75	-13.46	5.02	4.98	3.86	2	4.32	G8	III
3485D	DEL	VEL	8.73	-54.62	1.90	1.92	1.90	0	1.94	A0	V
3487			8.75	-45.96	3.86	3.88	3.86	0	3.90	A0	III
3518	GAM	PYX	8.82	-27.61	4.81	4.78	3.27	1	4.00	K4	III
3547	ZET	HYA	8.90	6.05	3.92	3.87	2.64	2	3.14	K0	II
3569D	IOT	UMA	8.96	48.13	3.34	3.33	3.07	2	3.17	A7	V
3571D			8.91	-60.55	3.71	3.75	3.82	0	3.84	B8	II
3576	RHO	UMA	9.00	67.73	5.74	5.76	3.41	2	4.80	M3	III
3614			9.05	-47.00	4.61	4.57	3.10	0	3.74	K2	III
3615	ALF	VOL	9.03	-66.30	4.15	4.14	3.91	0	4.00	A5	V
3628D	KAP	PYX	9.12	-25.75	5.43	5.44	3.49	1	4.56	M0	
3634D	LAM	VEL	9.12	-43.33	3.15	3.12	1.44	0	2.20	K5	I
3639	RS	CNC	9.15	31.08	6.34	6.57	3.23	0	5.85	M6	
3659	A	CAR	9.17	-58.86	3.07	3.17	3.43	0	3.44	B2	IV
3663			9.18	-62.21	3.64	3.74	3.97	0	3.98	B3	IV
3665D	THE	HYA	9.22	2.42	3.83	3.85	3.93	2	3.92	B9.5	V
3685	BET	CAR	9.22	-69.61	1.69	1.70	1.63	0	1.68	A1	IV
3690D	38	LYN	9.29	36.92	3.91	3.90	3.80	2	3.84	A3	V
3696			9.26	-57.43	5.28	5.25	3.57	0	4.33	K5	
3698			9.33	56.82	6.50	6.64	3.69	0	5.77	M4	
3699	IOT	CAR	9.27	-59.16	2.53	2.51	2.11	0	2.25	F0	I
3705	ALF	LYN	9.33	34.50	4.14	4.15	2.10	2	3.16	M0	III
3718	THE	PYX	9.34	-25.86	5.56	5.59	3.43	1	4.72	M1	III
3726			9.35	-42.09	6.38	6.49	3.73	0	5.57	M3	I
3731D	KAP	LEO	9.39	26.29	5.34	5.30	3.75	2	4.45	K2	III
3734	KAP	VEL	9.36	-54.91	2.12	2.22	2.48	0	2.49	B2	IV
3748	ALF	HYA	9.44	- 8.56	3.00	2.97	1.20	2	2.02	K4	III
3751			9.56	81.43	5.28	5.26	3.45	2	4.29	K3	III
3757D	23	UMA	9.49	63.17	3.92	3.91	3.47	2	3.66	F0	IV
3765	EPS	ANT	9.47	-35.84	5.45	5.48	3.24	0	4.50	K4	III
3769	8	LMI	9.50	35.21	6.29	6.34	3.94	0	5.37	M1	
3773	LAM	LEO	9.50	23.09	5.33	5.33	3.30	2	4.35	K5	III
3775D	THE	UMA	9.52	51.80	3.52	3.52	2.93	2	3.19	F6	IV
3803	N	VEL	9.51	-56.92	4.07	4.04	2.36	0	3.12	K5	III
3816D	R	CAR	9.53	-62.69	4.62	4.81	1.66	0	4.00	M5	
3820			9.59	31.28	6.43	6.51	3.94	0	5.56	M2	
3825			9.56	-59.12	3.81	3.88	4.06	0	4.07	B5	II
3834			9.62	4.76	5.63	5.60	3.91	2	4.69	K3	III
3845	IOT	HYA	9.64	- 1.02	4.85	4.81	3.17	2	3.91	K3	III
3852D	OMI	LEO	9.66	10.01	3.94	3.92	3.32	2	3.54	A2	
3866	PSI	LEO	9.71	14.15	6.28	6.36	3.79	0	5.41	M2	
3870			9.75	57.23	6.01	6.12	3.36	0	5.20	M3	
3873	EPS	LEO	9.74	23.88	3.62	3.58	2.59	2	2.99	G0	II
3882	R	LEO	9.77	11.55	4.57	4.90	1.21	0	4.40	M8	

YBS#	NAME		RA	DEC	S20	CDS	SIL	S	VIS	SP.TYPE	
3884	L	CAR	9.74	-62.40	3.95	3.93	2.98	0	3.40	G2	
3888D	UPS	UMA	9.82	59.17	4.00	3.99	3.61	2	3.77	F2	IV
3890D	UPS	CAR	9.77	-64.95	3.41	3.39	3.02	0	3.15	A9	II
3903	UPS1	HYA	9.84	-14.73	4.85	4.80	3.66	2	4.12	G8	III
3905	MU	LEO	9.86	26.13	4.82	4.77	3.26	2	3.91	K2	III
3923			9.89	-18.88	5.86	5.91	3.51	0	4.94	M1	III
3940D	PHI	VEL	9.93	-54.46	3.28	3.35	3.53	0	3.54	B5	II
3950	PI	LEO	9.98	8.15	5.69	5.72	3.43	2	4.72	M2	III
3975	ETA	LEO	10.10	16.89	3.41	3.45	3.48	2	3.53	A0	I
3980D	31	LEO	10.11	10.12	5.35	5.33	3.48	2	4.37	K4	III
3982D	ALF	LEO	10.12	12.09	1.17	1.22	1.41	2	1.40	B7	V
3994D	LAM	HYA	10.16	-12.24	4.40	4.35	3.11	2	3.60	K0	III
4023			10.23	-42.01	3.89	3.89	3.78	0	3.84	A2	V
4031	ZET	LEO	10.26	23.54	3.72	3.70	3.26	2	3.44	F0	III
4033	LAM	UMA	10.26	43.04	3.48	3.47	3.42	2	3.44	A2	IV
4037	OMG	CAR	10.22	-69.91	3.14	3.19	3.29	0	3.31	B7	IV
4045			10.26	-51.07	6.91	7.10	3.95	0	6.29	M5	
4050			10.27	-61.21	4.33	4.30	2.62	0	3.38	K5	I
4063			10.31	-54.91	5.37	5.33	3.97	0	4.56	K	
4069	MU	UMA	10.35	41.62	4.06	4.07	1.96	2	3.09	M0	III
4088	44	LEO	10.40	8.91	6.42	6.53	3.77	0	5.61	M3	
4094	MU	HYA	10.41	-16.72	4.79	4.78	2.87	2	3.81	K4	III
4100D	BET	LMI	10.44	36.83	4.89	4.85	3.71	2	4.17	G8	III
4102			10.40	-73.90	4.32	4.30	3.79	0	3.98	F3	IV
4104	ALF	ANT	10.43	-30.95	5.19	5.22	2.98	0	4.24	M0	III
4114			10.45	-58.62	4.09	4.07	3.67	0	3.81	F0	II
4127	46	LEO	10.51	14.26	6.41	6.49	3.92	0	5.54	M2	
4133	RHO	LEO	10.52	9.43	3.30	3.44	3.82	2	3.83	B1	I
4140			10.52	-61.55	3.05	3.12	3.30	0	3.31	B5	V
4159			10.58	-57.42	5.34	5.30	3.77	0	4.44	K3	
4162			10.60	-27.29	5.75	5.83	3.26	0	4.88	M2	
4163	U	HYA	10.61	-13.25	5.98	6.17	3.38	2	4.99	C73	
4174	GAM	CHA	10.59	-78.47	5.09	5.12	2.88	0	4.14	M0	III
4180D			10.64	-55.47	4.81	4.79	3.84	0	4.26	G2	II
4184			10.68	31.83	6.78	6.97	3.82	0	6.16	M5	
4199	THE	CAR	10.70	-64.25	2.32	2.44	2.72	0	2.76	O9.5	V
4200			10.71	-60.44	5.37	5.33	3.97	0	4.56	K	
4216D	MU	VEL	10.76	-49.30	3.32	3.30	2.19	0	2.68	G5	III
4232	NU	HYA	10.81	-16.05	4.03	3.99	2.46	2	3.13	K3	III
4247	46	LMI	10.87	34.35	4.61	4.57	3.26	2	3.81	K0	III
4257			10.87	-58.72	4.59	4.55	3.19	0	3.78	K0	III
4267	56	LEO	10.91	6.32	6.43	6.62	3.47	0	5.81	M5	III
4287	ALF	CRT	10.98	-18.17	4.92	4.87	3.53	2	4.09	K0	III
4295	BET	UMA	11.01	56.52	2.36	2.36	2.37	2	2.37	A1	V
4299	61	LEO	11.01	- 2.35	5.75	5.76	3.61	2	4.76	K5	III
4301D	ALF	UMA	11.04	61.88	2.63	2.58	1.25	2	1.81	K0	II
4333			11.13	36.44	6.51	6.64	3.78	0	5.74	M3.5	
4335	PSI	UMA	11.14	44.62	3.90	3.85	2.44	2	3.03	K1	III
4337			11.13	-58.85	4.43	4.42	3.58	0	3.94	G0	I
4357	DEL	LEO	11.21	20.65	2.71	2.69	2.51	2	2.58	A4	V

YBS#	NAME		RA	DEC	S20	CDS	SIL	S	VIS	SP.TYPE	
4359	THE	LEO	11.22	15.57	3.35	3.35	3.31	2	3.34	A2	V
4362	72	LEO	11.23	23.22	5.59	5.64	3.15	2	4.66	M3	III
4377D	NU	UMA	11.29	33.22	4.45	4.42	2.69	2	3.49	K3	III
4382	DEL	CRT	11.30	-14.63	4.44	4.39	3.02	2	3.60	G8	III
4386	SIG	LEO	11.33	6.17	4.00	4.02	4.08	2	4.08	B9	V
4399D	IOT	LEO	11.38	10.67	4.24	4.24	3.73	2	3.93	F2	IV
4434	LAM	DRA	11.50	69.47	4.84	4.86	2.70	2	3.86	M0	III
4449			11.53	-30.95	5.96	6.04	3.47	0	5.09	M2	III
4450D	XI	HYA	11.53	-31.71	4.20	4.17	3.06	1	3.54	G7	III
4463D			11.57	-47.23	6.51	6.62	3.86	0	5.70	M3	III
4467D	LAM	CEN	11.58	-62.88	3.05	3.08	3.10	0	3.13	B9	II
4471	UPS	LEO	11.59	- 0.68	5.08	5.03	3.81	2	4.32	G9	III
4483	OMG	VIR	11.62	8.27	6.07	6.21	3.26	0	5.34	M4	III
4517	NU	VIR	11.74	6.66	5.02	5.02	2.92	2	4.05	M1	III
4518	CHI	UMA	11.75	47.92	4.59	4.54	3.06	2	3.71	K0	III
4520D	LAM	MUS	11.74	-66.58	3.84	3.82	3.52	0	3.63	A7	II
4522			11.75	-61.03	4.68	4.66	3.65	0	4.10	G3	III
4532			11.79	-26.61	5.84	5.98	3.03	0	5.11	M4	III
4534D	BET	LEO	11.80	14.71	2.21	2.20	2.09	2	2.11	A3	V
4537			11.81	-63.65	3.97	4.07	4.30	0	4.31	B3	V
4540	BET	VIR	11.82	1.91	3.96	3.95	3.27	2	3.55	F8	V
4546			11.83	-45.03	5.38	5.34	3.74	0	4.45	K4	III
4554	GAM	UMA	11.88	53.84	2.43	2.42	2.43	2	2.42	A0	V
4608	OMI	VIR	12.07	8.87	4.86	4.82	3.63	2	4.12	G8	III
4621D	DEL	CEN	12.12	-50.58	2.26	2.36	2.62	0	2.63	B2	V
4623	ALF	CRV	12.12	-24.58	4.22	4.22	3.83	1	4.00	F2	V
4630	EPS	CRV	12.15	-22.48	1.60	2.01	2.17	1	2.98	K3	III
4638	RHO	CEN	12.17	-52.23	3.66	3.74	3.96	0	3.96	B4	V
4656	DEL	CRU	12.23	-58.61	2.44	2.54	2.80	0	2.81	B2	IV
4660	DEL	UMA	12.24	57.17	3.41	3.40	3.30	2	3.32	A3	V
4662	GAM	CRV	12.24	-17.40	2.37	2.42	2.58	2	2.59	B8	III
4671	EPS	MUS	12.27	-67.81	4.75	4.94	1.79	0	4.13	M5	III
4679D	ZET	CRU	12.28	-63.86	3.72	3.82	4.05	0	4.06	B3	IV
4682D			12.29	-55.00	5.81	5.92	3.16	0	5.00	M3	
4689	ETA	VIR	12.31	- 0.53	3.92	3.92	3.89	2	3.88	A2	V
4700	EPS	CRU	12.33	-60.26	4.49	4.45	2.92	0	3.59	K3	
4726	71	UMA	12.40	56.92	6.62	6.73	3.97	0	5.81	M3	
4737	GAM	COM	12.43	28.40	5.21	5.15	3.78	2	4.34	K1	III
4739			12.44	-58.85	6.23	6.37	3.42	0	5.50	M4	
4743	SIG	CEN	12.44	-50.10	3.54	3.64	3.90	0	3.91	B2	V
4745	73	UMA	12.44	55.85	6.48	6.56	3.99	0	5.61	M2	
4755			12.48	-41.60	6.75	6.89	3.94	0	6.02	M4	
4757D	DEL	CRV	12.48	-16.38	2.90	2.91	2.98	2	2.96	B9.5	V
4763D	GAM	CRU	12.50	-56.97	2.47	2.58	-0.18	0	1.66	M3	II
4765	4	DRA	12.48	69.34	5.73	5.87	2.92	0	5.00	M4	
4773	GAM	MUS	12.52	-72.00	3.62	3.69	3.87	0	3.88	B5	V
4785	BET	CVN	12.54	41.49	4.66	4.66	3.96	2	4.26	G0	V
4786	BET	CRV	12.55	-23.26	3.27	3.24	2.24	1	2.64	G5	III
4787	KAP	DRA	12.54	69.92	3.53	3.61	3.85	2	3.87	B7	
4798D	ALF	MUS	12.59	-69.00	2.36	2.46	2.69	0	2.70	B3	IV

YBS#	NAME		RA	DEC	S20	CDS	SIL	S	VIS	SP.TYPE	
4800	T	UMA	12.59	59.62	6.23	6.37	3.42	0	5.50	M4	
4802	TAU	CEN	12.61	-48.40	3.90	3.90	3.79	0	3.85	A2	V
4807			12.62	1.99	6.52	6.63	3.87	0	5.71	M3	
4846	Y	CVN	12.73	45.57	6.30	6.53	3.53	2	5.30	C54	
4853D	BET	CRU	12.77	-59.56	0.85	0.97	1.25	0	1.27	B0.5	IV
4888			12.86	-48.81	5.26	5.23	3.55	0	4.31	K2	
4898D	MU1	CRU	12.89	-57.05	3.76	3.83	4.01	0	4.02	B3	IV
4902	PSI	VIR	12.88	- 9.41	5.67	5.73	3.23	2	4.77	M3	III
4905	EPS	UMA	12.88	56.09	1.77	1.77	1.77	2	1.78	A0	
4909			12.90	47.34	6.45	6.64	3.49	0	5.83	M5	III
4910	DEL	VIR	12.91	3.52	4.31	4.36	1.84	2	3.41	M3	III
4915D	ALF2	CVN	12.91	38.45	2.74	2.79	2.96	2	2.94	B9.5	
4920	36	COM	12.96	17.55	5.76	5.77	3.64	2	4.79	M0	III
4923	DEL	MUS	13.01	-71.42	4.48	4.44	2.97	0	3.61	K2	III
4932	EPS	VIR	13.02	11.10	3.59	3.54	2.39	2	2.85	G9	II
4942D	XI2	CEN	13.09	-49.77	3.89	3.99	4.25	0	4.26	B2	V
4949	40	COM	13.09	22.75	6.24	6.43	3.28	0	5.62	M5	III
4954	41	COM	13.10	27.77	5.80	5.79	3.83	2	4.82	K5	III
4983	BET	COM	13.18	28.01	4.62	4.62	3.92	2	4.21	G0	
5015	SIG	VIR	13.27	5.60	5.66	5.74	3.17	0	4.79	M2	
5020	GAM	HYA	13.29	-23.05	3.64	3.60	2.56	1	2.98	G8	III
5028	IOT	CEN	13.32	-36.58	2.75	2.75	2.70	1	2.73	A2	V
5056	ALF	VIR	13.40	-11.02	0.38	0.52	1.01	2	0.99	B1	V
5062	80	UMA	13.40	55.13	4.14	4.12	3.92	2	3.99	A5	V
5064	68	VIR	13.42	-12.57	6.18	6.21	3.97	0	5.23	M0	III
5080D	R	HYA	13.47	-23.15	4.95	5.35	1.24	1	4.98	M7	
5095	74	VIR	13.51	- 6.12	5.70	5.74	3.41	2	4.74	M2	III
5101	S	VIR	13.53	- 7.07	6.34	6.62	3.10	0	6.00	M7	
5107	ZET	VIR	13.56	- 0.47	3.46	3.45	3.34	2	3.35	A3	V
5132D	EPS	CEN	13.64	-53.34	1.89	2.00	2.27	0	2.29	B1	V
5134			13.64	-49.82	6.17	6.50	2.81	0	6.00	M8	III
5150	82	VIR	13.67	- 8.57	5.87	5.95	3.38	0	5.00	M2	III
5154	83	UMA	13.66	54.81	5.64	5.67	3.36	2	4.67	M2	III
5190	NU	CEN	13.80	-41.56	3.03	3.13	3.39	0	3.40	B2	IV
5191	ETA	UMA	13.78	49.44	1.46	1.56	1.90	2	1.87	B3	V
5192	2	CEN	13.80	-34.32	4.70	4.88	1.71	1	4.21	M4	III
5193D	MU	CEN	13.80	-42.36	2.60	2.70	2.96	0	2.97	B2	V
5200	UPS	BOO	13.80	15.92	5.03	5.03	3.03	2	4.06	K5	III
5219			13.84	34.56	5.71	5.77	3.25	2	4.78	K5	III
5226D	10	DRA	13.85	64.84	5.51	5.56	2.99	2	4.61	M3	
5228			13.88	-28.46	5.36	5.32	3.96	0	4.55	K0	
5231	ZET	CEN	13.90	-47.17	2.17	2.27	2.53	0	2.54	B2	IV
5235	ETA	BOO	13.89	18.52	3.10	3.08	2.37	2	2.65	G0	IV
5241			13.93	-63.56	5.63	5.59	3.99	0	4.70	K4	III
5248	PHI	CEN	13.95	-41.98	3.45	3.55	3.81	0	3.82	B2	IV
5249	UPS1	CEN	13.95	-44.68	3.49	3.59	3.85	0	3.86	B2	V
5261	THE	APS	14.05	-76.68	6.23	6.37	3.42	0	5.50	M4	
5267D	BET	CEN	14.03	-60.25	0.21	0.32	0.59	0	0.61	B1	II
5285	CHI	CEN	14.08	-41.06	3.98	4.08	4.34	0	4.35	B3	V
5287	PI	HYA	14.08	-26.56	4.03	4.00	2.66	1	3.28	K2	III

YBS#	NAME		RA	DEC	S20	CDS	SIL	S	VIS	SP.TYPE	
5288	THE	CEN	14.09	-36.26	2.86	2.82	1.46	0	2.05	K0	III
5291	ALF	DRA	14.06	64.49	3.58	3.59	3.67	2	3.65	A0	III
5299			14.12	43.97	6.03	6.16	3.05	2	5.27	M4	III
5300	13	BOO	14.12	49.58	6.12	6.20	3.63	0	5.25	M2	
5301			14.16	-16.18	5.69	5.80	3.04	0	4.88	M3	
5315	KAP	VIR	14.19	-10.17	5.14	5.10	3.41	2	4.20	K3	III
5326D	R	CEN	14.25	-59.80	6.03	6.17	3.22	0	5.30	M4	
5334			14.19	69.55	6.11	6.19	3.62	0	5.24	M2	
5338	IOT	VIR	14.25	- 5.88	4.43	4.43	3.79	2	4.07	F7	IV
5339	DEL	OCT	14.38	-83.55	5.15	5.11	3.70	0	4.31	K1	
5340	ALF	BOO	14.24	19.31	0.83	0.79	-0.81	2	-0.07	K2	III
5354	IOT	LUP	14.30	-45.95	3.22	3.32	3.55	0	3.56	B3	IV
5367D	PSI	CEN	14.32	-37.78	4.00	4.02	4.00	0	4.04	A0	IV
5404	THE	BOO	14.41	51.97	4.38	4.38	3.80	2	4.03	F7	V
5429D	RHO	BOO	14.51	30.49	4.53	4.49	2.88	2	3.60	K3	III
5430D	5	UMI	14.46	75.80	5.23	5.20	3.44	2	4.25	K4	III
5435D	GAM	BOO	14.52	38.42	3.24	3.22	2.99	2	3.05	A7	III
5440D	ETA	CEN	14.57	-42.04	1.91	2.02	2.29	0	2.30	B1.5	V
5453	RHO	LUP	14.60	-49.31	3.78	3.85	4.03	0	4.04	B5	V
5463D	ALF	CIR	14.67	-64.86	3.46	3.44	3.04	0	3.18	F0	V
5469D	ALF	LUP	14.67	-47.29	1.89	2.00	2.27	0	2.29	B2	II
5470	ALF	APS	14.75	-78.93	4.80	4.77	3.09	0	3.85	K5	III
5471			14.67	-37.69	3.65	3.75	3.98	0	3.99	B3	V
5485			14.70	-35.07	4.99	4.96	3.28	0	4.04	K5	III
5487	MU	VIR	14.70	- 5.54	4.12	4.12	3.64	2	3.85	F3	IV
5490	34	BOO	14.71	26.62	5.74	5.79	3.31	2	4.80	M3	
5511	109	VIR	14.75	2.00	3.71	3.71	3.72	2	3.72	A0	V
5512			14.75	15.24	6.44	6.63	3.48	0	5.82	M5	
5526	58	HYA	14.81	-27.86	5.24	5.23	3.55	1	4.41	K4	
5531D	ALF2	LIB	14.82	-15.95	2.90	2.89	2.71	2	2.76	A	
5540	R	APS	14.92	-76.55	5.95	5.98	3.74	0	5.00	M0	
5563	BET	UMI	14.85	74.25	3.08	3.06	1.22	2	2.10	K4	III
5571	BET	LUP	14.95	-43.03	2.30	2.40	2.66	0	2.67	B2	IV
5576D	KAP	CEN	14.96	-42.00	2.75	2.85	3.11	0	3.12	B2	V
5589			14.95	66.03	5.50	5.62	2.58	2	4.73	M5	III
5600	OMG	BOO	15.02	25.10	5.80	5.79	3.84	2	4.82	K4	III
5601	110	VIR	15.03	2.18	5.14	5.09	3.79	2	4.34	K0	III
5602	BET	BOO	15.02	40.48	4.24	4.20	3.03	2	3.50	G8	III
5603	SIG	LIB	15.04	-25.18	4.07	4.12	1.72	1	3.26	M4	III
5616	PSI	BOO	15.06	27.05	5.43	5.38	3.84	2	4.51	K2	III
5646D	KAP	LUP	15.17	-48.64	3.63	3.66	3.68	0	3.71	B9	V
5649D	ZET	LUP	15.17	-52.00	4.14	4.11	2.85	0	3.40	G8	III
5654			15.18	19.06	6.51	6.65	3.70	0	5.78	M4	
5670	BET	CIR	15.26	-58.71	4.15	4.14	3.99	0	4.06	A3	V
5671	GAM	TRA	15.28	-68.59	2.90	2.91	2.84	0	2.89	A1	V
5681D	DEL	BOO	15.24	33.41	4.24	4.19	2.99	2	3.50	G8	III
5685	BET	LIB	15.26	- 9.29	2.40	2.45	2.63	2	2.62	B8	V
5686	2	LUP	15.27	-30.06	5.06	5.03	3.74	1	4.32	K0	
5695	DEL	LUP	15.33	-40.56	2.84	2.94	3.20	0	3.21	B2	IV
5705D	PHI1	LUP	15.34	-36.17	4.50	4.47	2.79	0	3.55	K5	III

YBS#	NAME		RA	DEC	S20	CDS	SIL	S	VIS	SP.TYPE	
5735	GAM	UMI	15.35	71.92	3.10	3.10	2.97	2	3.04	A3	II
5739	TAU1	SER	15.41	15.52	6.09	6.14	3.74	0	5.17	M1	III
5744	IOT	DRA	15.41	59.05	4.19	4.14	2.70	2	3.31	K2	III
5747	BET	CRB	15.45	29.19	3.91	3.89	3.62	2	3.66	F0	III
5763	NU1	BOO	15.50	40.92	6.06	6.07	4.00	2	5.07	K5	III
5771D	EPS	TRA	15.57	-66.23	4.91	4.87	3.51	0	4.10	K0	III
5778	THE	CRB	15.53	31.45	3.85	3.93	4.19	2	4.16	B7	
5787D	GAM	LIB	15.57	-14.70	4.66	4.62	3.37	2	3.90	G8	III
5793	ALF	CRB	15.56	26.80	2.19	2.20	2.23	2	2.22	A0	V
5794D	UPS	LIB	15.59	-28.05	4.41	4.39	2.77	1	3.56	K5	III
5797D	OMG	LUP	15.61	-42.48	5.27	5.30	3.06	0	4.32	M0	III
5800	MU	CRB	15.57	39.10	6.00	6.08	3.51	0	5.13	M2	
5812	TAU	LIB	15.62	-29.70	3.31	3.39	3.69	1	3.65	B2.5	V
5838	KAP	LIB	15.68	-19.59	5.75	5.76	3.66	2	4.78	K5	III
5849D	GAM	CRB	15.69	26.38	3.83	3.83	3.84	2	3.83	A0	IV
5854D	ALF	SER	15.72	6.50	3.53	3.47	2.05	2	2.64	K2	III
5867D	BET	SER	15.75	15.50	3.76	3.74	3.66	2	3.67	A2	IV
5879	KAP	SER	15.79	18.21	5.09	5.11	2.92	2	4.11	M1	III
5881	MU	SER	15.81	- 3.34	3.50	3.52	3.57	2	3.56	A0	V
5883	CHI	LUP	15.82	-33.54	3.90	3.92	3.90	0	3.94	A0	III
5892	EPS	SER	15.83	4.56	3.86	3.85	3.69	2	3.72	A	
5894	R	SER	15.83	15.21	5.94	6.22	2.70	0	5.60	M7	
5897	BET	TRA	15.88	-63.35	3.16	3.14	2.67	0	2.84	F2	IV
5899	RHO	SER	15.84	21.06	5.74	5.74	3.74	2	4.76	K5	III
5908	THE	LIB	15.87	-16.66	4.90	4.86	3.58	2	4.11	K0	III
5928D	RHO	SCO	15.92	-29.14	3.43	3.53	3.87	1	3.85	B2	V
5932	2	HER	15.90	43.22	6.16	6.27	3.51	0	5.35	M3	III
5933	GAM	SER	15.92	15.73	4.15	4.15	3.56	2	3.83	F6	IV
5944D	PI	SCO	15.96	-26.05	2.48	2.58	2.94	1	2.92	B1	V
5947D	EPS	CRB	15.94	26.95	5.05	5.01	3.48	2	4.15	K3	III
5948D	ETA	LUP	15.97	-38.33	3.03	3.13	3.39	0	3.40	B2	V
5953	DEL	SCO	15.98	-22.55	1.96	2.06	2.33	1	2.33	B0	V
5984D	BET1	SCO	16.07	-19.73	2.11	2.23	2.52	2	2.53	B0.5	V
5986	THE	DRA	16.02	58.63	4.38	4.37	3.74	2	4.00	F8	IV
5987	THE	LUP	16.08	-36.73	3.85	3.95	4.21	0	4.22	B2	V
5993	OMG1	SCO	16.09	-20.60	3.58	3.70	3.94	2	3.96	B1	V
5997	OMG2	SCO	16.10	-20.80	4.95	4.92	3.90	2	4.30	G2	
6001			16.11	-26.27	6.26	6.34	3.77	0	5.39	M2	
6010	47	SER	16.12	8.60	6.53	6.64	3.88	0	5.72	M3	
6020D	DEL1	APS	16.28	-78.64	5.46	5.60	2.65	0	4.73	M4	III
6027D	NU	SCO	16.18	-19.40	3.76	3.85	3.91	2	3.99	B2	IV
6030D	DEL	TRA	16.22	-63.62	4.39	4.37	3.42	0	3.84	G2	II
6039	10	HER	16.18	23.55	6.69	6.83	3.88	0	5.96	M4	
6055			16.25	-53.75	6.17	6.25	3.68	0	5.30	M2	
6056	DEL	OPH	16.22	- 3.62	3.71	3.73	1.54	2	2.74	M1	III
6072D	GAM2	NOR	16.30	-50.10	4.75	4.72	3.46	0	4.01	G8	III
6075	EPS	OPH	16.28	- 4.64	3.98	3.94	2.72	2	3.23	G9	III
6081	OMI	SCO	16.32	-24.11	5.15	5.14	3.83	1	4.57	A5	II
6084D	SIG	SCO	16.33	-25.52	2.78	2.86	2.77	1	2.89	B1	III
6086			16.28	59.81	6.24	6.38	3.43	0	5.51	M4	

YBS#	NAME	RA	DEC	S20	CDS	SIL	S	VIS	SP.TYPE
6092D	TAU HER	16.32	46.37	3.57	3.65	3.94	2	3.92	B5 IV
6095D	GAM HER	16.35	19.21	4.01	3.98	3.60	2	3.75	A9 III
6102	GAM APS	16.49	-78.83	4.69	4.65	3.29	0	3.88	K0 IV
6107	NU1 CRB	16.36	33.86	6.07	6.15	3.58	0	5.20	M2
6119	U HER	16.41	18.94	7.04	7.32	3.80	0	6.70	M7
6128		16.44	- 7.54	6.11	6.19	3.62	0	5.24	M2 III
6132D	ETA DRA	16.39	61.56	3.44	3.40	2.29	2	2.73	G8 III
6134D	ALF SCO	16.46	-26.38	1.71	1.78	-0.64	1	0.89	M1 I
6143		16.50	-34.65	3.86	3.96	4.22	0	4.23	B2 IV
6146	30 HER	16.46	41.94	5.55	5.84	1.99	2	5.06	M6 III
6147D	PHI OPH	16.50	-16.56	4.98	4.93	3.85	2	4.25	G8 III
6148	BET HER	16.49	21.54	3.51	3.46	2.34	2	2.78	G8 III
6149D	LAM OPH	16.49	2.04	3.84	3.83	3.79	2	3.81	A1 V
6159	29 HER	16.52	11.54	5.82	5.82	3.88	2	4.85	K4 III
6163D	BET APS	16.66	-77.46	5.04	5.00	3.64	0	4.23	K0 III
6165	TAU SCO	16.57	-28.17	2.18	2.33	2.85	2	2.81	B0 V
6166		16.58	-35.20	5.11	5.09	3.33	0	4.15	K6
6175	ZET OPH	16.60	-10.52	2.21	2.34	2.52	2	2.57	O9.5 V
6200D	42 HER	16.63	48.97	5.77	5.85	3.28	0	4.90	M2
6212D	ZET HER	16.67	31.65	3.24	3.23	2.44	2	2.77	G0 IV
6217	ALF TRA	16.77	-68.99	2.86	2.82	1.22	0	1.93	K4 III
6220	ETA HER	16.70	38.98	4.21	4.17	3.05	2	3.51	G7 III
6227		16.74	15.80	6.45	6.56	3.80	0	5.64	M3
6229D	ETA ARA	16.79	-59.00	4.70	4.67	2.99	0	3.75	K5 III
6241	EPS SCO	16.81	-34.25	3.17	3.12	1.73	2	2.29	K2 III
6242		16.78	42.28	6.71	6.85	3.90	0	5.98	M4
6247D	MU1 SCO	16.84	-38.01	2.63	2.74	3.01	0	3.02	B1.5 V
6252D	MU2 SCO	16.84	-37.97	3.19	3.29	3.55	0	3.56	B2 IV
6257		16.87	-43.01	6.40	6.54	3.59	0	5.67	M4
6271	ZET SCO	16.88	-42.31	4.41	4.40	2.72	1	3.59	K5 III
6285	ZET ARA	16.94	-55.95	4.07	4.04	2.36	0	3.12	K5 III
6295	EPS1 ARA	16.96	-53.11	4.95	4.91	3.38	0	4.05	K3 III
6299	KAP OPH	16.94	9.42	4.08	4.03	2.60	2	3.21	K2 III
6322D	EPS UMI	16.81	82.07	4.89	4.85	3.75	2	4.20	G5 III
6324	EPS HER	16.99	30.95	3.88	3.89	3.93	2	3.93	A0 V
6337		17.03	14.12	5.94	5.99	3.52	2	5.02	M3 III
6380	ETA SCO	17.17	-43.20	3.67	3.66	3.15	2	3.34	F0 IV
6393D	37 OPH	17.19	10.61	6.20	6.28	3.71	0	5.33	M2
6396	ZET DRA	17.15	65.75	2.92	2.99	3.19	2	3.19	B6 III
6406D	ALF1 HER	17.23	14.41	3.72	3.92	0.49	2	3.14	M5 II
6410D	DEL HER	17.23	24.86	3.21	3.21	3.08	2	3.13	A3 IV
6418	PI HER	17.24	36.83	4.16	4.13	2.38	2	3.18	K3 II
6452		17.32	18.09	5.87	5.95	3.38	0	5.00	M2
6453	THE OPH	17.34	-24.97	2.75	2.87	3.29	2	3.26	B2 IV
6461	BET ARA	17.39	-55.51	3.74	3.70	2.17	0	2.84	K3 I
6462D	GAM ARA	17.39	-56.36	2.92	3.03	3.30	0	3.32	B1 III
6498	SIG OPH	17.42	4.17	5.35	5.33	3.50	2	4.35	K3 II
6500D	DEL ARA	17.48	-60.66	3.46	3.50	3.57	0	3.59	B8 V
6508	UPS SCO	17.48	-37.28	2.16	2.28	2.72	2	2.68	B3 I
6510D	ALF ARA	17.50	-49.86	2.58	2.68	2.93	0	2.94	B2.5 V

YBS#	NAME		RA	DEC	S20	CDS	SIL	S	VIS	SP.TYPE	
6526	LAM	HER	17.50	26.12	5.41	5.38	3.62	2	4.43	K4	III
6527	LAM	SCO	17.53	-37.08	1.08	1.21	1.67	2	1.63	B1	V
6536D	BET	DRA	17.50	52.33	3.53	3.49	2.33	2	2.80	G2	II
6546			17.58	-38.62	5.09	5.05	3.69	0	4.28	K0	III
6553	THE	SCO	17.59	-42.98	2.14	2.12	1.72	0	1.86	F0	I
6556	ALF	OPH	17.56	12.58	2.24	2.23	2.03	2	2.09	A5	III
6561D	XI	SER	17.60	-15.38	3.76	3.74	3.40	2	3.53	F0	IV
6580	KAP	SCO	17.68	-39.02	1.85	1.98	2.45	2	2.41	B2	IV
6582	ETA	PAV	17.72	-64.72	4.46	4.42	3.01	0	3.62	K1	III
6588	IOT	HER	17.65	46.03	3.39	3.49	3.84	2	3.83	B3	V
6603	BET	OPH	17.70	4.58	3.65	3.60	2.17	2	2.77	K2	III
6615D	IOT1	SCO	17.76	-40.11	3.49	3.45	2.75	2	3.02	F2	I
6623D	MU	HER	17.76	27.75	4.00	3.96	3.07	2	3.43	G5	IV
6629	GAM	OPH	17.78	2.72	3.78	3.78	3.74	2	3.75	A0	V
6630			17.80	-37.04	4.04	4.00	2.59	0	3.20	K1	III
6688	XI	DRA	17.88	56.87	4.63	4.58	3.11	2	3.75	K2	III
6693D			17.96	-30.26	6.14	6.22	3.65	0	5.27	M2	I
6695	THE	HER	17.92	37.25	4.83	4.79	3.22	2	3.86	K1	II
6698	NU	OPH	17.96	- 9.78	4.11	4.05	2.85	2	3.32	G9	III
6702			17.93	45.35	6.71	6.94	3.60	0	6.22	M6	
6703	XI	HER	17.95	29.25	4.45	4.40	3.24	2	3.72	G9	III
6705D	GAM	DRA	17.93	51.49	3.24	3.24	1.26	2	2.26	K5	III
6714D	67	OPH	17.99	2.93	3.75	3.84	3.92	2	3.97	B5	I
6743	THE	ARA	18.08	-50.10	3.23	3.36	3.65	2	3.66	B0.5	II
6746	GAM	SGR	18.07	-30.43	3.81	3.76	2.49	2	2.99	K0	III
6765	98	HER	18.08	22.23	5.93	6.01	3.44	0	5.06	M2	
6771D	72	OPH	18.10	9.56	3.87	3.85	3.69	2	3.74	A4	V
6779	OMI	HER	18.11	28.76	3.79	3.80	3.81	2	3.83	B9	V
6787D	102	HER	18.13	20.81	3.90	4.02	4.39	2	4.38	B2	V
6812D	MU	SGR	18.20	-21.06	3.88	3.92	3.68	1	3.85	B8	I
6815	104	HER	18.18	31.40	5.78	5.89	3.13	0	4.97	M3	
6832D	ETA	SGR	18.27	-36.77	4.02	4.06	1.59	2	3.11	M3	II
6834			18.25	2.37	6.73	6.87	3.92	0	6.00	M4	
6842			18.27	-27.06	5.52	5.53	3.57	1	4.63	K5	
6855D	XI	PAV	18.35	-61.50	5.23	5.19	3.72	0	4.36	K2	III
6859D	DEL	SGR	18.32	-29.83	3.69	3.65	1.98	2	2.70	K2	III
6861			18.33	-24.93	6.87	7.06	3.91	0	6.25	M5	
6868	106	HER	18.32	21.95	5.91	5.94	3.73	2	4.94	M0	III
6869	ETA	SER	18.33	- 2.89	3.95	3.91	2.72	2	3.23	K0	IV
6872	KAP	LYR	18.32	36.05	5.23	5.18	3.74	2	4.35	K2	III
6879D	EPS	SGR	18.38	-34.40	1.81	1.82	1.84	2	1.85	B9	IV
6891			18.35	49.10	5.92	6.00	3.43	0	5.05	M2	
6895	109	HER	18.38	21.75	4.72	4.68	3.20	2	3.84	K2	III
6896D	21	SGR	18.40	-20.56	5.68	5.67	3.91	2	4.79	K2	II
6897	ALF	TEL	18.42	-45.98	3.16	3.26	3.49	0	3.50	B3	III
6905	ZET	TEL	18.45	-49.08	4.88	4.83	3.57	2	4.13	K0	
6913	LAM	SGR	18.44	-25.45	3.65	3.59	2.30	2	2.81	K2	III
6973	ALF	SCT	18.56	- 8.27	4.80	4.77	3.11	2	3.86	K3	III
6982D	ZET	PAV	18.67	-71.45	4.87	4.83	3.39	2	4.01	K2	III
6991			18.63	-43.20	6.17	6.25	3.68	0	5.30	M2	

YBS#	NAME		RA	DEC	S20	CDS	SIL	S	VIS	SP.TYPE	
7001D	ALF	LYR	18.60	38.76	0.05	0.05	0.04	2	0.04	A0	V
7009	XY	LYR	18.62	39.65	6.53	6.67	3.72	0	5.80	M4	
7039	PHI	SGR	18.74	-27.02	2.95	3.01	3.18	2	3.16	B8	III
7061D	110	HER	18.74	20.52	4.50	4.50	3.97	2	4.19	F6	V
7063	BET	SCT	18.76	- 4.77	5.03	4.99	3.59	2	4.21	G5	II
7074D	LAM	PAV	18.83	-62.21	3.81	3.92	4.19	0	4.21	B1	V
7106D	BET	LYR	18.82	33.34	3.12	3.21	3.29	2	3.37	B7	V
7107	KAP	PAV	18.91	-67.28	4.28	4.27	3.67	0	3.90	F5	
7121	SIG	SGR	18.90	-26.33	1.59	1.69	2.08	2	2.03	B2	V
7139D	DEL2	LYR	18.89	36.87	5.06	5.18	2.19	2	4.25	M4	II
7150	XI2	SGR	18.94	-21.13	4.28	4.24	2.91	1	3.49	K1	III
7157	13	LYR	18.91	43.92	4.82	5.00	1.62	2	4.14	M5	III
7176	EPS	AQL	18.97	15.03	4.88	4.83	3.52	2	4.05	K2	III
7178D	GAM	LYR	18.97	32.65	3.17	3.19	3.23	2	3.24	B9	III
7193	12	AQL	19.01	- 5.78	4.86	4.81	3.47	2	4.03	K1	III
7217D	OMI	SGR	19.05	-21.77	4.49	4.44	3.32	1	3.77	G8	
7234	TAU	SGR	19.09	-27.70	4.20	4.15	2.70	2	3.31	K1	III
7235D	ZET	AQL	19.07	13.83	2.99	2.99	2.97	2	2.98	A0	V
7236	LAM	AQL	19.08	- 4.92	3.28	3.31	3.46	2	3.44	B9	V
7242	DEL	CRA	19.11	-40.54	5.42	5.38	3.97	0	4.58	K1	
7243	R	AQL	19.09	8.20	5.84	6.12	2.60	0	5.50	M7	
7259	BET	CRA	19.14	-39.37	5.01	4.96	3.53	2	4.11	G3	
7264D	PI	SGR	19.14	-21.06	3.23	3.21	2.70	2	2.88	F2	II
7310	DEL	DRA	19.21	67.62	3.85	3.81	2.58	2	3.08	G9	III
7314	THE	LYR	19.26	38.09	5.26	5.21	3.70	2	4.34	K0	II
7328	KAP	CYG	19.28	53.32	4.51	4.47	3.30	2	3.77	K0	III
7337D	BET1	SGR	19.35	-44.51	3.88	3.92	3.99	0	4.01	B8	V
7340	RHO1	SGR	19.34	-17.90	4.11	4.09	3.80	2	3.91	F0	IV
7348	ALF	SGR	19.37	-40.66	3.88	3.91	3.93	0	3.96	B9	III
7352	TAU	DRA	19.27	73.30	5.39	5.34	3.80	2	4.46	K3	III
7377	DEL	AQL	19.40	3.07	3.58	3.57	3.20	2	3.35	F0	IV
7405	ALF	VUL	19.46	24.62	5.43	5.43	3.34	2	4.48	M0	III
7414	36	AQL	19.49	- 2.84	5.94	5.99	3.59	0	5.02	M1	III
7417D	BET	CYG	19.50	27.91	3.87	3.86	2.39	2	3.09	K5	II
7420	IOT	CYG	19.48	51.68	3.93	3.92	3.72	2	3.79	A5	V
7429D	MU	AQL	19.55	7.33	5.34	5.29	3.84	2	4.46	K3	III
7442			19.55	49.20	6.79	6.93	3.98	0	6.06	M4	
7488	BET	SGE	19.67	17.42	5.21	5.16	3.90	2	4.40	G8	II
7509			19.69	55.39	5.97	6.16	3.01	0	5.35	M5	
7525	GAM	AQL	19.75	10.55	3.75	3.73	1.89	2	2.75	K3	II
7528D	DEL	CYG	19.74	45.07	2.84	2.85	2.89	2	2.90	B9.5	III
7536	DEL	SGE	19.77	18.47	4.70	4.75	2.37	2	3.87	M2	II
7557D	ALF	AQL	19.83	8.80	0.92	0.91	0.65	2	0.74	A7	V
7564	CHI	CYG	19.83	32.85	7.88	8.71	3.03	2	8.40	S71	
7566D	19	CYG	19.83	38.65	6.07	6.15	3.58	0	5.20	M2	
7570	ETA	AQL	19.85	0.94	4.52	4.48	3.38	2	3.81	F6	I
7581	IOT	SGR	19.89	-41.93	4.95	4.92	3.56	2	4.12	K0	III
7582D	EPS	DRA	19.80	70.20	4.54	4.50	3.41	2	3.86	G8	III
7590	EPS	PAV	19.96	-72.97	3.92	3.94	3.92	0	3.96	A0	V
7602D	BET	AQL	19.90	6.34	4.37	4.34	3.29	2	3.73	G8	IV

YBS#	NAME		RA	DEC	S20	CDS	SIL	S	VIS	SP.TYPE	
7604	59	SGR	19.92	-27.23	5.37	5.35	3.69	1	4.50	K3	
7615D	ETA	CYG	19.96	35.02	4.69	4.64	3.38	2	3.90	K0	III
7625			19.99	-59.45	5.49	5.72	2.38	0	5.00	M6	
7635	GAM	SGE	19.96	19.42	4.54	4.55	2.49	2	3.56	K5	III
7645D	13	SGE	19.98	17.45	6.12	6.26	3.31	0	5.39	M4	
7650	62	SGR	20.02	-27.77	5.46	5.54	2.77	2	4.59	M4	III
7652			20.03	-38.00	5.74	5.72	3.96	2	4.77	K5	
7665	DEL	PAV	20.10	-66.25	4.18	4.14	3.22	2	3.56	G8	V
7673	XI	TEL	20.09	-52.95	5.92	5.93	3.78	2	4.93	M2	III
7676	64	DRA	20.02	64.75	6.19	6.24	3.84	0	5.27	M1	III
7680D			20.07	15.43	6.25	6.33	3.76	0	5.38	M2	III
7685	RHO	DRA	20.05	67.80	5.48	5.44	3.83	2	4.53	K3	III
7704			20.08	67.95	6.31	6.36	3.96	0	5.39	M1	
7710	THE	AQL	20.17	- 0.89	3.09	3.11	3.20	2	3.19	B9.5	III
7735D	OMI1	CYG	20.21	46.66	4.61	4.62	2.98	2	3.80	K2	II
7744	23	VUL	20.25	27.72	5.41	5.39	3.76	2	4.52	K3	III
7747D	ALF1	CAP	20.27	-12.58	5.04	5.00	3.72	2	4.24	G3	I
7751	OMI2	CYG	20.24	47.62	4.96	4.99	2.97	2	4.04	K3	I
7754D	ALF2	CAP	20.28	-12.61	4.31	4.27	3.11	2	3.59	G9	III
7776D	BET	CAP	20.33	-14.86	3.66	3.64	2.62	2	3.08	F8	V
7790	ALF	PAV	20.39	-56.81	1.52	1.63	1.99	2	1.94	B3	IV
7796D	GAM	CYG	20.36	40.17	2.80	2.75	1.92	2	2.22	F8	I
7804			20.33	68.80	6.61	6.80	3.65	0	5.99	M5	
7806	39	CYG	20.38	32.10	5.38	5.35	3.65	2	4.44	K3	III
7834	41	CYG	20.47	30.28	4.36	4.33	3.78	2	3.99	F5	II
7851	OMG2	CYG	20.51	49.13	6.29	6.37	3.80	0	5.42	M2	
7852	EPS	DEL	20.53	11.22	3.74	3.81	4.05	2	4.04	B6	III
7866	47	CYG	20.55	35.16	5.55	5.60	3.49	2	4.64	K2	I
7869D	ALF	IND	20.60	-47.37	3.90	3.86	2.63	2	3.11	K0	III
7884D	71	AQL	20.62	- 1.19	5.04	4.99	3.81	2	4.31	G8	III
7886			20.61	18.18	6.76	6.99	3.65	0	6.27	M6	
7900	UPS	CAP	20.64	-18.22	5.97	6.05	3.48	0	5.10	M2	III
7906D	ALF	DEL	20.64	15.83	3.65	3.68	3.77	2	3.77	B9	V
7913	BET	PAV	20.71	-66.29	3.62	3.60	3.36	2	3.42	A5	IV
7924D	ALF	CYG	20.68	45.18	1.25	1.28	1.18	2	1.28	A2	I
7936	PSI	CAP	20.74	-25.36	4.43	4.43	3.92	2	4.13	F5	V
7941	U	DEL	20.74	18.01	6.22	6.41	3.26	0	5.60	M5	II
7942D	52	CYG	20.74	30.62	5.00	4.95	3.66	2	4.20	K0	III
7949D	EPS	CYG	20.75	33.87	3.24	3.19	1.92	2	2.46	K0	III
7950	EPS	AQR	20.77	- 9.59	3.79	3.79	3.76	2	3.78	A1	V
7951	3	AQR	20.77	- 5.12	5.43	5.49	2.92	2	4.51	M3	III
7957D	ETA	CEP	20.75	61.74	4.12	4.08	2.90	2	3.41	K0	IV
7980	OMG	CAP	20.84	-27.02	5.11	5.14	3.02	2	4.12	K5	III
7986	BET	IND	20.88	-58.55	4.59	4.55	3.06	2	3.65	K0	III
8028	NU	CYG	20.94	41.07	3.96	3.96	3.93	2	3.97	A0	V
8044			20.99	19.22	6.54	6.65	3.89	0	5.73	M3	
8079	XI	CYG	21.07	43.83	4.72	4.74	2.67	2	3.72	K5	I
8080D	24	CAP	21.09	-25.10	5.49	5.51	3.34	2	4.49	M1	III
8089D	63	CYG	21.10	47.55	5.58	5.57	3.62	2	4.57	K4	II
8092	OMI	PAV	21.18	-70.23	5.88	5.96	3.39	0	5.01	M2	III

YBS#	NAME		RA	DEC	S20	CDS	SIL	S	VIS	SP.TYPE	
8113	T	CEP	21.15	68.38	5.54	5.82	2.30	0	5.20	M7	
8115	ZET	CYG	21.20	30.13	4.00	3.95	2.77	2	3.22	G8	II
8128	29	CAP	21.24	-15.27	6.09	6.20	3.44	0	5.28	M3	
8130D	TAU	CYG	21.23	37.94	4.04	4.04	3.54	2	3.74	F0	IV
8131	ALF	EQU	21.24	5.15	4.32	4.29	3.59	2	3.89	G0	III
8146D	UPS	CYG	21.28	34.80	3.95	4.07	4.31	2	4.38	B2	V
8162D	ALF	CEP	21.30	62.48	2.64	2.63	2.35	2	2.45	A7	IV
8167	IOT	CAP	21.35	-16.94	4.96	4.92	3.83	2	4.27	G8	III
8173D	1	PEG	21.35	19.71	4.92	4.87	3.50	2	4.08	K1	III
8181	GAM	PAV	21.41	-65.48	4.54	4.55	3.93	2	4.22	F8	V
8196	SX	PAV	21.44	-69.61	5.54	5.82	2.30	0	5.20	M7	
8204D	ZET	CAP	21.42	-22.52	4.52	4.47	3.33	2	3.74	G4	I
8223			21.46	22.07	6.66	6.80	3.85	0	5.93	M4	
8225D	2	PEG	21.48	23.52	5.52	5.54	3.36	2	4.55	M1	III
8232D	BET	AQR	21.50	- 5.69	3.55	3.51	2.49	2	2.89	G0	I
8238D	BET	CEP	21.47	70.44	2.61	2.76	3.28	2	3.24	B2	III
8252	RHO	CYG	21.55	45.49	4.66	4.63	3.48	2	3.98	G8	III
8262	W	CYG	21.58	45.27	5.91	6.25	2.18	2	5.46	M4	
8278	GAM	CAP	21.64	-16.78	3.97	3.94	3.56	2	3.68	A	
8284D	75	CYG	21.65	43.15	6.02	6.07	3.67	0	5.10	M1	III
8289	7	PEG	21.68	5.55	6.21	6.29	3.72	0	5.34	M2	
8306			21.70	41.04	6.26	6.34	3.77	0	5.39	M2	
8308D	EPS	PEG	21.72	9.77	3.43	3.42	1.60	2	2.42	K2	I
8313	9	PEG	21.72	17.23	5.14	5.10	3.72	2	4.29	G5	I
8316D	MU	CEP	21.71	58.67	4.95	5.19	1.81	2	4.10	M2	I
8317	11	CEP	21.69	71.20	5.39	5.33	3.98	2	4.53	K0	III
8322D	DEL	CAP	21.76	-16.25	3.11	3.11	2.72	2	2.86	A	
8334	NU	CEP	21.75	61.02	4.67	4.67	3.94	2	4.29	A2	I
8335	PI2	CYG	21.76	49.20	3.85	3.95	4.24	2	4.24	B3	III
8353	GAM	GRU	21.87	-37.48	2.81	2.87	3.04	2	3.01	B8	III
8383	VV	CEP	21.93	63.51	5.60	5.71	3.17	1	4.90	M2	I
8411	LAM	GRU	22.08	-39.67	5.39	5.42	3.18	0	4.44	K2	III
8413	NU	PEG	22.07	4.93	5.85	5.83	4.00	2	4.88	K4	III
8414	ALF	AQR	22.07	- 0.44	3.71	3.67	2.50	2	2.95	G2	I
8416	18	CEP	22.05	63.00	5.90	6.09	2.94	0	5.28	M5	
8421			22.07	46.63	6.29	6.62	2.93	0	6.12	M8	
8425D	ALF	GRU	22.11	-47.09	1.47	1.54	1.76	2	1.74	B5	V
8430	IOT	PEG	22.10	25.21	4.05	4.05	3.50	2	3.75	F5	
8433	UPS	PSA	22.12	-34.17	5.91	5.96	3.56	0	4.99	M1	
8450	THE	PEG	22.15	6.07	3.62	3.61	3.51	2	3.53	A2	V
8465	ZET	CEP	22.17	58.07	4.39	4.37	2.54	2	3.37	K1	I
8481	EPS	OCT	22.29	-80.56	5.58	5.81	2.47	0	5.09	M6	III
8485D			22.21	39.59	5.45	5.42	3.68	2	4.49	K3	III
8498	1	LAC	22.25	37.62	5.11	5.08	3.34	2	4.12	K3	II
8499	THE	AQR	22.26	- 7.91	4.93	4.88	3.68	2	4.16	G8	III
8518D	GAM	AQR	22.34	- 1.51	3.78	3.80	3.86	2	3.86	B9	III
8521D			22.35	-46.07	7.28	7.59	3.57	2	6.62	S47	
8538	BET	LAC	22.38	52.11	5.18	5.14	3.86	2	4.41	G9	III
8556	DEL1	GRU	22.46	-43.61	4.79	4.74	3.50	2	3.97	G5	
8560D	DEL2	GRU	22.47	-43.88	5.00	5.07	2.39	2	4.11	M4.5	III

YBS#	NAME		RA	DEC	S20	CDS	SIL	S	VIS	SP.TYPE	
8571D	DEL	CEP	22.47	58.29	4.93	4.89	3.83	2	4.25	F5	I
8572	5	LAC	22.47	47.59	5.32	5.38	3.09	2	4.38	M0	I
8582	NU	TUC	22.52	-62.11	5.67	5.76	2.95	2	4.80	M4	
8585D	ALF	LAC	22.50	50.15	3.75	3.75	3.75	2	3.75	A2	V
8597	ETA	AQR	22.57	- 0.25	3.87	3.91	4.04	2	4.04	B8	V
8621D			22.63	56.67	5.82	5.96	3.01	0	5.09	M4	
8628	EPS	PSA	22.65	-27.18	3.98	4.02	4.17	1	4.16	B8	V
8632	11	LAC	22.66	44.14	5.42	5.38	3.73	2	4.49	K3	III
8634D	ZET	PEG	22.67	10.70	3.24	3.28	3.42	2	3.42	B8	V
8636	BET	GRU	22.69	-47.01	2.95	3.06	0.16	2	2.11	M3	II
8637	19	PSA	22.68	-29.50	6.79	6.98	3.83	0	6.17	M5	
8649	66	AQR	22.70	-18.96	5.62	5.60	3.86	2	4.67	K4	III
8650D	ETA	PEG	22.70	30.09	3.59	3.55	2.49	2	2.92	G8	II
8665D	XI	PEG	22.76	12.05	4.51	4.51	3.89	2	4.17	F7	V
8667	LAM	PEG	22.76	23.43	4.76	4.71	3.42	2	3.94	G8	II
8675	EPS	GRU	22.78	-51.45	3.59	3.58	3.45	2	3.48	A2	V
8679	TAU	AQR	22.80	-13.72	5.02	5.03	2.94	2	4.04	M0	III
8684	MU	PEG	22.81	24.47	4.23	4.19	3.02	2	3.51	G8	III
8694	IOT	CEP	22.81	66.07	4.29	4.24	2.94	2	3.48	K1	III
8698	LAM	AQR	22.86	- 7.72	4.69	4.74	2.34	2	3.74	M2	III
8699D	15	LAC	22.85	43.18	5.89	5.92	3.68	0	4.94	M0	
8709	DEL	AQR	22.89	-15.95	3.34	3.33	3.23	2	3.26	A3	V
8720D	DEL	PSA	22.91	-32.67	4.96	4.92	3.74	2	4.21	G8	
8726			22.92	49.60	5.83	5.86	3.71	1	4.94	K5	I
8728	ALF	PSA	22.94	-29.75	1.26	1.25	1.15	2	1.15	A3	V
8747	ZET	GRU	22.99	-52.88	4.86	4.82	3.58	2	4.11	G5	III
8748			22.91	84.22	5.65	5.62	3.83	2	4.67	K4	III
8752			22.98	56.82	5.96	5.98	3.97	2	4.99	G0	I
8762	OMI	AND	23.01	42.18	3.33	3.41	3.62	2	3.64	B6	
8775D	BET	PEG	23.04	27.95	3.42	3.48	0.89	2	2.49	M2	II
8781	ALF	PEG	23.06	15.07	2.47	2.47	2.50	2	2.50	B9.5	III
8789D	86	AQR	23.09	-23.88	5.11	5.08	3.99	1	4.48	G9	
8795	55	PEG	23.10	9.27	5.53	5.55	3.37	2	4.57	M2	III
8812	88	AQR	23.14	-21.30	4.56	4.51	3.03	2	3.64	K0	III
8815D	57	PEG	23.14	8.55	5.87	6.01	3.06	0	5.14	M4	
8819D	PI	CEP	23.12	75.25	5.02	4.98	3.98	2	4.39	G2	III
8820	IOT	GRU	23.15	-45.38	4.71	4.66	3.43	2	3.90	K0	III
8834	PHI	AQR	23.22	- 6.18	5.19	5.21	2.98	2	4.24	M2	III
8841D	PSI1	AQR	23.24	- 9.22	5.08	5.03	3.66	2	4.24	K0	III
8848	GAM	TUC	23.27	-58.37	4.28	4.28	3.81	2	3.99	F0	III
8850	CHI	AQR	23.26	- 7.85	5.65	5.84	2.69	0	5.03	M5	
8852	GAM	PSC	23.26	3.15	4.39	4.36	3.19	2	3.69	G7	III
8860D	8	AND	23.28	48.88	5.80	5.84	3.41	2	4.85	M2	
8863	GAM	SCL	23.29	-32.67	5.28	5.23	3.86	2	4.41	G8	III
8892	98	AQR	23.36	-20.24	4.75	4.71	3.32	2	3.93	K0	III
8904	4	CAS	23.40	62.15	5.89	5.94	3.54	0	4.97	M1	III
8906	99	AQR	23.41	-20.77	5.40	5.39	3.49	2	4.42	K5	III
8916	THE	PSC	23.44	6.25	5.11	5.06	3.73	2	4.28	K1	III
8940	71	PEG	23.54	22.36	5.96	6.15	3.00	0	5.34	M5	
8961	LAM	AND	23.61	46.33	4.47	4.44	3.13	2	3.73	G8	III

YBS#	NAME		RA	DEC	S20	CDS	SIL	S	VIS	SP.TYPE	
8969	IOT	PSC	23.64	5.50	4.45	4.45	3.84	2	4.10	F7	V
8974	GAM	CEP	23.64	77.48	4.02	3.96	2.68	2	3.22	K1	IV
8991	77	PEG	23.70	10.20	5.93	6.01	3.44	0	5.06	M2	
8992	R	AQR	23.71	-15.42	6.14	6.42	2.90	0	5.80	M7	
9030	80	PEG	23.83	9.18	6.60	6.71	3.95	0	5.79	M3	
9036	PHI	PEG	23.85	18.98	5.92	6.00	3.43	0	5.05	M2	
9045	RHO	CAS	23.89	57.36	5.38	5.35	3.88	2	4.52	F8	I
9047			23.89	- 0.04	6.23	6.42	3.27	0	5.61	M5	
9064	PSI	PEG	23.94	25.00	5.57	5.63	3.09	2	4.67	M3	III
9072	OMG	PSC	23.97	6.73	4.31	4.31	3.79	2	4.01	F4	IV
9089	30	PSC	0.01	- 6.15	5.37	5.44	2.77	2	4.47	M3	IV

APPENDIX C

STAR DISTRIBUTION RESULTS

The plots of star distributions resulting from the Star Availability Studies described in subsection 5.3 are presented in this Appendix. Refer to subsection 5.3.5 for explanation of the plots and their symbology. Following is a guide to the location of the individual plots:

STAR MAPPER RESULTS

Detector	FOV (deg)	Page
CdS	4	C-3
"	6	C-4
"	8	C-5
"	10	C-6
S-20	4	C-7
"	6	C-8
"	8	C-9
"	10	C-10
Si	4	C-11
"	6	C-12
"	8	C-13
"	10	C-14

STAR TRACKER RESULTS (S-20)
(All Stars Plotted - No Selection)

Date	Page
7/71	C-15
8/71	C-16
9/71	C-17
10/71	C-18
11/71	C-19
12/71	C-20

STAR TRACKER RESULTS (S-20)

(Only Target Stars Plotted - Stars Selected for Use)

Measurement Interval - Deg	Date	Page
8	7/71	C-21
"	8/71	C-22
"	9/71	C-23
"	10/71	C-24
"	11/71	C-25
"	12/71	C-26
20	7/71	C-27
"	8/71	C-28
"	9/71	C-29
"	10/71	C-30
"	11/71	C-31
"	12/71	C-32
40	7/71	C-33
"	8/71	C-34
"	9/71	C-35
"	10/71	C-36
"	11/71	C-37
"	12/71	C-38

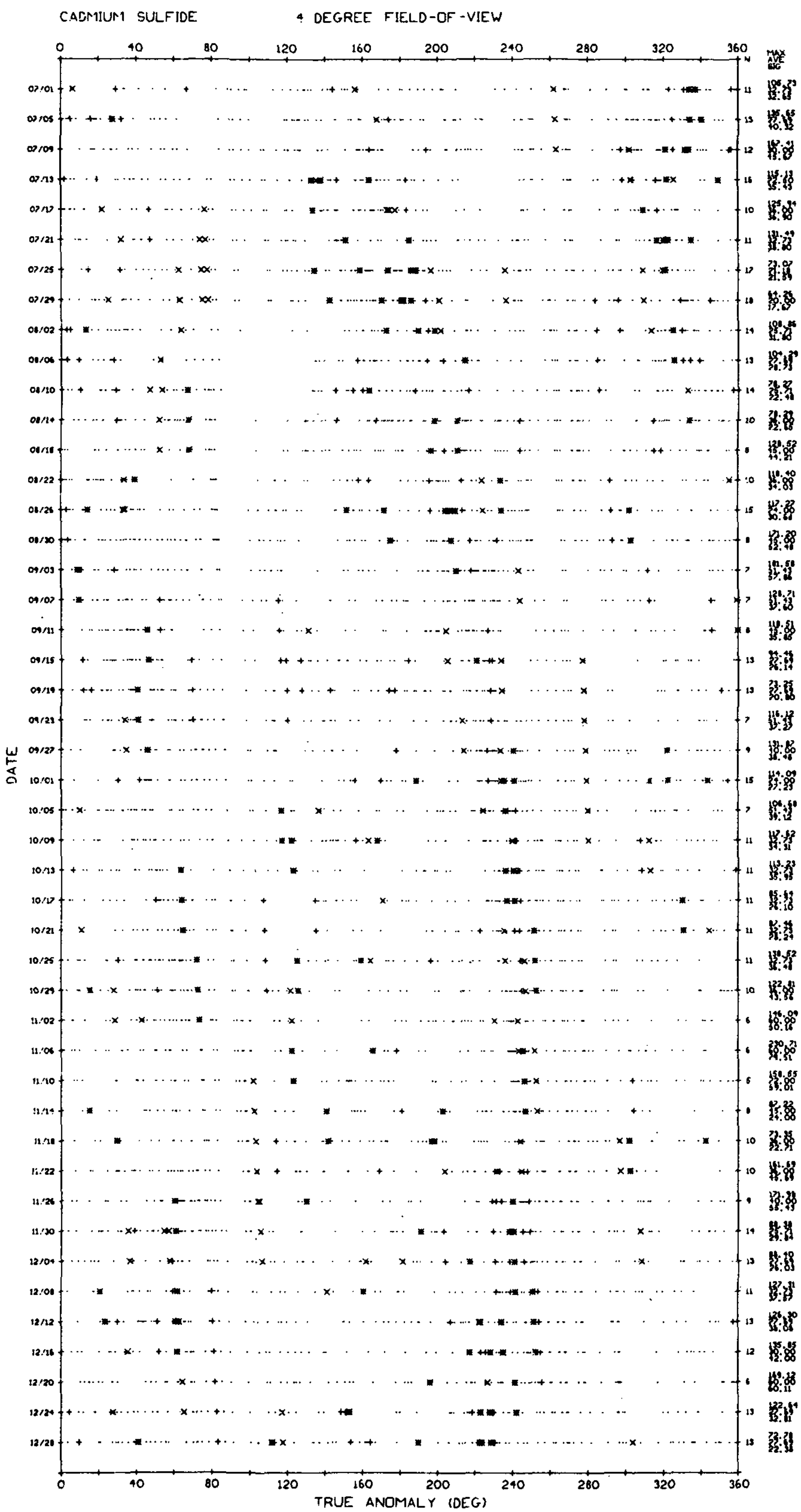
CADMIUM SULFIDE
4 DEGREE FIELD-OF-VIEW
DATE
TRUE ANOMALY (DEG)

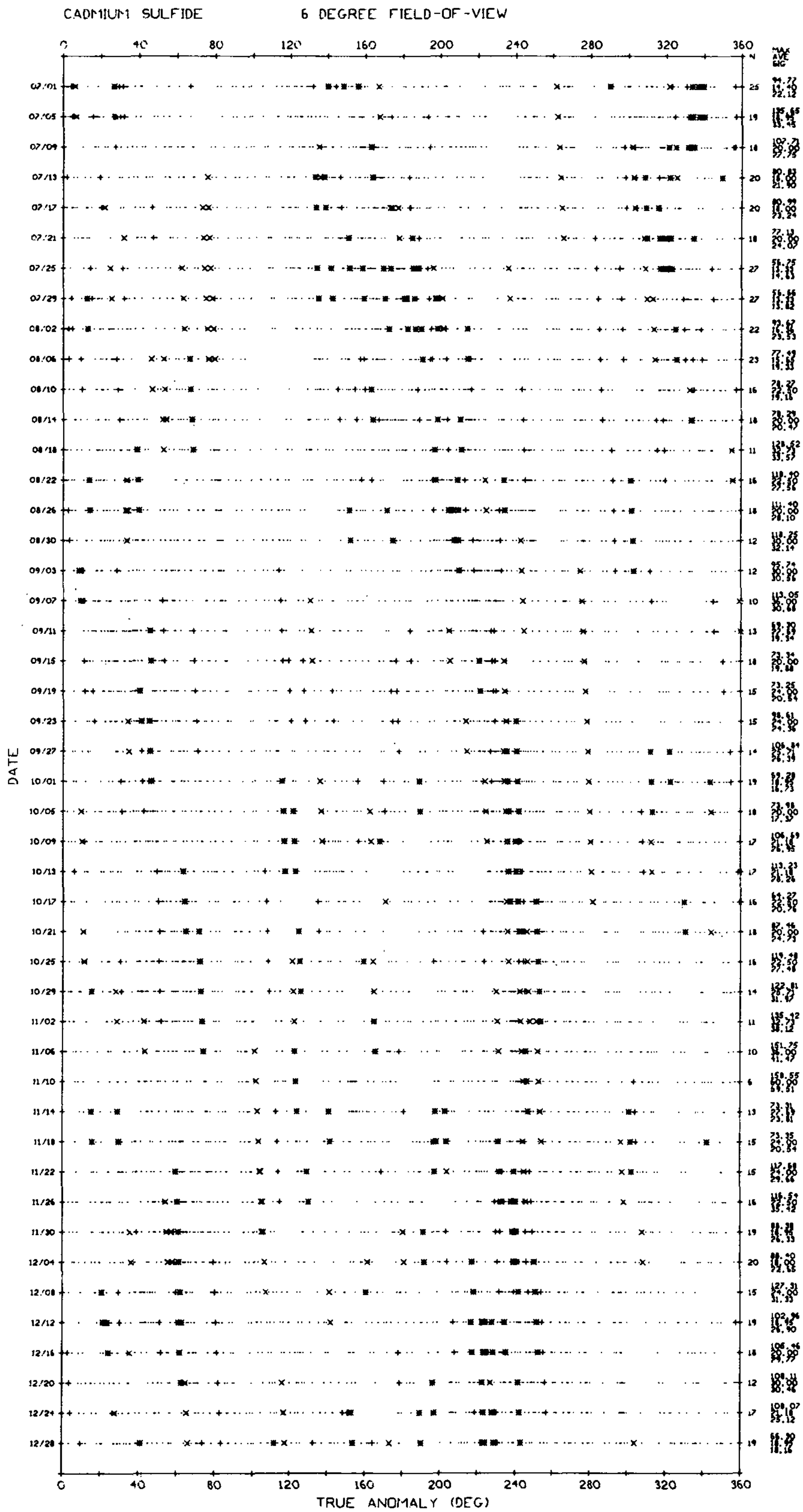
CADMIUM SULFIDE
6 DEGREE FIELD-OF-VIEW
DATE
TRUE ANOMALY (DEG)
0
40
80
120
160
200
240
280
320
360

CADMIUM SULFIDE 8 DEGREE FIELD-OF-VIEW

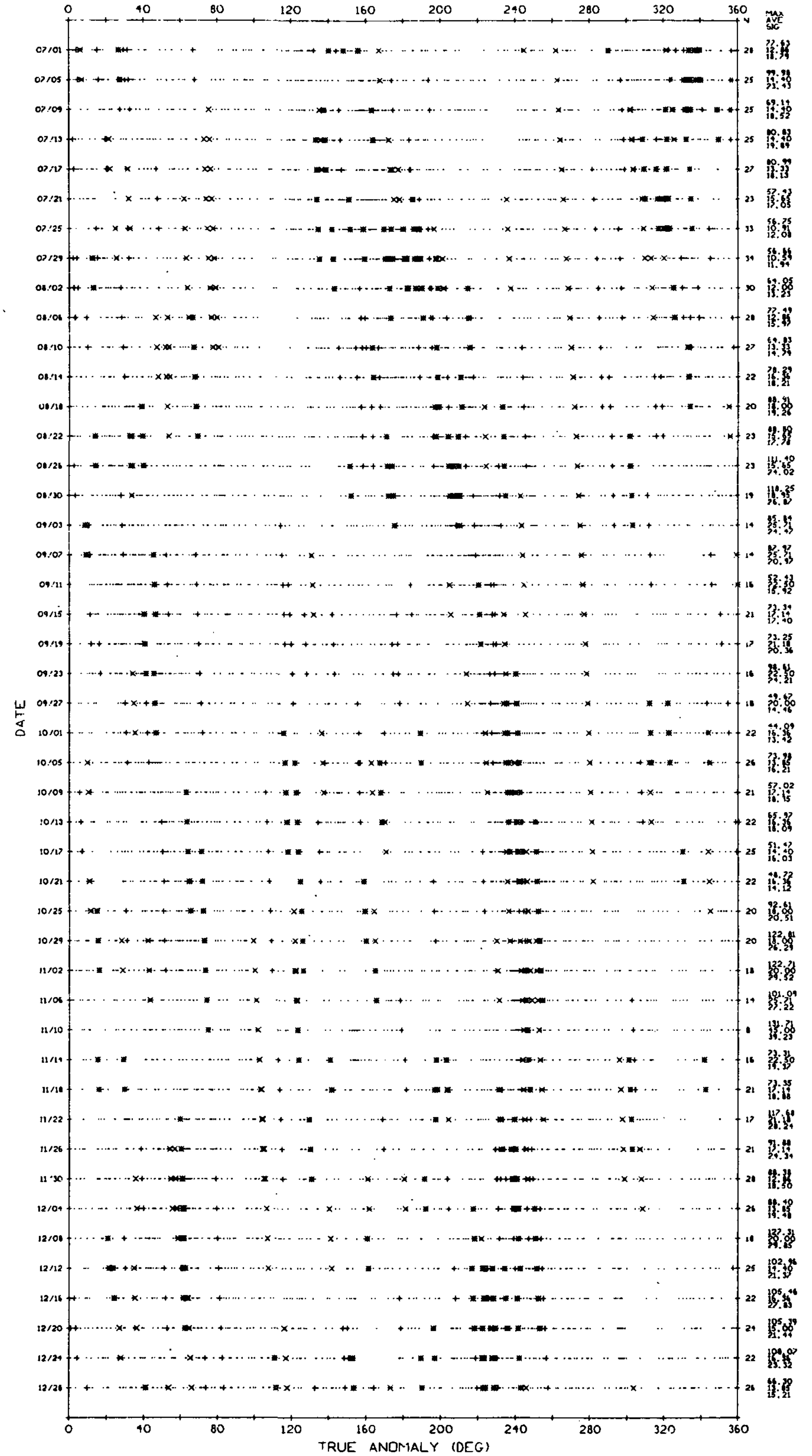

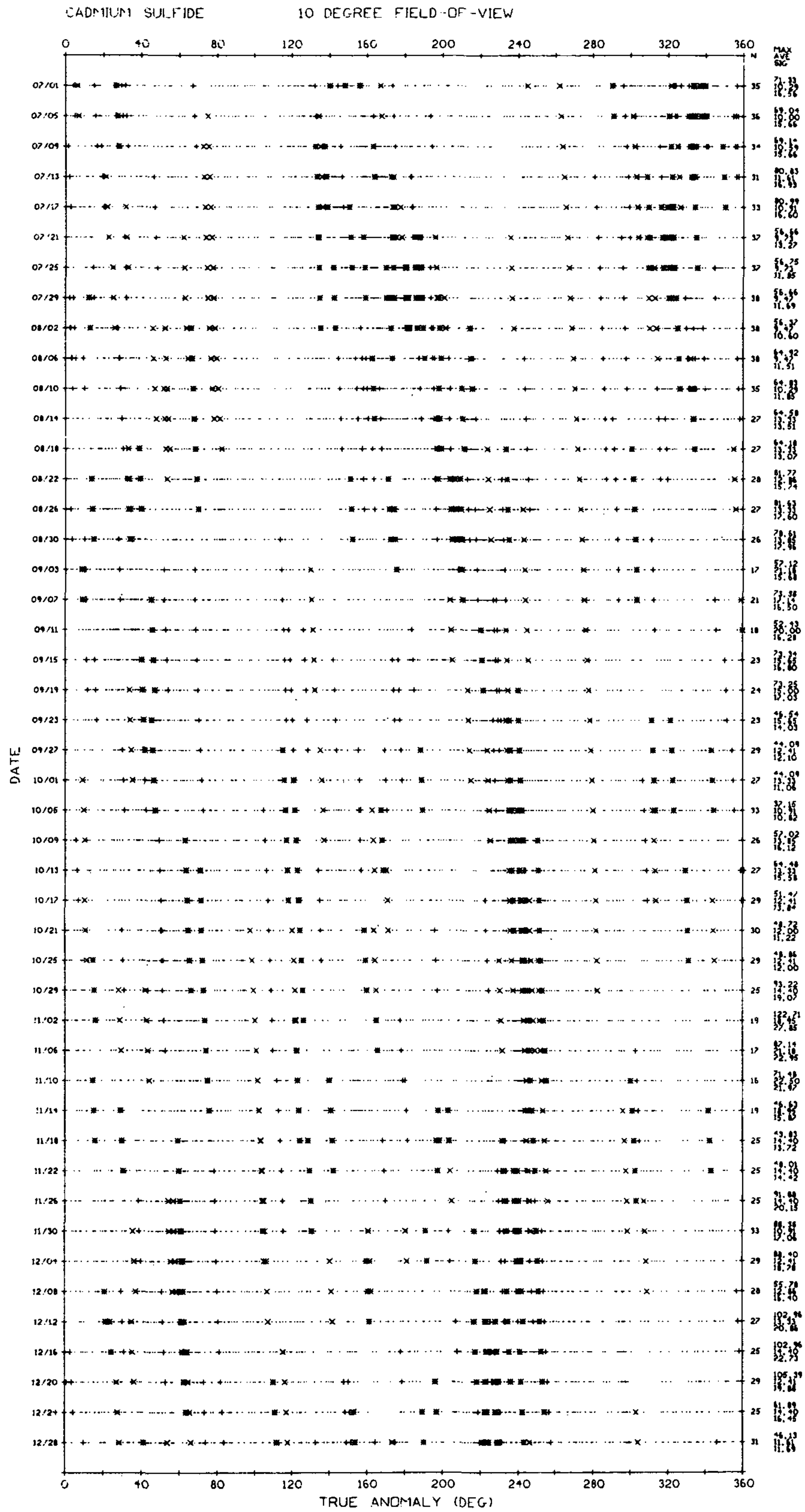
CADMIUM SULFIDE
10 DEGREE FIELD-OF-VIEW
DATE
TRUE ANOMALY (DEG)
0
40
80
120
160
200
240
280
320
360

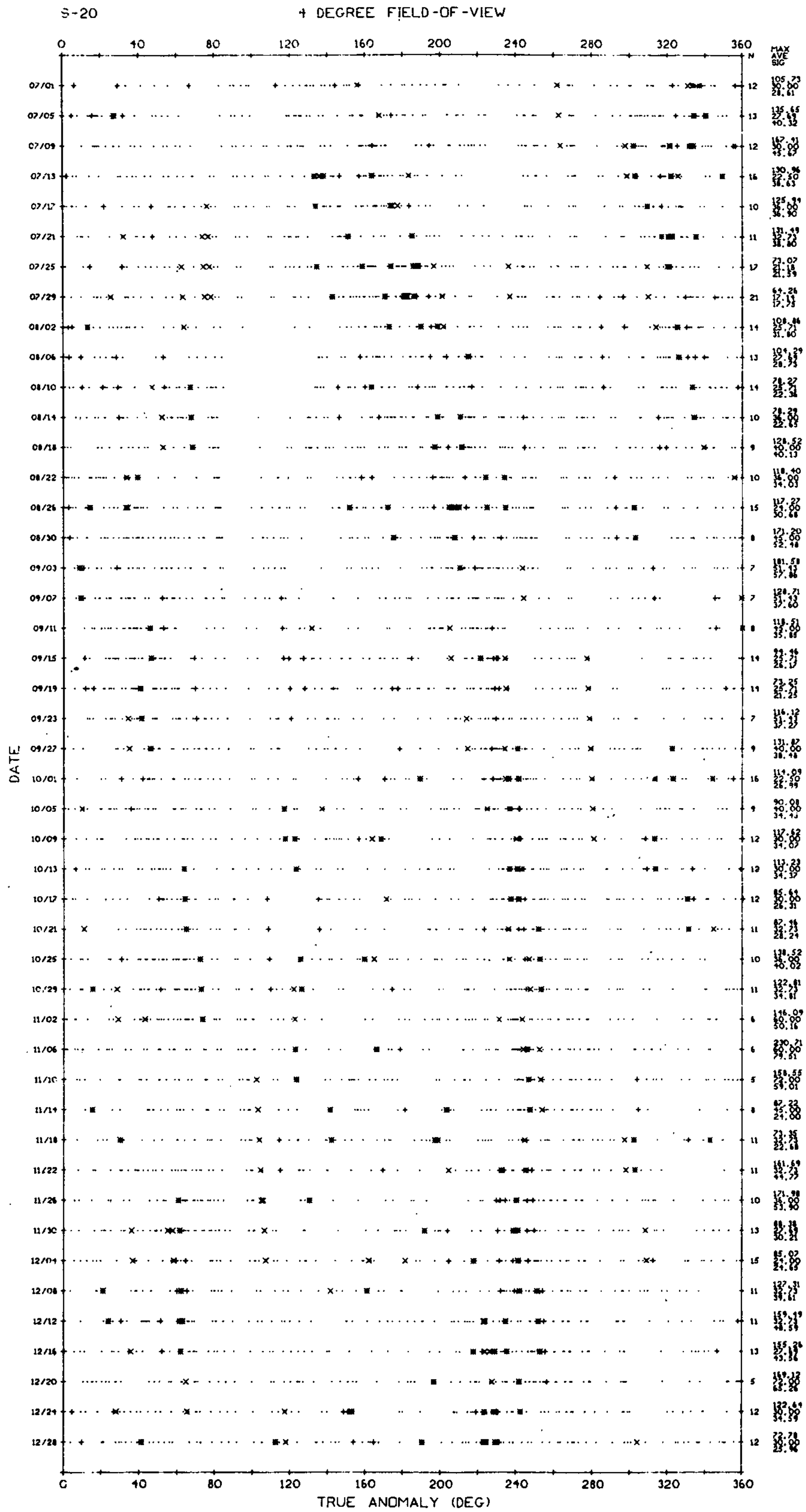
S-20
+ DEGREE FIELD-OF-VIEW
TRUE ANOMALY (DEG)
DATE
N
MAX
AVE
SIG
0
40
80
120
160
200
240
280
320
360

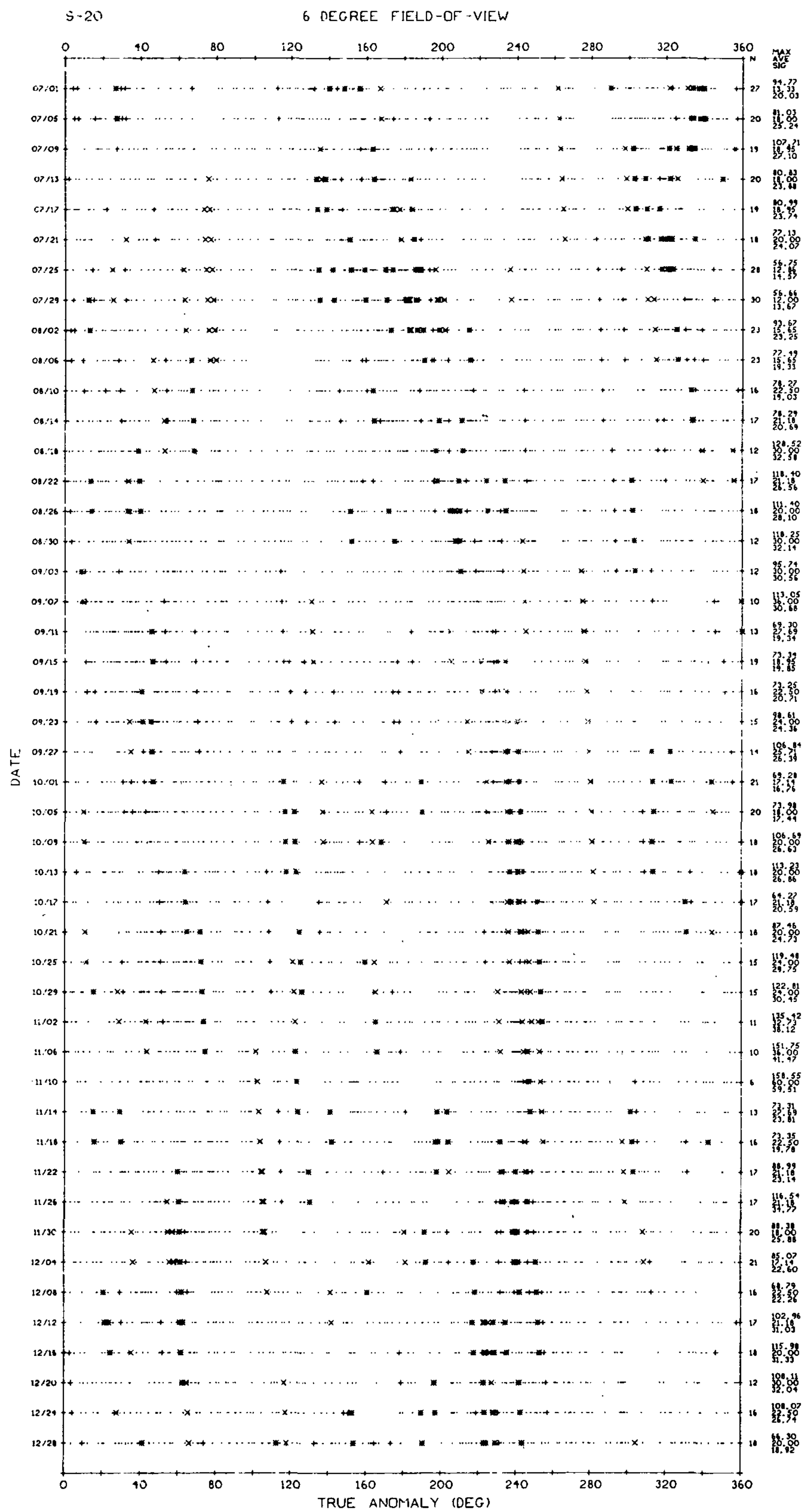
S-20
6 DEGREE FIELD-OF-VIEW
TRUE ANOMALY (DEG)
DATE
N
MAX
AVE
SIG

8 DEGREE FIELD-OF-VIEW

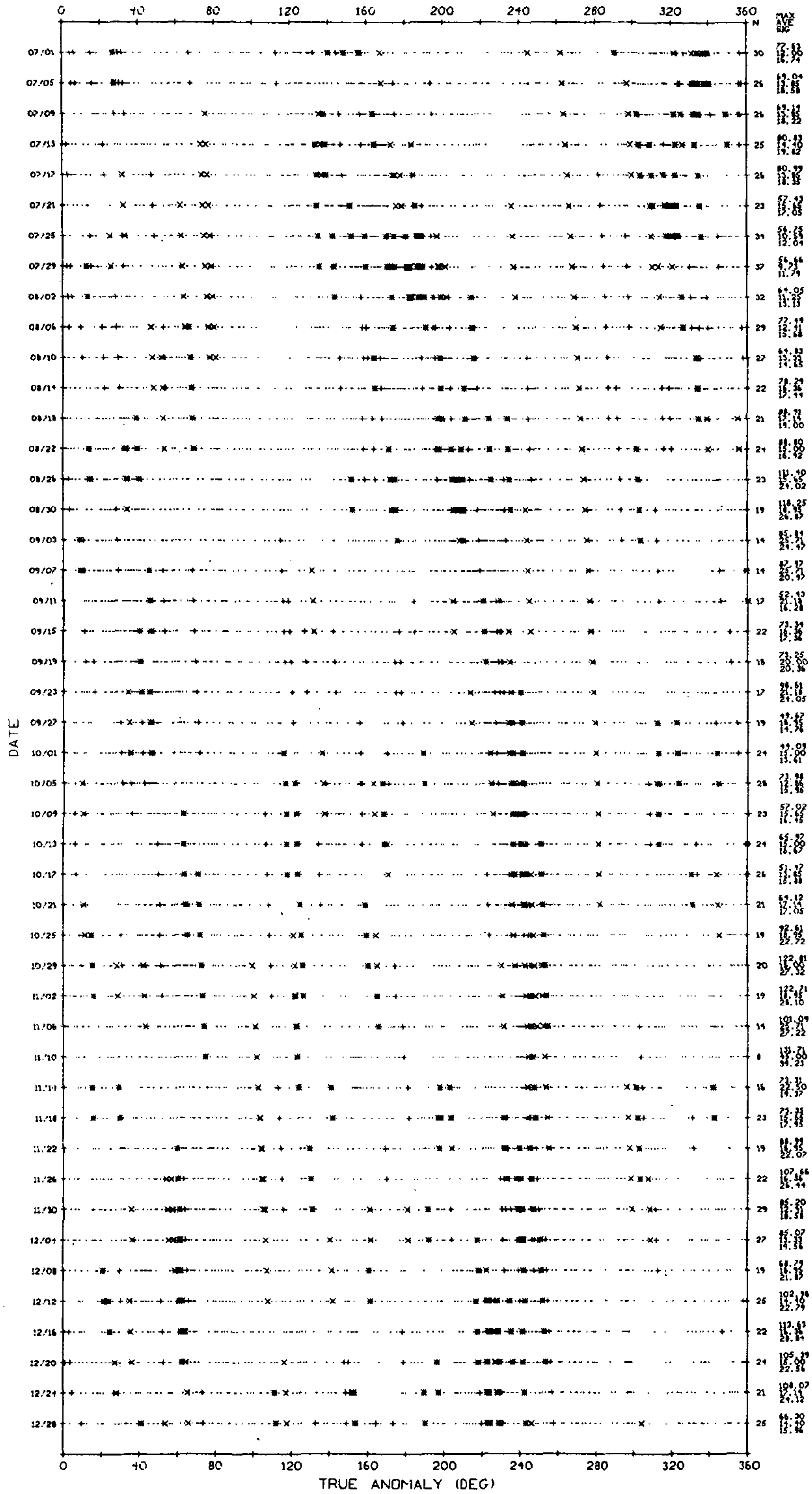

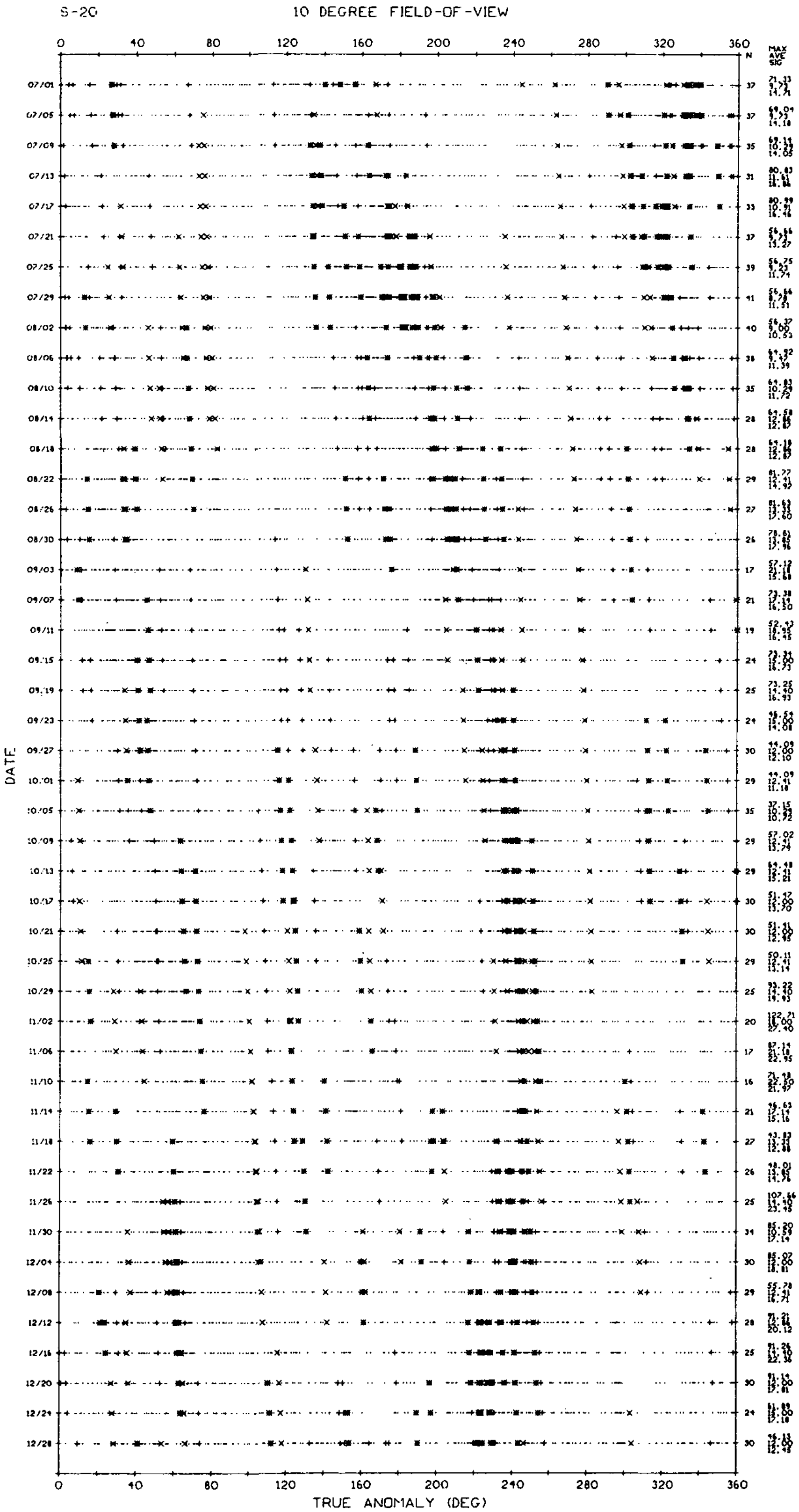
S-20
10 DEGREE FIELD-OF-VIEW
TRUE ANOMALY (DEG)
DATE
MAX
AVE
SIG
N

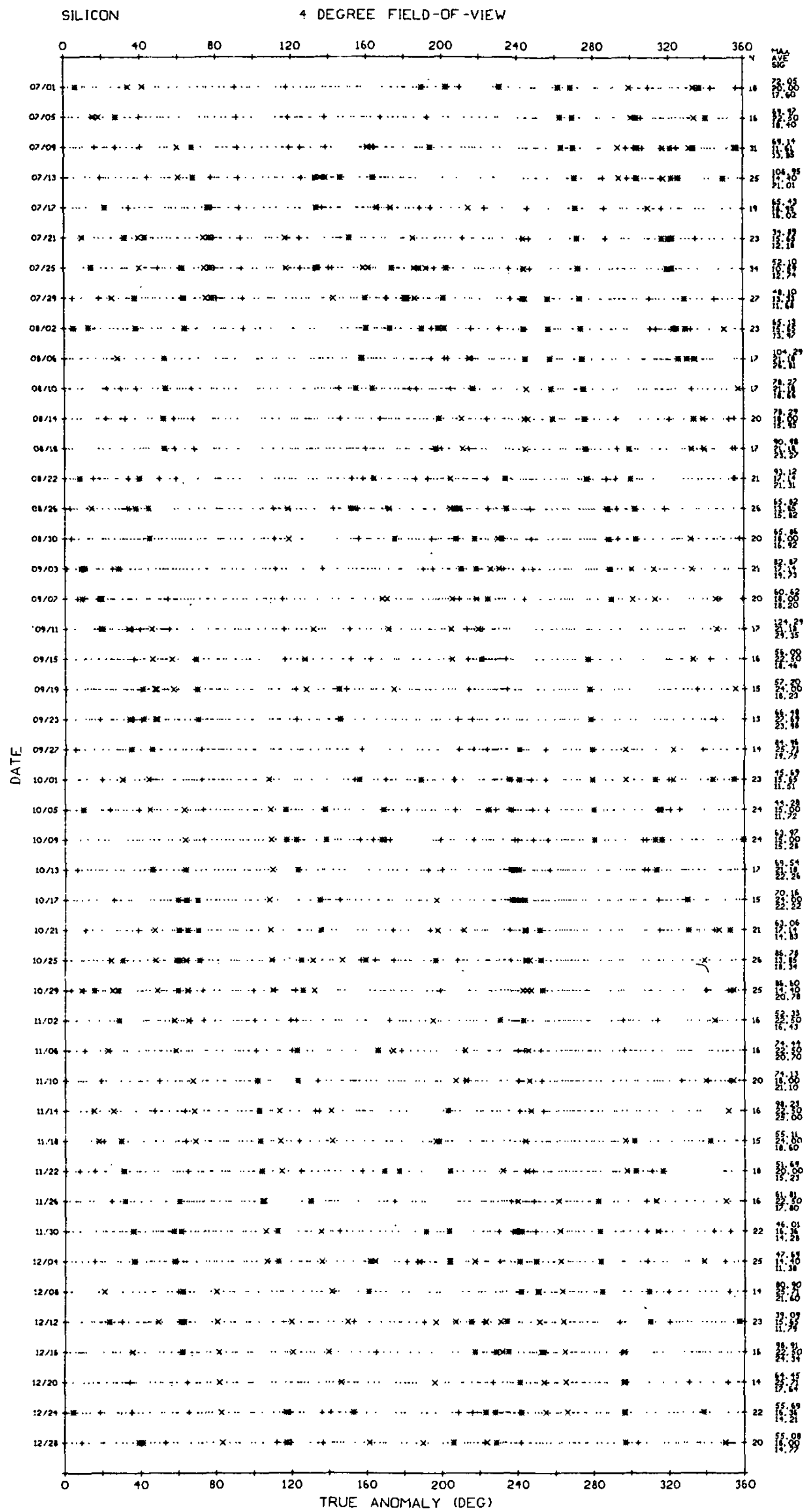
SILICON
4 DEGREE FIELD-OF-VIEW
DATE
TRUE ANOMALY (DEG)
0 40 80 120 160 200 240 280 320 360
MAX AVE SIG
07/01
07/05
07/09
07/13
07/17
07/21
07/25
07/29
08/02
08/06
08/10
08/14
08/18
08/22
08/26
08/30
09/03
09/07
09/11
09/15
09/19
09/23
09/27
10/01
10/05
10/09
10/13
10/17
10/21
10/25
10/29
11/02
11/06
11/10
11/14
11/18
11/22
11/26
11/30
12/04
12/08
12/12
12/16
12/20
12/24
12/28

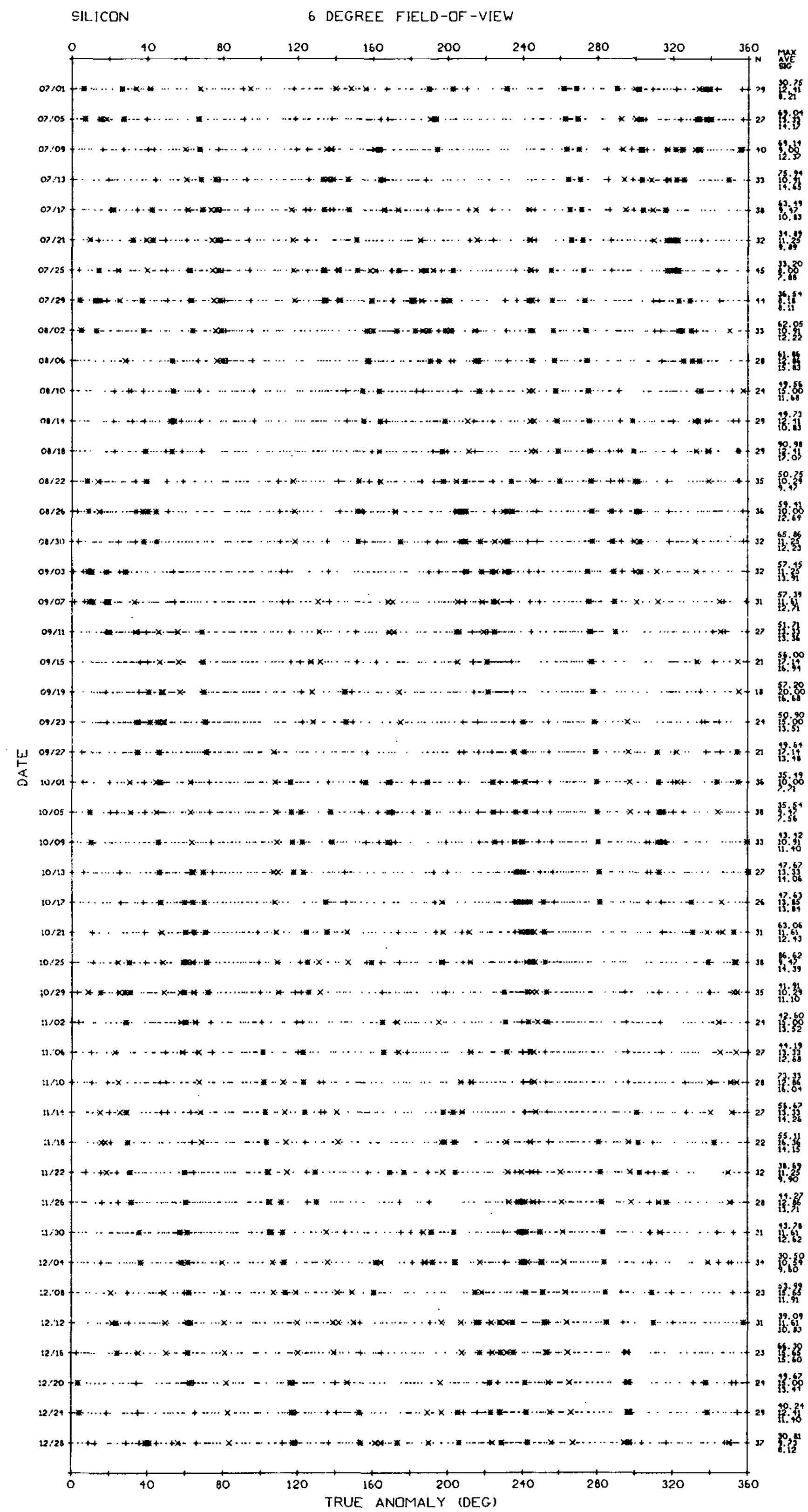

SILICON
6 DEGREE FIELD-OF-VIEW
TRUE ANOMALY (DEG)
DATE

SILICON 8 DEGREE FIELD-OF-VIEW

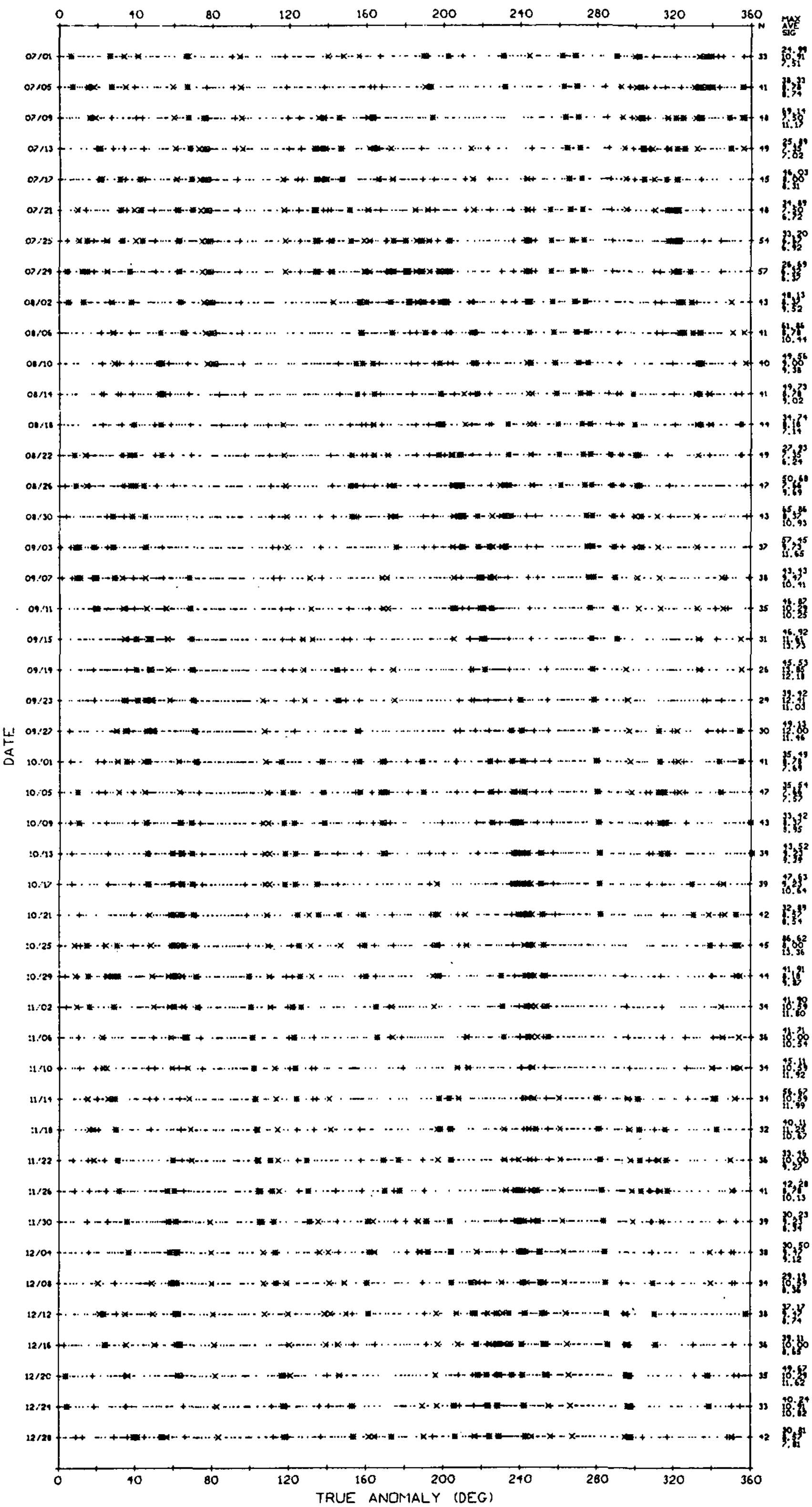

SILICON 10 DEGREE FIELD-OF-VIEW

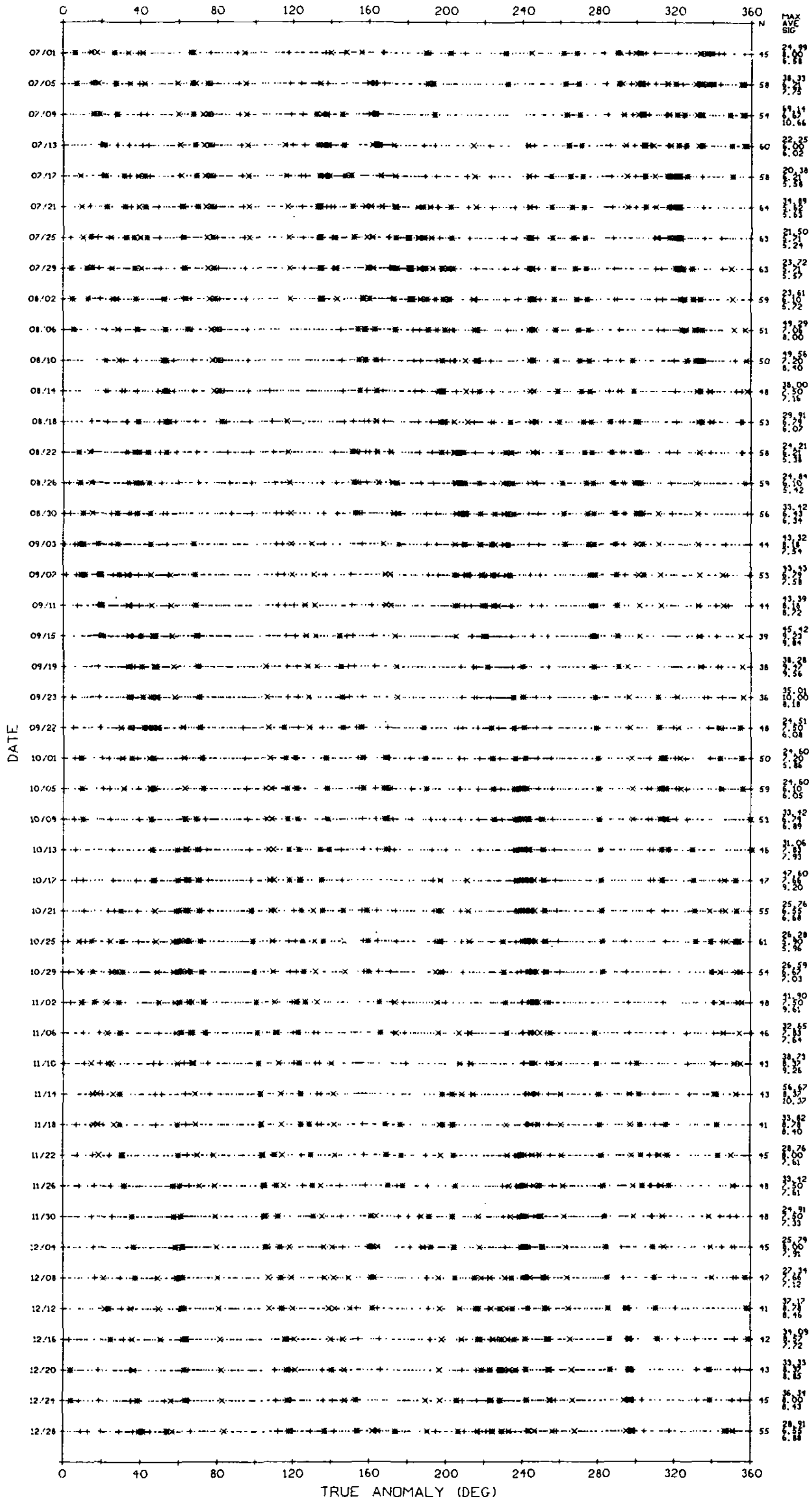

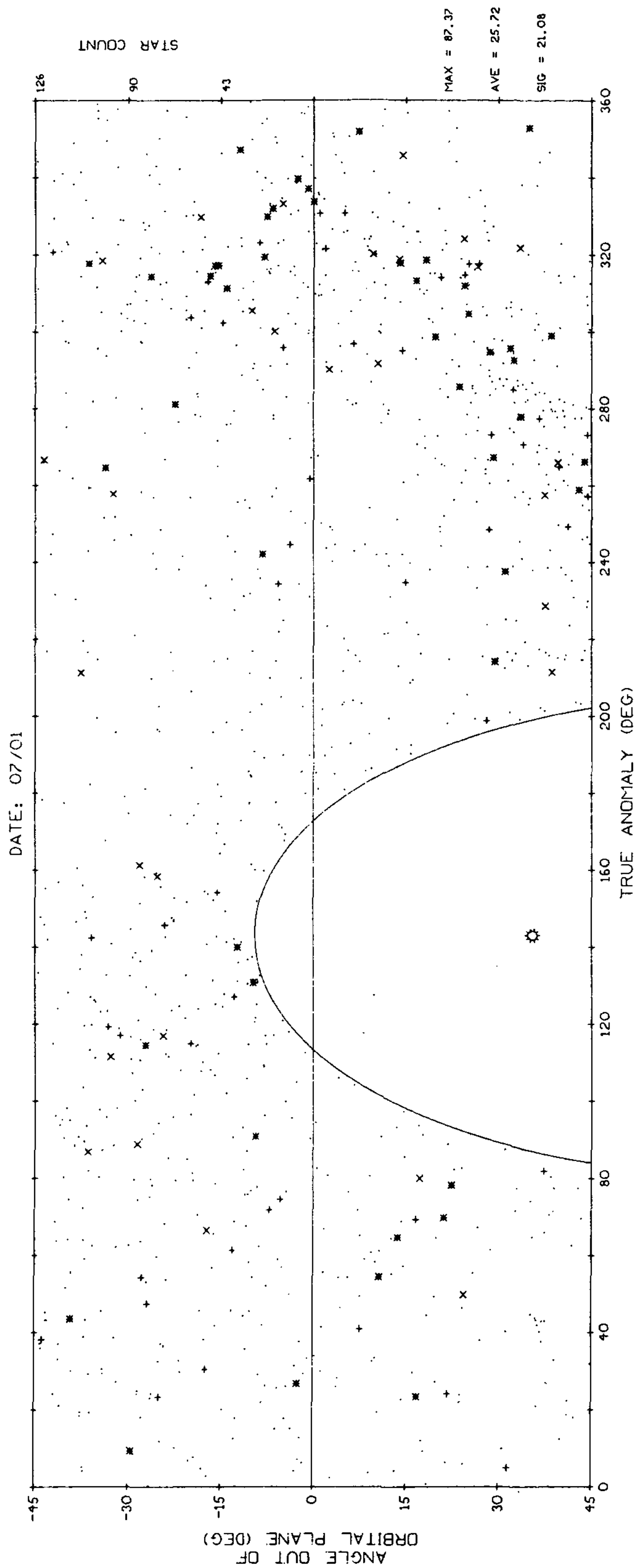
DATE: 07/01
STAR COUNT
126
90
43
MAX = 87.37
AVE = 25.72
SIG = 21.08
TRUE ANOMALY (DEG)
0
40
80
120
160
200
240
280
320
360
ANGLE OUT OF ORBITAL PLANE (DEG)
-45
-30
-15
0
15
30
45

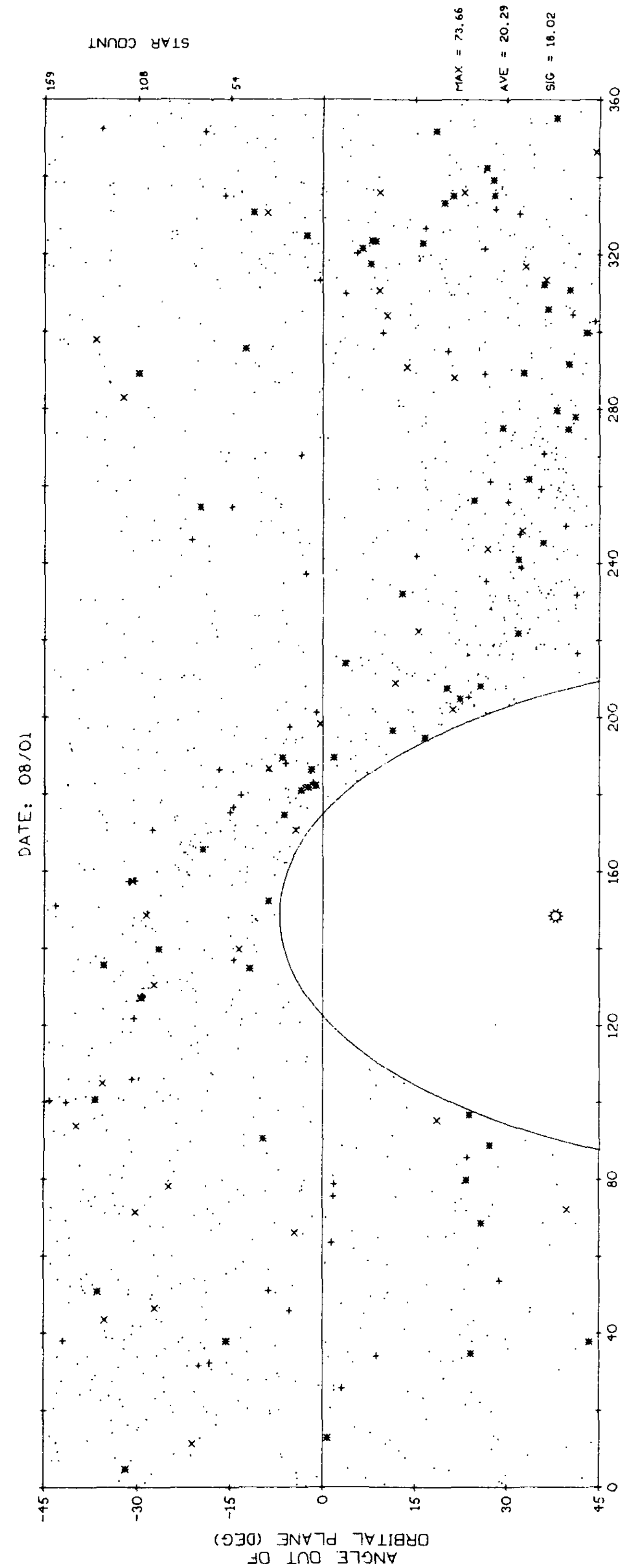
DATE: 08/01
STAR COUNT
159
108
54
MAX = 73.66
AVE = 20.29
SIG = 18.02
ANGLE OUT OF ORBITAL PLANE (DEG)
-45
-30
-15
0
15
30
45
TRUE ANOMALY (DEG)
0
40
80
120
160
200
240
280
320
360

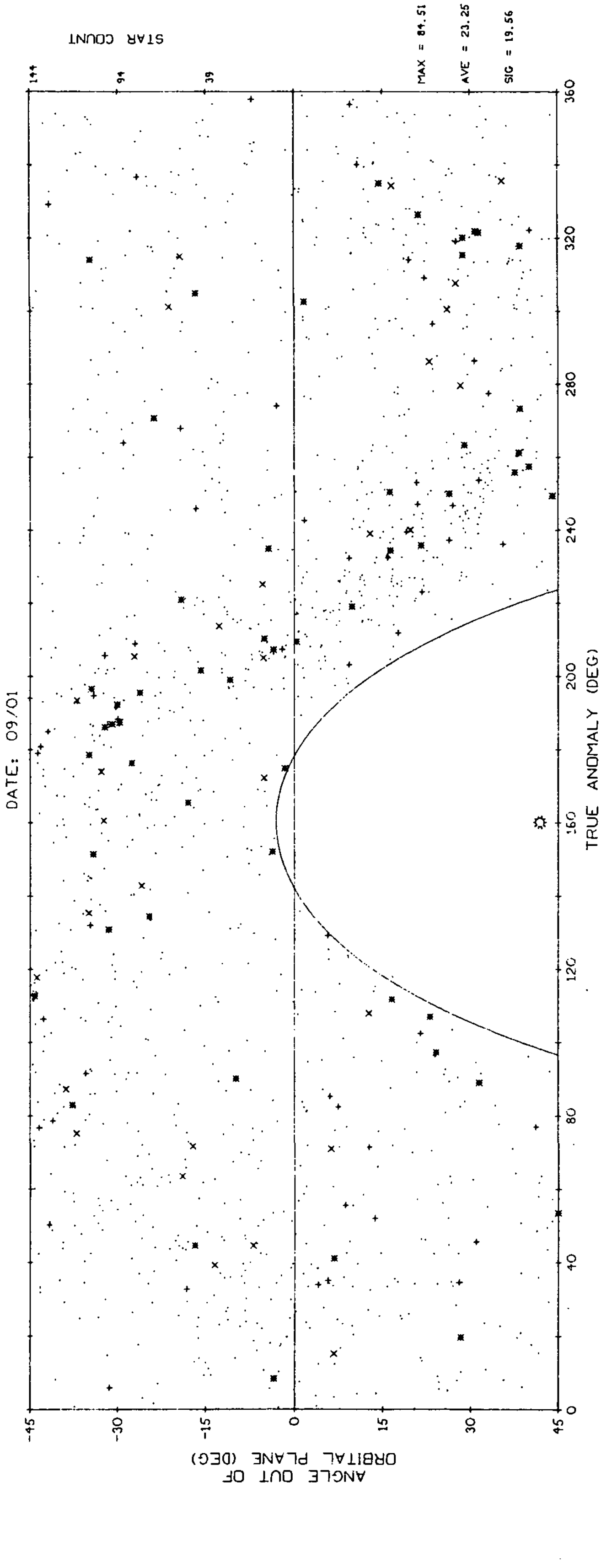
DATE: 09/01
STAR COUNT
MAX = 84.51
AVE = 23.25
SIG = 19.56
TRUE ANOMALY (DEG)
ANGLE OUT OF ORBITAL PLANE (DEG)

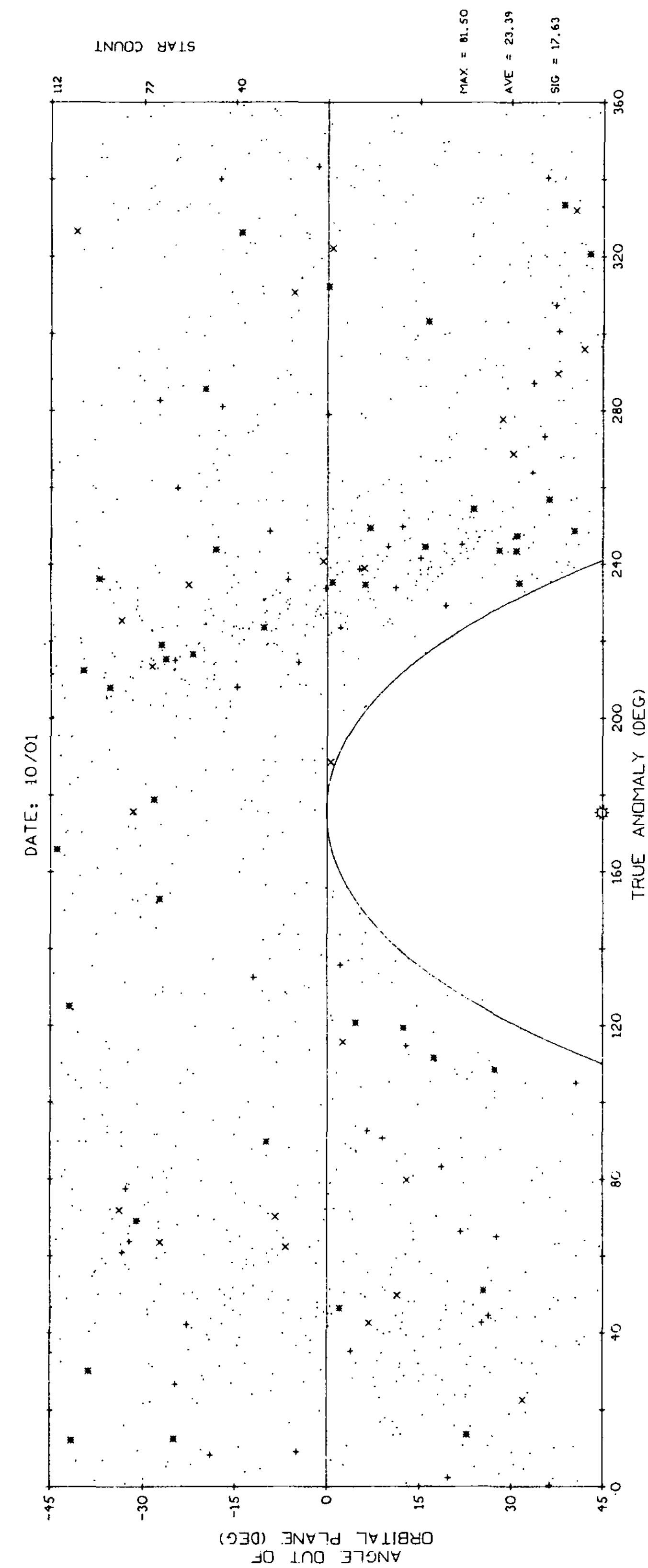

DATE: 10/01
STAR COUNT
112
77
40
MAX = 81.50
AVE = 23.39
SIG = 17.63
TRUE ANOMALY (DEG)
0
40
80
120
160
200
240
280
320
360
ANGLE OUT OF ORBITAL PLANE (DEG)
-45
-30
-15
0
15
30
45

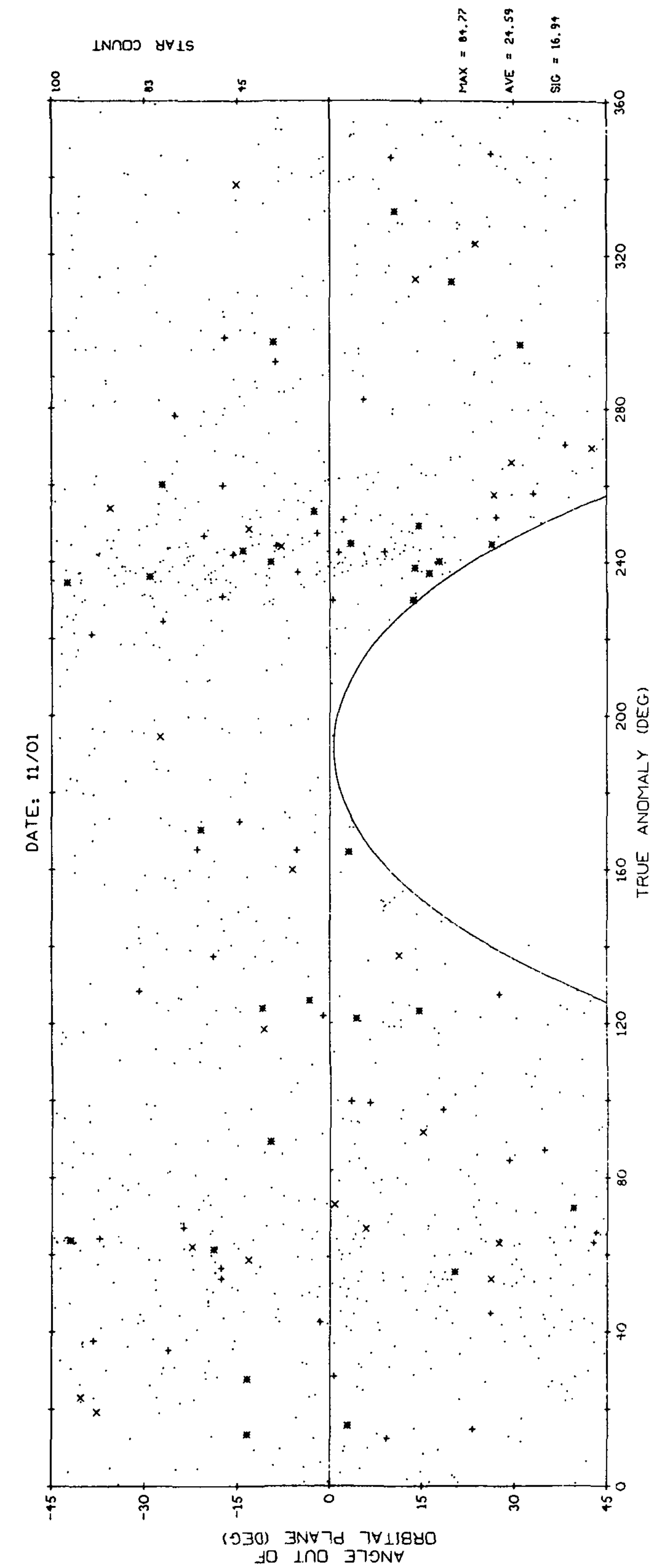
DATE: 11/01
TRUE ANOMALY (DEG)
ANGLE OUT OF ORBITAL PLANE (DEG)
STAR COUNT
MAX = 84.77
AVE = 24.59
SIG = 16.94

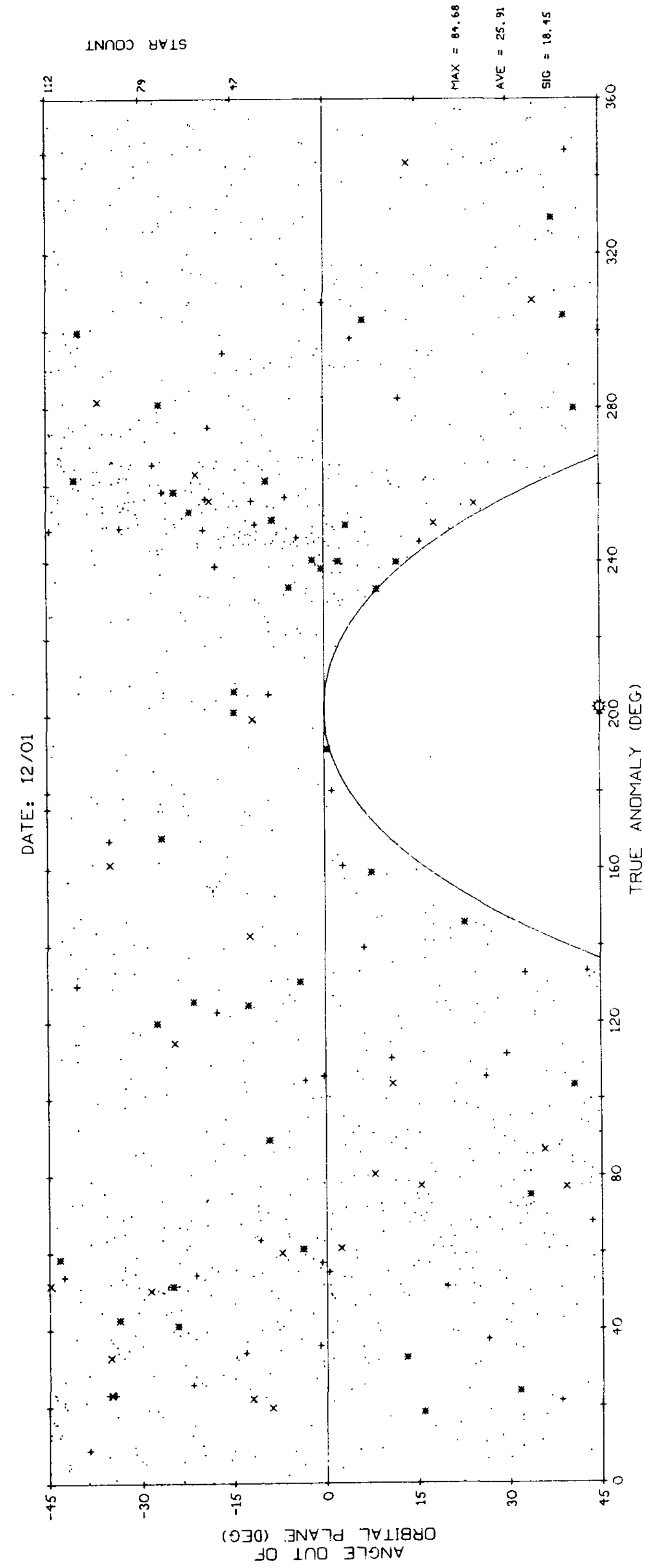
DATE: 12/01
STAR COUNT
112
79
47
MAX = 84.68
AVE = 25.91
SIG = 18.45
TRUE ANOMALY (DEG)
0
40
80
120
160
200
240
280
320
360
ANGLE OUT OF
ORBITAL PLANE (DEG)
-45
-30
-15
0
15
30
45

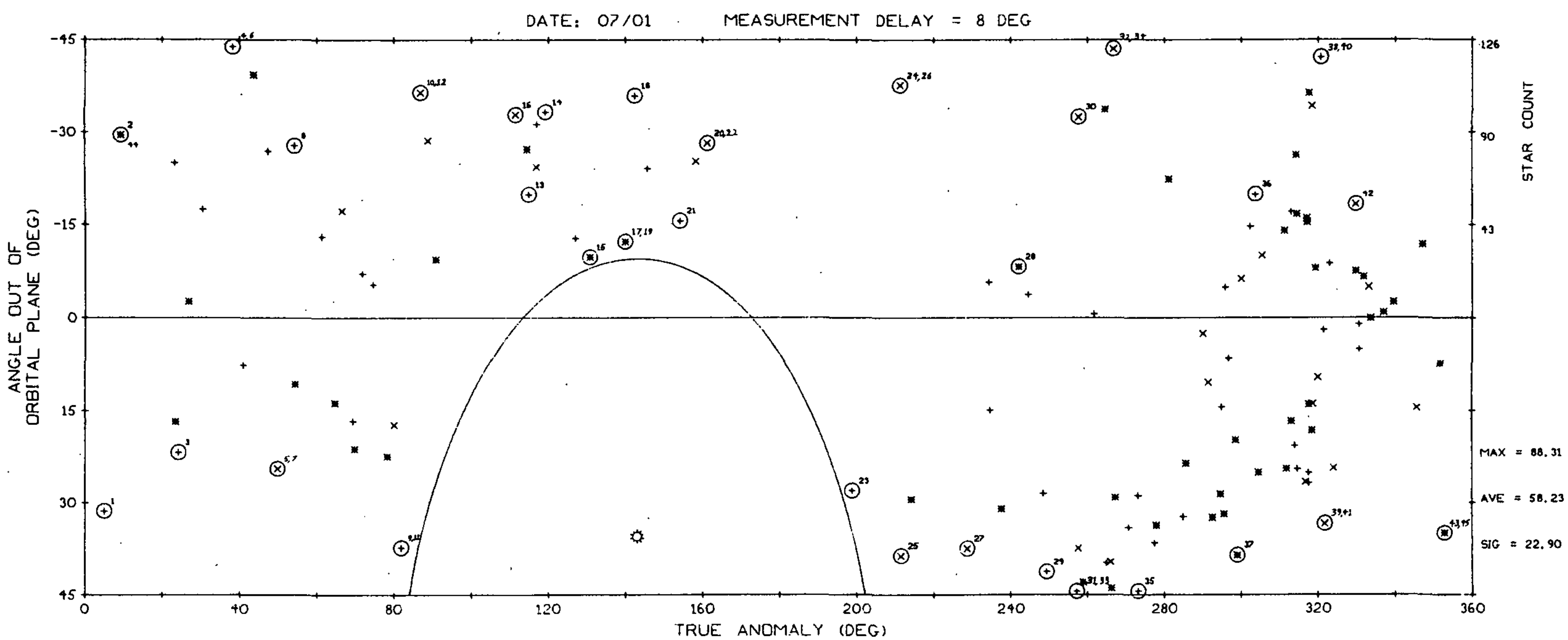
DATE: 07/01
MEASUREMENT DELAY = 8 DEG
ANGLE OUT OF ORBITAL PLANE (DEG)
TRUE ANOMALY (DEG)
STAR COUNT
-45
-30
-15
0
15
30
45
0
40
80
120
160
200
240
280
320
360
126
90
43
MAX = 88.31
AVE = 58.23
SIG = 22.90

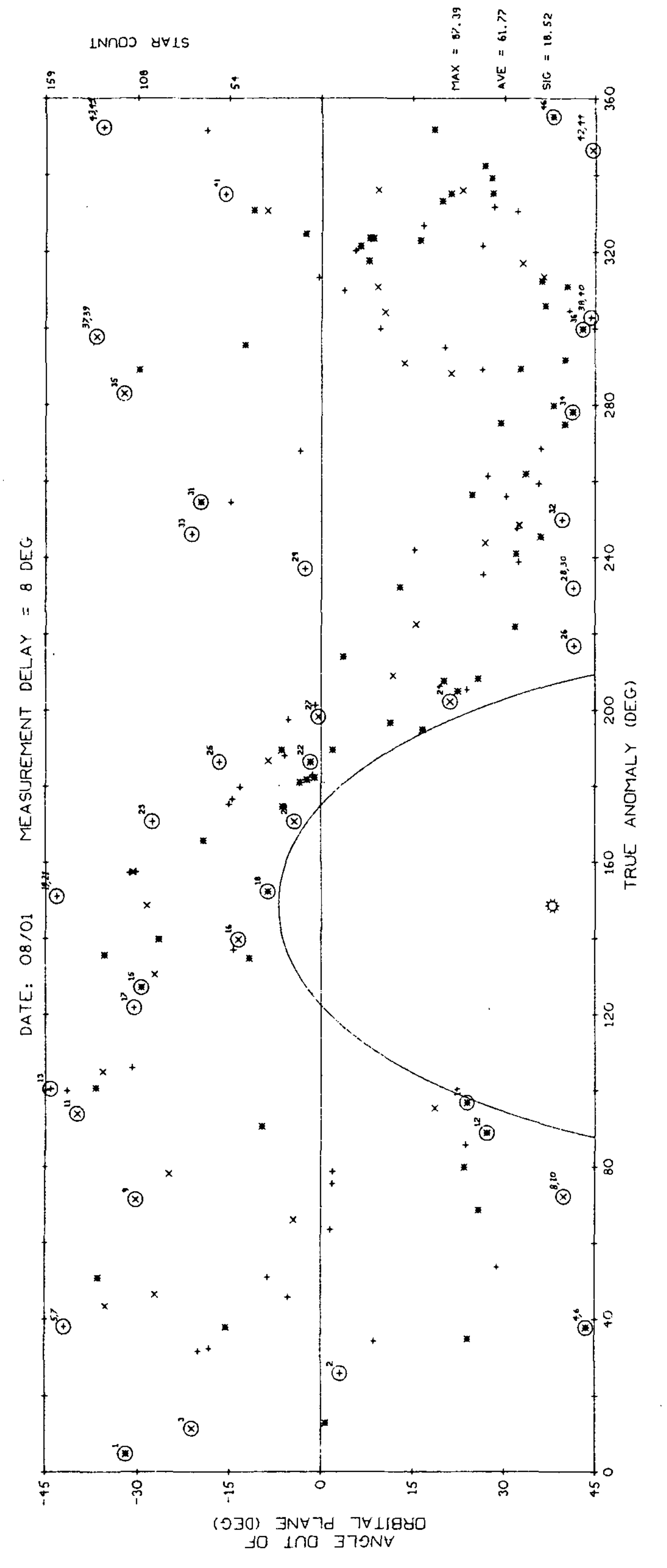
DATE: 08/01
MEASUREMENT DELAY = 8 DEG
STAR COUNT
159
108
54
MAX = 87.39
AVE = 61.77
SIG = 18.52
ANGLE OUT OF ORBITAL PLANE (DEG)
-45
-30
-15
0
15
30
45
TRUE ANOMALY (DEG)
0
40
80
120
160
200
240
280
320
360

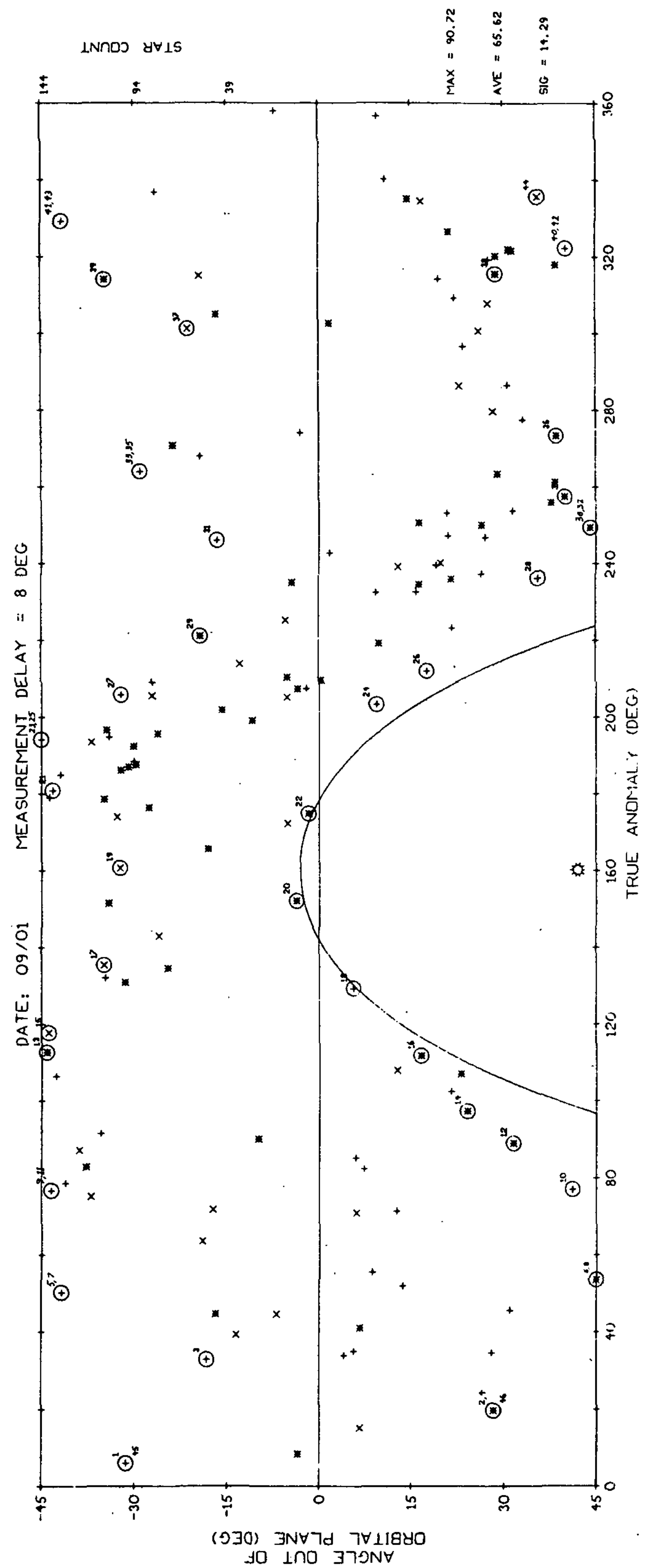

DATE: 09/01
MEASUREMENT DELAY = 8 DEG
STAR COUNT
144
94
39
MAX = 90.72
AVE = 65.62
SIG = 14.29
TRUE ANOMALY (DEG)
ANGLE OUT OF ORBITAL PLANE (DEG)
-45
-30
-15
0
15
30
45
0
40
80
120
160
200
240
280
320
360

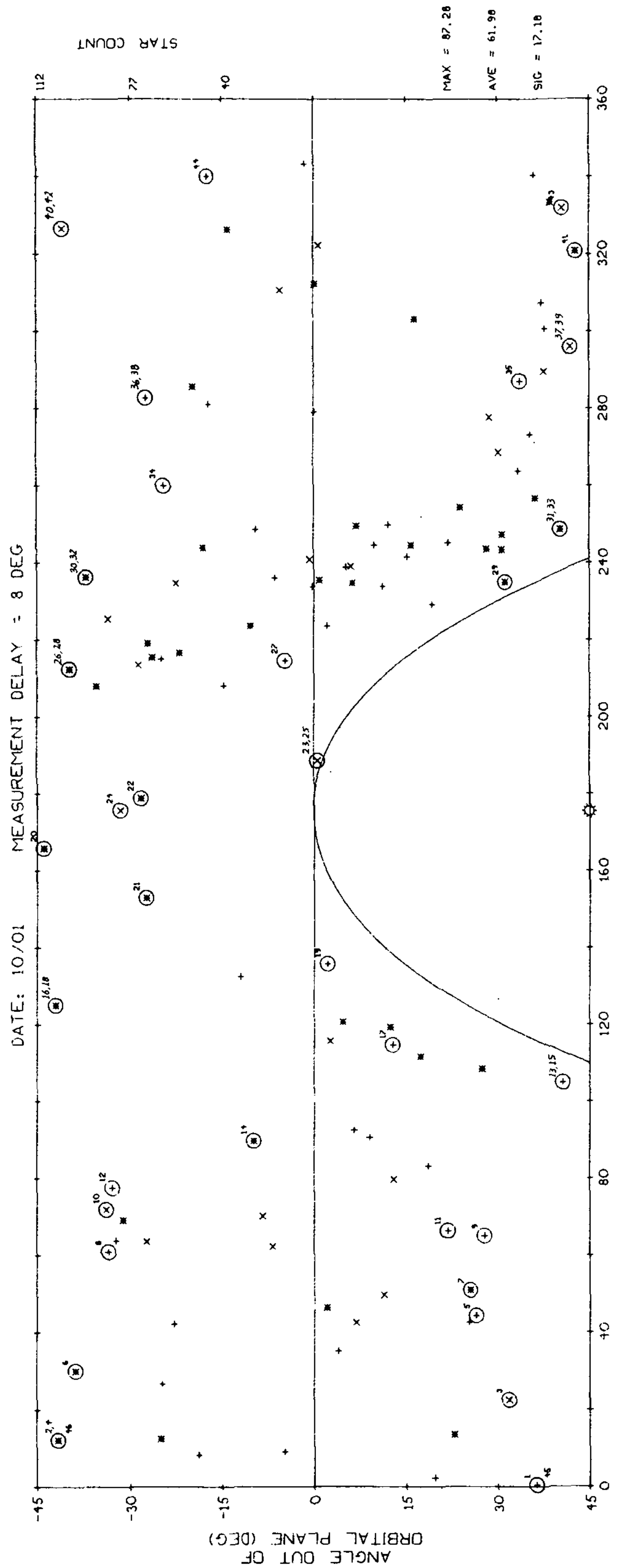
DATE: 10/01
MEASUREMENT DELAY = 8 DEG
TRUE ANOMALY (DEG)
ANGLE OUT OF ORBITAL PLANE (DEG)
STAR COUNT
MAX = 87.28
AVE = 61.98
SIG = 17.18

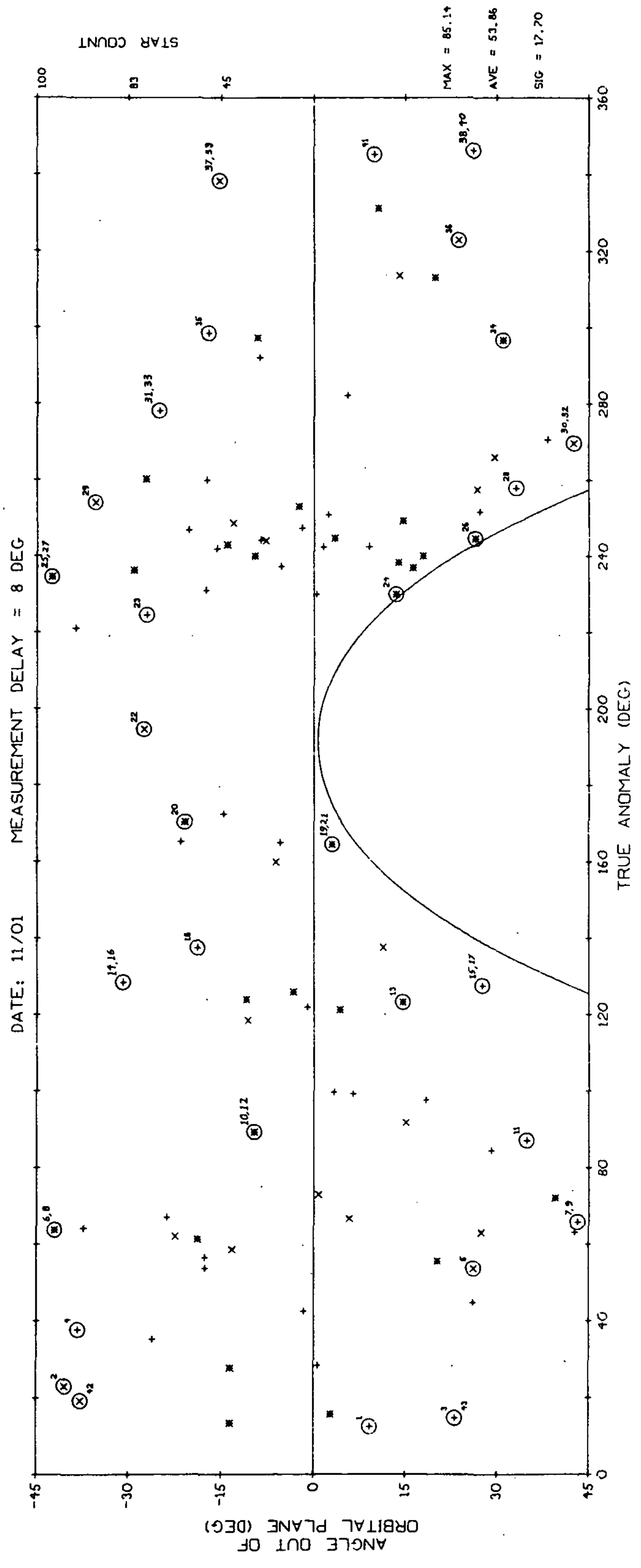
DATE: 11/01
MEASUREMENT DELAY = 8 DEG
TRUE ANOMALY (DEG)
ANGLE OUT OF ORBITAL PLANE (DEG)
STAR COUNT
MAX = 85.14
AVE = 53.86
SIG = 17.70

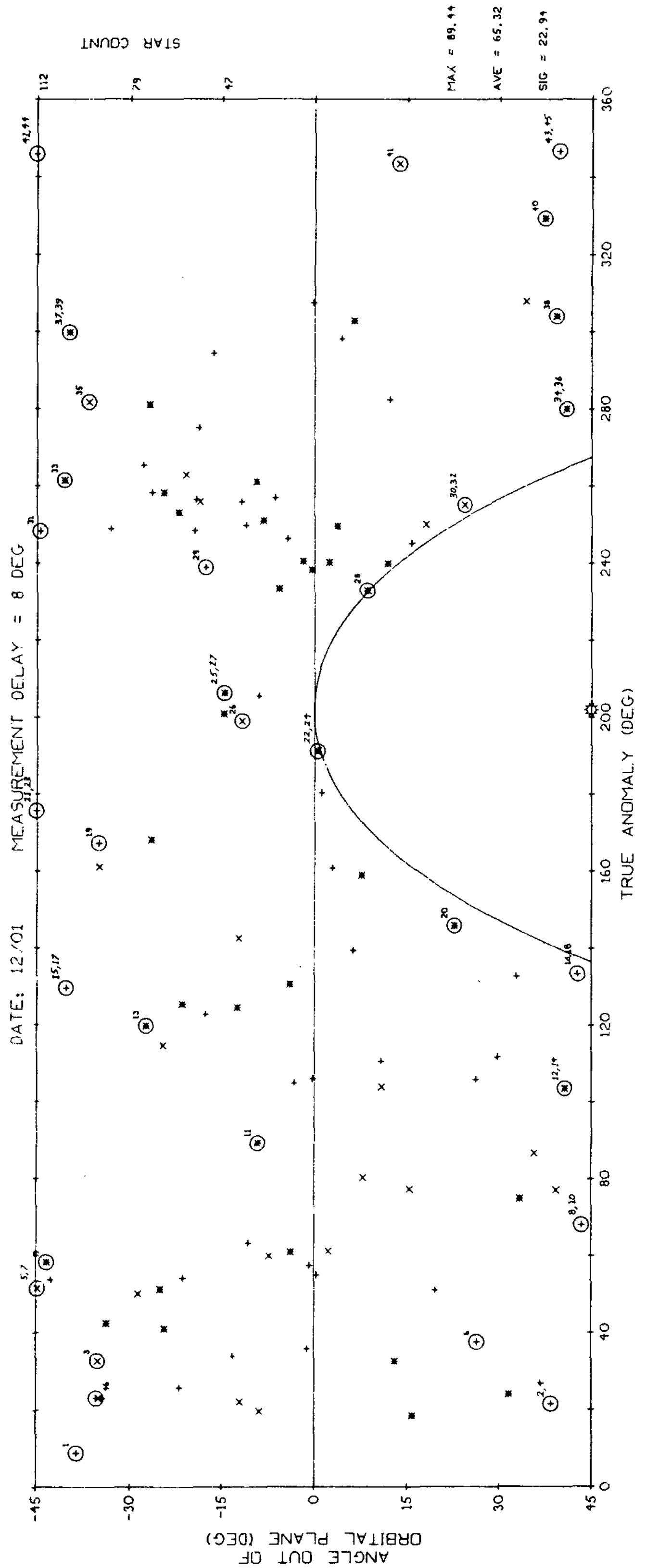
DATE: 12/01
MEASUREMENT DELAY = 8 DEG
TRUE ANOMALY (DEG)
ANGLE OUT OF ORBITAL PLANE (DEG)
STAR COUNT
MAX = 89.44
AVE = 65.32
SIG = 22.94
0
40
80
120
160
200
240
280
320
360
-45
-30
-15
0
15
30
45
112
79
47

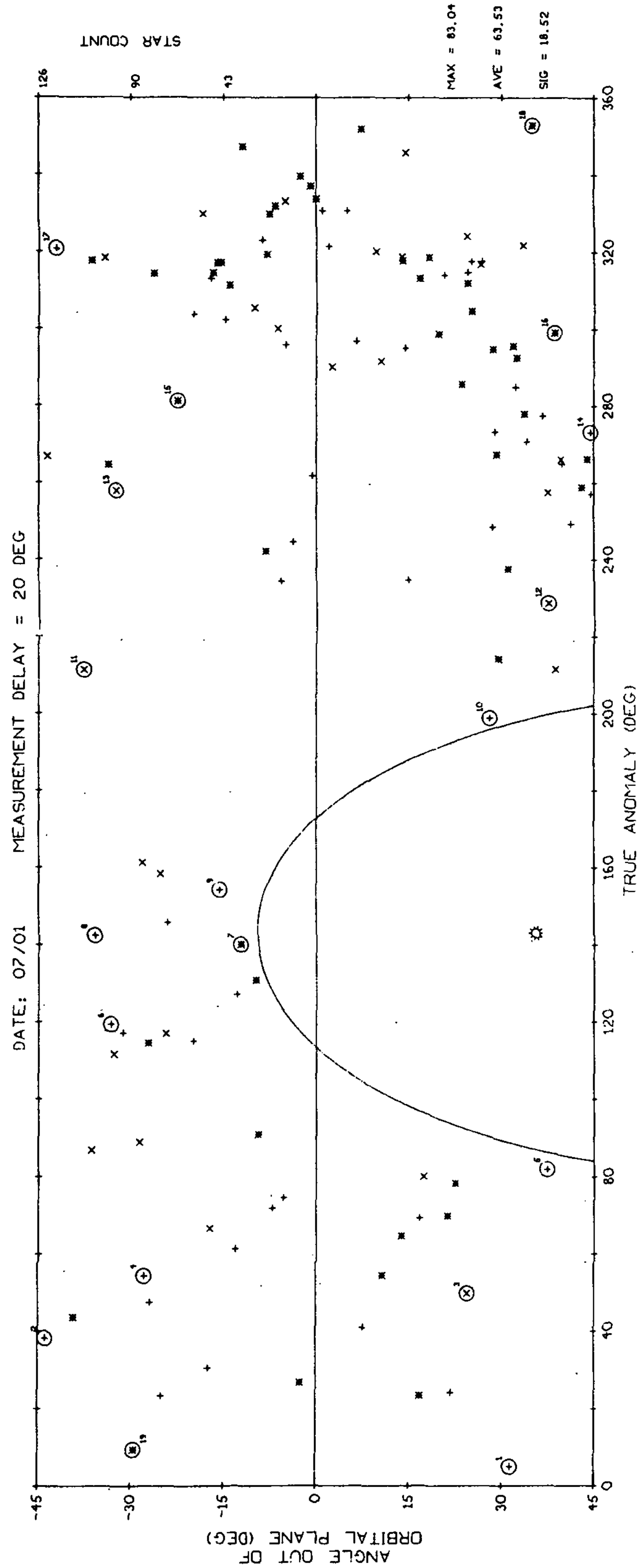

DATE: 07/01
MEASUREMENT DELAY = 20 DEG
STAR COUNT
126
90
43
MAX = 83.04
AVE = 63.53
SIG = 18.52
ANGLE OUT OF ORBITAL PLANE (DEG)
-45
-30
-15
0
15
30
45
TRUE ANOMALY (DEG)
0
40
80
120
160
200
240
280
320
360

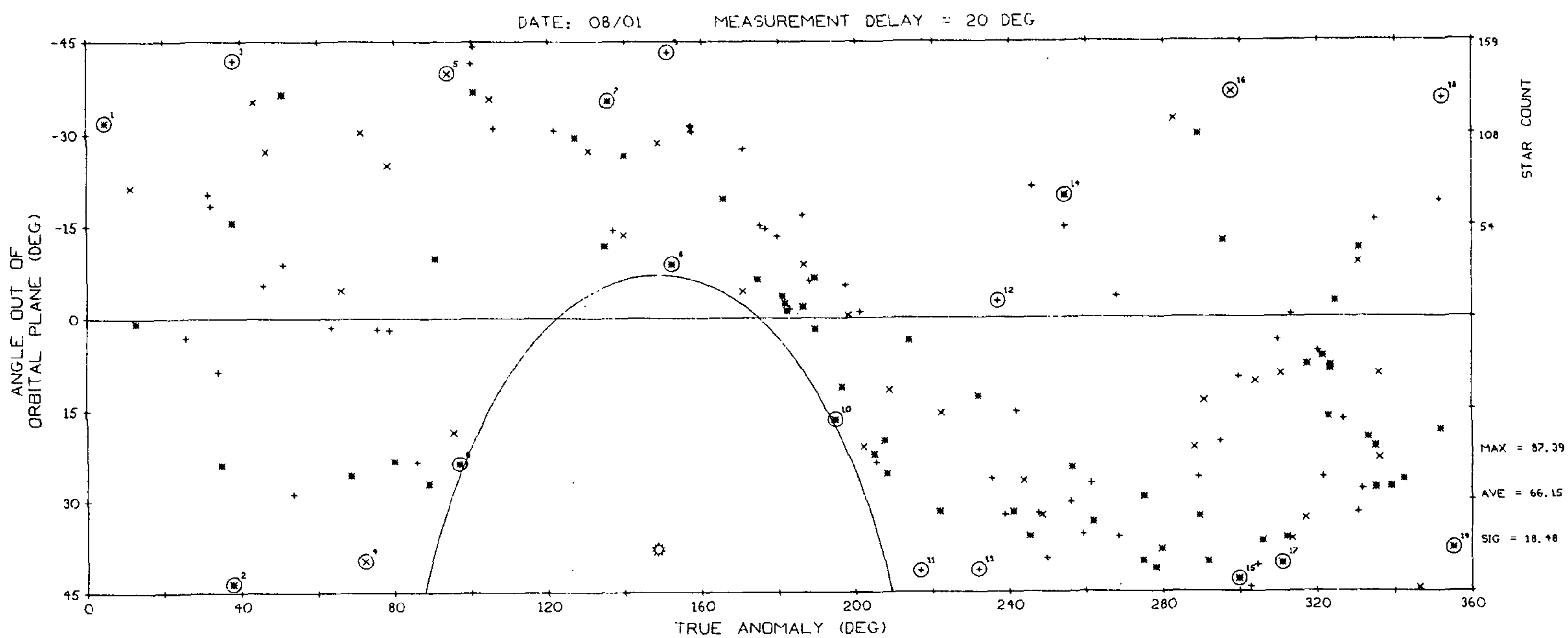

DATE: 08/01
MEASUREMENT DELAY = 20 DEG
ANGLE OUT OF ORBITAL PLANE (DEG)
-45
-30
-15
0
15
30
45
TRUE ANOMALY (DEG)
0
40
80
120
160
200
240
280
320
360
STAR COUNT
159
108
54
MAX = 87.39
AVE = 66.15
SIG = 18.48

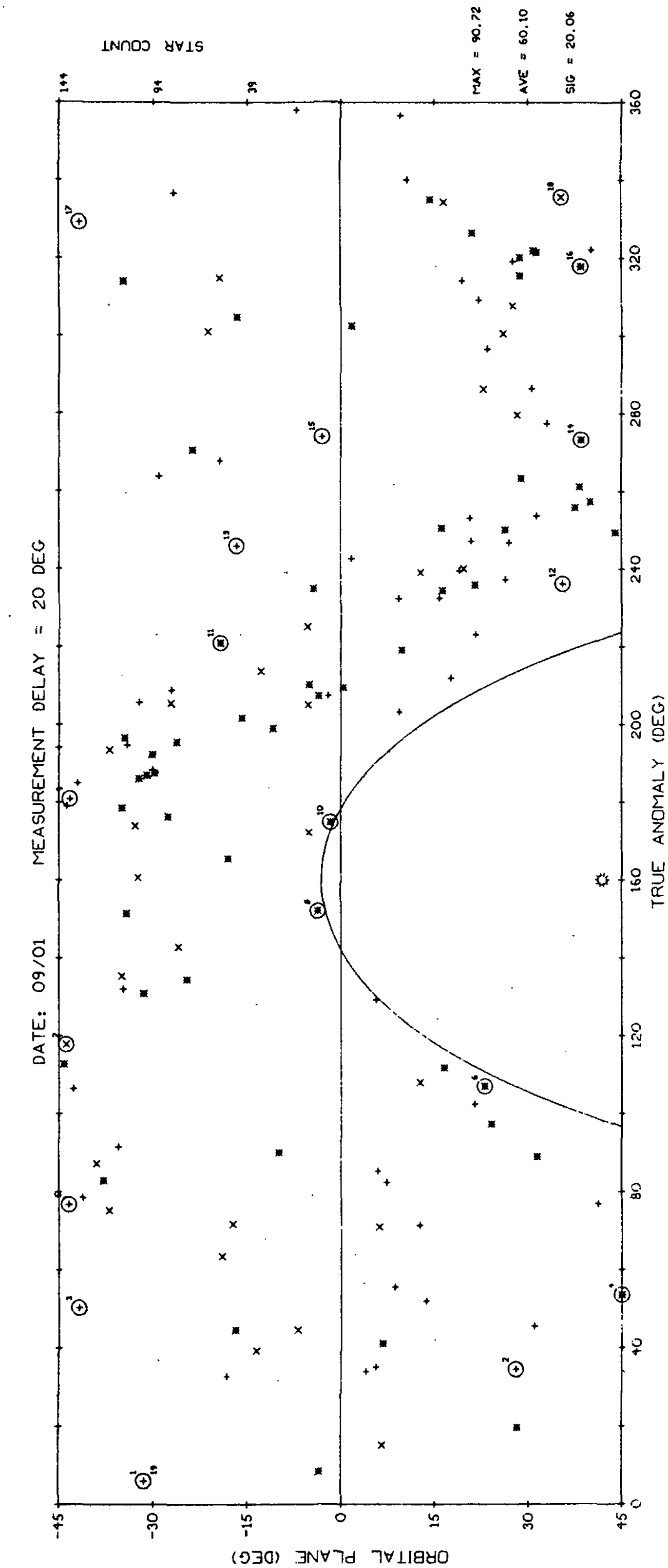
DATE: 09/01
MEASUREMENT DELAY = 20 DEG
STAR COUNT
MAX = 90.72
AVE = 60.10
SIG = 20.06
TRUE ANOMALY (DEG)
ANGLE OUT OF ORBITAL PLANE (DEG)

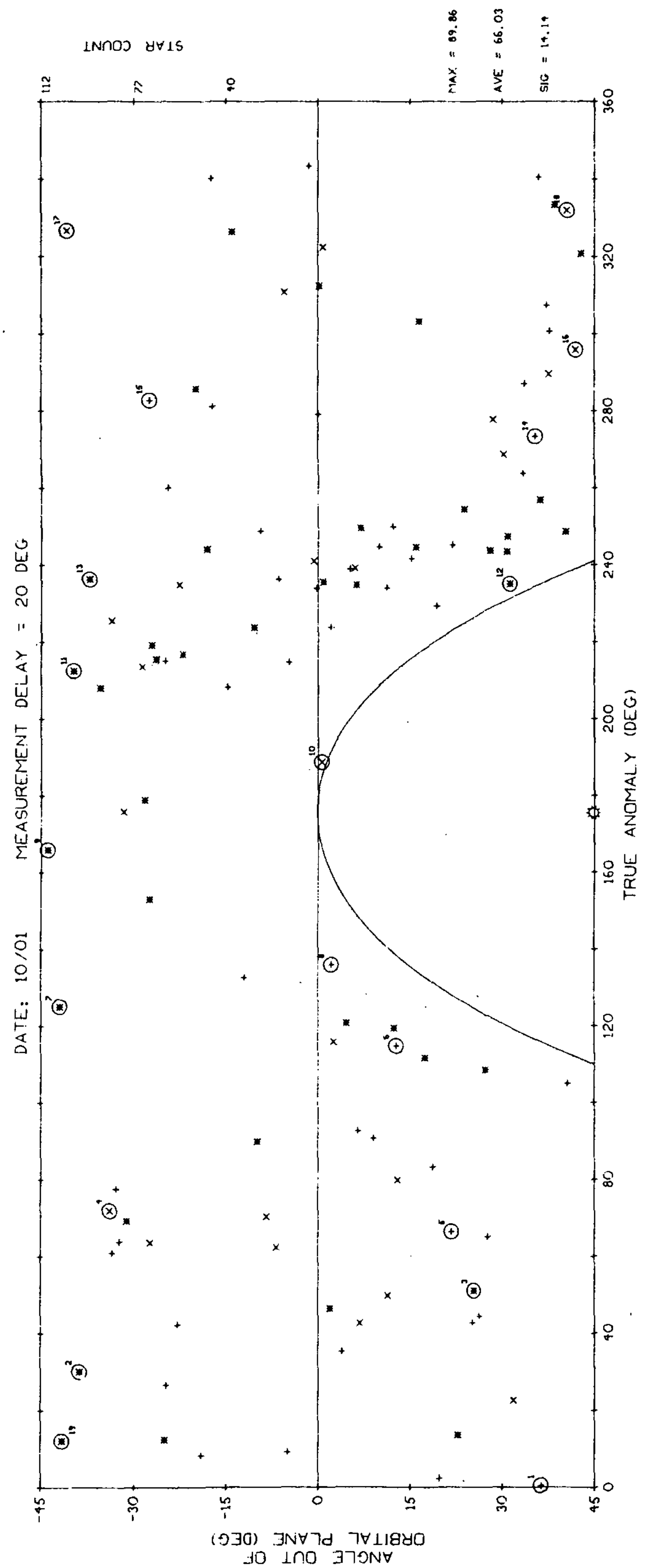
DATE: 10/01
MEASUREMENT DELAY = 20 DEG
STAR COUNT
112
77
40
MAX = 69.86
AVE = 66.03
SIG = 14.14
ANGLE OUT OF ORBITAL PLANE (DEG)
-45
-30
-15
0
15
30
45
TRUE ANOMALY (DEG)
0
40
80
120
160
200
240
280
320
360

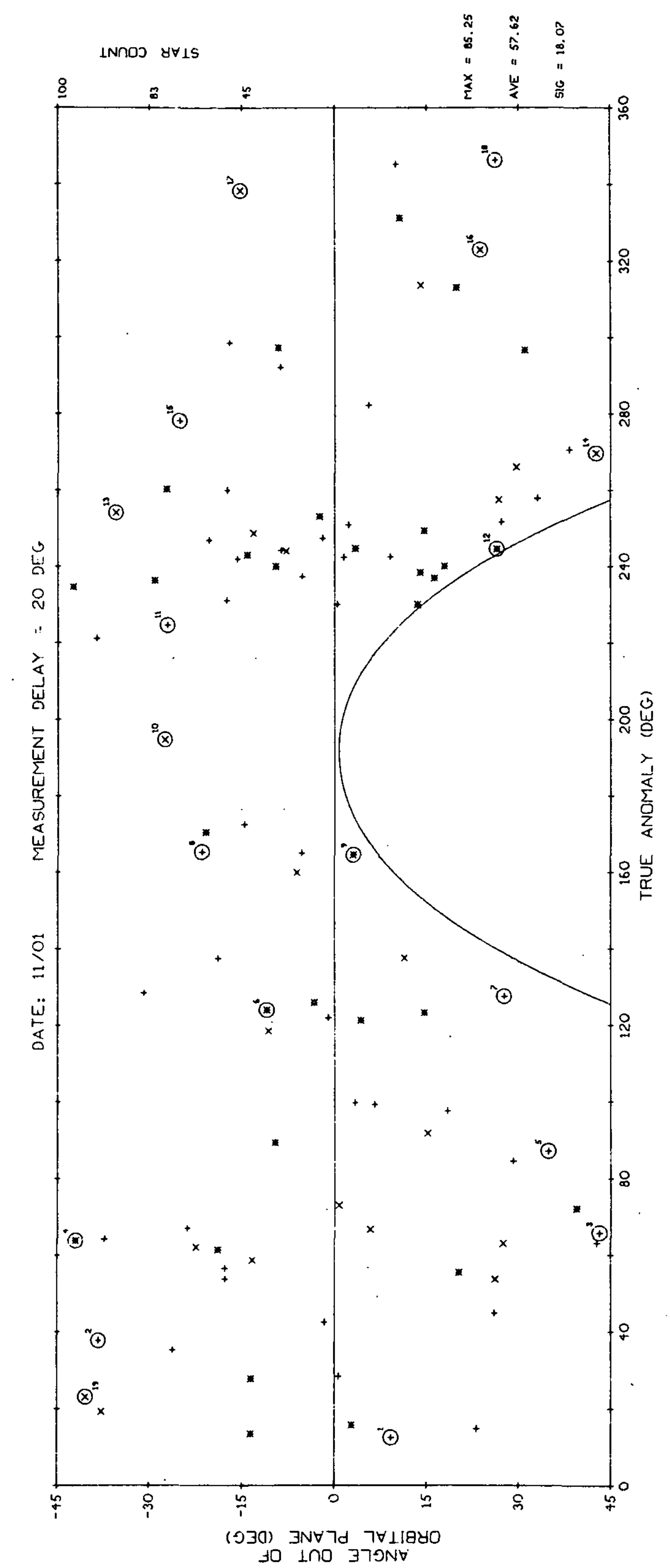
DATE: 11/01
MEASUREMENT DELAY = 20 DEG
STAR COUNT
100
83
45
MAX = 85.25
AVE = 57.62
SIG = 18.07
TRUE ANOMALY (DEG)
0
40
80
120
160
200
240
280
320
360
ANGLE OUT OF ORBITAL PLANE (DEG)
-45
-30
-15
0
15
30
45

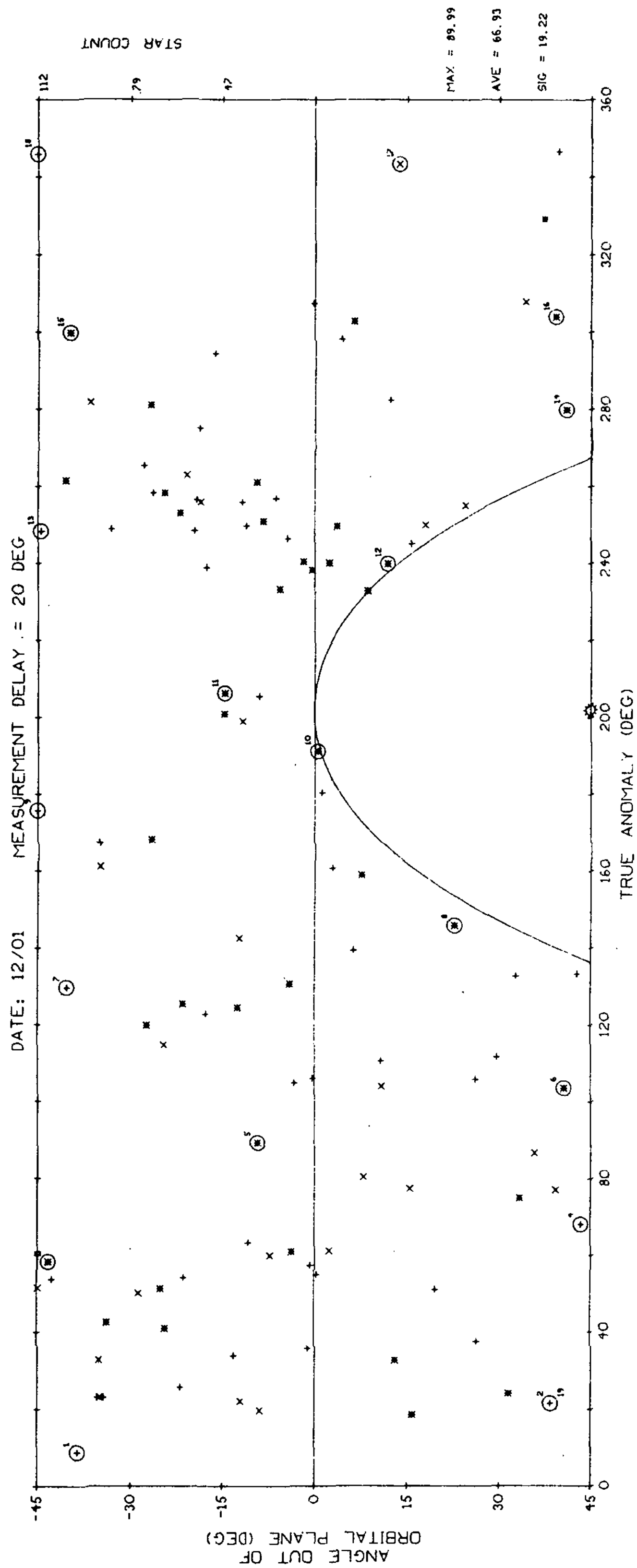
DATE: 12/01
MEASUREMENT DELAY = 20 DEG
TRUE ANOMALY (DEG)
ANGLE OUT OF ORBITAL PLANE (DEG)
STAR COUNT
MAX = 89.99
AVE = 66.93
SIG = 19.22
-45
-30
-15
0
15
30
45
0
40
80
120
160
200
240
280
320
360
112
79
47

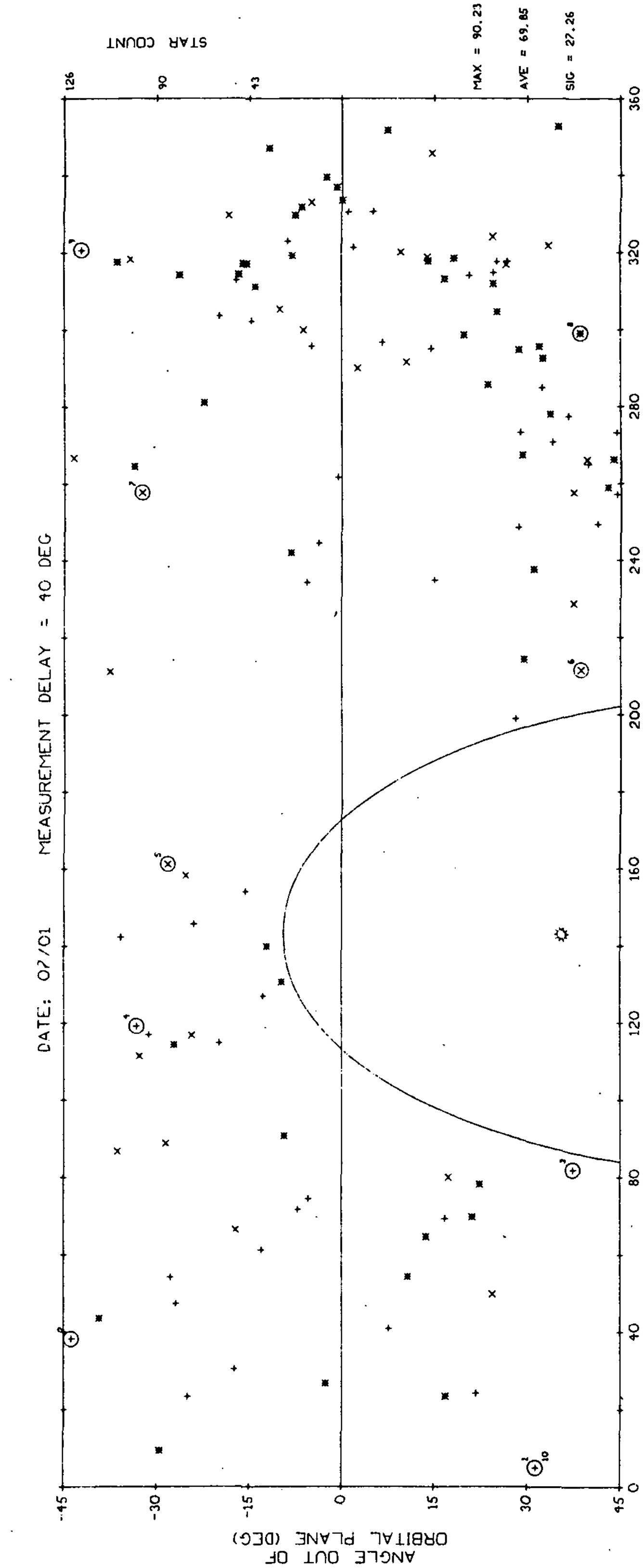
DATE: 07/01
MEASUREMENT DELAY = 40 DEG
TRUE ANOMALY (DEG)
ANGLE OUT OF ORBITAL PLANE (DEG)
STAR COUNT
MAX = 90.23
AVE = 69.85
SIG = 27.26

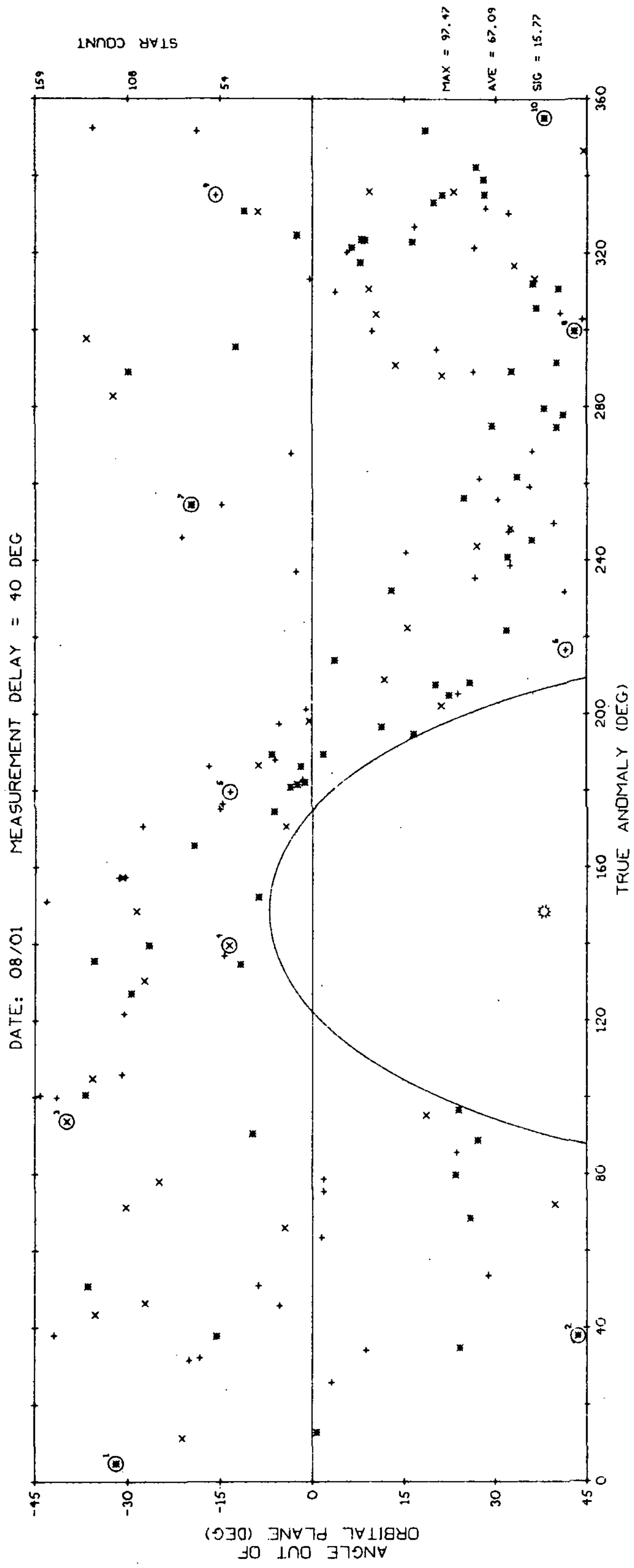
DATE: 08/01
MEASUREMENT DELAY = 40 DEG
STAR COUNT
159
108
54
MAX = 97.47
AVE = 67.09
SIG = 15.77
-45
-30
-15
0
15
30
45
ANGLE OUT OF ORBITAL PLANE (DEG)
0
40
80
120
160
200
240
280
320
360
TRUE ANOMALY (DEG)

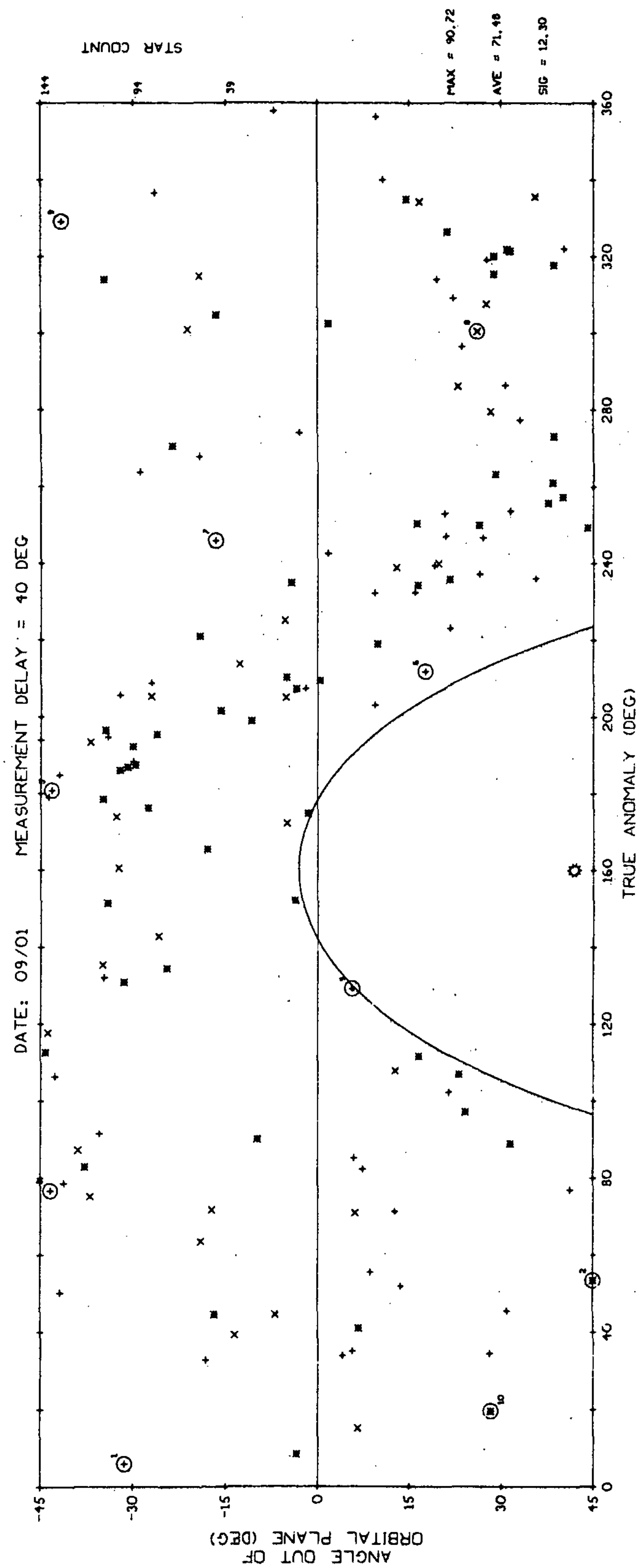
DATE: 09/01
MEASUREMENT DELAY = 40 DEG
TRUE ANOMALY (DEG)
ANGLE OUT OF ORBITAL PLANE (DEG)
STAR COUNT
MAX = 90.72
AVE = 71.48
SIG = 12.30

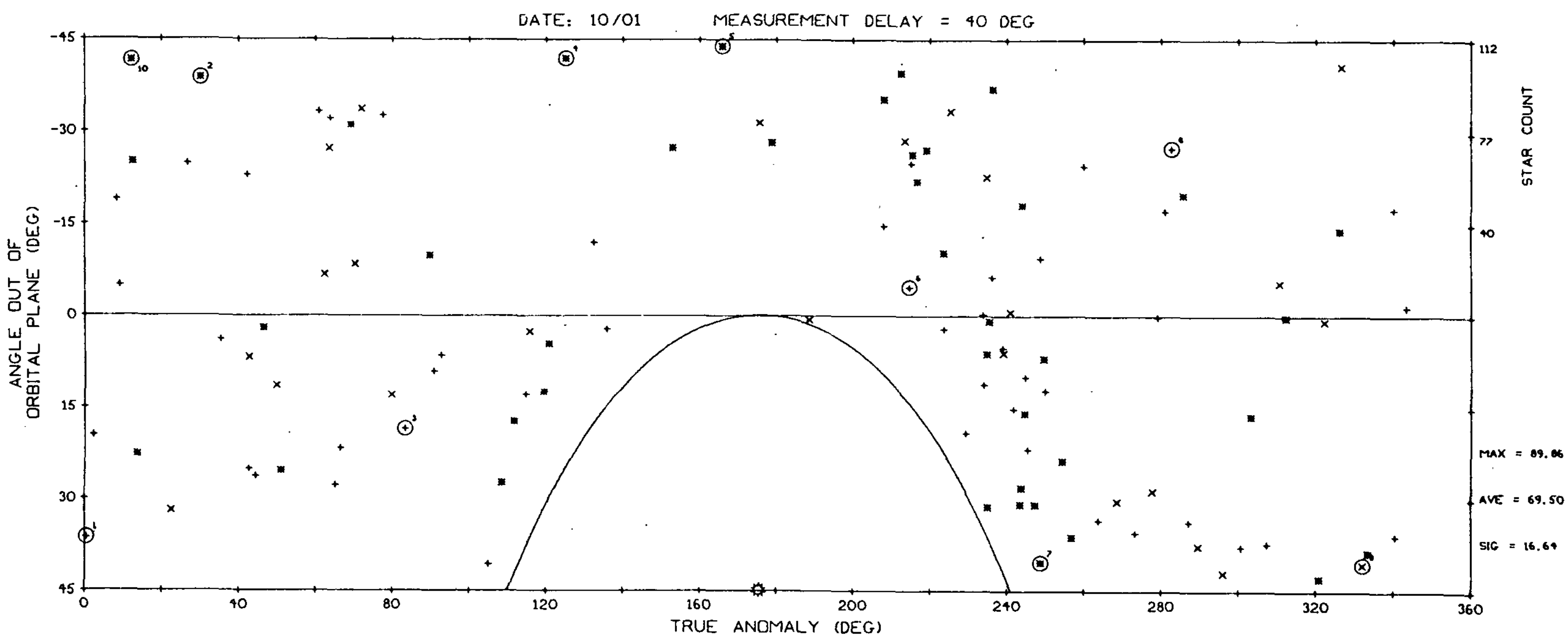
DATE: 10/01
MEASUREMENT DELAY = 40 DEG
ANGLE OUT OF ORBITAL PLANE (DEG)
-45
-30
-15
0
15
30
45
TRUE ANOMALY (DEG)
0
40
80
120
160
200
240
280
320
360
STAR COUNT
112
77
40
MAX = 89.86
AVE = 69.50
SIG = 16.69

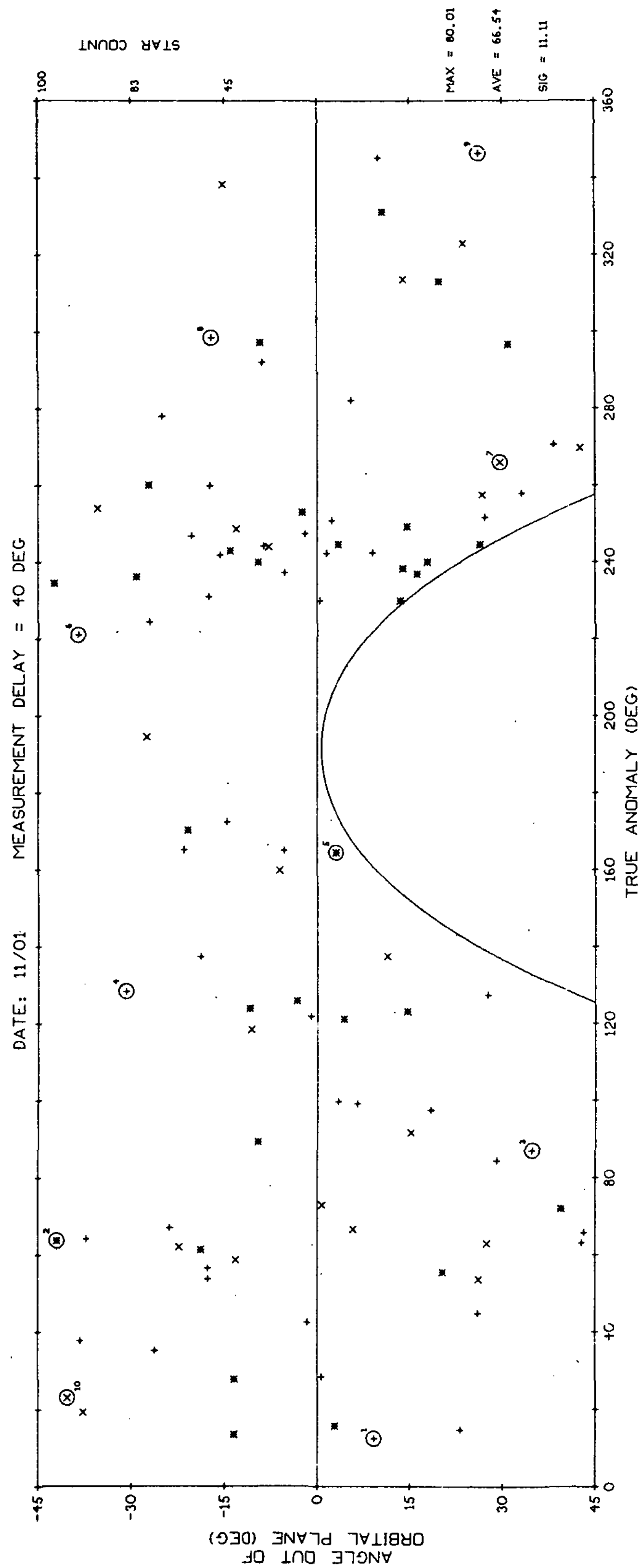

DATE: 11/01
MEASUREMENT DELAY = 40 DEG
TRUE ANOMALY (DEG)
ANGLE OUT OF ORBITAL PLANE (DEG)
STAR COUNT
MAX = 80.01
AVE = 66.54
SIG = 11.11

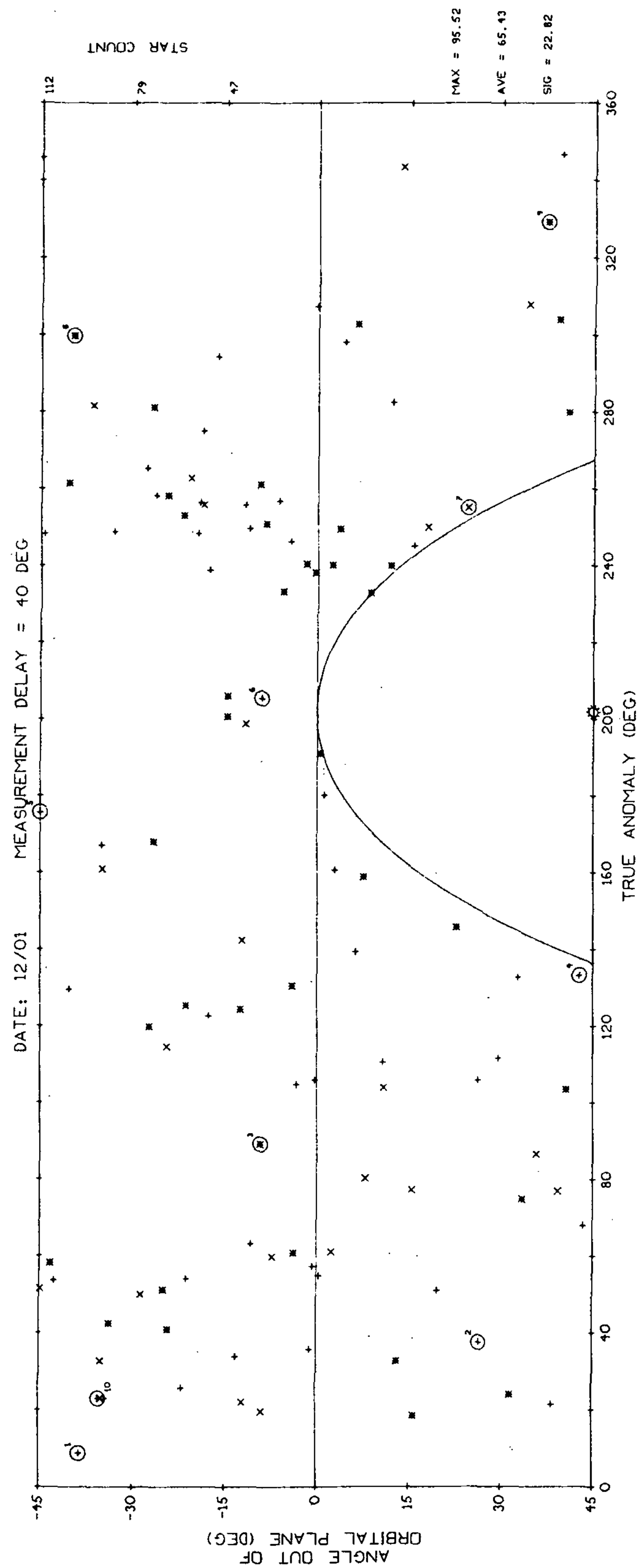
DATE: 12/01
MEASUREMENT DELAY = 40 DEG
STAR COUNT
112
79
47
MAX = 95.52
AVE = 65.43
SIG = 22.82
ANGLE OUT OF
ORBITAL PLANE (DEG)
-45
-30
-15
0
15
30
45
TRUE ANOMALY (DEG)
0
40
80
120
160
200
240
280
320
360

SECTION 7

REFERENCES

1. through 84. (These are the references contained in reference 85.)

85. Glenn Ogletree, with J. Coccoli, R. McKern, M. Smith, R. White, "Interim Technical Report No. 1, Candidate Configuration Trade Study, Stellar-Inertial Measurement System (SIMS) for an Earth Observation Satellite (EOS)," Report E-2616, MIT/CSDL, 5 November 1971.

86. MIT/CSDL Letter Report 71-392L-4, G. Ogletree to Hollie R. Hodges, NASA/MSC, "NAS 9-4065, T.O. 42 (SIMS Configuration Trade Study)", (Fourth) Monthly Letter Report, 8 November 1971.

87. MIT/CSDL Letter Report 71-392L-5, G. Ogletree to Hollie R. Hodges, NASA/MSC, "NAS 9-4065, T.O. 42 (SIMS Configuration Trade Study)", (Fifth) Monthly Letter Report, 9 December 1971.

88. MIT/CSDL Letter Report 72-392L-1, G. Ogletree to Hollie R. Hodges, NASA/MSC, "NAS 9-4065, T.O. 42 (SIMS Configuration Trade Study)", (Sixth) Monthly Letter Report, 10 January 1972.

89. Excerpts from Unpublished Draft, Phase A Report, "EOS System Definition Studies," 1971, under the direction of Wilbur B. Huston, EOS Study Manager, NASA/GSFC.

90. G.B. Autio, D.C. Susens and R.E. Ekstrom to G.W. Tye (of Lockheed Missiles and Space Co.), "GG2200 (P-95) Analysis," Customer Engineering Letter, C.E.L. No. WH-15, 8 May 1968, Honeywell Aerospace Division.

91. G.B. Autio, D.C. Susens and R.E. Ekstrom to J.J. O'Brien (of Lockheed Missiles and Space Co.), "GG2200(P-95) Performance," Customer Engineering Letter, C.E.L. No. WH-34, 6 June 1968, Honeywell Aerospace Division.

92. D.H. Barnhill, J.E. Erickson, D.C. Susens and R.E. Ekstrom to J.J. O'Brien (of Lockheed Missiles and Space Co.), "P-95 IRA Rate Uncertainty Tests," Customer Engineering Letter, C.E.L. No. WH-40, 15 July 1968, Honeywell Aerospace Division.

93. Ronald A. Harris, "Gyro Noise Models for the SIMS Study," SOS-SYS Memo No. 72017, 17 January 1972, MIT/CSDL, (included in this report, with editing for such inclusion, as subsection 5.5).

94. G. Yamamura, "Statistical Analysis of ISA Calibration Data," Interdepartmental Communication, Lockheed Missiles & Space Co., 18 October 1971.

95. David W. Dove, "A Performance Evaluation of A Strapdown Inertial Measurement Unit in the Presence of a Severe Dynamic Environment," Report T-544, MIT/CSDL, January 1971.

96. Jerold P. Gilmore, "A Non-Orthogonal Gyro Configuration," Report T-472, MIT Instrumentation Laboratory (now MIT/CSDL), January 1967, (Chapter VI).

97. D.K. Lloyd and M. Lipow, Reliability: Management Methods and Mathematics, Prentice-Hall, 1962, (p.243).

98. SPARS Phase 1B Star Sensor Electronics, "Preliminary Functional Description", Appendix 19 in Lockheed Missile and Space Corp. Document #690535, July Progress Report to AF/SAMSO.

99. "Analysis of Star Sensor Light Transmitting Areas for Various Aperture and Central Blocking Conditions", Appendix 51 in Lockheed Missile and Space Corp. (LMSC) Document No.A959427, Monthly Progress Report to AF/SAMSO.

100. "Optimization and Evaluation of the SPARS Mod 1B Star Sensor Optical System", prepared by Control Data Corp. Edina Space and Defense Systems, for Appendix 53 in LMSC Document No. A959427, Monthly Progress Report to AF/SAMSO.

101. "Optical System Performance Computer Printout", Appendix 54 in LMSC Document No. A959427, Monthly Progress Report to AF/SAMSO.

102. SPARS Phase 1B Star Sensor Electronics, "Preliminary Breadboard Bench Tests", Appendix 56 in LMSC Document No. A959427, Monthly Progress Report to AF/SAMSO.

103. SPARS Phase 1B Star Sensor Electronics, "Preamplifier Noise Characteristics", Appendix 57 in LMSC Document No. A959427, Monthly Progress Report to AF/SAMSO.

104. "Optical Land Selection for (Uniform) Thermo Tracking", TM-9800-20, SPARS, Control Data Corp, Edina Space and Defense Systems, Oct 15, 1969; Appendix 75 for LMSC Document No. A960503, Monthly Progress Report to AF/SAMSO.

105. "SSA Thermo-Radiant Analysis", TM 9800-22, SPARS, Control Data Corp. Edina Space and Defense Systems, Oct 15, 1969; Appendix 76 for LMSC Document #A960503, Monthly Progress Report to AF/SAMSO.

106. "SPARS Phase 1B - Star Sensor Electronics Dynamic Range Test", TM-9800-23, SPARS, Control Data Corp., Edina Space and Defense Systems, Oct 17, 1969; Appendix 78 for LMSC Document #A960503, Monthly Progress Report to AF/SAMSO.

107. "ENL Photodiode Detector Data", prepared by Control Data Corp., Edina Space and Defense Systems, Nov. 20, 1969, for Appendix 94 for LMSC Document #A960557, Monthly Progress Report to AF/SAMSO.

108. "Honeywell Systems and Research Status Report on SPARS CdS Detectors", prepared by Honeywell, Incorporated, Systems Research, Sept 16, 1970, Appendix 203 for LMSC Document #A977763, Monthly Progress Report to AF/SAMSO.

109. Forbes, F.F. and Mitchell, R.I., "Stellar Photometric Data for Six Different Photocathode Materials and the Silicon Detector", Comm. LPL No. 141, 9, pp 99-119, Dec. 5, 1968.

110. A document from Honeywell Radiation Center submitted to MIT in Response to a request for SIMS-DA Star Mapper Candidate, Jan 1972.

111. "Design and Development of Solid State Detector for SCADS - Final Technical Report", Honeywell Radiation Center, Oct 1971, prepared for NASA GSFC under Contract #NAS 5-11270.

112. "Technical Proposal - Strapdown Solid State Star Sensor, Kollsman KI-494A", Dec 1971, submitted to MIT in response to a request for SIMS-DA Star Mapper Candidate.

113. MIT memo, J.D. Coccoli to M. Smith, "CdS Uniformity," 29 Dec 1971, (Deriving the Distribution of CdS Responsivity Along a Slit from Material in Reference 111).

114. "Star Sensor - Kollsman KI-465A", Feb 1971, prepared by Kollsman Instrument Corp. under an Air Force sub-contract.

115. R.I. Mitchell, and H.L. Johnson, "Thirteen-Color Narrow-Band Photometry of One Thousand Bright Stars," 24 February 1969, Communications of the Lunar and Planetary Laboratory, No. 132, University of Arizona.

116. H.L. Johnson, R.I. Mitchell, B. Triarte, and W.Z. Wisniewski, "UBVRIJKL Photometry of the Bright Stars," 15 April 1966, Comm LPL, No. 63, University of Arizona.

117. D. Hoffleit, 1964, Catalogue of Bright Stars, Yale University Observatory, New Haven, Connecticut.

118. F.F. Forbes, and R.I. Mitchell, "Stellar Photometric Data for Six Different Photocathode Materials and the Silicon Detector," 5 December 1968, Comm. LPL, No. 141, University of Arizona, page 101.

119. Data supplied by Honeywell Inc., Aerospace Division, in letter to Glenn Ogletree, 30 October 1971, from John O. Boutelle.

120. Kollsman Instrument Corp., KS199 SUBSYSTEM Star Catalog, Revision A, 28 April 1969, KS-69-112, pages 1-5.

121. Mitchell & Johnson, Comm LPL, #132, page 15.

122. H.L. Johnson, "The Absolute Calibration of the Arizona Photometry," 15 May 1965, Comm. LPL, no. 53, page 75.

123. Gauss, K.F., Theory of the Motion of the Heavenly Bodies Moving About the Sun in Conic Sections, Dover Press, New York, 1964.

124. Lee, R.C.K., Optimal Estimation, Identification, and Control, MIT Press, Cambridge, Mass., 1964.

125. Kaminski, P.G., "Square Root Filtering and Smoothing for Discrete Processes", Ph.D. Thesis, Department of Aeronautics and Astronautics, Stanford University, Stanford, California, July 1971.

126. Golub, G.H., "Numerical Methods for Solving Linear Least Squares Problems", Numerische Mathematik, Vol. 7, pp. 206-216, 1965.

127. Bryson, A.E., and Frazier, M., "Smoothing for Linear and Nonlinear Dynamic Systems", Wright Patterson Air Force Base, Ohio, Aeronautical Systems Division TDR-63-119, pp. 353-364, September 1962.

128. Cox, H., "On the Estimation of State Variables and Parameters for Noisy Dynamics Systems", IEEE Transactions on Automatic Control, Vol. AC-9, pp. 5-12, January 1964.

129. Rauch, H.E., "Solutions to the Linear Smoothing Problem", IEEE Transactions on Automatic Control, Vol. AC-8, pp. 371-372, October 1963.

130. Rauch, H.E., Tung, F., Striebel, C.T., "Maximum Likelihood Estimates of Linear Dynamic Systems", AIAA Journal, Vol. 3, No. 8, pp. 1445-1450, August 1965.

131. Kalman, R.E., "A New Approach to Linear Filtering and Prediction Theory", Transactions of the ASME, Journal of Basic Engineering, March 1960.

132. Fraser, D.C., "A New Technique for the Optimal Smoothing of Data", MIT Instrumentation Laboratory Report T474, Cambridge, Mass., January 1967.

133. Fraser, D.C., and Potter, J.E., "The Optimum Linear Smoother as a Combination of Two Optimum Linear Filters", IEEE Transactions on Automatic Control, Vol. AC-14, No. 4, pp. 387-390, August 1969.

134. Mayne, D.Q., "A Solution to the Smoothing Problem for Linear Dynamic Systems", Automatica, Vol. 4, pp. 73-92, December 1966.

135. Dyer, P., and McReynolds, S., "Extension of Square Root Filtering to Include Process Noise", Journal of Optimization Theory and Applications, Vol. 3, No. 6, pp. 444-459, 1969.

136. Joseph, P.D.. "Automatic Rendezvous, Part II: Onboard Navigation for Rendezvous Missions", Course notes for "Space Control Systems - Attitude, Rendezvous, and Docking", U.C.L.A. Engineering Extension Course, Los Angeles, California, 1964.

137. "GG334, Gas-Bearing Gyro for Strapped-Down and Gimbaled Inertial Applications," Honeywell Product Data Brochure, anon., undated, (Printer's Data: AD346 12/66).

138. "GI-K7G Miniature Rate Integrating Gyro," Northrup Nortronics Brochure, anon., undated, (Printer's Data: C/N 130-1-68.)

139. Acceptance Data Packages for the Inertial Reference (OAO) for S/N's FS 1, FS 2 and FS 3 - MIT/CSDL documents.

140. "Spectral Density Measurements of Gyro Noise", MIT/CSDL Skipper Group, note SOSS-TST-72005 by A. Truncale, et al, to be published as an E-note.

E-2630

SECTION 8

DISTRIBUTION

EXTERNAL

NASA (MSC) Library (3)

NASA (GSFC) Library (3)

NASA (Hq) Library (3)

NASA/MSC (H.R. Hodges) (5 + 1R)

NASA/GSFC (J.W. Kelly) (20 + 1R)

USAF/SAMSO (Maj. H.A. Briesacher, SYGS) (2)

INTERNAL

MIT/CSDL

Apollo Central Files (2)

Apollo Library (2)

Technical Documentation Center (10)

R. Battin

P. Bowditch

A. Boyce

J. Coccoli

R. Cooper

D. Cox

B. Cuevas

R. Cushing

B. Dane

W. Denhard

C. Draper

W. Drohan

R. Duffy

J.B. Feldman

Julius Feldman

P. Felleman

K. Fertig

K. Fox

D. Fraser

J. Gilmore

F. Grant

G. Grover

Edw. Hall

Eldon Hall

J. Harper

R. Harris
S. Helfant
E. Hickey
F. Houston
B. Hildebrant
D. Hoag
A. Hoch
J. Hursh
R. Hutchinson
J. Kirk
M. Landey
H. Laning
L.E. Larson
J. Lawrence
R. Marshall
P. Matthews
G. Mayo
R. McKern
H. McOuat
E. Mechler
H. Musoff
J. Nelson
J. Nugent
G. Ogletree
R. Ragan
G. Quinn
M. Sappupo
L. Schnee
N. Sears
M. Smith
G. Stubbs
G. Suntheimer
K. Tompkins
M. Trageser
P. Vernam
R. White
R. Woodbury
W. Wrigley
L. Yorgy

MIT

Charles Hayden Library (3)
Engineering Library (3)
Aeronautics and Astronautics Library (3)
Professor Rene Miller
Arthur Smith (Patent Office)
Robert Byers
ILO Files (2)